Modelling Micromechanical Damage of Fusion Reactor Materials

Alvaro Martinez Pechero

St Cross College

Supervisors: Prof. Ed Tarleton, Dr. Yevhen Zayachuk & Dr Anna Widdowson

This thesis has been submitted to the University of Oxford

for the degree of *Doctor of Philosophy*

in the Department of Engineering Science

September 2025

Abstract

Nuclear Fusion presents a promising long-term solution to global energy demands. However, the successful operation of a fusion reactor depends on developing advanced materials capable of withstanding extreme operational conditions. This thesis employs Finite Element Models (FEM) to study the fracture properties of key candidate materials. It investigates the damage mechanisms from brittle fracture to complex orientation-dependent ductile-brittle fracture.

The first chapters focus on the fracture mechanics of Silicon Carbide (SiC) fibre-reinforced composites with PyC interphase. FEM simulations of fibre push-out experiments characterised interfacial properties and determined the optimal length in fibre tests to be more effective for isolating interfacial debonding stress from frictional effects. This establishes the debond stress as a consistent and predictable material property, whereas friction was found to be dependent on fibre geometry and residual stresses.

Subsequently, a crystal plasticity open-access code (OXFORD-UMAT) was developed to model plastic deformation through Geometrically Necessary Dislocation (GND) densities. The code includes internal physical mechanisms for a more accurate GND calculation, which prevents erroneous hardening.

This framework was then applied to model the Bauschinger effect in copper, a material employed for stress relief during the cyclic fusion reactor operations. The results showed that existing kinematic hardening models fail to capture initial loading cycles. A new proposed model proved to be successful by incorporating the conversion of part of the GNDs into statistically stored dislocations, consistent with experimental evidence.

Finally, a comprehensive fracture model in single-crystal beryllium was developed by integrating the OXFORD-UMAT with eXtended Finite Element Method (XFEM). This approach simulates the entire failure process from plastic deformation to fracture, successfully reproducing experimental data for different crystal orientations. The model reveals that the material's strong orientation-dependent failure is governed by the combined effect of Mode I (elastic) and Mode II (plastic) fracture.

Acknowledgments

This dissertation is dedicated to my family and my partner. Their countless sacrifices and support have been instrumental in my journey. Without their encouragement, guidance, and the confidence they've instilled in me, pursuing this academic path thousands of miles from home would not have been possible.

I extend my heartfelt gratitude to my supervisors, Prof. Edmund Tarleton, Dr. Yevhen Zayachuk, and Dr. Anna Widdowson, for their patience and dedicated mentorship throughout this project. Collaborating with them has been both enjoyable and enriching, and their support, advice, and optimism were crucial in ensuring the progression of my work. I couldn't have asked for better guidance during the PhD.

I am also deeply grateful to Dr Eralp Demir for his guidance and invaluable contributions. His expertise in crystal plasticity has significantly enhanced my understanding of the subject, and he has played a crucial role in shaping my research. His willingness to engage in thoughtful conversations has fostered a collaborative atmosphere that enriched my academic experience.

Additionally, I would like to express my sincere gratitude to Dr Slava Kuksenko, Dr Alex Leide, Dr Daniel J. Long, Dr Christopher D. Hardie, Prof. David Armstrong, Dr Luke Hewitt, Prof. Jan Coenen, Dr Rui Shu, and Dr Yiran Mao for their collaborative efforts and the engaging conversations we shared. Their contributions through high-quality experiments were essential to the success of this work, and their welcoming attitudes fostered a supportive environment throughout the research process. I would also like to extend special thanks to Prof. Felix Hoffmann and Prof. John Huber for their insightful guidance and constructive feedback during the evaluation of my progress.

I appreciate all my colleagues, friends and office-mates in the Engineering Department for fostering a pleasant work atmosphere. I am particularly thankful to Gordon Kumar, Beatrix Curtis, Anna Taipale and Pablo Soëtard for their friendship and support, which have greatly alleviated stress throughout this journey.

I would also like to thank the staff and friends from St Cross College, who have made my stay at Oxford greatly enjoyable. Finally, I would like to thank the Oxford Department of Engineering Science, the UKAEA and the EPSRC Energy Programme [grant number EP/W006839/1] who gave me this opportunity 4 years ago.

Glossary

A-F Armstrong-Frederick

Be Beryllium

CP Crystal Plasticity

CRSS Critical Resolved Shear Stress

Cu Copper

CVD Chemical Vapour Decomposition

CVI Chemical Vapour Infiltration

DEMO Demonstration Fusion Power Reactor

DT Deuterium-Tritium

ESBD Electron Backscattered Diffraction

FCC Faced-Centred Cubic

FEM Finite Element Modelling

FIB Focused Ion Beam

GND Geometrically Necessary Dislocations

HCCB Helium Cooled Ceramic Breeding Blanket

HCP Hexagonal Close Packed

IP Integration Points

ITER International Thermonuclear Experimental Reactor

JET Joint European Torus

KAM Kernel Average Misorientation

KKT Karush-Kuhn Tucker

L2 Least Squares

LEFM Linear Elastic Fracture Mechanics

LRIS Long-Range Internal Stresses

MCF Magnetic Confinement Fusion

PCF Plasma Facing Components

PFM Phase field modelling

PSB Persistent Slip Bands

PyC Pyrolytic Carbon

RVE Representative Volume Element

SEM Scanning Electron Microscopy

SiC Silicon Carbide

SSD Statistically Stored Dislocations

STEP Spherical Tokamak for Energy Production

SVD Singular Value Decomposition

TEM Transmission Electron Microscopy

UKAEA UK Atomic Energy Authority

VCCT Virtual Crack Closure Technique

XFEM Extended Finite Element Modelling

Contents

1 Introduction **1**

2 Scientific background & Methods **4**
2.1 Fracture Mechanics . . . 4
2.1.1 Linear Elastic Fracture Mechanics . . . 4
2.1.2 J-Integral . . . 6
2.1.3 Virtual Crack Closure Technique . . . 6
2.1.4 Cohesive zone modelling . . . 7
2.1.5 Bilinear law . . . 8
2.1.6 Toughness in LEFM versus CZM . . . 9
2.1.7 EXtended Finite Element Method (XFEM) . . . 11
2.1.8 Other methods: phase field modelling and peridynamics theory . . . 11
2.2 Crystal plasticity . . . 12
2.2.1 Semi-Implicit method . . . 13
2.2.2 Fully Implicit method . . . 15
2.2.3 Forward-Gradient method . . . 15
2.2.4 Sinh slip law . . . 16
2.3 SiC fibre-reinforcement composites . . . 17
2.3.1 Push-out theory . . . 18
2.3.2 Short fibre . . . 19
2.4 Copper . . . 20
2.4.1 Bauschinger effect . . . 20
2.5 Beryllium . . . 22
2.5.1 Hexagonal Close Packed slip systems of Be . . . 23
2.5.2 Cantilever experiments . . . 24

3 Obtaining SiC fibres-PyC interfacial properties through push-outs FEM Models **26**
3.1 Abstract . . . 27
3.2 Introduction . . . 27
3.3 Push-out experiments . . . 28
3.3.1 Fibre-reinforced ceramic composites . . . 29
3.3.2 Fibres and PyC interphase . . . 29
3.3.3 Push-out measurements . . . 30
3.4 Finite element models . . . 31
3.4.1 Elastic Models of SiC matrix . . . 32
3.4.2 Cohesive zone model (CZM) . . . 33
3.4.3 Nelder-Mead optimisation . . . 35
3.5 Results and discussion . . . 37
3.5.1 SiC matrix Nanoindentations . . . 37
3.5.2 Fibre Push-outs . . . 39
3.5.3 Shear strength for high stiffness interfaces . . . 44
3.6 Conclusions . . . 45
3.7 Statement of Authorship form . . . 46

4 Progress towards a micro fibre push-out method for measuring fibre-matrix interface properties in SiC composites **47**
4.1 Abstract . . . 48

4.2 Introduction . . . 48
4.3 Methodology . . . 49
4.3.1 Materials . . . 49
4.3.2 Sample preparation . . . 50
4.3.3 Push out testing . . . 51
4.3.4 Characterisation . . . 51
4.3.5 Modelling . . . 51
4.4 Results . . . 53
4.4.1 Fibre push-out testing . . . 53
4.4.2 Weibull analysis . . . 55
4.4.3 Microstructural analysis . . . 56
4.4.4 FEM simulations of micro push-out experiments . . . 57
4.4.5 Parametric study – interfacial properties . . . 64
4.4.6 Parametric study – axial misorientation angle . . . 65
4.4.7 Parametric study – taper . . . 68
4.5 Discussion . . . 73
4.5.1 Considerations for short fibre push-out testing . . . 73
4.5.2 Fibre push-out mechanisms and implications . . . 74
4.6 Conclusions . . . 76
4.7 Statement of Authorship form . . . 78

5 Restraining geometrically necessary dislocations to the active slip systems in a crystal plasticity finite element framework 80
5.1 Abstract . . . 81
5.2 Introduction . . . 81
5.3 Modelling . . . 83
5.3.1 Crystal plasticity kinematics . . . 83
5.3.2 Constitutive laws . . . 84
5.3.3 Strain-gradient models . . . 85
5.3.4 Summary of GND models . . . 95
5.3.5 Gradient operator (element type specific) . . . 96
5.3.6 Numerical method and important constraints . . . 99
5.4 Results and Discussion . . . 99
5.4.1 Strain-gradient-free uniaxial tension (single crystal single slip) . . . 100
5.4.2 Simple shear of a strip . . . 101
5.4.3 Uniaxial tension with strain gradient . . . 103
5.4.4 Four-point bending . . . 107
5.4.5 Polycrystal . . . 116
5.5 Conclusions . . . 119
5.6 Statement of Authorship form . . . 121

6 Modelling the Bauschinger effect in copper during preliminary load cycles 123
6.1 Abstract . . . 124
6.2 Introduction . . . 124
6.3 Cantilever Experiment . . . 126
6.4 Crystal plasticity framework . . . 127
6.4.1 Crystal plasticity kinematics . . . 128
6.4.2 Constitutive laws . . . 129
6.5 GND model . . . 130
6.6 Modelling Bauschinger effect . . . 130
6.6.1 Armstrong-Frederick model . . . 131
6.6.2 Orowan-Sleeswyk model . . . 133
6.6.3 Finite Element Method (FEM) . . . 134

6.7 Results and Discussion . . . 135
6.7.1 Armstrong Frederick based models . . . 135
6.7.2 Orowan-Sleeswyk models . . . 139
6.7.3 Modelling bending/straightening 1^{st} cycle . . . 142
6.7.4 Comparison of A-F model with Voce-type hardening and Orowan-Sleeswyk model with SSD . . . 144
6.7.5 Improvement to the *Orowan-Sleeswyk* model with SSD after multiple cycles . . . 145
6.8 Conclusions . . . 146
6.9 Statement of Authorship form . . . 148

7 Single-Crystal Beryllium Cracking: A Crystal Plasticity XFEM Model 149
7.1 Abstract . . . 150
7.2 Introduction . . . 150
7.3 Cantilever experiments . . . 151
7.4 Modelling . . . 155
7.4.1 Crystal plasticity framework . . . 155
7.4.2 Extended Finite Element Method (XFEM) . . . 158
7.4.3 Boundary conditions, mesh, and Indenter Modelling . . . 162
7.5 Modelling Results . . . 163
7.5.1 Parameter Sensitivity . . . 168
7.6 Conclusions . . . 169

8 Thesis Conclusions and Future Work 171
8.1 Conclusions . . . 171
(a) SiC fibre-reinforced composite with PyC interphase . . . 172
(b) Modelling plasticity in metals based on GNDs . . . 173
(c) Modelling Bauschinger effects during preliminary load cycles . . . 174
(d) Modelling fracture in Single-Crystal Beryllium . . . 175
8.2 Future work . . . 175

Appendix A: Short fibre push-outs 177
A.1 Experimental indenter tip effects . . . 177
A.2 Axial misorientation geometry . . . 177
A.3 Failure process of a short fibre . . . 179
A.4 Mesh of the fibre-push out model. . . . 180
A.5 Shear stress over the interface of Fibre F6 . . . 182

Appendix B: Restaining GNDs to active slip systems 183
B.1 Crystal to sample transformation . . . 183
B.2 Emergence of GNDs in inactive slip systems using L^2 . . . 183
B.3 Noise analysis of L2 and KKT models . . . 187

Appendix C: Modelling Bauschinger effect 190
C.1 Comparison of Node Line and Indenter of Copper . . . 190
C.2 Convergence study of Copper . . . 191
C.3 Slip systems activation of Copper . . . 192

Appendix D: Single-Crystal Beryllium Cracking: A Crystal Plasticity XFEM Model 194
D.1 Corrections of the force-displacement experimental curves of Beryllium cantilevers . . . 194
D.2 Berkovich indenter effect in Beryllium . . . 195

References 196

Chapter 1: Introduction

The demand for energy increases every year with the growth of human development and population. International Energy Agency studies [1] predict a 50% increase in energy demand between 2018 to 2040, a challenge that is very difficult to achieve with renewable energy sources alone, as traditional fossil fuel sources must disappear due to the negative effects on the climate change and fission nuclear energy it is not always well accepted by the population because of its radioactive waste and the danger of an accident like Fukushima. In this context, nuclear fusion could be a solution to the energy crisis; it is reliable, safe, potentially abundant and produces very little long-lived radioactive waste [2].

Nuclear fusion is a reaction in which two atomic nuclei combine to form a heavier nucleus that subsequently may decay into different products. The energy released by the reaction is obtained from the strong nuclear force, which is the result of the difference in atomic binding energy between the initial nuclei and the final products [3].

Before two nuclei can interact via the strong nuclear force, they must overcome the Coulomb barrier potential, which is proportional to the expression $e^2/(4\pi\varepsilon_0 r_{\mathrm{m}})$ (where r_m is the minimum distance without influence of the strong force and ε_0 is the vacuum permittivity). To overcome the Coulomb barrier, the most common method for fusion is to heat fuels to extremely high temperatures and pressures. Deuterium-tritium (DT) is the preferred fuel for fusion reactors because it has the largest cross-section to fuse [4], through the reaction:

$$ {}^{2}_{1}D + {}^{3}_{1}T \rightarrow {}^{4}_{2}\mathrm{He}(3.52\mathrm{MeV}) + \mathrm{n}^{0}(14.06\mathrm{MeV}). \tag{1.0.1} $$

For the DT reaction, temperatures of $15{\cdot}10^{6}$°C and pressure of $100 \cdot 10^{9}$ atm are required [5]. While these conditions are found in the centre of stars, where immense gravitational pressure sustains the reaction, replicating such pressure on Earth is not possible and must be compensated by higher temperatures than those found in stars. Given these extreme conditions, scientists have developed various approaches to achieve fusion on Earth, with *Magnetic Confinement Fusion* (MCF) [6] being the most used. In this approach, the DT fuel is heated to a plasma state while it is confined in a toroidal structure and separated from the *first wall* by high magnetic fields generated by superconductors. Inside this toroidal magnetic confinement, particles move from the edges towards the centre, where they fuse and release energy.

MCF faces significant challenges, particularly with the materials used in the reactor. The primary issue is

that plasma instabilities can damage the reactor's *first wall*, the inner lining that directly faces the plasma [7]. To protect the structure, *plasma-facing materials* must have exceptional properties, including high-energy particle and high thermal load resistance [8].

Behind the *first wall*, the *blanket* structure protects the reactor from the irradiation of neutrons produced during fusion. These neutrons are captured by an outer layer of lithium [9], which is converted into tritium that is used as fuel for subsequent fusion reactions (see Eq. (1.0.2)). To achieve this reaction efficiently in terms of tritium inventory (more than one tritium is generated for each tritium/neutron consumed), neutrons need to multiply through materials such as Beryllium.

$$\mathrm{Li}^6 + \mathrm{n} \rightarrow \mathrm{T} + \mathrm{He}^4 + 4.8\mathrm{MeV}; \quad \mathrm{Li}^7 + \mathrm{n} \rightarrow \mathrm{T} + \mathrm{He}^4 + \mathrm{n} - 2.5\mathrm{MeV} \tag{1.0.2}$$

Protecting the fusion reactor from plasma, neutron irradiation, tritium permeation, and thermal stresses on its structures presents a significant engineering challenge. Addressing this challenge requires not only experimentally assessing the lifespan of materials [10, 11], but also employing advanced computational models capable of explaining fracture experiments or predicting new scenarios.

Among the computational models, *Finite Element Modelling* (FEM) [12] is an essential tool to accurately simulate the initiation and propagation of cracks within the reactor structures. Its advantages include flexibility in handling complex geometries, reduced cost, speed and accuracy.

This thesis research, entitled ***"Modelling Micromechanical Damage of Fusion Reactor Materials"***, is composed of several FEM studies of different materials used or being developed for the *blanket* and the *first wall* of fusion reactors: *Silicon Carbide - Pyrolytic Carbon (SiC-PyC) fibre-reinforcement composites*, *Copper* and *Beryllium*. Additionally, it includes a computational study to calculate the density of *geometrically necessary dislocations* (GND), defects in the crystalline structure of metals responsible of fatigue, hardening and crack formation.

The thesis is integrated by a collection of journal publications (published or pre-print), with **Chapter 2** serving as a literature review of Fracture Mechanics, Crystal Plasticity, and an overview of the materials and experiments studied.

Chapter 3 is based on the article ***Obtaining SiC fibres-PyC interfacial properties through push-outs FEM Models*** published in the Journal of the European Ceramic Society [13]. Where we proposed an approach based on *Cohesive Zone Modelling (CZM)* [14] combined with *Nelder-Mead optimisation* [15] to estimate fracture parameters like toughness, interfacial shear strength, and Coulomb friction of *SiC-PyC fibre-reinforced composites*, a material proposed for the structure of the breeding blanket.

Chapter 4 is based on the article ***Progress towards a micro fibre push-out method for measuring fibre-matrix interface properties in SiC composites*** published in the Journal of the European Ceramic Society [16], in which short-fibre experiments of SiC fibre-reinforced composites designed to mitigate the friction due to fibre swelling are modelled.

Chapter 5 is based on the article ***Restraining geometrically-necessary dislocations to the active slip systems in a crystal plasticity-based finite element framework*** published in the International Journal of Plasticity [17]. In this work, various methods for calculating *Geometrically Necessary Dislocations (GNDs)* were implemented in a Crystal Plasticity FEM code known as OXFORD-UMAT [18]. GNDs are dislocations generated by strain gradients within a material [19] and are responsible for strain hardening, softening, creep, and crack formation. The article compares these different methods, presents improvements to some techniques, and explains the framework of the code, which is designed to assess a wide variety of materials used in fusion reactors.

Chapter 6 is based on the article ***Modelling the Bauschinger effect in copper during preliminary load cycles*** published in Acta Materialia [20]. This work focuses on the role of GNDs in the Bauschinger effect of metals. The chapter studies various kinematic hardening models in combination with isotropic hardening models, and a new relationship between them is proposed. These models were used to reproduce the experiments of copper monocrystal cantilevers that were bent in different directions [21].

Chapter 7 includes the preprint article ***Single-Crystal Beryllium Cracking: A Crystal Plasticity XFEM Model***. This chapter applies the *OXFORD-UMAT FEM* code to replicate fracture in notched cantilevers made of monocrystal beryllium, a neutron multiplier used in fusion reactors [22]. Beryllium is an *Hexagonal Close-Packed* (HCP) material whose fracture properties present a significant challenge due to its anisotropic nature, exhibiting either very plastic or brittle behaviour depending on crystallographic orientation. This research combined several fracture techniques: *eXtended Finite Element Method* (XFEM) [23] to calculate crack direction, *Cohesive Zone Modelling* to model crack formation (similar to Chapters 3 and 4), and *Crystal Plasticity* to determine the stress-strain relation (similar to Chapters 5 and 6).

Finally, in **Chapter 8**, the thesis presents its overall conclusions and proposes future work.

Chapter 2: Scientific background & Methods

This chapter reviews the literature on the modelling techniques and materials used in the thesis, which include SiC fibre-reinforced, Copper, and Beryllium. Section 2.1 provides an overview of fracture mechanics techniques applied with *Finite Element Modelling*. Section 2.2 reviews the Crystal Plasticity Framework and the plasticity laws used to model metals. Sections 2.3, 2.4, 2.5 summarise the uses of SiC fibre-reinforced, Copper, and Beryllium in fusion energy and the techniques used to study them.

2.1 Fracture Mechanics

Fracture is the separation of a solid material into two or more pieces under the action of stress. Inside fusion reactors, the constant mechanical stresses can lead to fractures inside the components, leading to potential issues like dust formation, reactor underperformance, and even fuel leaks [24].

Fracture mechanics studies the initiation and propagation of cracks in materials. In elastic material, continuum mechanics theory predicts that the stress ahead of the crack tip becomes infinite and cannot be used to describe the state around the crack [25]. The following sections are an overview of the theory and numerical techniques developed to study the formation and propagation of cracks that overcome the limitations of continuous mechanics.

2.1.1 Linear Elastic Fracture Mechanics

Linear Elastic Fracture Mechanics (LEFM) was the first theory to overcome the issue of infinite stress at the crack tip. It applies the theory of continuum mechanics to the material except around the crack. To describe the degradation in this region, it defines the *stress intensity factors* K_i, and classifies the fractures into three types according to the direction of the deformation (Fig. 2.1):

- *Mode I - Opening mode*: Tensile stress is normal to the crack plane.
- *Mode II - Sliding mode*: Shear stress acts parallel to crack plane and perpendicular to the crack front.
- *Mode III - Tearing mode*: Shear stress acts parallel to both the crack plane and crack front.

The first study to apply these concepts and the principle of minimal energy to define crack formation was conducted by Griffith [26]. In this work, a crack was approximated by an elliptical hole (with a major axis a and minor axis $\sim$0) located at the centre of an infinite plane. This plane was under tension in the minor

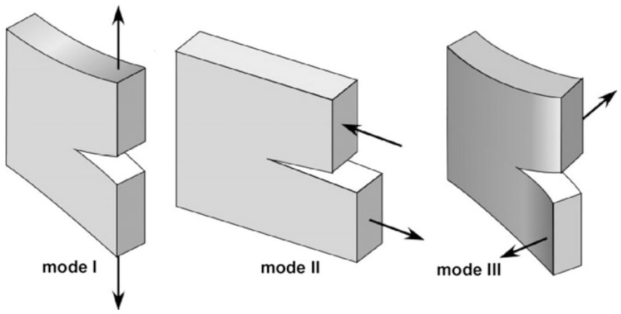

Figure 2.1: Mode crack types according to Irwin's theory [26].

axis direction to increase its opening. In this model, the strain energy U_{rel} of the aperture can be determined using Inglis's equations [27] and the derivative of the energy necessary to increase the crack area U_{sep} is obtained by the Eq. (2.1.1)

$$\frac{\partial U_{\text{sep}}}{\partial(2a)} = \frac{\partial U^{\text{e}}_{\text{rel}}}{\partial(2a)} \tag{2.1.1}$$

During the first half of the 20^{th} century, other fundamental solutions for stress fields in elastic material singularities were published [27, 28]. Irwin [25] found a general form to describe stress σ and displacement fields u for 2D geometries in function of polar coordinates (r,θ) with respect to the point where the crack opens. In these formulas for stress and displacement, the subscripts *(i, j)* indicate Cartesian or cylindrical coordinates, the terms $f^{\text{I}}_{ij}, f^{\text{II}}_{ij}, f^{\text{III}}_{ij}$, $g^{\text{I}}_{i}, g^{\text{II}}_{i}, g^{\text{III}}_{i}$ are dimensionless angular functions of θ for a particular geometry, K_I, K_{II}, K_{III} are the stress intensity factors for the three crack opening modes, and S is the shear modulus of the material [29].

$$\begin{aligned}
\lim_{r\to 0} \sigma_{ij}(r,\theta) &= \frac{1}{\sqrt{2\pi r}}\left[K_{\text{I}} f^{\text{I}}_{ij}(\theta) + K_{\text{II}} f^{\text{II}}_{ij}(\theta) + K_{\text{III}} f^{\text{III}}_{ij}(\theta)\right] \\
\lim_{r\to 0} u_i(r,\theta) &= \frac{1}{2S}\sqrt{\frac{r}{2\pi}}\left[K_{\text{I}} g^{\text{I}}_{i}(\theta) + K_{\text{II}} g^{\text{II}}_{i}(\theta) + K_{\text{III}} g^{\text{III}}_{i}(\theta)\right]
\end{aligned} \tag{2.1.2}$$

Irwin also defined the relationship between the stress intensity and the energy release rate described by Griffith:

$$G = G_{\text{I}} + G_{\text{II}} + G_{\text{III}} = \frac{K^2_{\text{I}}}{E'} + \frac{K^2_{\text{II}}}{E'} + \frac{K^2_{\text{III}}}{2S}, \tag{2.1.3}$$

where E' and S are the generalized elastic modulus and shear modulus, respectively. He also established the $G_i > G_{ic}$ criterion to determine if the crack propagates, being G_{ic} a material property known as *fracture toughness*.

Following this work, Irwin extended his theory to the simplest plastic materials where the region around the crack tip experiences stress above the elastic limit [30]. For Mode I crack in these materials, the centre of the plastic zone is located at the crack tip and its boundary where the elastic stress equals the material's

yield stress σ_y. Inside this plastic zone, the stress presented is the yield stress.

$$\sigma_y = \sigma_{ij}(\theta, r_d) = \frac{K_I f_{ij}^I(\theta)}{\sqrt{2\pi r_d}} \rightarrow r_d = \frac{(K_I f_{ij}^I(\theta))^2}{2\pi\sigma_y} \tag{2.1.4}$$

LEFM is not effective in describing non-linear elasticity or complex plasticity, where other cracking modelling techniques are more appropriate, such as *the J-integral, Virtual crack closure, Cohesive Zone Models, eXtended FEM, phase field modelling* and *Perydynamics theory*.

2.1.2 J-Integral

Rice [31] extended fracture mechanics beyond the limits of LEFM by introducing the *J-integral*. This is used to characterise fractures in non-linear elastic materials or plastic materials under specific conditions [32]. The J-integral is defined as the integral of the potential energy in an arbitrary path (Γ) around the crack tip in a counter-clockwise direction.

$$J = -\frac{d\Pi}{dA} = \oint \left(w\delta_{iy} - T_i \frac{\partial u_i}{\partial x} \right) d\Gamma \quad w = \int_0^{\varepsilon_{ij}} \sigma_{ij} d\varepsilon_{ij} \quad T_i = \sigma_{ij} n_j, \tag{2.1.5}$$

where Π is the potential energy, A the crack area, w the strain energy density, δ_{iy} the delta function for y component, T_i the components of the traction vector, u_i the displacement vector components, $d\Gamma$ the length increment along the contour Γ, σ_{ij} and ε_{ij} the stress and strain tensor, and n_j the unit vector normal to Γ in every point. The determination of the J value where the crack propagates at the critical value J_c is the material's toughness.

2.1.3 Virtual Crack Closure Technique

Virtual crack closure technique (VCCT) [33] is a computational technique that uses FEM models to predict crack initiation and propagation. This technique is based on Irwin's assumption that the crack propagation is quasi-adiabatic, i.e. the energy released in the process is equal to the work required to close the crack to its original configuration.

This technique determines the force F_{cd} required to join nodes c and d (see Fig. 2.2), and it calculates the nodal displacement (v, u, w) using FEM, to subsequently calculate the energy release rate G_i [34] through the equations below, where b is the specimen thickness in z-direction and Δa is the distance between nodes. When $G_I + G_{II} + G_{III} \geq G_c$, the crack propagates.

$$G_{\mathrm{I}} = \frac{1}{2b\Delta a} F_{cd}^y (v_c - v_d); \quad G_{\mathrm{II}} = \frac{1}{2b\Delta a} F_{cd}^x (u_c - u_d); \quad G_{\mathrm{III}} = \frac{1}{2b\Delta a} F_{cd}^z (w_c - w_d), \tag{2.1.6}$$

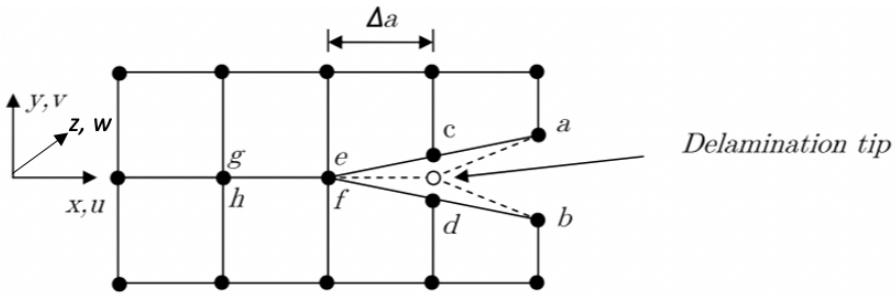

Figure 2.2: Scheme for calculating energy release rate using *Virtual Crack Closure Technique (VCCT)* [33].

The technique was simplified by Rybicki and Kanninen [35], who suggested that the nodal forces *c*-*d* could be approximated by the nodal forces *e*-*f*. This simplification enables the computation of displacements and forces at the same time, significantly reducing the computational costs.

J-integral and VCCT are effective for computing the energy area of non-linear or plastic materials. However, they are limited in calculating crack initiation or propagation in simple geometries and cannot calculate cracks in highly non-linear materials.

2.1.4 Cohesive zone modelling

Cohesive zone modelling (CZM) is an approach used to model fracture in highly non-linear materials. It is based on the idea that a crack can be modelled as the progressive rupture of interatomic bonds within a specific area called the cohesive zone.

CZM is flexible and numerically stable with a small number of parameters that can predict crack initiation and propagation over large areas. It provides a good physical interpretation of the fracture process. The method is particularly useful for modelling materials with complex fracture behaviours, such as composites and laminates, and can be used to study their mechanical response under a variety of loading conditions.

One of the earliest works on CZM was proposed by Dugdale [36] and Barenblatt [12]. They modelled the cohesive zone as a thin layer of material with reduced strength situated between two elastic regions. Whereas Dugdale assumed that the damage initiation stress was equal to the yield stress and remains constant until complete failure, Barenblatt assumed a stress distribution that varies with distance from the crack tip, independent of the applied load.

Barenblatt's model was modified for concrete by Hillerborg et al.[37]. They introduce a relationship between stress and nodal separation, known as the *fictitious crack model*. This model has become the foundation for all modern cohesive model theories. In this model, the initial thickness of the cohesive element deforms across the normal (n) and two tangential crack directions (t,s), simulating Mode I, II, and III cracks. The element deformation causes a progressive loss of stiffness until it reaches 0 at a critical point

where the crack is completed. The relationship between the critical separations δ, the stress due to the applied force $\sigma(\delta)$, and the toughness G is described by the following:

$$G_n < \int_0^{\delta_n^c} \sigma_n(\delta_n)\Big|_{\delta_n=0} \mathrm{d}\delta_n \quad \text{or} \quad G_t < \int_0^{\delta_t^c} \sigma_t(\delta_t)\Big|_{\delta_t=0} \mathrm{d}\delta_t \tag{2.1.7}$$

Subsequently, other CZM approaches have been developed according to different traction-separation laws $\sigma(\delta)$, such as linear [37], bilinear [38], trilinear [39] or exponential [40]. The next subsection explains the bilinear law in more detail, as it is the one used in our work.

In general terms, CZM is a simple method for predicting crack initiation and propagation. Its main limitation is that the direction of the crack must be predefined within the cohesive zone.

2.1.5 Bilinear law

Alfano [41] studied the influence of the shape of cohesive laws by comparing bilinear, trapezoidal, and exponential in double-cantilever-beam FEM simulations.

The choice of shape influenced numerical performance and accuracy. In particular, the exponential law was optimal in accuracy but requires high computational costs and produces convergence issues in the FEM simulations, the trapezoidal gave the worst results in terms of accuracy and convergence. The bilinear was the best compromise between computational cost and accuracy giving very similar results than exponential but generating much less convergence issues.

The Bilinear law was implemented by Mi et al. [38] as the simplest constitutive equation. It assumes a linear elastic response up to a maximum stress at which the crack initiation occurs (segment A-B of Fig. 2.3). The maximum stress represents the stress limit where the resistance of the element starts to decay. After this maximum, the stiffness of the material decreases linearly until the failure of the material is complete (segment B-C). The area of the function corresponds to the *toughness* of the material. The phases are described in detail below.

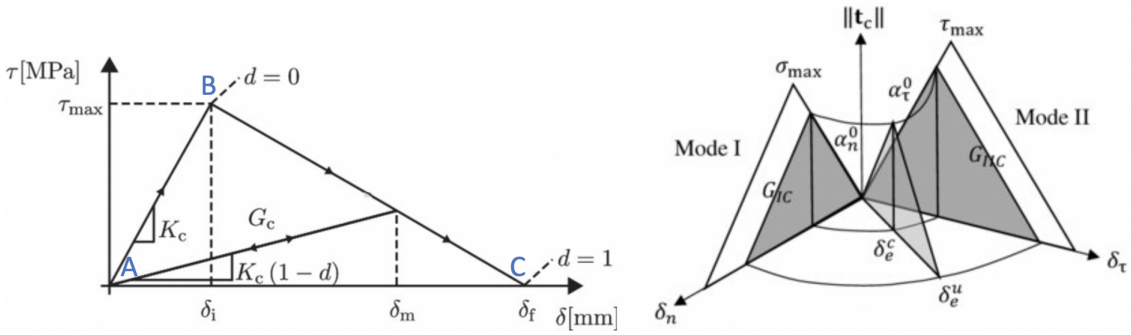

Figure 2.3: Scheme of bilinear law (left). Scheme of bilinear law for mixed failure mode (right) [38].

Segment A-B: The slope of the linear elastic section is defined by the stiffness parameter K_c. The compliance of the cohesive region should not contribute to the total deformation of the material since the only purpose of the cohesive region is to simulate the fracture. The effective elastic modulus E_{eff} of a piece of material with a cohesive region is calculated by the Eq. (2.1.8) [33], where t is the cohesive element thickness and $K_c t \gg E$ to approximate $E_{\text{eff}} \approx E$.

$$E_{\text{eff}} = E\left(\frac{1}{1+\frac{E}{K_c t}}\right) \tag{2.1.8}$$

Point B: The damage at the cohesive zone starts when the traction reaches the maximum nominal interfacial strength τ_{max}. For mixed-mode failure (Fig. 2.3, right side), there are different criteria for reaching this limit, being the quadratic-onset criterion, the most employed [42] method.

Segment B-C: As the deformation continues, the stress is reduced progressively by $(1-D)\sigma^{max}$, where D is a damage evolution parameter with range [0,1]. In the case of unloading and reloading, the region will present a new stiffness defined by $K_c(1-D)$.

Point C: Crack propagation occurs when the energy release rate per unit area reaches a toughness value G_c. For mixed-mode failures, there are several criterion, one of the most commonly used is the mixed interaction criterion.

2.1.6 Toughness in LEFM versus CZM

Assuming a case of no twisting (no mode III), two toughness values need to be determined to understand the energy release during fracture: Mode I toughness, G_{IC}, which represents the energy required to open a crack by creating new fracture surfaces, and Mode II toughness, G_{IIC}, which represents the energy required to propagate the crack under in-plane shear.

In Linear Elastic Fracture Mechanics (LEFM), fracture toughness is defined as the critical energy release rate required for crack propagation in a material that behaves elastically. The fracture process zone is assumed to be small compared to the structural dimensions (Small Scale Yielding), and consequently, all non-linear processes are idealized as occurring at the crack tip. Toughness is related with the stress intensity factor K_i by Eq.2.1.3, which describes the stress field magnitude at the tip. As consequence the crack will propagate when the stress intensity factor reaches its critical value $K_{i,C}$.

In contrast, the Cohesive Zone Model (CZM) represents the crack tip as a region undergoing progressive damage, where the separation of material surfaces occurs gradually governed by a traction–separation law

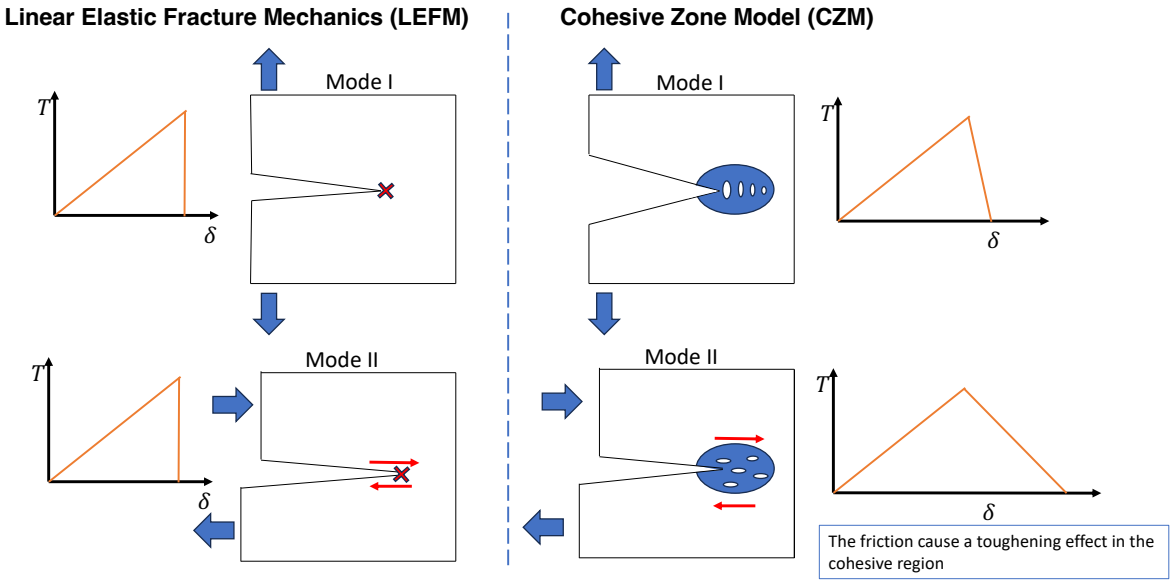

Figure 2.4: A comparison of crack propagation in LEFM and CZM for modes I and II reveals distinct behaviours. In LEFM, the force-displacement curve exhibits a sharp discontinuity (a sudden drop) upon crack initiation. Conversely, CZM displays a progressive negative slope, representing gradual softening that is less steep in Mode II due to the influence of friction inside the micro-cracks of the zone.

(see Fig. 2.4). While LEFM assumes that fracture energy is released instantaneously at the crack tip, implying an abrupt drop in stress from a maximum value σ^{max} to zero, CZM introduces a gradual degradation of stiffness, essential for maintaining numerical stability during FEM simulations.

In CZM, the fracture toughness G_{ic}^{CZM} is defined as the work separation per unit area, representing the total area under the traction-separation curve. This model incorporates the energy dissipation effects within the crack-affected region (such as microcracking, complex crack trajectory, plasticity or some friction effects) into the cohesive law. Modelling different types of friction during the cohesive degradation is complex and often are implicitly subsumed into the calibrated cohesive toughness value G_{ic}^{CZM}.

As consequence, the relationship between LEFM and CZM depends on the fracture mode in brittle materials. While in Mode I, the toughness values measured for brittle interfaces are generally similar (similar area under the curve), as both primarily capture the work of adhesion, in Mode II a significant discrepancy arises being $G_{IIC}^{CZM} \gg G_{IIC}^{LEFM}$. This discrepancy is because CZM captures part of the static friction that occur at low sliding velocities or low relative displacements between elements [43]. In this context, G_{IIC}^{CZM} is not merely the energy for surface creation, it is an apparent toughness that includes other frictional effects as the rugosity [44, 45].

2.1.7 EXtended Finite Element Method (XFEM)

FEM allows traditional fracture mechanics techniques like LEFM, J-integral and VCCT to be used on complex structures. However, FEM requires a very fine mesh around the crack to prevent divergence issues. As the crack propagates, the geometry and position of the tip change, which necessitates continuous re-meshing that increases computational time.

Moës et al. [23] introduced *eXtended Finite Element Method (XFEM)* for modelling crack growth without re-meshing. The authors proposed a method for enriching the element solution space (the set of functions used to solve the stress-strain equation of each element) with additional functions that capture the behaviour of cracks. The enriched elements increase as the crack propagates, avoiding re-meshing. XFEM was designed to determine the crack direction and can be combined with the bilinear law to represent the physical behaviour of the fracture. Further details of XFEM are explained in Chapter 7 Subsect. 7.4.2 where it is applied to model crack propagation in cantilever experiments of beryllium.

2.1.8 Other methods: phase field modelling and peridynamics theory

Finally, other methods used for fracture modelling are briefly described here. Even though their performance could be superior for modelling multicrack or complex materials, their difficult implementation and high computational costs make them less effective for modelling the experiments studied in this thesis compared to CZM and XFEM. However, they could be valuable techniques for future work, especially if materials are modelled at larger (Phase-Field Modelling) or smaller (Peridynamics theory) scales.

Phase-Field Modelling (PFM) [46] is a continuum mechanics method used to predict how fractures initiate and propagate in materials. Unlike XFEM, which models cracks as sharp geometric discontinuities, PFM represents a crack as a diffuse interface of finite thickness. The model is based on Griffith's thermodynamic framework [26], which states that a cracks grow if the energy released by the fracture exceeds the material's toughness. Computationally, this is achieved by introducing a scalar, the *phase-field*, that varies continuously from 0 (intact state) to 1 (fully broken state), which allows the crack evolution to be managed through a system of partial differential equations solved using numerical methods like FEM. This converts the sharp crack discontinuity into a field, avoiding the need for complex crack front tracking algorithms.

Peridynamics theory [47] is another method focused on a physical understanding of the crack. It was designed to model the dynamic response of materials subjected to high-rate loading and impact. The theory is based on the concept of peridynamics, which uses a non-local integral formulation of solid mechanics that models the interactions between points within a material as a function of their relative distances. The

major weakness of this model is that the computing time scales exponentially with sample size, therefore, it is more effective to use other techniques for large cracks.

2.2 Crystal plasticity

This section outlines the core concepts of the crystal plasticity modelling used in the OXFORD-UMAT code, a project implemented by Prof. Edmund Tarleton's group, of which the thesis author is a member [18]. The origin of this work was the *user-element* code developed by Prof. Fionn Dunne [48]. The code is available in [49].

In a crystal under stress, the deformation gradient of the structure can be defined as $\mathbf{F}_{tot} = \mathbf{F}_e \mathbf{F}_p \mathbf{F}_{th}$, where $\mathbf{F}_e$ is the mechanical elastic deformation, $\mathbf{F}_p$ the plastic deformation, and $\mathbf{F}_{th}$ the thermal deformation (see Fig. 2.5) [50]. For measurements at a constant temperature, the thermal deformation can be neglected.

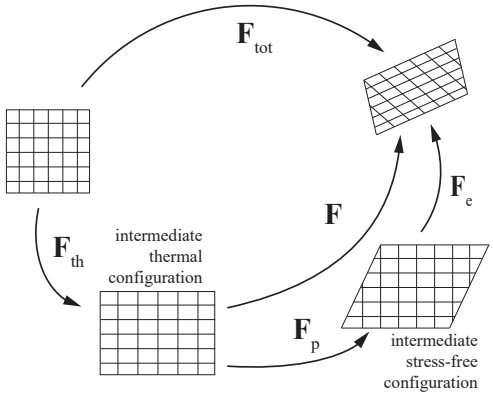

Figure 2.5: Multiplicative decomposition of total deformation.

The elastic deformation $\mathbf{F}_e = I + \varepsilon_e$, where the elastic strain $\varepsilon_e = \varepsilon - \varepsilon_p$, depends on the total strain (obtained through FEM) minus the plastic deformation component.

Plastic deformation $\mathbf{F}_p = I + \varepsilon_p$ is computed with the plastic velocity gradient $\mathbf{L}_p$, which is the sum of the slip rates $\dot{\gamma}^a$ multiplied by the dyadic product of slip direction $\mathbf{s}^a$ and plane normal $\mathbf{n}^a$ of each slip system a, known as the *Schmidt tensor*.

$$\mathbf{L}_p = \dot{\mathbf{F}}_p \mathbf{F}_p^{-1} = \sum_a \dot{\gamma}^a \mathbf{s}^a \otimes \mathbf{n}^a = \sum_a \dot{\gamma}^a \mathbf{S}^a \tag{2.2.1}$$

When the reference system of the experiment and crystal orientation do not coincide, a transformation to the slip system $(\mathbf{s}^a, \mathbf{n}^a)$ is required using the matrix $\mathbf{g}_{ij}$, which is based on the Bunge Euler angles convention, where ϕ_1, Φ, and ϕ_2 represent the rotation angles about Z, rotated X', and twice-rotated Z" axes, respectively [51] (see Appendix B.1 for detail definition of $\mathbf{g}_{ij}$).

At the same time, the slip systems suffer elastic deformations (see Eq.(2.2.2)), transforming the slip direction and normal to the deformed reference:

$$\mathbf{s}_e^a = \mathbf{F}_e \mathbf{s}^a; \quad \mathbf{n}_e^a = \mathbf{F}_e^{-T} \mathbf{n}^a = \mathbf{n}^a \mathbf{F}_e^{-1} \tag{2.2.2}$$

The problem is not straightforward to solve, since the elastic strain ε_e depends on the total strain ε (computed by FEM), the plastic strain ε_p depends on the slip rates $\dot{\gamma}^a$, and the slip system (n^a, s^a), which is deformed elastically. To solve it, an iterative method is used for successive time steps [18], where the rotation matrix g_{ij} is updated:

$$\mathbf{g}_{ij,(t+\Delta t)} = \mathbf{g}_{ij,t} + \Delta\boldsymbol{\Omega}_e \Delta t \cdot \mathbf{g}_{ij,t}; \quad \Delta\boldsymbol{\Omega}_e = \Delta\boldsymbol{\Omega} - \Delta\boldsymbol{\Omega}_p; \quad \begin{cases} \Delta\boldsymbol{\Omega}_p = \sum_a \mathbf{W}^a \Delta\gamma^a \\ \Delta\boldsymbol{\Omega} = \dfrac{\mathbf{L} - \mathbf{L}^\mathbf{T}}{2} \Delta t \end{cases} \tag{2.2.3}$$

where $\Delta\boldsymbol{\Omega}_e$ is the variation of the elastic rotation, which is the antisymmetric matrix of the elastic deformation gradient ($\mathbf{L}^e$). $\Delta\boldsymbol{\Omega}$ is the variation of total rotation, $\Delta\boldsymbol{\Omega}_p$ the variation of plastic rotation, W^a the antisymmetric matrix of the Schmidt tensor ($\mathbf{S}^a$), and $\Delta\gamma^a = \dot{\gamma}^a \Delta t$ the variation of slip for the system a, which is determined by a constitutive slip law.

The OXFORD-UMAT code solves the system through a semi-implicit or a fully implicit FEM method, depending on the specific conditions of simulation (elasticity, plasticity, creep, and others). For both of these methods, the Forward-Gradient algorithm is used to obtain the approximate initial values [52].

2.2.1 Semi-Implicit method

The semi-implicit method is used to obtain the stress in a plastic material (explained by Dunne et al. [48]). The stress at the deformed configuration, known as Cauchy stress σ, is given by the following equation:

$$\boldsymbol{\sigma} = \mathbb{C} : \boldsymbol{\epsilon_e}; \quad \mathbb{C} = \mathbf{R}\mathbb{C}_0\mathbf{R}^T, \tag{2.2.4}$$

where $\mathbb{C}$ is the elasticity matrix in the deformed configuration, $\mathbb{C}_0$ the elastic matrix in the crystal reference [53, 54], and $\mathbf{R}$ a 6x6 rotation matrix that is constructed from the crystal-to-sample transformation matrix ($\mathbf{g}_{ij}$) [55] (see Appendix B.1).

The elastic strain is obtained by summing up the former elastic strain with the elastic strain increments. These elastic strain increments are calculated by subtracting the plastic strain increment $\Delta\boldsymbol{\epsilon}_p$ from the strain

increment $\Delta\boldsymbol{\epsilon}$:

$$\boldsymbol{\epsilon}_e(t+\Delta t) = \boldsymbol{\epsilon}_e(t) + \Delta\boldsymbol{\epsilon}_e. \quad \Delta\boldsymbol{\epsilon}_e = \Delta\boldsymbol{\epsilon} - \Delta\boldsymbol{\epsilon}_p \tag{2.2.5}$$

Substituting $\boldsymbol{\epsilon}_e$ in Eq. (2.2.4), the Cauchy stress results in the trial stress $\boldsymbol{\sigma}_{tr}$ minus the plastic correction $\mathbb{C} : \Delta\boldsymbol{\epsilon}_p$:

$$\boldsymbol{\sigma} = \mathbb{C} : (\boldsymbol{\epsilon}_e(t) + \Delta\boldsymbol{\epsilon}) - \mathbb{C} : \Delta\boldsymbol{\epsilon}_p = \boldsymbol{\sigma}_{tr} - \mathbb{C} : \Delta\boldsymbol{\epsilon}_p, \tag{2.2.6}$$

and the residual $\boldsymbol{\psi}$ minimised by the Newton-Raphson:

$$\boldsymbol{\psi} = \boldsymbol{\sigma} - \boldsymbol{\sigma}_{tr} + \mathbb{C} : \Delta\boldsymbol{\epsilon}_p \rightarrow \mathbf{0} \tag{2.2.7}$$

The plastic strain increment is the sum of the slip increments, considering only the stretch component (symmetric matrix) of the velocity gradient [52]:

$$\Delta\boldsymbol{\varepsilon}_p = \text{sym}\left(\sum_a \dot{\gamma}^a \mathbf{S}^a\right)\Delta t \tag{2.2.8}$$

The differentiation of the residual with respect to the Cauchy stress gives:

$$\frac{\partial\boldsymbol{\psi}}{\partial\boldsymbol{\sigma}} = \mathbb{I} + \mathbb{C}\mathbb{P} \quad \text{where} \quad \mathbb{P} = \frac{\partial\Delta\boldsymbol{\varepsilon}_p}{\partial\boldsymbol{\sigma}} = \frac{\partial\sum_a \dot{\gamma}^a \mathbf{S}^a}{\partial\boldsymbol{\sigma}}\Delta t = \sum_a \frac{\partial\dot{\gamma}^a}{\partial\tau^a}\mathbf{S}^a\frac{\partial\tau^a}{\partial\boldsymbol{\sigma}}\Delta t$$

Note that the derivative of resolved shear stress with respect to the stress is simply the Schmidt tensor $\dfrac{\partial\tau^a}{\partial\boldsymbol{\sigma}} = \mathbf{S}^a$, giving the expression:

$$\mathbb{P} = \Delta t \sum_a \frac{\partial\dot{\gamma}^a}{\partial\tau^a}\mathbf{S}^a \otimes \mathbf{S}^a \tag{2.2.9}$$

Newton-Raphson calculates the residual $\boldsymbol{\psi}$ and its derivative to determine the stress increment $\Delta\boldsymbol{\sigma}^k$ for an imposed deformation. The stress is then updated as $\boldsymbol{\sigma}^{k+1} = \boldsymbol{\sigma}^k + \Delta\boldsymbol{\sigma}^k$, and the increment can be reduced until it is smaller than a tolerance $\|\boldsymbol{\Delta\sigma}\| < 10^{-8}$ MPa, in which case it would be updated explicitly ($\|\boldsymbol{\Delta\sigma}\| = 10^{-8}$ MPa).

$$\Delta\boldsymbol{\sigma} = -\left[\frac{\partial\boldsymbol{\psi}}{\partial\boldsymbol{\sigma}}\right]^{-1}\{\boldsymbol{\psi}\} = -\left[\mathbf{I} + \mathbb{C} : \mathbb{P}\right]^{-1}\left\{\boldsymbol{\sigma} - \boldsymbol{\sigma}_{tr} + \mathbb{C} : \text{sym}\left(\sum_a \dot{\gamma}^a \mathbf{S}^a\right)\Delta t\right\} \tag{2.2.10}$$

The initial guess for the Newton-Raphson method is crucial for its performance. It is obtained by a weighted average ϕ of the fully-elastic $\boldsymbol{\sigma}_{tr}$ and fully-plastic $\boldsymbol{\sigma}_{pl}$ obtained by the Forward-Gradient method. The

weighting parameter ϕ is adjusted during the calibration of the model.

$$\boldsymbol{\sigma}^0 = (1-\phi)\,\boldsymbol{\sigma}_{tr} + \phi\,\boldsymbol{\sigma}_{pl}. \tag{2.2.11}$$

After updating the stress σ, the plastic shear within the crystal influences the critical resolved shear stress (τ_c) causing either hardening or softening inside the material [18, 17].

In the semi-implicit method, τ_c is updated in a second loop using hardening and softening equations. When the increment of τ_c exceeds the tolerance $\Delta\tau_c^a > \text{tol}$, τ_c^a are updated inside the first loop, and the stress is calculated again to improve the accuracy of the stress-strain equilibrium. This avoids the jumps in the stress-strain curves that occurs in the explicit methods while it is computationally faster than other methods.

2.2.2 Fully Implicit method

The fully implicit integration method [52, 56] calculates the critical resolved shear stress τ_c^a at the same time that the calculus of σ. It uses the slip increments of the previous time step $\Delta\gamma^a$ to obtain the plastic deformation, the stress σ, the RSS, the CRSS and it calculates the slip rate $\dot{\gamma}^a$.

After the slip rate calculus, it updates the slip increments in order to minimise the residual between the slip increments assumed initially and the slip increments obtained by the calculated slip rate. The solver iterates through a Newton-Raphson loop until the residual is below some tolerance.

The fully implicit method implies a much bigger Jacobian matrix than the semi-implicit, increasing the computing cost and time. However, it offers some advantages over the semi-implicit method when there are convergence problems after applying certain hardening/softening laws.

2.2.3 Forward-Gradient method

The Forward-gradient method [52] is a non-iterative method, that calculates the initial guess of other iterative methods or as an alternative solution when the Newton-Raphson method does not converge. The stress is updated by the following expression:

$$\sigma_t = \sigma_{t-1} + \Delta\sigma; \qquad \Delta\boldsymbol{\sigma} = \mathbb{C} : \Delta\boldsymbol{\epsilon} - \boldsymbol{\sigma}\,\mathrm{tr}(\Delta\boldsymbol{\epsilon}) - \sum_a \left(\mathbb{C} : \mathbb{P}^a + \mathbf{W}^a\,\boldsymbol{\sigma} - \boldsymbol{\sigma}\,\mathbf{W}^a\right)\Delta\gamma^a, \tag{2.2.12}$$

where $\mathbb{C}$ is the elastic matrix, $\mathbb{P}$ the derivative of the plastic strain with respect to the stress, and $\mathbf{W^a}$ the antisymmetric matrix of the Schmidt tensor for the slip system ^{a}. $\Delta\boldsymbol{\varepsilon}$ is the total strain increment obtained through FEM and $\Delta\gamma^a$ the plastic slip increment of ^{a} which depends on the slip law used.

2.2.4 Sinh slip law

A slip rate law $\dot{\gamma}^{\alpha}$ is fundamental for determining the plasticity of a slip system and other material properties such as GNDs and the influence of temperature on a material's behaviour.

Crystal plasticity is based on the theory of dislocation motion [57, 58], where dislocations (line defects in the crystal lattice) move along slip planes and enable plastic deformation. The motion is described by the dislocation energy E_d and the energy necessary to surpass different obstacles in the materials (voids or defects) E_o. The Boltzmann distribution defines the probability,p, of overcoming an obstacle:

$$p = \exp\left(-\frac{\Delta E}{kT}\right) = \exp\left(-\frac{\Delta H - PV}{kT}\right) = \exp\left(-\frac{\Delta G + T\Delta S}{kT}\right), \tag{2.2.13}$$

where P is pressure, V volume, kT temperature, ΔH enthalpy, ΔG Gibbs energy, $T\Delta S$ the change of entropy multiplied by temperature, $\Delta E = E_d\text{-}E_o = \Delta H - PV \approx \Delta H = \Delta G + T\Delta S$ (PV is negligible compared to the enthalpy change ΔH associated with dislocation motion).

The frequency of successful obstacle jumps ν_j is related to $p = \nu_j/\nu_0$, being ν_0 the vibration frequency of dislocations. Dunne et al. [48] proposed an expression for the average velocity of dislocations v_g based on the size of the obstacles and their frequency:

$$v_{\mathrm{g}} = \frac{d \cdot b}{2l}\nu_j = \frac{d \cdot b}{2l}\nu_0 \exp\left(-\frac{\Delta G + T\Delta S}{kT}\right), \tag{2.2.14}$$

where b is the length of the Burgers vector of the slip system, l the pinning distance (distance between obstacles) and d the length of the average dislocation movement to surpass the obstacle (see Fig. 2.6).

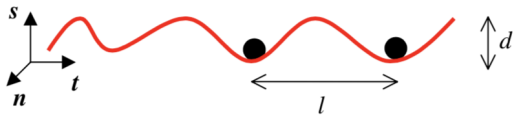

Figure 2.6: Diagram of a pinned dislocation on a slip plane with normal n.

The Gibbs energy can be simplified to the Helmholtz Energy or the activation energy for slip minus the work done by the shear stress: $\Delta G = \Delta F - \tau\Delta V$. Substituting ΔG into the Eq. (2.2.14), where $d \approx l$ [59] and $T\Delta S \approx \tau_c \Delta V$, we obtain:

$$v_g = \frac{d \cdot b}{2l}\nu_0 \exp\left(\frac{-\Delta F + \tau\Delta V - T\Delta S}{K_B T}\right)\mathrm{sign}(\tau) = \frac{b}{2}\exp\left(\frac{-\Delta F + \Delta V(\tau - \tau_c)}{K_B T}\right)\mathrm{sign}(\tau) \tag{2.2.15}$$

The slip rate $\dot{\gamma}$ is defined as $\dot{\gamma} = \rho_m b v_g$, where ρ_m is the mobile dislocation density. Considering forward and backwards movement of dislocations (both $\mathrm{sign}(\tau)$), we obtain a general expression for the slip rate of

a slip system (^{a}):

$$\dot{\gamma}^a = \alpha \sinh \beta \left(|\tau^a| - \tau_c^a \right) \operatorname{sign}(\tau^a) \tag{2.2.16}$$

$$\alpha = \rho_m b^2 \nu_0 \exp\left(-\frac{\Delta F}{K_B T} \right); \quad \beta = \frac{\Delta V^a}{K_B T} \tag{2.2.17}$$

The code allows adjusting the plastic parameters α and β as constants or the parameters of Eq. (2.2.17).

parameter	**definition**	**unit**
b	burgers vector length	nm
ΔF	activation energy for slip	eV/mol
ν_0	attempt frequency	1/s
K_B	Boltzmann constant	$\mathrm{eV \cdot K^{-1}}$
T	Temperature	K
ρ_m	mobile dislocation density	$1/\mu m^2$
ΔV	Activation Volume	$\mathrm{b^3}$

2.3 SiC fibre-reinforcement composites

Silicon carbide (SiC) is a covalent compound with exceptional properties such as high thermal, mechanical and chemical stability [60]. Its low activation under neutron radiation makes it one of the most attractive structural materials for nuclear fission [61] and fusion [62] reactors, or the aerospace sector [63].

Its main application for fusion reactor is as structural component of the *breeding blanket* [62, 22]. The blanket is the component responsible for converting the energy from the 14 MeV neutrons produced by fusion reactions (∼80% of the total energy produced) and generating the tritium needed for subsequent operations.

SiC	Melting point	Specific weight	Mechanical strength	Elastic modulus	Thermal conductivity
Pure	2730 °C	3.21 $\mathrm{g/cm^3}$	>600 MPa	>400 GPa	490 W/m-K

Table 2.1: Properties of Pure SiC [60].

The principal limitation of pure SiC is its inherent brittle nature and hence, a high probability of catastrophic failure under excessive stresses. To ensure sufficient fracture toughness and reliability, a SiC_f/SiC composite is proposed. This composite consists of a SiC matrix reinforced with continuous SiC fibres woven into a 2D or 3D structure [64].

The study of the material that connects the fibres and the matrix (*interphase*), and the surface where the interphase connects with the matrix (*interface*), is of great importance for ensuring the fibres can resist cracking. Pyrolytic carbon (PyC) is used as the *interphase* in nuclear applications due to its ability to withstand moderate radiation [65]. Several experimental methods have been proposed to analyse the *fibre-*

matrix interphase: micropillar compression, micro-cantilever fracture, and push-out cantilever.

Micropillar compression [66] involves the fabrication of micro-sized pillars from the composite material that are then compressed to measure their stress-strain response and assess the interfacial shear strength.

Micro-cantilever fracture [10] involves creating a small cantilever beam from the fibre-matrix region with a notch at the *interface* using a focused ion beam. The cantilever is then bent until it fractures, enabling the determination of the interfacial fracture toughness.

The fibre push-out method [67], is used to assess friction and mode II cracks at the *interphase* and *interface* while it maintains the integrity of the fibre. When the fibre is compressed, it swells radially, causing friction that compensates for the loss of overall stiffness and slows down the crack propagation [14]. This method is studied in Chapters 3 and 4.

2.3.1 Push-out theory

One of the first studies of fibre push-out was developed by Shetty et al. [68], who established a relation between the complete debonding load P_{debond} and the Coulomb friction coefficient μ. In the formula, σ_0 is a residual compressive (clamping) stress on the filament, R the fibre radius, t the fibre length or sample thickness, and k a dimensionless parameter.

$$P_{debond} = \frac{\pi R^2 \sigma_0}{k}\left[\exp\left(\frac{2\mu k t}{R}\right) - 1\right] \quad \text{where} \quad k = \frac{E_m \nu_f}{E_f\,(1+\nu_m)} \tag{2.3.1}$$

Lawrence [69] and Greszczuk [70] simplified the formalism, establishing a friction-independent relationship between the interface shear strength τ_s and the load when the crack form P. When a load in the x direction is applied to a fibre, the stress is distributed as shear stress at the *interphase* or *interface* where the crack occurs: $\mathrm{d}P = 2\pi R\tau(x)\mathrm{d}x$ [70]. If we assume that $\tau(x) = K(u-v)$, where K is the interface stiffness, u the displacements of the fibre, and v the displacement of the matrix, we can differentiate to obtain:

$$\frac{\mathrm{d}^2 P}{\mathrm{d}x^2} = 2\pi RK\left(\frac{\mathrm{d}u}{\mathrm{d}x} - \frac{\mathrm{d}v}{\mathrm{d}x}\right) = 2\pi RK\left(\varepsilon_{\text{fibre}} - \varepsilon_{\text{matrix}}\right) = 2\pi RKP\left(\frac{(1+\nu_{fibre})}{A_{\text{fibre}}E_{\text{fibre}}} - \frac{(1+\nu_{Matrix})}{A_{\text{Matrix}}E_{\text{Matrix}}}\right), \tag{2.3.2}$$

where ε_i is the strain, E_i is the Young modulus, ν_i the Poisson ratio and A_i the cross sectional area of the fibre and matrix. For fibre push-out $A_{fibre} = A_{matrix} = 2\pi Rt$, and the solution of the ODE is:

$$P = \tau_s \frac{\sqrt{a}}{K}\tanh(\sqrt{a}t)\left(\frac{(1+\nu_{fibre})}{A_{\text{fibre}}E_{\text{fibre}}} - \frac{(1+\nu_{Matrix})}{A_{\text{Matrix}}E_{\text{Matrix}}}\right)^{-1}; \quad \text{where } a = 2\pi RK\left(\frac{(1+\nu_{fibre})}{A_{\text{fibre}}E_{\text{fibre}}} - \frac{(1+\nu_{Matrix})}{A_{\text{Matrix}}E_{\text{Matrix}}}\right) \tag{2.3.3}$$

For short fibres or those with low interface stiffness K, the Eq. (2.3.3) can be reduced when $\tanh(\sqrt{a}t) \approx$

$\sqrt{at}$, giving the simplified interfacial shear strength Eq. (2.3.4) [71]. This expression becomes independent of K, which is a parameter very difficult to obtain experimentally. The physical interpretation is that damage in short fibres tends to occur more homogeneously across the entire cross-sectional area, whereas in long fibres, the crack propagates from top to bottom.

$$\tau_s = \frac{P}{2\pi Rt} \tag{2.3.4}$$

2.3.2 Short fibre

The length of the fibres is a key factor in push-out experiments to obtain measurements used in subsequent modelling. Short fibres allow the use of simplified formulations (see Eq. (2.3.4)), avoiding the need to obtain material properties like interface stiffness or Poisson's ratio of the fibre. Short fibres also facilitate other experimental aspects, such as accurate *transmission electron microscopy* (TEM) imaging of the crack propagation and the analysis of the neutron-irradiated material. The limited penetration power of neutrons irradiation means that long fibres would have unirradiated portions, leading to inaccurate measurements.

Sample thinning for short fibres (in the range of μm) is challenging due to the hardness and brittle nature of the ceramic composites. To overcome this, De Meyere et al. [72] developed a novel 'trench push-out' method (see Fig. 2.7) to obtain shorter SiC-Boron nitrite fibres. The thinning process was performed with a dual SEM–FIB column Zeiss Auriga using milling currents of 0.24-4 nA.

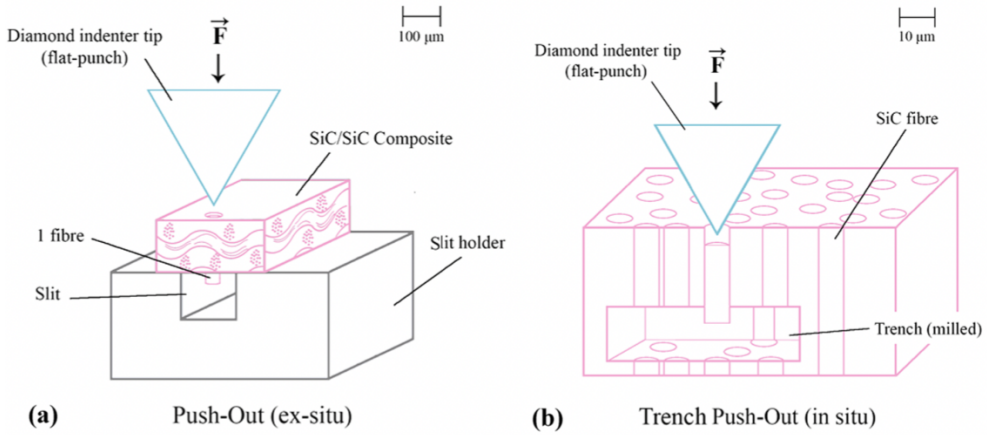

Figure 2.7: (a) Ex-situ push-outs and (b) novel SEM in-situ trench push-outs.

Typical cracks in short fibre push-out experiments usually form in the bottom half of the *interface* surrounding the fibre and then propagate quasi-instantaneously upwards to the fibre's tip. Once the crack is fully developed, the fibre is pushed out with only frictional resistance remaining. The instantaneous crack propagation allows the model to see the effect of fracture and friction in separate stages, isolating fracture

properties, something not possible in long fibres, where part of the interface is suffering friction while the bottom of the fibre remains unbroken.

2.4 Copper

In *plasma-facing components* (PFCs) of fusion reactors like DEMO [73], a copper interlayer is often employed to relieve stress between tungsten monoblocks. Additionally, copper alloys such as CuCrZr are used at the bond interface between the radiation shield and the heat sink in order to dissipate temperature and stress in reactors such as Wendelstein-7X, JET, and ITER [74, 75].

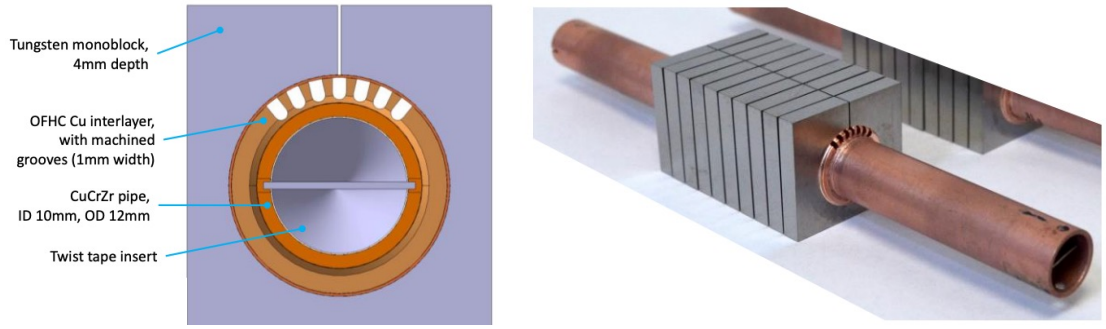

Figure 2.8: Geometry of the divertor (plasma-facing components). Mock-up designed for DEMO [73].

Density [76]	Fracture Toughness (K_{IC}) [77]	Elastic Modulus [78]	Poisson Ratio[78]	Melting Point [79]
8960 kg/m^3	33-160 MPa m$^{1/2}$	130 GPa	0.34	1357.77 K

Table 2.2: Properties of pure Copper.

Copper (Cu) combines excellent thermal conductivity and adequate mechanical strength, making it a suitable candidate for high thermal stress environments (see Table 2.2). However, the cyclic high-heat-flux loads caused by pulsed plasma operations generate repeated thermal stress variations within the PFC structure. This subjects the copper bond layer to alternating loads that generate plastic strain accumulations. The material exhibits hardening during deformation (expansion or contraction) and softening when the direction of deformation reverses, this repeated process leads to fatigue in the material [75, 20]. Chapter 6 focuses on this alternating hardening and softening behaviour (Bauschinger effect), investigating the underlying single-crystal deformation mechanisms in copper.

2.4.1 Bauschinger effect

The Bauschinger effect or kinematic hardening is a decrease in a material's yield stress when the applied load direction is reversed [80]. During the cyclic deformations that occur within the reactor, the Bauschinger

effect can explain the stress saturation at relatively low stress of copper or its alloys, and the formation of *persistent slip bands* (PSBs) inside the material [81, 82]. These PSBs are characterised by the accumulation of dislocations that can act as nucleation sites for fatigue cracks (see Fig. 2.9).

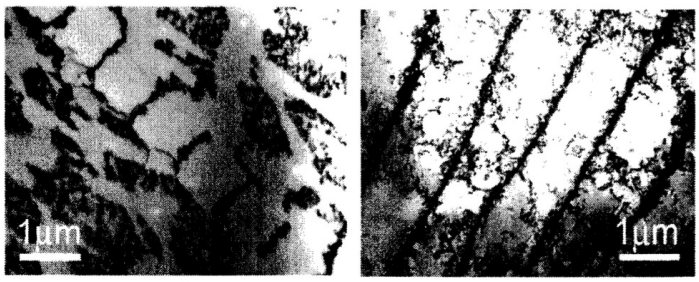

Figure 2.9: *Persistent slip bands* (PSB) in a single-crystal of copper by TEM [81].

The origin of the Bauschinger effect is generally associated with the boundaries in polycrystals and is primarily attributed to internal stresses arising from polarised arrays of dislocations accumulated at the grain boundaries [83, 84]. However, experimental evidence indicates that the Bauschinger effect is not negligible in single crystals [83, 21, 85], particularly when the material is curved. In this context, the effect occurs around the neutral axis of curvature, which is the boundary separating regions of tensile strain from the regions of compressive strain. Despite this, the dislocation structures responsible for the Bauschinger effect in single crystals remain a subject of debate [83].

Currently, the Bauschinger effect is mainly explained by two dislocation structures: stable dislocation structures and directional dislocation structures that evolve over time. Stable dislocation structures are known as *dislocation cells*, which form during plastic deformation after several cycles of deformation. The walls of these cells are dense and act as strong barriers, generating long-range internal stresses in the material in a specific deformation direction, while the interior of the cells offers lower resistance to deformation in the reverse direction [86]. On the other hand, *directional dislocation* structures generate internal stresses that act as obstacles or facilitate slip in specific directions and are evolving during the deformation cycles [87, 88].

Recent research on metal single crystals [89, 82] suggests that both mechanisms are significant. This is supported by findings that the measured internal stresses from cell structures are lower than initially theorised. The explanation becomes more complex during initial bending cycles, where the cells are not fully formed and the lattice curvature introduces *geometrically necessary dislocations* (GNDs), enhancing the importance of the obstacle-based model.

The models of the Bauschinger effect are explained in more detail in Chapter 6, Sect. 6.6. The main approaches consist of:

- *Slip-based models*: Models such as the Armstrong-Frederick [90] describe the effect through a differential equation composed of a linear growth term and a saturation term. Other variations of this equation include the Chaboche model [91] and the Ohno-Wang model [92]. These models are characterised by their simplicity and effectiveness in polycrystals, grouping all the effects to achieve an accurate stress-strain response of the entire sample. However, they do not describe the underlying physics of the effect, particularly in experiments involving single-crystal bending.
- *Dislocation-based models*: The calculation of GNDs through the plastic strain gradient [17, 93] reveals the distribution and the sign of dislocations based on the curvature strain, enabling a more physically grounded modelling of the Bauschinger effect. Models such as Orowan-Sleeswyck [87, 94] theorised a Taylor-type equation [95] ($\tau_B \propto \sqrt{\rho}$) to characterise the Bauschinger effect, while Beyerlein et al. [96] proposed ($\tau_B \propto \rho$) and introduced a reversibility term to indicate the direction of the stress relative to the new deformation, something useful for the modelling framework.

Additionally, it is necessary to combine the formulation of kinematic hardening with the *isotropic hardening* (hardening independent of the direction[95, 97]), something explored in polycrystals [96] but remains to be analysed in monocrystal where there is less experimental evidence and where the Bauschinger effect appears to be significant [21, 85].

2.5 Beryllium

Tritium, a scarce natural resource, is an essential fuel for fusion reactors. To overcome this limitation, *beryllium* (Be) serves as an ideal material for neutron multiplication, ensuring that more tritium is produced than consumed in each fusion reaction.

During the fusion reaction, a tritium atom is consumed, releasing a neutron that reacts with a lithium atom to produce another tritium atom (see Eq. (1.0.2)). Nevertheless, each time a released neutron fails to react with lithium, the tritium supply is reduced. To address this issue, Be is used as a neutron multiplier, as shown in the following chemical reaction [22]:

$$^{9}\mathrm{Be} + \mathrm{n} \rightarrow 2\alpha + 2\mathrm{n}' - 2.5\mathrm{MeV} \tag{2.5.1}$$

The *blanket*, located behind the first wall in a fusion reactor, was designed to capture neutrons and convert their kinetic energy into heat. The ITER prototype of *Helium-Cooled Ceramic Breeder Blanket (HCCB)* use alternating layers of beryllium and lithium ceramic pebbles to generate tritium [22]. This entire structure is made of SiC and utilises helium at $600/900^{o}C$ as coolant. These high temperatures cause the structure to

expand and compress, leading to high stress. Since both Be and SiC are brittle, this stress can cause cracks; therefore, studying their cracking properties is essential for ensuring the structural integrity of the blanket.

Density [54]	Stress intensity (polycrystal) [98]	Elastic modulus [53]	Poisson ratio [53]	Melting point [54]
1850 kg/m^3	6.8-11.0 MPam$^{1/2}$	311 GPa	0.047	1287 K

Table 2.3: Properties of Beryllium.

Be is a metal with excellent structural properties and good radiation resistance. It has a high elastic modulus, low Poisson's ratio, low density, and high melting point [54]. Be is a hexagonal close-packed (HCP) crystal with c/a ratio of 1.567 at room temperature [54]. The plasticity of HCP materials is controlled by several factors, including crystal orientation, grain size [99], and the presence of material defects [100]. The primary mechanisms for plasticity are: *slip* [101] when the atoms of the material slide over each other along specific crystalline planes, and *twinning* when the crystal lattice splits, and the new sections are mirror images of each other.

Fracture in Be is a complex process where slip plasticity, which is dependent on crystal orientation, plays a very important role. In the Chapter 7, the fracture properties of beryllium monocrystals are studied, avoiding grain boundary effects such as crystal twinning and grain boundary defects.

2.5.1 Hexagonal Close Packed slip systems of Be

HCP crystals exhibit different sliding systems responsible for plasticity. The slip occurs when the resolved stress defined by Schmidt's law $\tau = \sigma \cdot cos\theta \cdot cos\phi$ exceeds the *Critical Resolved Shear Stress* (CRSS) τ_c, being θ and ϕ the angles of the stress applied with respect to the slip plane normal and slip direction. The structure may exhibit plasticity or not, depending on the load direction relative to the crystal.

HCP slip systems in Be are represented in Fig: 2.10 [102], where CRSS is: τ_c=15.2 MPa for $<a>$ basal, τ_c= 67.7 MPa for $<a>$ prismatic, and τ_c=172.5 MPa for $<c+a>$ second-order pyramidal slip systems [103]. The mobility of the 18 remaining $<c+a>$ systems is lower according to dislocation models [104], and they are neglected.

On the other hand, Be has anisotropy according to the following elastic constants $E_1 = E_2$ = 289 GPa, E_3 = 335 GPa, G_{12} = 138 GPa, $G_{13} = G_{23}$ = 162 GPa and v_{12} = 0.09, $v_{13} = v_{23}$ = 0.04 [105, 101].

In HCP materials, the microstructure is crucial for impeding crack growth. Modelling [106, 107] and experimental [108] studies on HCP materials like zirconium alloys and titanium have shown that short cracks are often significantly diverted or even stopped. The interaction between crystal orientation, grain boundary characteristics, and the anisotropic availability of slip systems makes predicting crack trajectories

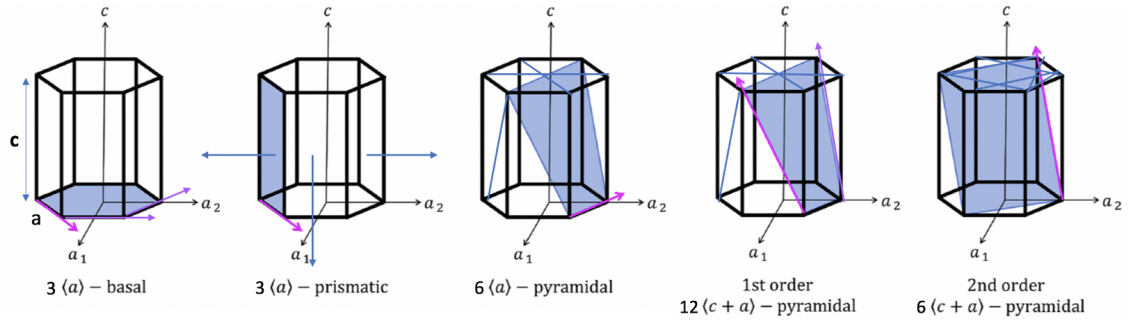

Figure 2.10: Slip systems of HCP material, also definition of c and a magnitude.

and growth rates extremely difficult.

Therefore, to better understand this complexity, it is essential to isolate these effects. The single-crystal experiments modelled in Chapter 7 are designed to isolate the influence of crystal orientation on crack properties, such as toughness and initiation stress, eliminating the confounding effects of grain boundaries.

2.5.2 Cantilever experiments

Beryllium fracture experiments are restricted to highly specialised facilities because they produce toxic dust [24]. The *Materials Research Facility* at the *UK Atomic Energy Authority* (UKAEA) uses remote handling and advanced air filtration systems to control and monitor the dust levels and develop Be experiments.

Obtaining the mechanical properties of Be monocrystal is difficult due to its small grain size. The classical method for measuring fracture properties involves fracturing a pre-notched cantilever. However, this method is particularly delicate for beryllium because of its brittleness in certain directions.

Di Mario et al. [109] used *Focused Ion Beam* (FIB) to create a pentagonal cross-section cantilever from a *bulk* specimen of brittle material. By applying nanoindentation, they were able to obtain the material's properties from the load-displacement curves.

In micro-fabrication, the shape of a cross-section significantly affects its second moment of area, which measures its resistance to bending. In a pentagonal cross-section, by strategically placing material below the neutral axis of the cantilever, higher stiffness can be achieved without adding more material. This promotes more stable bending without abrupt cracks that cannot be measured.

FIB technique is similar to a *Scanning Electron Microscope* (SEM) [110], but it uses a gallium ion beam (Ga+) instead of an electron beam to remove material from the sample surface. The *UKAEA Materials Research Facility* uses a FEI Helios FIB system for radioactive and toxic materials [105]. The indentations were performed using a *Keysight G200 nanoindentation system* with a three-sided diamond pyramid *Berkovich tip*, and the *Continuous Stiffness Measurement* (CSM) technique [111] was employed with a 42 Hz oscillation and 2 nm amplitude.

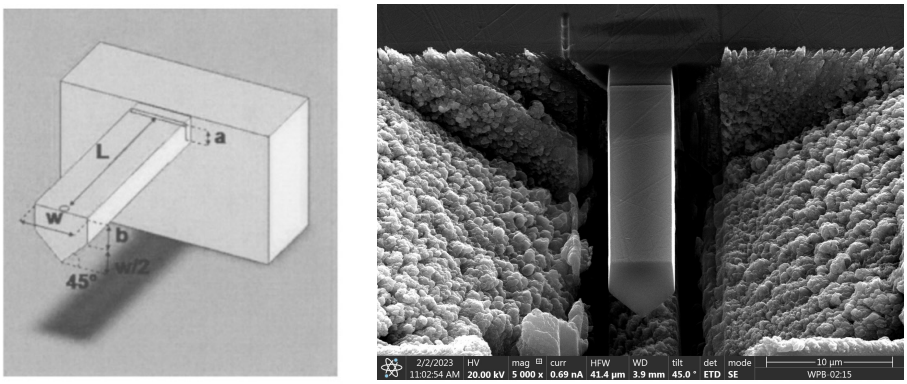

Figure 2.11: Cantilever geometric parameters from Di Mario [109] (left). SEM image of a beryllium cantilever studied after crack propagation (right).

Using *Linear Elastic Fracture Mechanics* formulation, the toughness of the material can be calculated:

$$G = \frac{K_{\mathrm{Ic}}^2}{E}; \quad K_{\mathrm{Ic}} = \sigma_{\mathrm{c}}\sqrt{\pi a}F\left(\frac{a}{b}\right) \tag{2.5.2}$$

$$\sigma_c = \frac{F_{peak}Ly}{I}; \qquad I = \frac{wb^3}{12} + \left(y-\frac{b}{2}\right)^2 bw + \frac{w^4}{288} + \left[\frac{b}{6}+(b-y)\right]^2 \frac{w^2}{4}; \qquad y = \frac{\frac{b^2w}{2} + \frac{w^2}{4}\left(b+\frac{w}{6}\right)}{bw+\frac{w^2}{4}}, \tag{2.5.3}$$

where a, w and b are defined in Fig. 2.11, E is the Young modulus, F_{peak} the applied bending force when the stiffness of the cantilevers starts to drop, L the distance between the crack and the point where the force is applied, I the moment of inertia of the beam cross-section, and y the vertical distance between the upper surface and the neutral plane. F is a dimensionless shape factor determined through fitting methods such as boundary element [109] or the J-Integral [112].

$$F(a/b) = 1.85 - 3.38\left(\frac{a}{b}\right) + 13.24\left(\frac{a}{b}\right)^2 - 23.26\left(\frac{a}{b}\right)^3 + 16.8\left(\frac{a}{b}\right)^4 \qquad \text{by boundary element method} \tag{2.5.4}$$

$$F(a/b) = 3.710\left(\frac{a}{b}\right)^3 - 0.630\left(\frac{a}{b}\right)^2 + 0.242\frac{a}{b} + 0.974 \qquad \text{by J-Integral method} \tag{2.5.5}$$

Eq. (2.5.2) and (2.5.4) work well for isotropic brittle materials that exhibit very low plasticity, about $\sim 1\%$ of scattering in measurements [109]. However, they perform poorly for beryllium, where the anisotropy and the basal plasticity cause differences in the F_{peak} of the cantilevers on the order of $\sim 50\%$. Additionally, the formalism does not provide information about the material's degradation, slip processes, or the direction of the crack propagation.

In Chapter 7, the pentagonal cross-section cantilever was employed in combination with *Crystal Plasticity Extended Finite Element Modelling* (CP-XFEM) to get the fracture properties from the experimental data.

Chapter 3: Obtaining SiC fibres-PyC interfacial properties through push-outs FEM Models

Chapter 3 of the thesis is based on the publication in the Journal of European Ceramic Society, titled "Obtaining SiC fibres–PyC interfacial properties through push-out FEM Models", Martinez-Pechero, A., Zayachuk, Y., Widdowson, A., Armstrong, D. E., & Tarleton, E. (2024), available at: https://www.sciencedirect.com/science/article/pii/S0955221923007823. For the statement of authorship, refer to Section 3.7.

This chapter presents Finite Element Method (FEM) simulations of fibre push-out experiments conducted on SiC/PyC fibre-reinforced composites, a critical material for the blanket design of fusion reactors. These simulations enable the isolation and analysis of key interfacial properties, including Coulomb friction, fracture toughness, and shear strength. The FEM results are further contextualised through a discussion of relevant literature and supported by analytical calculations.

Obtaining SiC fibres-PyC interfacial properties through push-outs FEM Models

3.1 Abstract

Silicon carbide (SiC) has attractive properties for use in nuclear reactors. However, it is hampered by inherent brittleness that is overcome through a fibre-reinforced composite. A finite element model based on cohesive zone contact coupled to Coulomb friction is proposed to simulate the push-out response of isolated fibres in SiC/PyC fibre-reinforced composites. The model reproduces the measurements obtained during push-out experiments of isolated fibres in different configurations and predicts interfacial failure between the PyC interphase and fibre. The brittle properties predicted coincide with literature indicating that fibre-PyC interface could prevent the crack propagation through the fibre, fulfilling the function of the structure.

3.2 Introduction

Silicon carbide (SiC) possesses many attractive properties to be a structural material, able to withstand extreme temperature environments such as nuclear fission [61] or fusion [62] reactors, or aerospace applications [63]. These characteristics include low density [63], good oxidation resistance [113], high-temperature tolerance, and creep resistance [114].

However, its practical use is hampered by inherent brittleness [115]. To overcome this, the structure of a continuous SiC fibre-reinforced composite has been proposed [116].

The fibre composite technique consists of growing a SiC matrix over a structure of woven or braided reinforcing SiC fibres. In this way, when a crack grows it is deflected upon contact with the fibres, leaving them undamaged thus reinforcing the overall structure. The friction between the matrix and the undamaged fibres reduces the crack separation increasing the toughness of the composite and leading to pseudo-ductile behaviour.

The study of the fibre-matrix interphase material and its contact area with the fibre, known as the interface is fundamental to evaluate the role of fibres in crack resistance. For nuclear applications, pyrolytic carbon (PyC) is the material chosen for the interphase due to its resistance to moderate irradiation effects [65].

Various experimental methods have been suggested for the characterisation of the fibre-matrix interphase such as micropillar compression [66], micro-cantilever fracture [10] and fibre push-out [67].

Flat-tip push-out studies the role of friction and mode II cracks at the interphase maintaining the fibre integrity. However, it requires in-depth analysis for proper interpretation due to the complexity of the experiment. Compression of the fibre causes swelling in the radial direction producing friction that compensates for the loss of overall stiffness and slows down crack propagation. The load grows to a peak where interface cracking is complete and the resistance drops to a plateau region where friction dominates [14]. The nonlinearity of the process requires complex analytical models [69].

Numerous push-out experiments have been extensively documented in the literature [67, 117, 44, 118]. Some studies have highlighted significant variations in fibre attachment strength based on different factors, including the fibre nature (SA3 or NHS), interphase structure (monolayer or multilayer), PyC structure (isotropic or anisotropic)[117, 118], and interphase roughness (highly irregular [44] or flat [67]). However, it is worth noting that differentiating between the interphase link force and the resistance caused by friction is a seldomly explored aspect in push-out experiments [117, 44]. Existing studies have utilised simplified formulations [69], neglecting the influence of PyC toughness and gradual crack propagation. In this context, numerical models can play an important role in discerning the contributing factors affecting fibre resistance during push-out, thereby providing valuable physical insights that may not be readily measurable in experimental settings.

This contribution presents a Finite element model of two push-out experiments. Crack modelling is based on a cohesive zone model in combination with Coulomb friction. The material studied was a SiC sample produced by chemical vapor infiltration (CVI) [119] reinforced by Tyranno SA3 fibres which are separated by a PyC interphase and the push-out was performed in a bridge configuration [120].

The model parameters were obtained from the experiments and literature with a margin of uncertainty depending on measurements and references. To compensate this, push-out experiments were repeated at different positions of the bridge and an optimisation algorithm was applied to identify the combination of parameters that best fit the set of measurements.

Finally, the role of friction in crack propagation and the viability of PyC for crack deflection were studied. Based on push-out theory [69], some precautions in the way of calculating the interfacial shear strength were proposed to improve the accuracy of the measurements.

3.3 Push-out experiments

In this section, we discuss the details related to the fabrication, properties and push-out experiments of the Tyranno SA3 fibre-reinforced composite.

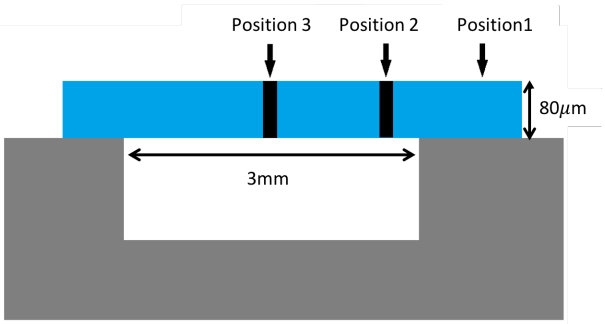

Figure 3.1: Bridge configuration of the sample and positions where experiments were performed.

3.3.1 Fibre-reinforced ceramic composites

There are many techniques of manufacturing SiC fibre-reinforced matrix such as melt infiltration [121], polymer infiltration and pyrolysis [61], transient eutectic phase [122] and chemical vapor infiltration (CVI) [119].

In the sample, the matrix was produced via the CVI technique. A gaseous SiC precursor as methyl trichlorosilane (CH3SiCl3) is mixed with hydrogen and introduced into a high-temperature chamber where the prefabricated fibre structure is located. The precursor decomposes in the presence of hydrogen and the gas-phase pyrolysis products chemically react with the substrate, forming a silicon carbide matrix within and around the fibre reinforcement [123]. CVI has the advantage of being able to produce very high purity β-phase SiC that exhibits good radiation resistance [124], making it suitable for nuclear cladding. However, the process might require several weeks of infiltration time and leaves a large porosity.

The sample studied contains Tyranno SA3 fibres (Ube Industries Ltd), characterised by their low oxygen concentration, which reduces creep and rupture mechanisms at high temperatures [125]. Fibres are uniformly coated with one interphase made of $\sim$100 nm PyC using the chemical vapour deposition (CVD) [116].

The sample was cut with a Capco diamond saw, obtaining a bar of 10mm x 1mm x 0.7mm with fibre bundles parallel and perpendicular to the surface. It was then mechanically ground with SiC grinding discs on the front and back surfaces to a final thickness of $\sim$80 μm, and polished with diamond suspension of 3-1 μm grain size. The sample was clamped, forming a 3mm length bridge configuration (see Fig. 3.1).

3.3.2 Fibres and PyC interphase

The fibres have a small diameter (7-9 μm) and are distributed in bundles with higher fibre density and porosity in the centre than in the periphery where the matrix is more homogeneous (see Fig. 3.2), being the fibres in the periphery the ones selected for the measurements in order to avoid undesired porosity

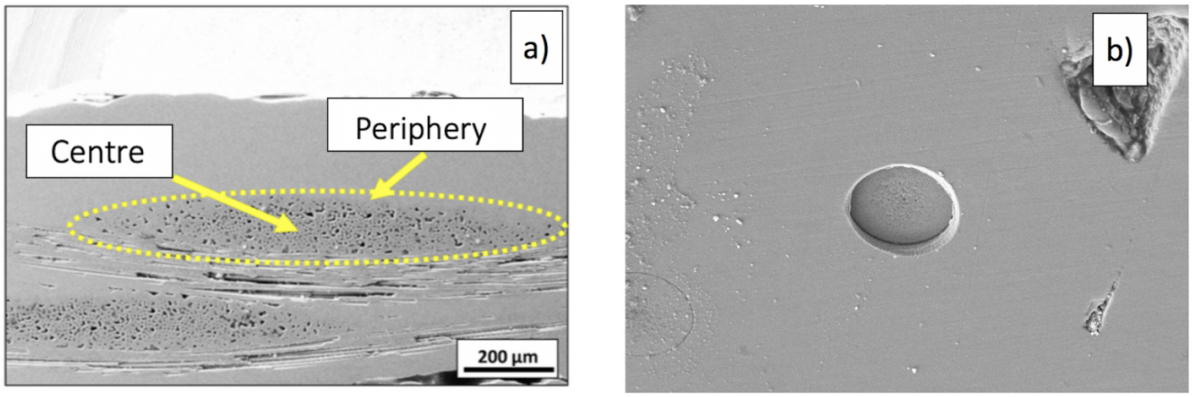

Figure 3.2: a) Left image: Bundle of fibres with higher density in the centre than in the periphery. b) Example of periphery fibre used in the push-out experiment because is isolated from other fibres and pores.

effects[67].

Zayachuk et al. [10] present the structure of the fibre as an agglomeration of equiaxed grains of size between 50-200 nm. The grain size of the fibres is radially non-uniform and increases towards the fibre periphery. On the other hand, the concentration of carbon inclusions decreases from the centre towards the periphery. This structure affects the elastic modulus of the fibre which increases linearly from E=250 GPa in the centre of the fibre up to E=450 GPa towards the periphery. The Poisson's ratio was assumed constant ν=0.17 [126].

The fibres are surrounded by a ∼100 nm PyC interphase that protects them from crack propagation in the matrix. The contact area between the fibre and the PyC interphase is known as the PyC-fibre interface. Push-out cracks may occur in the PyC interphase or the PyC-fibre interface [127].

In other similar samples, SEM images of push-out tests [67] showed no PyC deposits on the SA3 fibres, which is a good indicator that the crack did not occur across the PyC interphase. In addition, TEM images of a crack in a cantilever of the same material [10] showed a clear failure in the interface. There is no information about some crack properties of the interface, however some approaches such as molecular dynamics simulations [128] or theoretical fracture mechanics [129] provide information about the range of values of these magnitudes, which are subsequently adjusted using the FEM results and the experiments.

3.3.3 Push-out measurements

Push-out measurements were performed using an Agilent XP nanoindenter and a flat-punch indenter tip with a diameter of $\sim 5.4\mu$m. It was equipped with an x40 optical objective, capable of resolving individual fibres, and a movable stage to accurately place fibres under the indenter. Measurements were performed in a load-controlled mode with a constant strain rate of 0.05 s^{-1}. Experimental measures of space dimensions and Young's modulus of the matrix with the margins of error are presented in Table 3.1.

The curves resulting from the push-outs are characterised by several phases shown in Fig. 3.3:

A) Initial quasi-flat region corresponding to the approach of the tip to the fibre and its adaptation to the roughness of the surface.

B) Linear-elastic region, the indenter produces a response similar to matrix nanoindentation.

C) Crack initiation at the interface. It is difficult to determine when a crack initiates and its evolution, the reduction of stiffness due to crack initiation is compensated by fibre expansion and friction presenting a small reduction in the load-displacement slope curve.

D) Plateau load regime occurs after the crack has been propagated across the interface and the sample stiffness drops. Traditional push-outs models [130, 131] illustrate a peak load followed by an abrupt drop. In our experiments, we use a load control indenter and once the debonded fibre moves abruptly we cannot control the load for each displacement, being represented by a plateau with a similar load.

E) After the complete debonding of the fibre, the lateral edges of the tip, which has a shape of a truncated cone, touch the edges of the hole left by the fibre producing an additional increase in the load.

F) The unloading regime doesn't provide any physical information.

Our models are focused in the elastic and crack propagation regime which corresponds to B) and C).

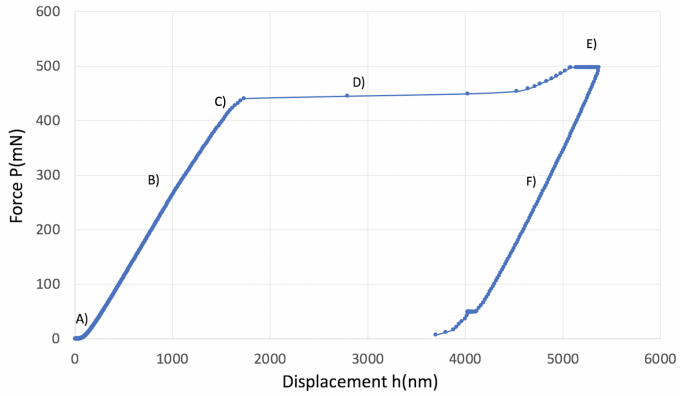

Figure 3.3: Stages of the curve during push-out experiments.

3.4 Finite element models

The need to model the behaviour of the fibres in a ceramic composite during crack formation led us to use Finite Element Modelling (FEM). Abaqus 2021 [42] was used as the FEM software for the simulations.

The models were designed to reproduce the flat-tip nanoindentation experiments in three positions of the ceramic matrix composite: $P1$: matrix area resting on a support of the bridge, $P2$: matrix area suspended but not in the centre of the bridge, $P3$: central section of the suspended matrix area, see Fig. 3.1.

Two types of FEM simulations were performed: *Elastic Models of SiC matrix* to characterise the parameters of the matrix and *Cohesive Zone Models* to characterise the behaviour of the interface during fibre push-out experiments.

3.4.1 Elastic Models of SiC matrix

Initially, the impact of tip compression was studied. For this purpose, a model with a virtual diamond flat tip and another model without a flat tip but imposing a homogeneous displacement in the indentation zone were compared on $P1$, Fig. 3.4.

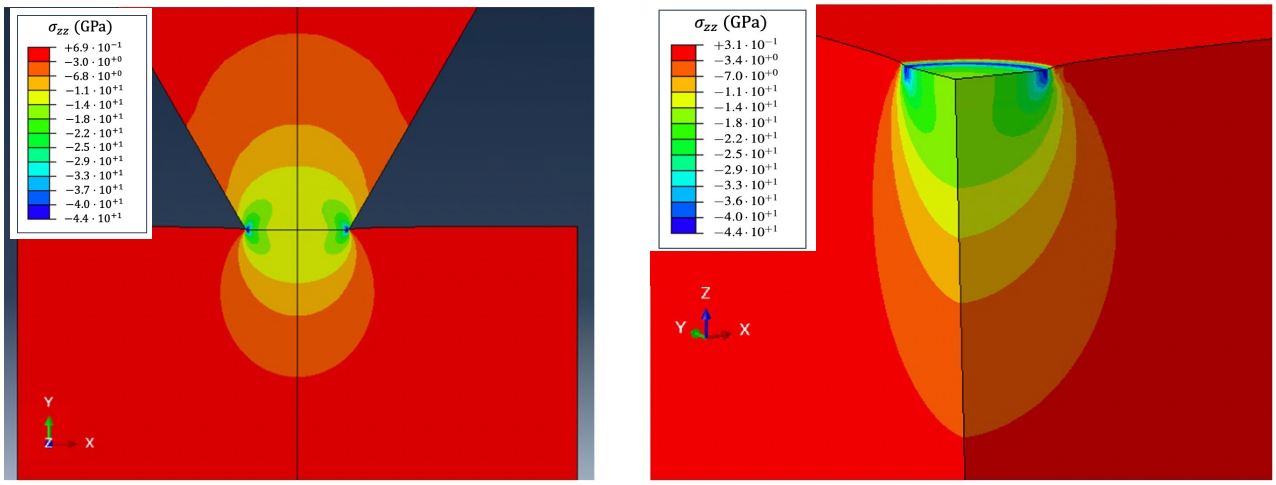

Figure 3.4: Left) σ_{zz} profile at position $P1$ using a flat tip and axisymmetric elements. Right) σ_{zz} profile for 3D model at position $P1$ using homogeneous displacement-control load.

Due to the cylindrical symmetry of $P1$, 85,633 8-node axisymmetric elements (CAX8) were employed to model the virtual tip and the sample made of SiC matrix material. Both parts were joined via rough contact formulation. The results of this model were compared with a 3D model using 120,915 20-node quadratic elements (C3D20) and homogeneous displacement-control load Fig. 3.4.

Once it was verified that the results of both boundary conditions were equivalent, the displacement-control was used for simplicity to characterise the matrix parameters in $P2$ and $P3$.

$P3$ indentation was simulated with a model of 1/4 of the sample (using 180,355 C3D20 elements) because the sample is symmetric in the centre of the bridge according to length and width directions. $P2$ indentation was simulated with 1/2 of the sample (using 212,980 C3D20 elements) because the sample's edge position is symmetric only in the width direction but not in the length direction (see Fig. 3.1).

3.4.2 Cohesive zone model (CZM)

Push-out experiments produce mode II crack propagation in the PyC-fibre interface [67, 10]. A *cohesive zone model* (CZM) coupled with Coulomb friction has been adopted to represent this failure behaviour. The CZM consists of a constitutive relation between the tractions acting on the interface and the corresponding interfacial separation. In the present work, we use a bilinear law [132] as the constitutive relation.

The known direction of the crack propagation and the physical interpretation of the parameters make a cohesive zone model very attractive compared to other methods such as J-integral or XFEM [42]. Furthermore, LAMMPS atomistic simulations [128] illustrate a bilinear traction-separation behaviour for mode II cracks formed between the PyC-fibre interface.

A bilinear law can be divided into an elastic undamaged regime, damage-initiation criteria, a damage propagation regime and complete failure criteria. Constitutive equations in the undamaged regime are:

$$\begin{bmatrix} \sigma_n \\ \tau_s \\ \tau_t' \end{bmatrix} = \begin{bmatrix} K_{nn} & K_{ns} & K_{nt} \\ K_{ns} & K_{ss} & K_{st} \\ K_{nt} & K_{st} & K_{tt} \end{bmatrix} \begin{bmatrix} \delta_n \\ \delta_s \\ \delta_t \end{bmatrix} \tag{3.4.1}$$

Where σ_n is the normal stress, $\tau_{s/t}$ are the shear stress in the two tangential directions, K_{ij} is the stiffness matrix and δ_i is the nodal displacement in the normal n or tangential directions t and s.

Damage initiation is represented via the quadratic onset criterion:

$$\begin{gathered} \sqrt{\left(\frac{\langle \sigma_n \rangle}{\sigma_I^{\max}}\right)^2 + \left(\frac{\tau_s}{\sigma_{II}^{\max}}\right)^2} = 1 \\ \langle \sigma_n \rangle = \sigma_n; \quad \sigma_n > 0 \\ \langle \sigma_n \rangle = 0; \quad \sigma_n < 0 \end{gathered} \tag{3.4.2}$$

where σ_I^{max} and σ_{II}^{max} are the cohesive interface strengths for mode I and II (mode III is ignored for this model because the geometric shape of the crack forms a cylinder).

Once the cohesive damage has initiated, the propagation regime begins. The interface shear stress has contributions from the cohesive model (for mode II) and the friction model (if $\sigma_n < 0$):

$$\sigma_n = \begin{cases} (1-D)\bar{\sigma}_n, & \text{if } \sigma_n > 0 \\ \bar{\sigma}_n, & \text{if } \sigma_n \leq 0 \end{cases} \qquad \tau_s = \begin{cases} (1-D)\bar{\tau}_s, & \text{if } \sigma_n > 0 \\ (1-D)\bar{\tau}_s + D\mu\bar{\sigma}_n, & \text{if } \sigma_n \leq 0 \end{cases} \tag{3.4.3}$$

where $\bar{\sigma}_n$ and $\bar{\tau}_s$ are the normal and shear components if the cohesive region were undamaged (defined by

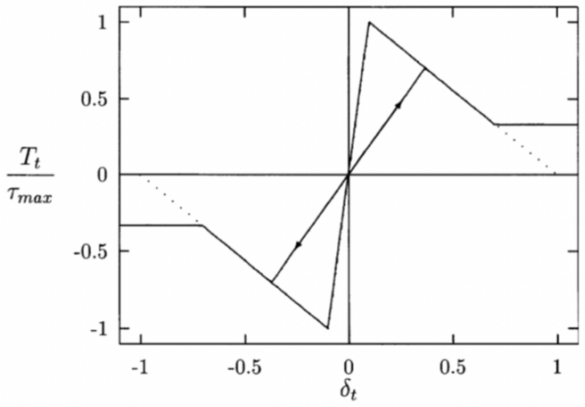

Figure 3.5: Representation of mode II bilinear law in combination with Coulomb friction [14].

Eq. (3.4.1)). μ is the Coulomb friction coefficient. The contribution from the friction model is weighted by the cohesive damage variable D, which is 0 when the quadratic onset criterion is accomplished and 1 when the failure is complete.

The complete failure is defined by the linear interaction criterion.

$$\frac{G_I}{G_{IC}} + \frac{G_{II}}{G_{IIC}} = 1, \tag{3.4.4}$$

where $G_I = \int \sigma_n d\delta_n$ and $G_{II} = \int \tau_s d\delta_s$ are the energetic work of fracture. Toughness $G_{IC/IIC}$ are material properties obtained experimentally that represent the energy released when failure is complete. After complete failure, friction remains governed by Coulomb's law.

A schematic response of the normalised traction-displacement with friction can be observed in Fig. 3.5. The implementation was done using surface cohesive elements of Abaqus combined with a tangential stiffness penalty. A viscosity coefficient of $\eta = 0.0005$ was introduced to facilitate calculations during the optimisation.

Push-out simulations were designed with 451,127 C3D8 elements for $P3$ and 650,208 C3D8 elements for $P2$. The boundary conditions are analogous to the elastic models. The fibre elastic modulus varies radially; this effect was implemented through an Abaqus USDFLD subroutine (see Subsect. 3.3.2).

The residual stress from the previous nanoindentation on the matrix and the thermal stress were neglected due to the lack of experimental measurements. The PyC layer surrounding the cohesive region was neglected in the model because it should not contribute to the global elastic conditions of the interface due to its low thickness ($\sim$100 nm).

3.4.3 Nelder-Mead optimisation

The uncertainty in geometrical parameters (length L, thickness t), and Young's modulus E supposed a difficulty in modelling the matrix force response in the push-out model (see Table 3.1 with the errors).

Variable	Experimental measurements	Raw error	%error	Model parameter	% Deviation from experimental
Length (μm)	3000	300	10%	2884.5	3.8%
Thickness (μm)	80	16	20%	93.1	16%
E (GPa)	460	50	10%	448.5	2%
Width (μm)	1000	100	10%	1000	0%
Tip diameter (μm)	5.4	0.2	3%	5.4	0%
fibre diameter (μm)	8	1	12%	8	0%
PyC interphase (nm)	100	50	50%	-	-
P2 from extreme (μm)	200	20	10%	200	0%

Table 3.1: Dimensions and Young's modulus of the sample and the optimised parameters for the FEM simulations. Measurement errors were obtained from the standard error after different measurements or from the precision of the instruments.

Nanoindentation in the matrix at $P3$ presents an elastic response that can be expressed by the following equation, showing the high impact of these parameters on the force ($P \propto t^3/L^3$ and $P \propto E^*$):

$$P = \frac{192E^* w t^3 h}{12L^3} \qquad \frac{1}{E^*} = \frac{\left(1-v^2\right)}{E} + \frac{\left(1-v'^2\right)}{E'} \tag{3.4.5}$$

P is the load, h the indenter displacement, v Poisson's ratio, E the Young's modulus, E^* the reduced Young's modulus and w the width of the sample.

With the objective to implement a homogeneous elastic matrix for push-out simulations, a Nelder-Mead [15] optimisation algorithm was implemented to identify the combination of values within the margins of errors that best fit the results obtained during matrix nanoindentation in the different positions. Nelder-Mead was chosen between other optimisation methods because it converges fast considering the time consumption for FEM simulations and doesn't require the calculation of the mathematical derivative of the distance function.

Nelder-Mead is a heuristic optimisation algorithm where the parameters are adjusted to minimise a distance function previously defined. It uses a geometrical shape called simplex, which corresponds to an n-dimensional version of a 'triangle' (n being the number of parameters). Starting with a simplex where one vertex's coordinates correspond to the initial values and the other vertices are randomly generated, it proceeds to reshape/move the simplex, one vertex at a time, towards an optimal region in the search space (Fig. 3.6). Starting from the experimental data as initial values, the search space was defined by the margins of error of L, t, and E. The optimisation algorithm compares the simulation curves with the experimental

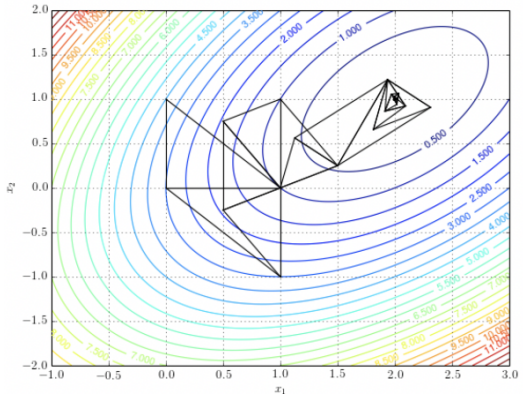

Figure 3.6: Nelder-Mead optimisation for 2D parameters. Contour lines represent points with equal values of the distance function; the triangles reduce their size while the algorithm approximates to the optimum parameters [133].

curves, trying to minimise the following distance function.

$$Dist = \max_{i=[2,3]} \left(\frac{\left| a^{exp}_{pos-i} - a^{model}_{pos-i} \right|}{| a^{exp}_{pos-i} |} \right) \tag{3.4.6}$$

where a is the slope of the linear fit of the experimental data (exp) or the Abaqus model (model) and $pos-i$ the different positions used during the optimisation.

The algorithm was implemented in the R language using the optimx library and a sockets-gateway to communicate with the Abaqus Python script that executes the FEM simulations, trying to minimise the distance function.

The optimisation algorithm progressively converges to a solution but does not guarantee that it is unique. To validate the solution, the algorithm was executed several times with different initial parameters to check the solution converges to similar values.

The same method was applied to find Coulomb friction parameter μ, mode II toughness G_{II} and the shear strength τ_s. In this case, the distance function was defined by the Euclidean distance between the maximum force values. The initial values come from literature [66, 128, 129].

$$Dist = \max_{i=[2,3]} \left(\frac{(P^{exp} - P^{sim})^2}{(P^{exp})^2} + \frac{(h^{exp} - h^{sim})^2}{(h^{exp})^2} \right) \tag{3.4.7}$$

where P is the load peak (mN) and h the nanoindenter displacement (nm).

3.5 Results and discussion

The objective of this work was to reproduce different nanoindentation and push-out experiments with FEM models to analyse in detail the internal processes of the material.

In the first phase, simulations of nanoindentations were carried out on positions of the matrix without fibres to characterise the properties of the SiC matrix (thickness, length and Young's modulus). Once the matrix was better characterised, fibre push-out models were developed to study in depth the propagation of cracks in a matrix with fibres.

3.5.1 SiC matrix Nanoindentations

The elastic response of the matrix was measured by means of 500 mN flat-tipped nanoindentations on a SiC matrix at different positions: $P1$, $P2$ and $P3$ (see Fig. 3.1). The high stress compresses the diamond tip, thereby increasing the measured displacement calculated from the indent.

To study the impact of tip compression, we utilised the $P1$ model (indentation over the SiC matrix), which does not require modelling the full sample since there is no bending (see Fig. 3.1). We employed two approaches: first, an analytical formula to estimate compression from experimental data, and second, a comparison between a model with a diamond flat tip and one where the tip is replaced by a homogeneous displacement load on the indentation zone (see Fig. 3.4).

Eq. (3.5.1) shows the experimental force-displacement relation (dP/dh) with respect to the reduced Young's modulus for a flat tip (E^*) and the real Young's modulus (E).

$$\frac{dP}{dh} = 2E^* \frac{\sqrt{A}}{\sqrt{\pi}} \quad \frac{1}{E^*} = \frac{\left(1-\nu^2\right)}{E} + \frac{\left(1-\nu_d^2\right)}{E_d} \tag{3.5.1}$$

Considering reported values of diamond flat-tip and SiC Poisson ratio E_d=1143 GPa, ν_d = 0.07 [134], ν = 0.22 [126] and measuring the area A and the ratio dP/dh from the experimental data, it was calculated a reduced Young's modulus of E^* = 272 GPa, a tip compression of 94 nm for 500 mN and Young's modulus E=372 GPa, a value that differs 19% from the value measured with a Berkovich tip for the same sample E=460 GPa [10].

Regarding the simulations, the model with the virtual tip (Fig. 3.4 Left) presented a compression of 77 nm (from top to bottom of the tip across the symmetry axis). This extra displacement associated with compression was added to the force-displacement curves in the model with displacement-control load showing both models a similar force-displacement response (see Fig. 3.7) and similar stress profiles with high-stress con-

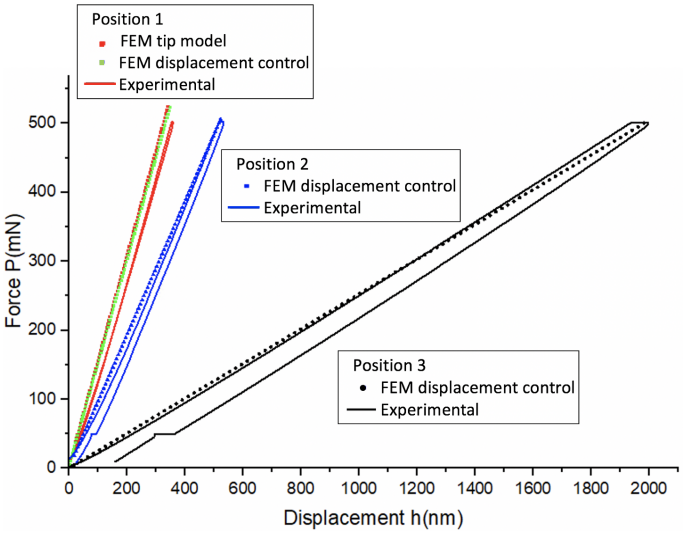

Figure 3.7: Nanoindentation load-displacement curves from experiments and FEM for positions 1, 2 and 3 on the SiC matrix.

centration at the edges of the contact zone with the tip (see Fig. 3.4). These similarities validate continuing the simulations of $P2$ and $P3$ using displacement-control load for simplicity.

The $P1$ models were adjusted to obtain the best fit to experimental data, obtaining E=392 GPa (14% below E=460 GPa [10]). However, $P1$ is a measure of a small region of the sample where pores or microfractures may alter the E adjustment. The results of the $P1$ simulations serve to calibrate the displacement (77 nm) caused by tip compression when it experiments 500 mN of force (see Fig. 3.7). The tip compression is proportional to the force (since all the materials are elastic), and it is used to calibrate $P2$ and $P3$ simulations.

$P2$ and $P3$ nanoindentations were measured to characterise the elastic response of the matrix in a bridge configuration (see Fig. 3.1), where the bending of the SiC bridge affects a bigger region of the sample than in $P1$. As a consequence, the calculation of Young's modulus in $P2$ and $P3$ gave a closer value to the average Young's modulus [10] than $P1$.

Through a Nelder-Mead optimisation and successive simulations, the optimum values that best fit the experimental data were obtained: Length=2884.5μm (3.8% of deviation from experimental data), thickness=93.1μm (16%) and E=448.5 GPa. (2.5%), see Table 3.1 for more details.

$P3$, as a central position in the bridge, could also be compared with the bridge elastic sample equation (see Eq. (3.4.5)). The slope of the load-displacement curve (Fig. 3.7) for $P3$ model was P/h=0.252 mN/nm and using Eq. (3.4.5) was P/h=0.241 mN/nm (4.5% of difference), being a good indicator that the matrix can be approximated to a homogeneous elastic material for posterior push-out modelling.

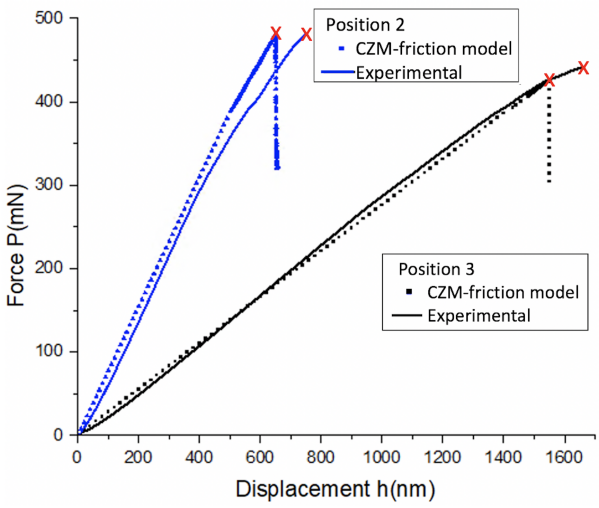

Figure 3.8: Push-out load-displacement curves from experiments and models for positions 2 and 3. Red "x" indicates the maximum load reached before the fibre is debonded.

3.5.2 Fibre Push-outs

Results of push-out models at $P2$ and $P3$ are presented in Fig. 3.9 and 3.10 respectively. The Von Mises stress profiles are represented in the lateral, top and bottom profiles of the fibre at different times. In both positions, the initial response is similar to matrix nanoindentations. The sample is bent until the stress at the interface initiates the crack that propagates from the top to the bottom of the fibre. The loss of stiffness due to cracking is compensated by fibre compression in the z-axis and by Coulomb friction stress due to the fibre expansion in the radial direction. When the crack tip reaches the bottom, the crack is complete and the resistance drops.

In $P2$ (Fig. 3.9), we can also appreciate how the asymmetric conditions affect the stress profile at the top of the fibre and how the friction is higher on the side closer to the sample attachment. As the crack propagates through the fibre, the asymmetry of the stress profile disappears.

Fig. 3.8 presents load-displacement curves during $P2$ and $P3$ fibres push-outs. The graph shows a very similar behaviour between the experimental results and those obtained in the finite element model based on cohesive zone contact coupled to Coulomb friction.

It can be observed how the force to failure on $P2$ is higher than $P3$, due to the toughening effect of friction, while $P3$ resists more displacement due to the bending of the sample. Experimental curves present a quasi-linear behaviour that suggests a brittle interface with high shear strength and abrupt failure.

The modelling was parameterised with values obtained from the literature. Stiffness $K_n = 2850 GPa/\mu m$ and $K_s = 1150 GPa/\mu m$ for normal and shear stress [128], and shear strength $\tau_n = 3.8 GPa$ [128] for crack mode I.

Other parameters with a large impact on the modelling results were adjusted by Nelder-Mead optimisation based on values indicated in the literature.

Friction Coulomb coefficient was fitted to $\mu = 0.15$ ($\mu = 0.15 - 0.36$ according to [66, 135]), toughness to $G_I = 5.3J/m^2$ ($G_I = 2.5 - 8.1J/m^2$ according to [66, 128]), $G_{II} = 22.3J/m^2$ ($G_{II} = 10.5 - 34J/m^2$ [66, 128]) and shear Strength to $\tau_s = 2.1GPa$ for crack mode II ($\tau_s = 1 - 2GPa$[117, 128]).

The adjusted values G_I and G_{II} differ significantly, primarily because $G_{II} = 22.3J/m^2$ is relatively high compared to similar materials such as SiC/BN/SiC. For instance, Gavalda-Diaz et al. [136] reported toughness values of $G_{II} = 1.2 - 3$J/m^2. This discrepancy may be attributed to additional friction sources beyond fibre Poisson expansion, such as interface roughness, which is also captured in this model by G_{II}. Fibre roughness can dissipate significant energy when the sliding velocity is very low and the crack is not fully developed [45, 41]. These frictional components could not be isolated in the current load-controlled experiments, where recording displacement response to force increments lacks sufficient resolution to capture sudden displacements that occur when the fibre is detached. According to Mueller et al [137], the energy dissipated for unit crack area (a more closer definition to G_{II} in CZM) during stable crack propagation could reach values of 75 J/m^2 for a 70 nm PyC interface, suggesting that frictional components should be significantly higher than the pure crack toughness. This limitation, among others, motivated a subsequent study using short fibres under displacement-controlled experiments.

On the other hand, the interface roughness can deviate the fracture from a straight path, making propagation energetically less efficient than the idealised flat cylindrical interface modelled. The connection between microcracks along the fracture trajectory may induce anisotropies in toughness measurements. Hutchinson et al. [129] estimated a difference of approximately $G_{II} \approx 4.2 \cdot G_I$ for large interfaces, a relation used by Kabel et al [66] to determine the relation between G_I and G_{II} for fibre reinforced SiC.

In summary, G_{II} in the modelling of this experiment should be understood as the energetic work required to overcome the resistance of the cohesive element, which combines interface toughness, frictional sources at very low velocities beyond the fibre Poisson expansion and energy dissipation due to non-planar path crack propagation.

When a crack occurs, its deflection in the PyC interphase or the PyC-fibre interface protects the fibre from damage and toughens the SiC composite. Lamon et al. [138] exposed two criteria (a, b) to determine if a crack formed in the matrix may be deflected in contact with the PyC interphase or the PyC-fibre interface protecting the fibre from crack propagation.

a) Deflection at the PyC interphase occurs if $G_{deflection}/G_{propagation} < 0.24$. Although PyC may present a layered crystal structure being highly anisotropic [139], TEM images of similar samples [10] demonstrate

that the PyC crystals are randomly oriented, being approximately isotropic in their cracking properties and this criterion is not met since there is no favourable direction.

b) The criteria for crack deflection at the fibre-PyC interface are $G_{interface} < 0.25 \cdot G_{fibre} < 4J/m^2$ [140] or $G_{interface} < 7J/m^2$ using the calculus exposed in [138] for $G_{fibre} = 16J/m^2$ [10] (assuming the deflection/propagation ratio is similar to [138]). Both conditions are not satisfied if we use experimental data $K_I = 0.8MPa \cdot m^{1/2}$ [10] in combination with Eq. (3.5.2) from [141], giving $G_I = 15.7J/m^2$.

$$G_I = \frac{1-\beta_D^2}{E_*} K_I^2; \quad \frac{1}{E_*} = \frac{1}{2}\left(\frac{1}{E_{PyC}} + \frac{1}{E_{fibre}}\right) \tag{3.5.2}$$

where $\beta_D = 0.26$ is the second Dundur parameter [142] and $E_{PyC} = 12.8GPa$ is the Young modulus of PyC and $E_{fibre} = 365GPa$ is the Young modulus of the fibre.

Type	SiC matrix [10]	fibre [10]	Interface [10]	PyC [138, 139]	Interface CZM
E (GPa)	460	250 (centre)	38-60	20-35	-
SIF(MPa $m^{1/2}$)	4.25	2	0.8	-	-
G_I (J/m^2)	39	16	15-10	21-34	5.1

Table 3.2: Matrix, fibre, PyC interphase and interface properties from bibliography [10, 138, 139].

However, the *b*) criteria is fulfilled for the toughness value of our model $G_I = 5.3J/m^2$. A possible explanation for the differences between the model values and the experimental values could be that Eq. (3.5.2) is designed for a planar interface (not the cylindrical shape). Also, the formulas used to obtain the stress intensity factor K_I in [10] are defined for cracks in homogeneous materials instead of interfaces.

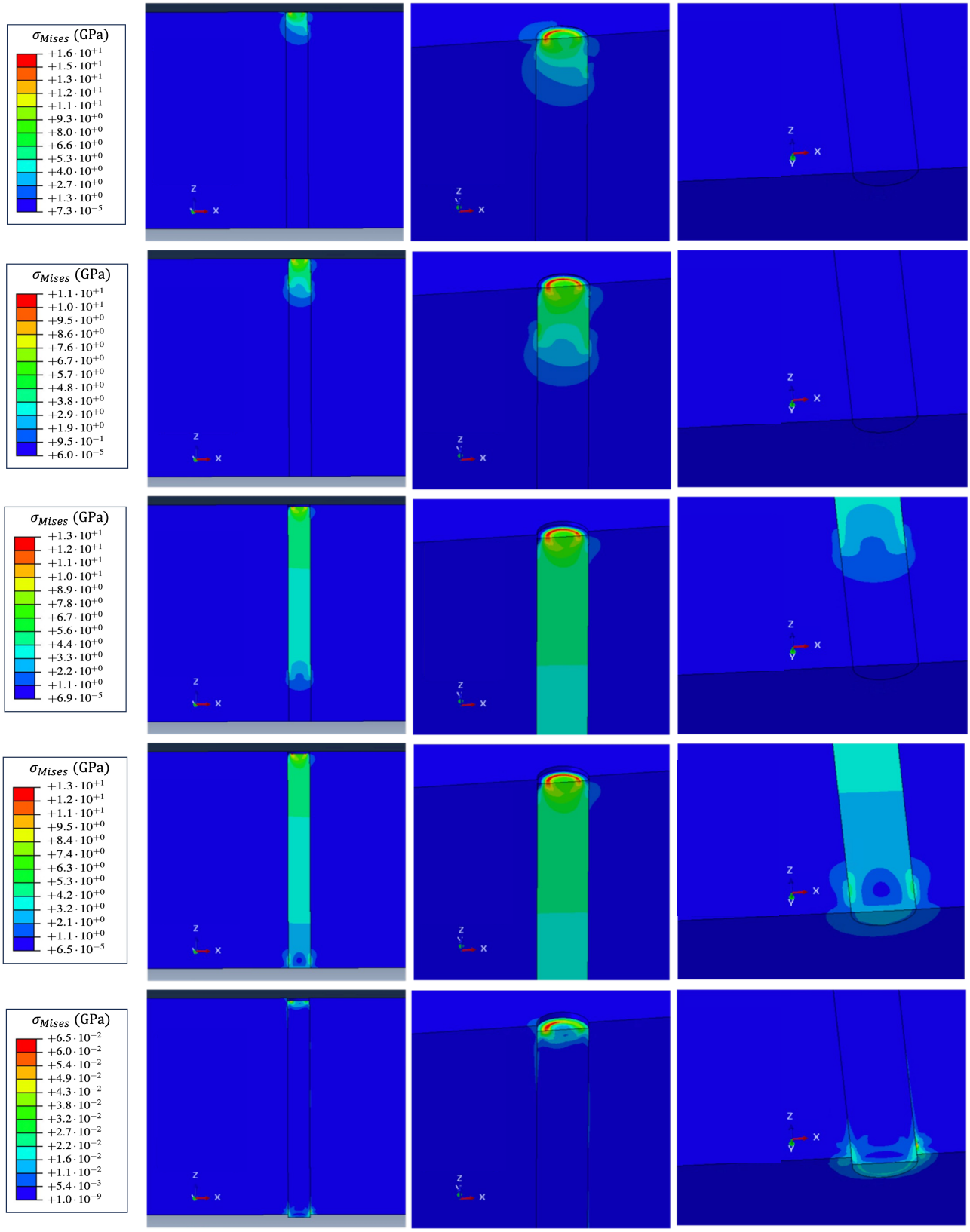

Figure 3.9: Von Mises stress propagation in the fibre during crack formation in position $P2$ from lateral, top and bottom perspectives for the same times.

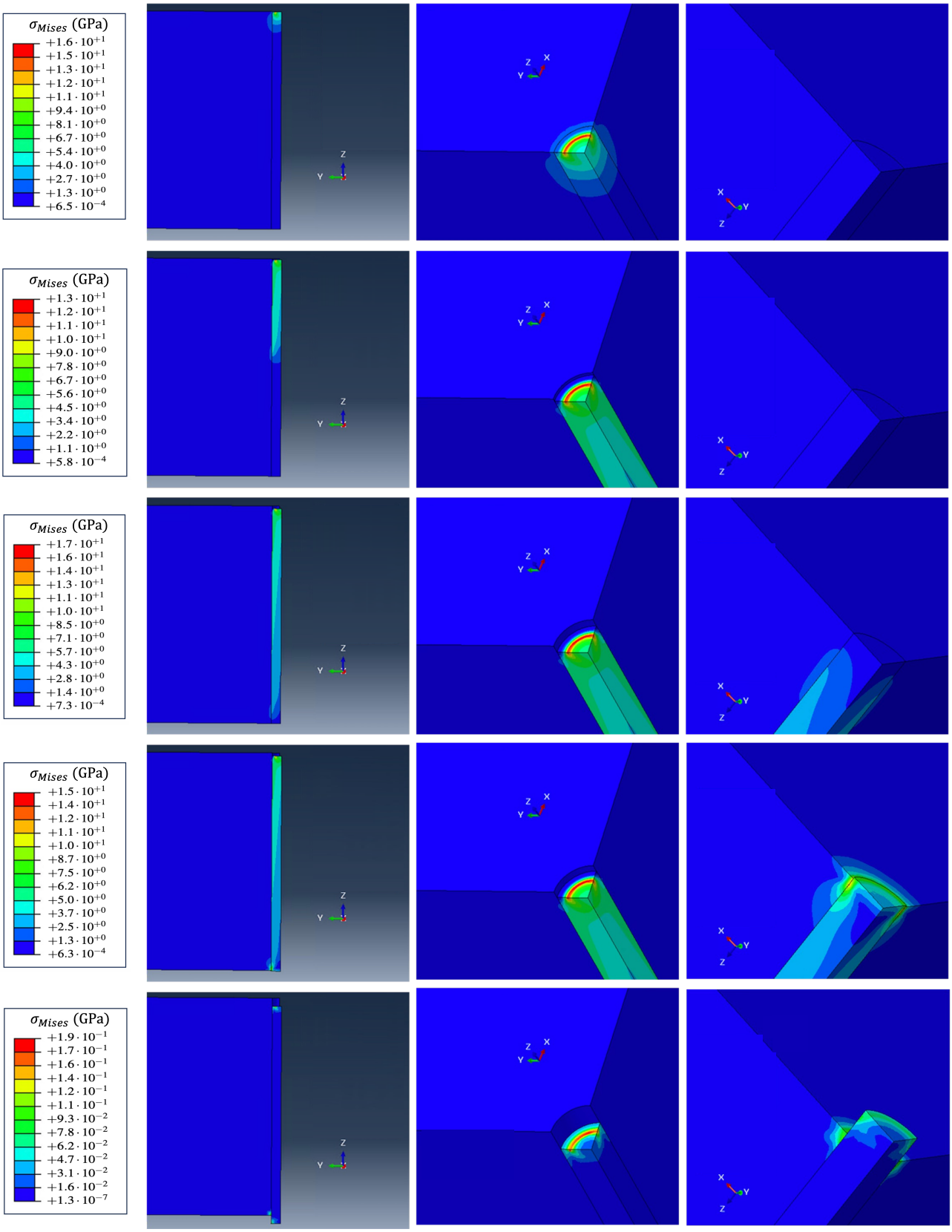

Figure 3.10: Von Mises stress propagation in the fibre during crack formation at position *P*3 from the lateral, top and bottom perspectives at the same time.

3.5.3 Shear strength for high stiffness interfaces

In previous works [67, 117, 44, 118], the interfacial shear strength τ_s was calculated by the equation:

$$\tau_s = \frac{P}{2\pi R t} \tag{3.5.3}$$

where P is the peak load (i.e., debonding load), R is the fibre radius and t is the sample thickness.

Based on the experimental data, Eq. (3.5.3) gives $\tau_s \sim 0.4$ GPa[67], which differs significantly from the value obtained from simulations $\tau_s \sim 2.1$ GPa. Other simulations based on atomistic codes give $\tau_s = 2.01$ GPa [128]. Zayachuk et al.[10] reported 2.6 GPa using a cantilever made of the same material as our sample. Rebillat et al. [117] reported $\tau_s = 1.3$GPa in a sample with the same characteristics as our experiments ($80\mu m$ thick and 100 nm PyC interphase), a value that could be underestimated since it was taken in the centre of the bulk of fibres where porosity and matrix cracking are more frequent.

A possible explanation for these discrepancies could be the fact that Eq. (3.5.3) gives the average shear stress across the interface during crack formation; this value would correspond to the shear strength if the entire interface experiences the same shear stress, something that occurs in samples of low thickness or with very flexible interfaces (low stiffness). These differences were studied in recent articles of SiC composites [44, 118], discerning between the shear strength obtained from Eq. (3.5.3) $\tau_s = 0.1$GPa and the shear strength necessary to break the interface and initiate the fracture which was estimated experimentally $\tau_s = 0.5 - 1$GPa.

Fig. 3.9 presents Von Mises stress in the fibre during crack formation. It can be appreciated how the process is gradual, requiring much lower thickness to accomplish Eq. (3.5.3). To overcome this limitation, a more general expression is given by [69]:

$$P = \tau_s \frac{\sqrt{a}}{K} \tanh(\sqrt{at}) \left(\frac{(1+\nu_{fibre})}{A_{\text{fibre}} E_{\text{fibre}}} - \frac{(1+\nu_{Matrix})}{A_{\text{Matrix}} E_{\text{Matrix}}} \right)^{-1}; \quad \text{where } a = 2\pi RK \left(\frac{(1+\nu_{fibre})}{A_{\text{fibre}} E_{\text{fibre}}} - \frac{(1+\nu_{Matrix})}{A_{\text{Matrix}} E_{\text{Matrix}}} \right) \tag{3.5.4}$$

where A_i is the cross-sectional area of the fibre and matrix respectively, ν_i is Poisson's ratio, E_i is Young's modulus, and K corresponds to the stiffness of the border between matrix and fibre ($K_s = 1150 GPa/\mu m$ in our case).

Eq. (3.5.3) is obtained through the approximation of $\tanh(\sqrt{at}) \sim \sqrt{at}$ when $\sqrt{at} \to 0$, a condition that is achieved for less stiff interfaces or thinner samples.

In this sample, we obtained $\sqrt{at} = 6.8$ and for $\sqrt{at} > 2$, it is possible to approximate $\tanh(\sqrt{at}) \sim 1$

simplifying calculations to:

$$\tau_s = \frac{PK}{\sqrt{a}} \left(\frac{(1+\nu_{fibre})}{A_{\text{fibre}} E_{\text{fibre}}} - \frac{(1+\nu_{Matrix})}{A_{\text{Matrix}} E_{\text{Matrix}}} \right) \tag{3.5.5}$$

We get $\tau_s = 1.8$ GPa, a value closer to $\tau_s = 2.1$ GPa of simulations. Eq. (3.5.5) requires detailed knowledge of the fibre, matrix and interfacial properties which are difficult to measure in some cases. Our proposal is not to substitute Eq. (3.5.3) by Eq. (3.5.5) but to prevent the need to measure push-out peak force with respect to different thicknesses to verify their linear relationship before applying Eq. (3.5.3) (when $\tanh(\sqrt{at}) \sim \sqrt{at}$ then P and t are linear in Eq. (3.5.4)). Fortunately, recent developments in techniques [72] allow thinner SiC samples, which may overcome the issue exposed and open a new area of more detailed push-out experiments.

3.6 Conclusions

SiC/PyC fibre-reinforced composite is a promising material to overcome the brittleness of SiC while maintaining its properties. This work studies how the PyC interface can be used to protect fibres from crack propagation. Push-out experiments of isolated fibres were done to characterise the fracture process and interface properties. The experiments have been complemented by FEM simulations trying to reproduce the results previously obtained in the experiments and provide a detailed analysis of the failure process. The following conclusions can be drawn.

It has been possible to reproduce with good accuracy the experimental behaviour of fibre-reinforced SiC using FEM simulations based on a cohesive zone model coupled with friction. Simulations allow us to obtain virtual experiments of the push-outs, easily understandable without the need of complex formulation. The FEM combination with optimisation algorithms provides an alternative to experimental data to characterise the properties of the SiC composite, such as Young's modulus, shear strength, and toughness of mode I and mode II cracks.

Based on the push-out theory, some recommendations were made for the calculation of interfacial shear strength to avoid incorporating errors of precision when the most common formula is used.

This work can be extended to model other more complex configurations, such as multiple fibre failures over different fibre distributions, and other types of fractures, or adapted to other fibre-reinforced materials.

3.7 Statement of Authorship form

Statement of Authorship for joint/multi-authored papers for PGR thesis

To appear at the end of each thesis chapter submitted as an article/paper

The statement shall describe the candidate's and co-authors' independent research contributions in the thesis publications. For each publication there should exist a complete statement that is to be filled out and signed by the candidate and supervisor **(only required where there isn't already a statement of contribution within the paper itself).**

Title of Paper	Obtaining SiC Fibers-PyC interfacial properties through push-outs FEM Models
Publication Status	☐Published ☐ Accepted for Publication ☐Submitted for Publication ☐Unpublished and unsubmitted work written in a manuscript style
Publication Details	Martinez-Pechero, A., Zayachuk, Y., Widdowson, A., Armstrong, D. E., & Tarleton, E. (2024). Obtaining SiC Fibers–PyC interfacial properties through push-out FEM Models. *Journal of the European Ceramic Society*, *44*(2), 784-794.

Student Confirmation

Student Name:	Alvaro Martinez Pechero		
Contribution to the Paper	The student is the corresponding author and was responsible for writing the document, analyzing experimental data, creating Finite Element models and the mathematical formalism, processing results, conducting the literature review, and formulating conclusions. The remaining authors performed the experimental measurements (Dr Yevhen Zayachuk), supervised the work, obtained the funding, provided support and advice for the modeling, and reviewed the writing.		
Signature		Date	28th July 2025

Supervisor Confirmation

By signing the Statement of Authorship, you are certifying that the candidate made a substantial contribution to the publication, and that the description described above is accurate.

Supervisor name and title: Professor Edmund Tarleton		
Supervisor comments		
Signature	Date	1st August 2025

This completed form should be included in the thesis, at the end of the relevant chapter.

Chapter 4: Progress towards a micro fibre push-out method for measuring fibre-matrix interface properties in SiC composites

Chapter 4 of the thesis is based on the publication in the Journal of European Ceramic Society, titled "Progress towards a micro fibre push-out method for measuring fibre-matrix interface properties in SiC composites", Leide, A., Martinez-Pechero, A. et al (2025), available at: https://www.sciencedirect.com/science/article/pii/S0955221925004443. For the statement of authorship, refer to Section 4.7.

Following the conclusions of the previous chapter, shortening the fibre length was an appropriate approach to isolate the fracture properties from the friction effects (including the non-Coulomb friction and the frictional effects not associated with fibre swelling). In this chapter, a complete analysis of short-fibre push-out is presented. FEM simulations are done to isolate properties and estimate the effect of some aspects associated with the geometry of the fibres.

Progress towards a micro fibre push-out method for measuring fibre-matrix interface properties in SiC composites

4.1 Abstract

Experiments and finite element modelling have been used to explore micro-fibre push-out experiments to subsequently scale the sample to layers thin enough for ion irradiation. Correlation of interfacial surface area to debond stress has been identified for short fibres, and is related to a size effect following a Weibull distribution. The distribution analysis may be used to provide size-independent interfacial properties for use in engineering scale models. Various parameters have been assessed for their relative importance: axial misorientation of fibres appears to have a negligible effect on push-out characteristics, while the taper of fibres does not alter the debond stress, but does alter the frictional component of micro push-out tests. Micro push-out testing directly measures properties of the interface, unlike in long fibre push-out testing, where fracture occurs locally and propagates along the interface, so debond stress as a material property is not directly measurable without assumptions or analytical adjustments.

4.2 Introduction

Next generation fusion and fission reactors require high-performance materials which are able to survive the high operating temperatures and high neutron irradiation doses predicted in operation [143]. SiC fibre-reinforced composites with *pyrolytic carbon* (PyC) interphase (SiC_f/SiC) are a leading candidate material for these applications. SiC_f/SiC is a class of ceramic matrix composite consisting of a complex architecture of SiC fibres within a SiC matrix and separated by a thin PyC interphase layer.

The high strength of SiC_f/SiC is provided by the presence of fibres and the transfer of stress from the matrix into these fibres via the interphase. The weak interface within the PyC interphase layer results in preferential cracking under load, generating fracture energy-consuming mechanisms such as crack deflection, fibre-bridging, fibre sliding, fibre pull-out and micro-cracking. These give SiC_f/SiC its high fracture toughness via extrinsic toughening mechanisms (20-30 MPa $\sqrt{m}$ vs 4MPa$\sqrt{m}$ for monolithic SiC)[144, 145].

As described, the interphase plays a critical role in the unique properties of SiC_f/SiC and is a key enabler in the materials' potential use for structural applications in nuclear environments. However, under high dose irradiation, the interphase can degrade due to the dimensional instability of residual carbon in SiC fibres and the pyrolytic carbon interphase, which in extreme cases can lead to radiation-induced debonding between the fibre and matrix [146, 147]. Quantifying the mechanical effect of radiation damage at low and

intermediate radiation doses is important for predicting lifetime performance.

The interfacial debond stress for mode II crack and interface friction of fibre-reinforced composites are critical parameters that determine the mechanical properties of components. Controlling these parameters during material design and predicting its evolution in service requires scientific tools to measure and understand the fibre debonding and sliding mechanisms. These tools should also apply to irradiated composites, necessitating a technique that minimises the material specimen dimensions and waste. The method should apply to thin ($<10\ \mu$m) layers to study ion-implanted samples, which are used to simulate the compositional changes from transmutation and accelerated displacement damage from the collision cascades caused by the incident ions.

Fibre push-out experiments of variable lengths have been performed on both aerospace composites with a Boron Nitride interphase [127, 136, 148] and nuclear with a carbon interphase [67, 149, 44] to explore test parameters and variables. Large scatter is typically found in these experiments due to microstructural variations such as porosity, fibre dimensions and position, and neighbouring fibres or matrix. The influence of experimental parameters has also been assessed, with recommendations that a flat punch tip with a diameter of approximately half the fibre diameter be used to avoid fracture or plastic deformation during the test while reducing the likelihood of mispositioning the tip over the fibre/matrix interface.

This paper presents results and a parametric study of a micromechanical method of short fibre push-out testing designed to posteriorly study the interfacial debond stress of ion irradiated SiC_f/SiC composites. The experimental development is combined with finite element modelling (FEM) to provide further insights into the mechanisms of fibre debonding and push-out. The modelling approach combines a cohesive zone model with Coulomb friction while accounting for radial stress caused by initial surface roughness and residual stresses [14, 44, 13]. A parametric study of the fracture parameters, Coulomb friction coefficients, the effect of rugosity on friction, the axial inclination of the fibres, and tapered fibre morphology are evaluated, and a detailed FEM analysis is performed of different fibres which were experimentally tested to validate the simulation's results.

4.3 Methodology

4.3.1 Materials

The silicon carbide fibre reinforced silicon carbide matrix composite (SiC_f/SiC) used in this work consisted of Tyranno SA4 fibres (Ube Corporation, Japan) with a 90° 2D weave, an 80-100 nm thick pyrolytic carbon (PyC) interphase coating, and a SiC matrix both grown by chemical vapour infiltration followed by over-

coating with SiC by chemical vapour deposition which resulted in a ∼4 mm thick panel. This is a typical approach to manufacturing nuclear grade SiC_f/SiC composite.

4.3.2 Sample preparation

Firstly, long fibre push-outs were performed to validate that the indenter and the sample work in expected conditions. The specimens were prepared by cutting 20 × 4 × 0.6 mm thick cross-sections of the panel using a precision diamond saw, followed by thinning from both sides to ∼180 μm using progressively finer diamond lapping films on an Allied Multimet precision polisher until final polishing with a 1 μm diamond lapping film, ensuring parallel faces. Actual thickness was measured using a Mitutoyo digital drop gauge. This thickness is within the recommended range from previous work. Specimens were mounted using Crystalbond mounting wax on polished 25 mm diameter pin stubs with slots laser milled into the surface in a grid pattern to receive the bottom of the fibre as it is pushed out.

For short fibre push-out, specimens were cut from the same panel of SiC_f/SiC to dimensions 12 × 4 × 4 mm. These were ground and polished on four sides using diamond lapping films in the precision polisher to achieve a cuboid with parallel faces. Grinding with coarse films continued through the CVD coating to reveal fibre tows aligned parallel to the faces of the specimen. Final polishing was using 1 μm diamond lapping films. Trenches were focussed ion beam (FIB) milled to create the micro-push-out specimens with varying short gauge lengths. A combination of xenon plasma ion source (P-FIB Thermo Fisher Helios) and gallium liquid metal ion source (Ga-FIB FEI Helios 600) were used to create trenches. The surfaces of trenches were polished with low beam currents to create a smooth surface and minimise any milling artifacts such as preferential etching of the carbon interphase. This is shown schematically in Fig. 4.1.

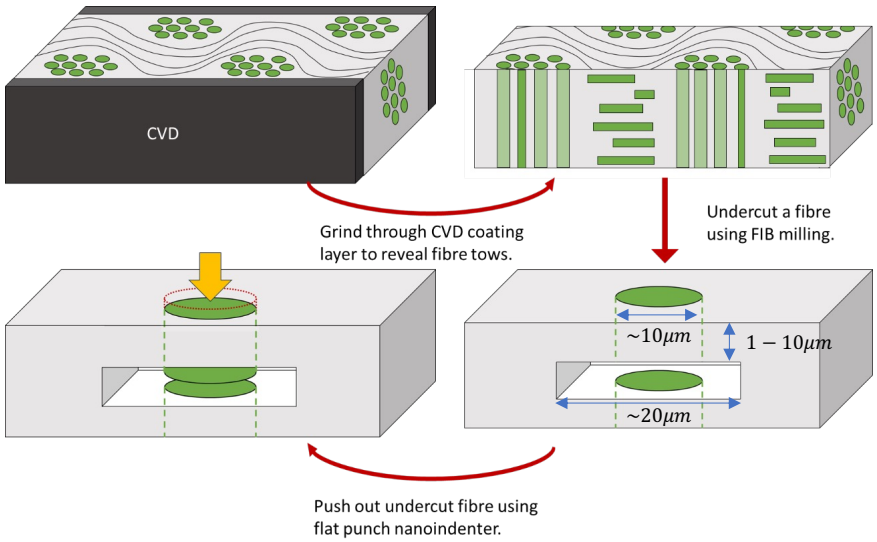

Figure 4.1: Schematic of preparing micro push-out specimens.

4.3.3 Push out testing

Long fibre push-outs were performed using a 5 μm diameter diamond flat punch tip in an Agilent G200 nanoindenter with a displacement rate of 30 nm/s (see Appendix A.1). The instrument itself is inherently load-controlled with displacement rate determined by a feedback loop via capacitance measurements of displacement. The grid of slots in the pin-stub aided alignment of the tip to the fibres using the mechanical stage in the nanoindenter. Load-displacement data were recorded and used for analysis along with dimensions of the actual fibre measured by optical microscopy and post-test scanning electron microscope images acquired using a Tescan Mira FE-SEM.

Short fibre push-outs were performed in-situ using an Alemnis Standard Assembly inside a Tescan Mira SEM. A 5 μm diameter diamond flat punch tip was used for all tests. Displacement rates were either 100 nm/s or 10 nm/s. No effect of displacement rate was observed and 10 nm/s was used for the majority of tests. The Alemnis Standard Assembly fundamentally works in displacement control, allowing measurement of load changes during the test, especially after fibre debonding. The frame compliance of the instrument is measured at 4.1 μm/N which causes $\sim$90 nm displacement offset for the highest loads in the longest gauge lengths of these experiments.

4.3.4 Characterisation

Following micromechanical testing, selected push-outs were imaged and cross-sectioned using a FEI Helios 600 FIB-SEM and one push-out was sequentially milled using the slice and view method with 10 nm step size at 30 kV 0.12 nA. Platinum protective layers were deposited to protect the surface of all cross-sections. The slice and view images were reconstructed into a 3D dataset using ORS Dragonfly Pro software and segmented into “fibre”, “PyC”, “matrix”, and “background” phases using U-Net Deep Learning algorithms trained by manually segmenting 7 slices of the dataset.

4.3.5 Modelling

Push-out experiments produce mode II crack propagation in the PyC-fibre interface [13, 67]. A cohesive zone model (CZM) coupled with Coulomb friction has been adopted to represent this failure behaviour. The cohesive zone model consists of a constitutive relation between the tractions acting on the interface and the corresponding interfacial separation. In the present work, we use a bilinear law [132].

A bilinear law can be divided into an elastic undamaged regime, damage-initiation criteria, a damage prop-

agation regime and complete failure criteria. Constitutive equations in the undamaged regime are:

$$\begin{bmatrix} \sigma_n \\ \tau_s \\ \tau_t \end{bmatrix} = \begin{bmatrix} K_{nn} & K_{ns} & K_{nt} \\ K_{ns} & K_{ss} & K_{st} \\ K_{nt} & K_{st} & K_{tt} \end{bmatrix} \begin{bmatrix} \delta_n \\ \delta_s \\ \delta_t \end{bmatrix}, \tag{4.3.1}$$

where σ_n is the radial stress, τ_s and τ_t are the shear stress in the two tangential directions, δ_i is the opening displacement in the normal n or tangential directions t and s and K_{ij} are the stiffness matrix components which are $K_{nn} = 2850$ GPa/μm, $K_{tt} = 1150$ GPa/μm, $K_{ss} = 1150$ GPa/μm [128] and K_{ij}=0 GPa/μm when $i \neq j$ (uncoupled behaviour between shear and tension fracture modes).

Damage initiation is represented via the quadratic onset criterion:

$$\sqrt{\left(\frac{\langle \sigma_n \rangle}{\sigma_I^{\max}}\right)^2 + \left(\frac{\tau_s}{\sigma_{II}^{\max}}\right)^2} = 1, \quad \langle \sigma_n \rangle = \sigma_n \text{ if } \sigma_n > 0, \quad \langle \sigma_n \rangle = 0 \text{ if } \sigma_n < 0, \tag{4.3.2}$$

where σ_I^{max} and σ_{II}^{max} are the cohesive interface strengths for modes I and II (mode III is ignored for this model because the cylindrical shape makes it impossible, since the fibres do not twist).

Once the cohesive damage has been initiated, the crack propagation regime begins. The interface resistance is affected by the damage caused by shear stress defined by the cohesive model and the friction (if $\sigma_n < 0$):

$$\sigma_n = \begin{cases} (1-D)\bar{\sigma}_n; & \sigma_n > 0, \\ \bar{\sigma}_n; & \sigma_n \leq 0, \end{cases} \qquad \tau_s = \begin{cases} (1-D)\bar{\tau}_s; & \sigma_n > 0, \\ (1-D)\bar{\tau}_s + D\mu\bar{\sigma}_n; & \sigma_n \leq 0, \end{cases} \tag{4.3.3}$$

where $\bar{\sigma}_n$ and $\bar{\tau}_s$ are the normal and shear components if the cohesive region were undamaged (defined by Eq. (4.3.1)). μ is the Coulomb friction coefficient. The contribution from the friction model is weighted by the cohesive damage variable D, which is 0 when the interface is undamaged and 1 when the failure is complete.

For fibre push-out, the normal component σ_n acts in the radial direction of the fibre, contributing to friction across the entire interface surface. This term can be decomposed into two components $\sigma_n = \sigma_{nv} + \sigma_{no}$. The component σ_{nv} arises from Poisson expansion (swelling) of the fibre or any geometrical deformation during push-out, and σ_{no} is the clamping stress constant.

The clamping stress represents other friction sources than Poisson expansion of the fibre during sliding (after the crack formation is completed). It is mainly attributed to interface roughness, but may also capture residual stresses produced by thermal mismatch between the fibre and matrix during fabrication, mechanical

deformations or irradiation [143]. In our case, the thermal stress is assumed to be small compared with the roughness contribution, since the fibre and the matrix are made of the same material.

The clamping stress was set to $\sigma_{no} = 420$ MPa through an optimisation process to calibrate the friction of multiple fibres. The total friction can be expressed as $\tau_{friction} = \mu\sigma_n = \mu\sigma_{nv} + \mu\sigma_{no} = \mu\sigma_{nv} + \tau_0$, recovering the expression used in other push-out models [44, 45]. Using a constant clamping stress σ_{no} and multiplying it by μ instead of imposing a constant sliding resistance τ_0 is easier to implement into the Abaqus framework and results in the same friction. During the adjustment, the adjustment of μ will affect the constant sliding resistance τ_0 and the friction associated with the Poisson fibre expansion $\mu\sigma_{nv}$ while the adjustment of σ_{no} only has effect on τ_0.

The complete failure is defined by the linear interaction criterion:

$$\frac{G_I}{G_{IC}} + \frac{G_{II}}{G_{IIC}} = 1, \tag{4.3.4}$$

where $G_I = \int \sigma_n d\delta_n$ and $G_{II} = \int \tau_s d\delta_n$ are the toughness values for mode I/II which are material properties obtained experimentally that represent the energy released when failure is complete. After complete failure, friction remains, being governed by Coulomb's law.

The FEM simulations were done by Abaqus 2021 software using C3D8 elements. It was used cohesive contact combined with tangential penalty friction [42].

4.4 Results

4.4.1 Fibre push-out testing

Conventional long-fibre push-out tests were performed to make a comparison with the short fibre push-out tests. Load-displacement curves for all the tests are shown in Fig. 4.2. The curves show elastic loading, followed by small displacement jumps corresponding to crack initiation, propagation, fibre debonding, and a large displacement jump corresponding to the fibre being pushed out completely. Debond stress of the PyC-SiC was calculated from the load at push-out divided by the interfacial surface area of the fibre, finding a mean value of 59.5 $\pm$ 17.5 MPa (standard deviation) with a minimum value of 39 MPa and an upper value of 116 MPa. This simple assumption leads to the misconception that the shear stress being uniform along the fibre length, which is not the case based on the modelling in [13] showing that the stress is localised near the surface and the crack propagates along the interface.

The fibre radius appears to affect the debonding stress, whereas smaller diameter fibres have a larger debond

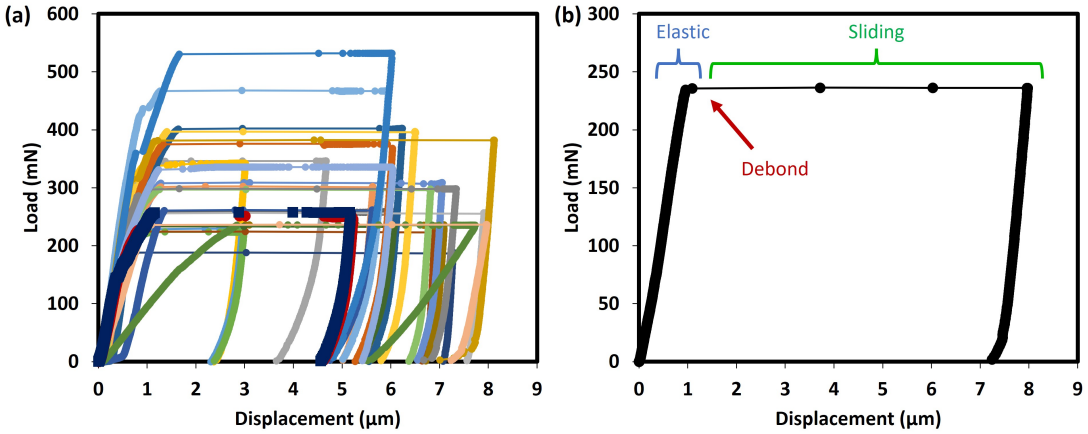

Figure 4.2: (a) Load displacement curves for all successful long fibre push-out tests. (b) Single load-displacement curve labelled to show elastic loading, debonding, and frictional sliding.

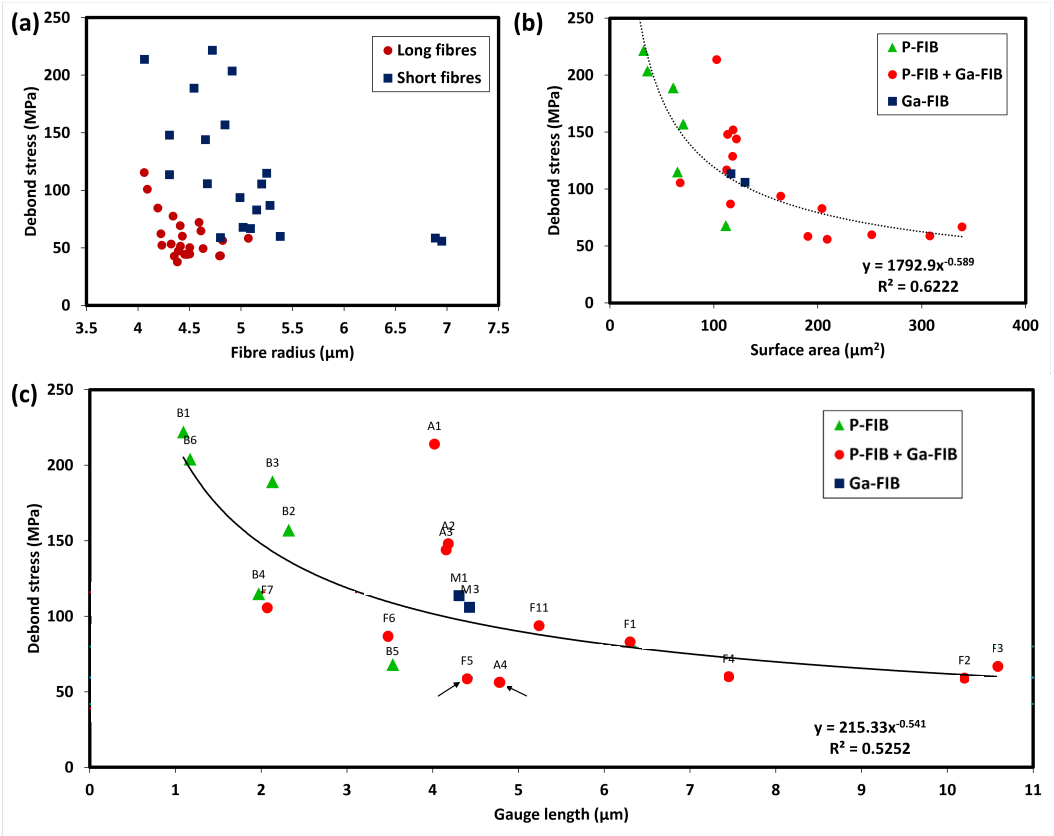

Figure 4.3: Debond stress as a function of (a) fibre radius, (b) fibre interfacial surface area for micro push-outs, and (c) gauge length for micro push-outs. Arrows in (c) indicate the tests with large radius fibres, which are outliers in (a). Trend line equations and R^2 fitting values are shown in (b) and (c). Data point labels in (c) refer to the specific push-outs IDs.

stress. This trend is most obvious for the long fibre push-outs in Fig. 4.3 (a) which are all tested in the same specimen with a thickness (gauge length) of 180 μm. Micro push-out data exhibit a greater range of debond stress, two abnormally large diameter fibres ($\sim$14 μm) present lower debond stress than expected according to the trend of gauge length shown in Fig. 4.3 (c) having gauge lengths of 4.4 μm and 4.79 μm (fibres F5

and A4). Trendlines for debond stress are also plotted as a function of the fibre surface area and gauge length, showing a stronger correlation to the fibre surface area. This is discussed in Subsect. 4.4.2 using Weibull fracture statistics. The micro push-out data points are also separated by their means of trench milling, whether by P-FIB or Ga-FIB or a combination. There was no clear trend of debond stress with the type of FIB used to prepare the push-out trenches.

4.4.2 Weibull analysis

The Weibull fracture theory is an established method to model the fracture of ceramic materials based on failure occurring from the weakest part [150]. The average fracture strength τ_s for shear debonding of the interface can be expressed in Eq. (4.4.1) as:

$$\tau_s = \int_{p=0}^{p=1} \tau dp = \int_0^{\infty} e^{-\int_S N(\tau) dS} d\tau, \tag{4.4.1}$$

where τ_s is the debond stress of the interface and p is the probability of fracture (both vary across the surface S of the interface due to different defects in the interface such as pores or micro-fractures due to fabrication), $N(\tau)$ is a stress function that depends on shear stress τ on the interface caused by fibre push-out. Assuming only shear load on the interface $N(\tau)$ can be approximated to $N(\tau) = k\tau^m$, m is known as the Weibull modulus, and k is a constant for adjustment. The integral can be simplified to:

$$\tau_s = \int_0^{\infty} e^{-\int_S k\tau^m dS} d\tau = \frac{1}{(kS)^{1/m}} \int_0^{\infty} e^{-z^m} dz = C \cdot S^{-1/m}, \tag{4.4.2}$$

where the following approximations have been used:

$$\int_S k\tau^m dS = k\tau^m S = \left((kS)^{1/m}\tau\right)^m = z^m, \text{ and } \int_0^{\infty} e^{-z^m} dz = \Gamma\left(\frac{m+1}{m}\right). \tag{4.4.3}$$

By plotting ln τ_s against ln S for micro push-out tests and conventional long fibre push-out tests, Fig. 4.4 is obtained where the gradient is $-1/m$. For short fibres, $-1/m = -0.58$, giving a Weibull modulus, $m = 1.71$, with a coefficient of determination for this linear regression, R^2 = 0.68. For long fibres, $-1/m = -2.53$, giving a Weibull modulus, $m = 0.40$, with a coefficient of determination, $R^2 = 0.22$ signifying a poor fit. This linear analysis is similar to the exponential fit shown in Fig. 4.3 (b) for short fibre tests.

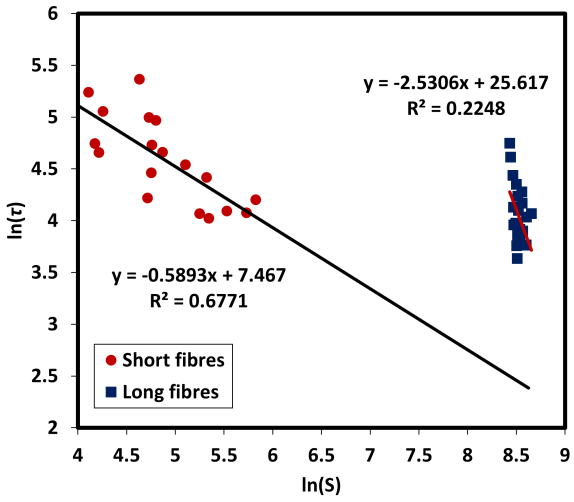

Figure 4.4: Weibull plot of micro push-out results with natural log of debond stress against natural log surface area showing good correlation.

4.4.3 Microstructural analysis

All push-out tests performed on this material responded by interface debonding between the PyC interphase and the fibre, remaining the carbon interphase attached to the matrix, similar to the observations in the literature [118, 67]. The slice imaging and 3D reconstruction in Fig. 4.5 confirm that the PyC layer is continuous, remaining attached to the SiC matrix during the entire push-out.

The circumference, which looks like an impression inside the top of the fibre in Fig. 4.5 is a result of uneven platinum deposition during the push-out 3D impression. No evidence of plastic deformation was seen on the surface of any fibres, and this circumference continues throughout the milling and appears in all slices - it is a result of FIB slicing rather than deformation from the mechanical test itself. Fig. 4.5 (b) is a horizontal slice taken halfway through the remaining fibre within the matrix, indicated by arrows in (a). This shows cracks around the fibre, on the inside surface of the PyC layer; the most apparent of these are indicated with arrows. Rather than a continuous crack around the fibre in the reconstructed 2D plane, there appear to be many individual holes which correspond to the vertical scratched texture in the PyC highlighted in green in (a) and also shown in Fig. 4.6 (a) and (c). No evidence of matrix cracking or crack deflection was observed in this 3D dataset.

The inner surface of the PyC adjacent to the fibres shows damage caused by the push-out process. Scratches parallel to the push-out direction are apparent in the PyC interphase caused by the surface of the fibres abrading the softer PyC, indicated by the white arrows in Fig. 4.6 (a) and (c). The appearance of these scratches appears to be independent of whether the frictional component of the push-out test has a positive or negative gradient with the fibre displacement, as shown by the force-displacement curves of the fibres in

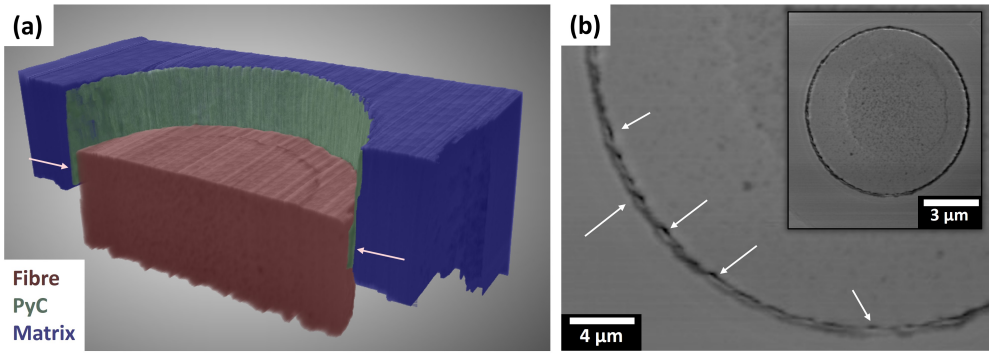

Figure 4.5: (a) Segmented and cropped 3D reconstruction. A continuous layer of PyC remains attached to the matrix. (b) Horizontal slice through the pushed-out fibre reconstruction from the plane indicated by arrows in (a). White arrows guide the eye to cracks between the PyC and fibre; no cracks are observed between the matrix and PyC.

Fig. 4.6 (b) and (d).

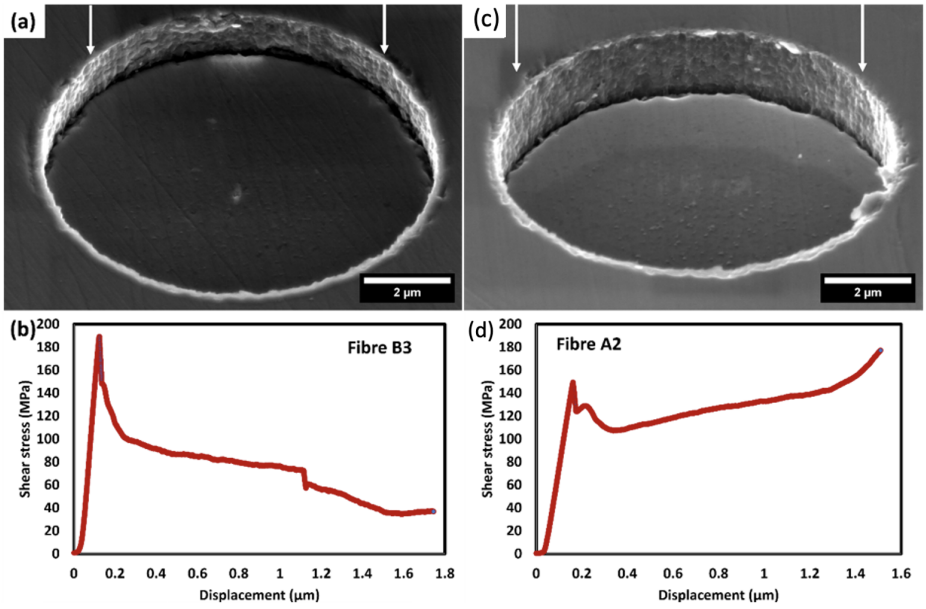

Figure 4.6: Post-test images of fibres B3 (a-b), and A2 (c-d) with their corresponding shear stress-displacement curves.

4.4.4 FEM simulations of micro push-out experiments

Different fibre experiments have been fully modelled using finite element methods with variables adjusted until the simulated load-displacement curves matched the experimental load-displacement curves as closely as possible. The geometry has been approximated to a bridge with one fixed side in y direction, two fixed sizes in x direction and one free side, as depicted in Fig. 4.7(a), given that three sides of the bridge are connected to the rest of the sample in the experiments while the other side remains unconnected after being milled to make a hole and create the short fibre (see the experimental scheme on Fig. 4.1). The load is

applied to the top surface of the indenter tip, being displacement-controlled. The geometry parameters of the different fibres are shown in Table 4.8 and the tip geometry is illustrated in Fig. A.1(b).

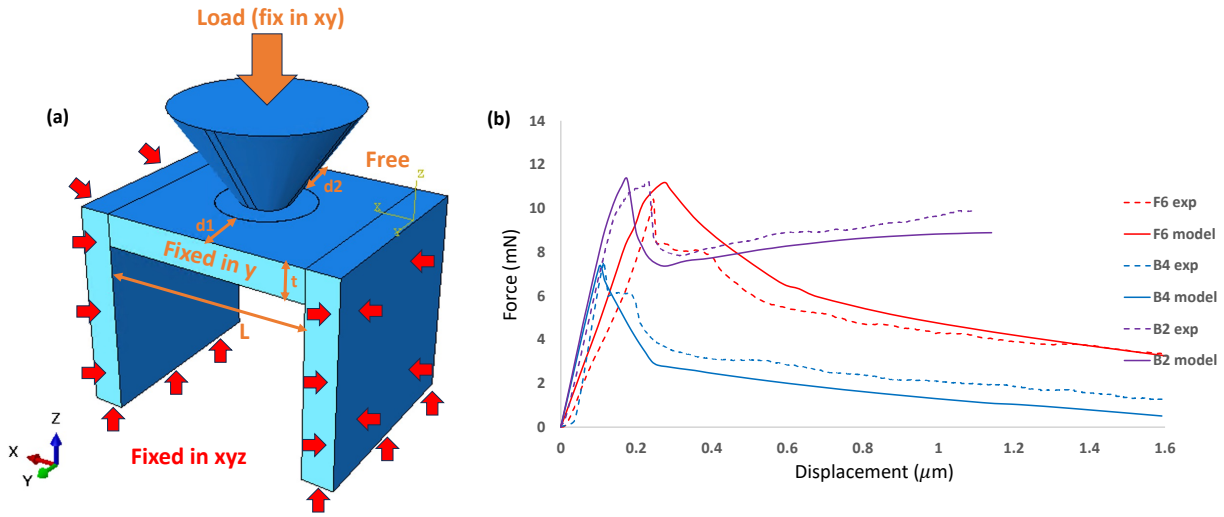

Figure 4.7: (a): Scheme of the geometry of push-out simulations. (b): Experimental and simulated load-displacement curves of three selected fibres.

The debond stress can be determined using the formula employed for short fibres [67] where F is the debonding force of the experiments, t is the thickness and R is the fibre radius:

$$\tau = \frac{F}{2\pi R t}. \tag{4.4.4}$$

The shear stress at the fibre-matrix interface in short fibres is considerably more homogeneous compared to that in long fibres, where damage initiation occurs gradually from the top to the bottom of the fibre. In short fibres, damage initiation occurs almost instantaneously across the entire contact interface, allowing for the application of Eq. (4.4.4) (see Appendix A.5).

For the models, Young's modulus of the fibre and matrix, $E_f = 365$ GPa and $E_M = 460$ GPa, respectively, have been sourced from [10], and the Poisson's ratio is $\nu_m = \nu_f = 0.22$ [126].

Thus, the parameters to be optimised are toughness, the clamping stress attributable to surface roughness,

Parameters	F6	B2	B4
L (μm)	22.50	23.00	21.00
t (μm)	3.49	2.32	1.97
d1 (μm)	5.97	10.33	17.01
d2 (μm)	5.97	20.00	17.01
Fib Diam top (μm)	10.56	9.67	10.50
Fib Diam bottom (μm)	10.56	9.60	10.50
Axial angle (°)	0	8	0

Figure 4.8: Table with the parameters for the geometry of the fibres F6, B2 and B4.

and the Coulomb modulus. The cohesive parameters also determine the optimum element size required to ensure mesh-independent fracture results, as it is explained in more detail in Appendix A.4.

These parameters were adjusted using the Nelder-Mead optimisation method through successive FEM Abaqus simulations, a procedure designed in [13]. The objective function used to optimise the parameter values was defined as:

$$D = \sum_{fibres} \frac{\int \mid F_{FEM}(u) - F_{EXP}(u) \mid du}{\mathrm{N}_{fibres} \int \mid F_{EXP}(u) \mid du}. \tag{4.4.5}$$

Where F_{FEM} and F_{EXP} are the modelled and experimental forces across indenter displacement u, and N_{fibres} is the number of fibres modelled.

The Coulomb friction coefficient was optimised to a value of $\mu = 0.15$, within a search domain of $0.1 \leq \mu \leq 0.3$. The sensitivity analysis gave us an interval corresponding to a 10% increase in the error metric D, this interval is $0.13 \leq \mu \leq 0.19$. The margins given by the literature [151, 66] are $0.1 \leq \mu \leq 0.36$.

The clamping stress was optimized to σ_{no}=420 MPa within a search domain of 0 MPa$\leq \sigma_{no} \leq$1000 MPa, with a sensitivity range of 375 MPa $\leq \sigma_{no} \leq$ 540 MPa corresponding to an additional 10% error. As the clamping stress is a modelling artifact used to represent surface rugosity, a direct comparison with experimental data in the literature is not straightforward. However, stresses attributed to rugosity on the order of $\sim$ 300 MPa have been reported in similar studies [152, 153, 45].

The mode II toughness was optimized to $G_{II} = 10.5$ J$/m^2$ within a search domain of 1 J$/m^2 \leq G_{II} \leq 40$ J$/m^2$, with a sensitivity range of 3.1 J$/m^2 \leq G_{II} \leq 12.5$ J$/m^2$ for an additional 10% error. The margins given by the literature [136, 128, 66] are 2.5 J$/m^2 \leq G_{II} \leq 34$ J$/m^2$.

The mode I toughness was set to $G_I = 2.5$ J$/m^2$. The range reported in the literature [66, 128] is 2.5 J$/m^2$ $\leq G_I \leq 8.1$ J$/m^2$. During the parametric study (See Sec. 4.4.5), we did not observe difference in the force-displacement curves associated with changes mode I toughness. Consequently, we adopted a value similar to other brittle interfaces, such as SiC/BN/SiC [136] to be consistent with the literature.

The $G_{II} = 10.5$ J$/m^2$ value is lower than that reported in the study with long fibres ($G_{II} = 22.3J/m2$), because this displacement-controlled experiment enabled us to incorporate the effect of interface roughness into the model during fibre sliding (the roughness should be higher during the crack formation but it progressively wears with the sliding).

Nevertheless, it remains relatively high compared to G_I which usually are similar in ceramic materials materials such as SiC/BN/SiC where Gavalda-Diaz et al. [136] reported toughness values of $G_I = G_{II} =$ $1.2 - 3$J/m^2.

The combination of two effects is proposed to explain this high value of G_{II}:

- Limitations of our friction model. Although the clamping component of the normal stress σ_{no} in Eq.4.3.3 is used to represent the constant friction component caused by rugosity during fibre sliding [44, 45], there are other terms that decay with the sliding velocity [43] and disappear when the crack is formed due to the wear of the rugosity. We were unable to isolate those terms and were captured by the augmented G_{II} value.
- The roughness of the interface can cause the fracture to deviate from a straight line, making propagation energetically less efficient than the flat cylindrical interface modelled. This crack trajectory effect induce anisotropies in toughness measurement. Xia et al. [129] estimated a difference of approximately $G_{II} \approx 4.2 \cdot G_I$ associated to a not straight trajectory of the crack for larger interfaces.

In summary, G_{II} could be understood as the energetic work required to overcome the resistance of the cohesive element, which combines interface toughness, energy dissipation due to non-planar crack propagation, and other frictional sources at very low sliding velocities.

The Von Mises stress profiles of different micro push-out experiments F6, B2 and B4 are shown in Fig. 4.9, 4.10 and 4.11 respectively; brief explanations of the different effects are exposed below:

Fibre F6: Initially, the radial stress is applied before load (Fig. 4.9-1). When the load initiates, there is no crack and the structure presents an elastic behaviour, the Von Mises stress profile resembles that of a bridge undergoing bending with an applied load at the centre, resulting in a notable concentration of stress in the corners (Fig. 4.9-2). Regarding the interface, it exhibits the highest stress concentration on the bottom of the fibre, serving as the initiation point for crack formation which propagates abruptly across the full interface which is already partially damaged being the crack propagation nearly instantaneous [72]. After crack formation, there is a relaxation in the matrix deformation (Fig. 4.9-3), and the interface presents higher stress in the direction parallel to the z-axis. The asymmetric stress profile in the interface is due to the boundary conditions shown in Fig. 4.7(a), where one of the bridge faces parallel to the y-axis is completely free while the other is fixed in the y-direction, reproducing the geometry of the experiments. Regarding the fibre, the greatest deformation is observed in the centre of the fibre (see Fig. 4.9-4), indicating both bending and swelling. In the final stage, the fibre is predominantly pushed-out, and the matrix ceases to undergo bending, resulting in a homogeneous stress profile across the interface.

Fibre B4: The process is similar to fibre F6 featuring initial radial stress across the interface to represent the friction caused by rugosity (Fig. 4.11-1), an elastic response preceding the crack (Fig. 4.11-2), crack propagation (Fig. 4.11-3), and a post-crack frictional response (Fig. 4.11-4). The main difference with F6 is the crack formation in the full interface instead of the abrupt propagation from the bottom. The low

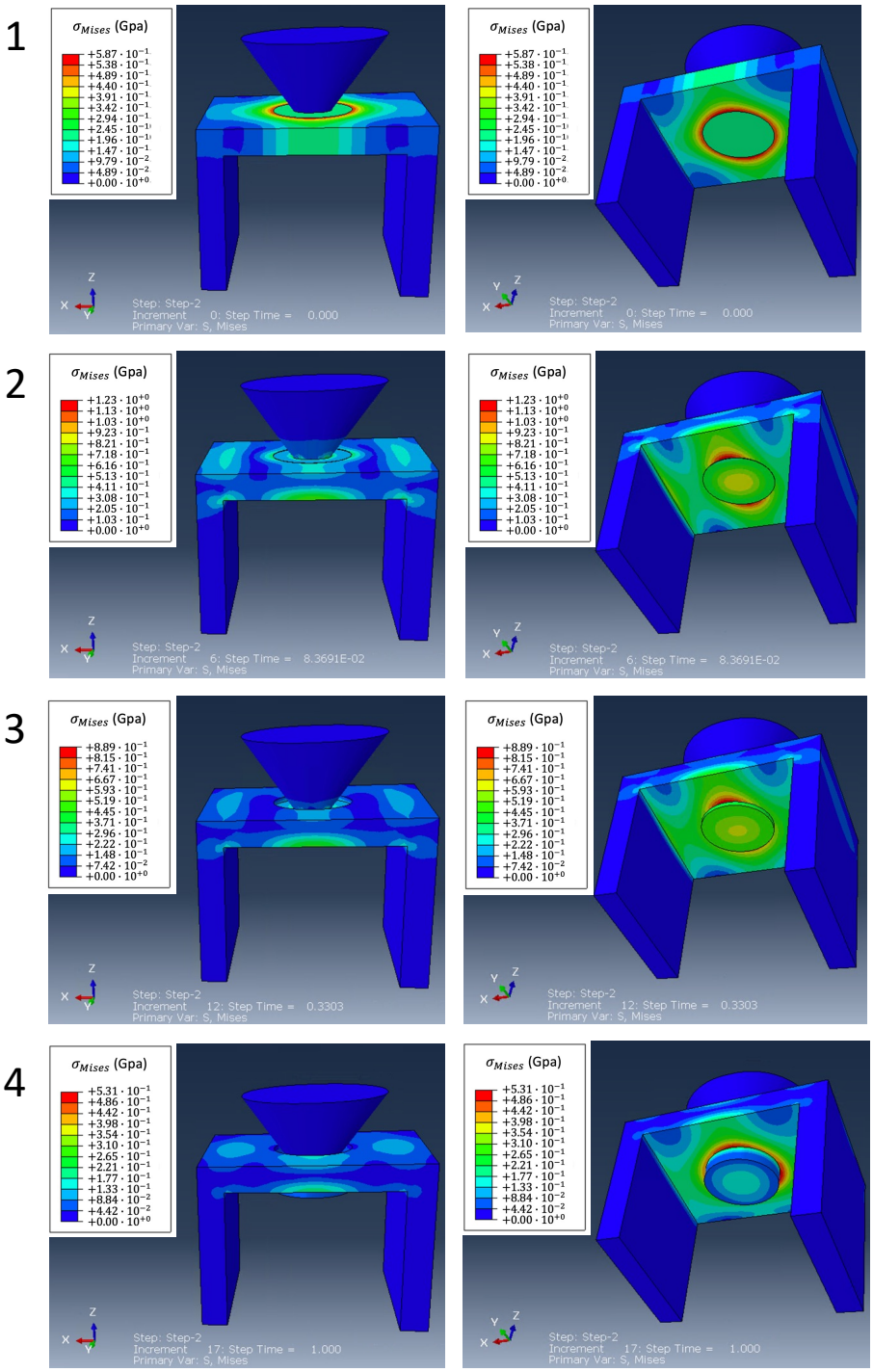

Figure 4.9: Von Mises Stress profile of F6 from up and down perspectives for the different stages of indentation.

thickness allows more bending of the fibre, deforming the full interface instead of localised points in the bottom face, which propagates the crack to the top of the fibre.

Fibre B2: This fibre model was designed to investigate a real case of fibres with a positive-taper shape (the top surface of the fibre is bigger than the bottom one) and with axial misorientation (the fibre has an angle of inclination with respect to the indentation direction). The Von Mises stress profile before crack completion

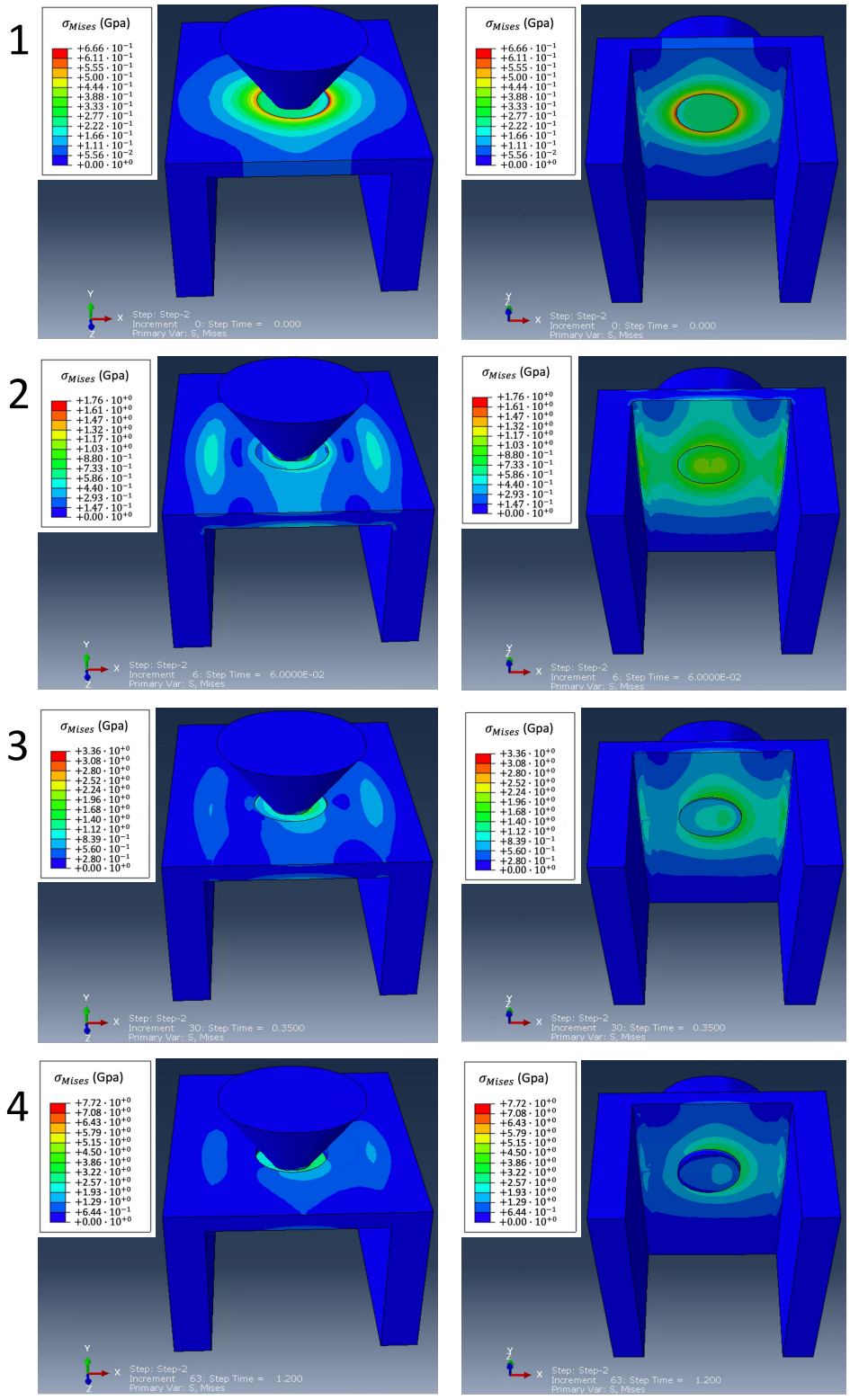

Figure 4.10: Von Mises Stress profile of B2 from up and down perspectives for the different stages of indentation.

is akin to F6 and B4 push-outs (Fig. 4.10-1,2). After failure, the most significant difference lies in the order of magnitude of friction, while F6 and B4 reduce their frictional stress values while they are pushed out, B2 increases its frictional stress due to the positive-taper shape up to values bigger than the peak stress before

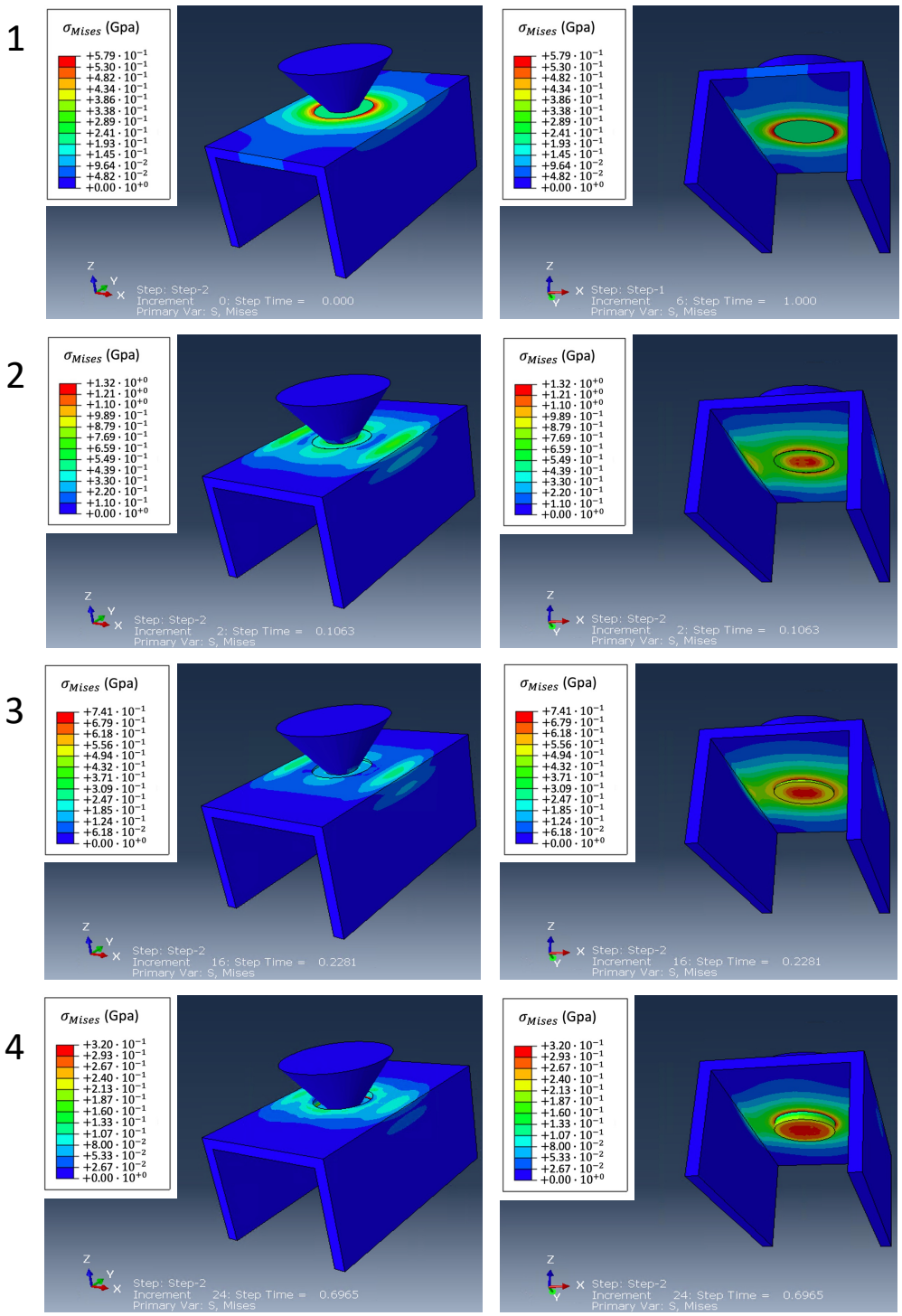

Figure 4.11: Von Mises Stress profile of B4 from up and down perspectives for the different stages of indentation.

crack formation (see Fig. 4.10-3,4). Furthermore, the maximum stress concentration occurs on one side of the fibre, because an inclination of 8° creates an asymmetry in the friction. It is concluded that the axial misorientation and the taper shape are two important parameters that influence the push-out, and they are explored in detail in Subsections 4.4.6 and 4.4.7.

Finally, the force-displacement adjustments for different push-outs are shown in Fig. 4.7 (b), models F6,

B4 and B2 present small differences compared to the experimental data. The main difference occurs after the peak where the models fail to predict the small quasi-flat region illustrated in the experimental curves. This flat region could result from higher friction at lower velocities (something that occurs when the fibre's interface starts to crack), our models based on the finite element implicit method do not consider velocity effects. This effect occurs during the first 0.05-0.1 μm of the indenter's movement after crack formation having a reduced impact in the full push-out process (1.2-1.6 μm of displacement). The following presents a parametric study of the interfacial properties, followed by an analysis of the geometry (axial misorientation angle and taper shape of the fibre).

4.4.5 Parametric study – interfacial properties

In setting up the finite element models of fibre push-out, various intrinsic properties of the material can be adjusted as variables which are broadly unknown, or difficult to measure. The Fibre F6 push-out test served as the "original" and the finite element model of this fibre was adjusted to fit the experimental result as shown previously. The effect of adjusting each variable in the model away from the optimised version is demonstrated here to assign their relative importance and effect on the load-displacement properties of a micro push-out test. Fig. 4.12 shows the effect of varying one parameter at a time, and these effects are summarised in Table 4.13.

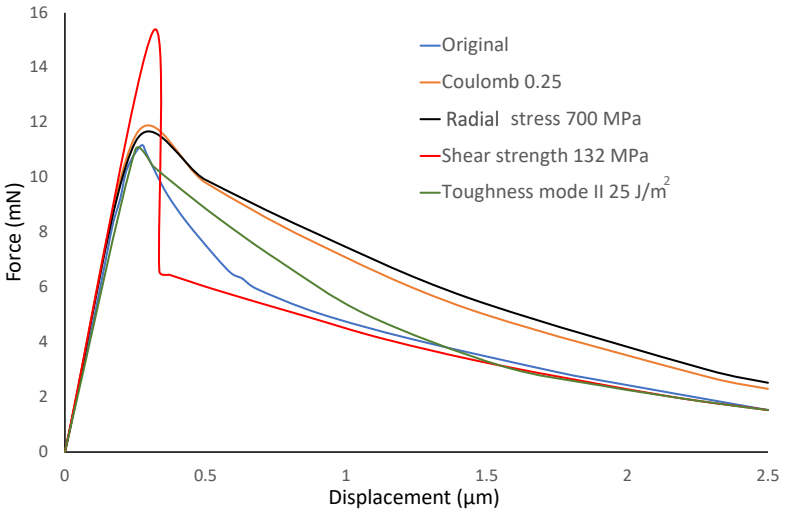

Figure 4.12: Effects of varying interfacial parameters.

A higher debond stress of the interface increases the debond force, but causes a more rapid crack propagation while the frictional push-out component is unchanged. The faster crack propagation is due to the larger elastic energy release once the crack initiates, leading to faster crack completion for the same toughness. Changes to the friction coefficient μ and the radial stress σ_{no} increase the friction in a similar proportion,

	Original	Modified	Qualitative Effect
Coulomb coefficient	0.15	0.25	Friction = Coulomb × normal force. Less sharp load drop. Increases friction throughout push-out.
Radial stress	420 MPa	700 MPa	Similar to Coulomb coefficient.
Debond stress (Mode II)	86.9 MPa	132 MPa	Increases debond stress. Friction unchanged
Mode II Toughness	10.5 J/m^2	25 J/m^2	Reduces load drop, but friction unchanged. Debond stress unchanged.
Tensile strength (Mode I)	86.9MPa	160MPa max 1 MPa min	No changes to debond, crack propagation or friction.
Mode I Toughness	2.5 J/m^2	100 J/m^2	No changes to debond, crack propagation or friction.

Figure 4.13: Values for the parametric study.

as they are directly related to the friction by their product $\mu \cdot \sigma_{no}$. Increasing friction appears to increase debond stress, and slow crack completion, extend the load drop and increase the force for frictional sliding. Increasing Mode II toughness has no effect on the debond force or friction, but extends the crack completion phase. Changes to Mode I properties have no discernible effect.

Of these interfacial properties, the most impactful to engineering properties is the frictional force, which is caused by the Coulomb friction coefficient and the interface normal force, which is the radial residual stress caused by a combination of surface roughness, chemical friction effects, and forces arising from residual stresses in the composite. Surface roughness is difficult to control; it is a property of the selected fibres, and chemical interactions on friction are determined by the material combination e.g. SiC sliding on PyC. Residual stresses are related to microstructure, manufacturing, and operating conditions and are expected to vary with operating temperature and radiation dose.

4.4.6 Parametric study – axial misorientation angle

Despite best efforts to align the specimen during preparation so that fibres are perpendicular to the surface of the specimen, it is impossible to achieve this in practice due to misorientation within fibre tows and the weaving angle of the 2D fabric. All fibres which were selected for undercutting appeared to have circular cross-sections on the surface which would indicate they are normal to the surface. FIB cross-sections of four fibres post-test reveal that these fibres are axially misoriented. The angle of misorientation θ of the cross-sectioned fibres is determined by measuring the angle of the interphase relative to the normal of the specimen surface and it is plotted with the debond stress in Fig. 4.14. No significant effect of apparent misorientation angle on debond stress or sign (positive or negative slope) of friction component is observed for the range of angles experimentally measured here. The angle of the FIB cross-sectioning plane may

impact the dimensions which are measured. All these axial angles and tapers (see below) are measured from single cross-sections except B3 which is determined from measurements throughout the 3D slice and view dataset.

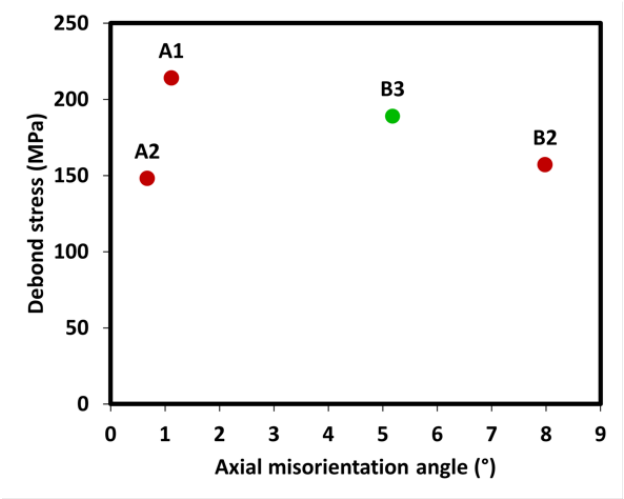

Figure 4.14: Effect of fibre misorientation angle on debond stress. B3 is highlighted in green as having a negative friction gradient (when the fibre is sliding, the force decreases with the displacement) whereas other tests have a positive gradient.

An alternative approach to estimate the misorientation angle of a fibre is based on measuring the length of the two perpendicular radius of the faces with the highest difference in length. Assuming the fibre initially had a perfect cylindrical shape (circular faces), misorientation causes the fibre's face to become an ellipsoid (Fig. A.2). In this case, the minimum radius represents the original fibre radius, and the maximum radius can be determined as:

$$r_{max} = \frac{r_{min}}{\cos(\theta)} \quad \Rightarrow \theta = \arccos\left(\frac{r_{min}}{r_{max}}\right). \tag{4.4.6}$$

To investigate the effect of misorientation angle further, a FE model for a prototypical fibre push-out is evaluated with varying misorientation angle up to a highly exaggerated 20°. The simulations have been conducted on a geometry as depicted in Fig. 4.15, formed by a square of 22 μm of side, 7.45 μm gauge length and a fibre of 13.08 μm diameter, where all sides of the matrix are fixed. In this case, the fibre has perfectly parallel sides. The parameters of the cohesive contact remain consistent with those outlined in Subsect. 4.4.4, except for the interfacial debond strength, which is set to 130 MPa. Inspecting the von Mises stress distribution of the fibre push-out model in Fig. 4.15, there is stress localisation on the bottom of the matrix around the fibre, with a maximum on the acute angled side of the fibre and a minimum on the opposite side. This is related to the component of force normal to the interface applied by the push-out test. Repeating these simulations across many axial misorientation angles with otherwise identical fibre characteristics shows an increase in maximum force for debonding, and very minor variation in the frictional

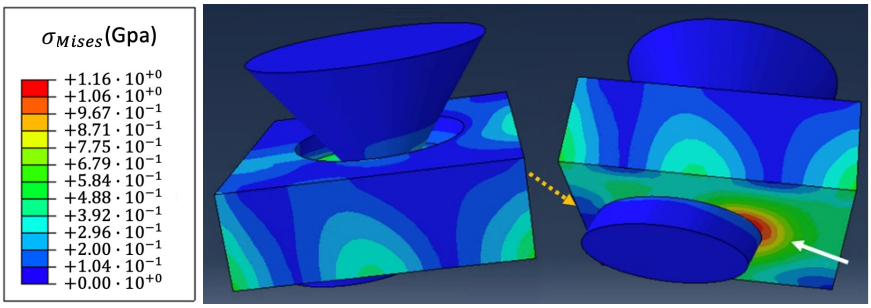

Figure 4.15: FEM simulation of fibre with exaggerated axial angle of 20°. Solid white arrow indicates stress maximum on the bottom of the matrix on the acute angled interface. Orange dashed arrow indicates a stress minimum on the opposite side of the matrix.

sliding component of the test after complete interfacial debonding (Fig. 4.16).

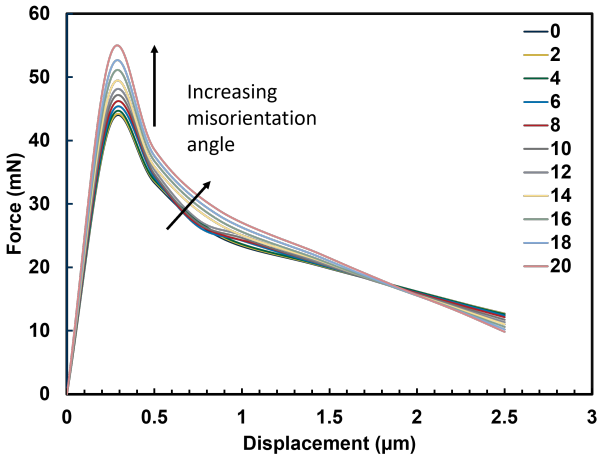

Figure 4.16: Effect of misorientation angle on load-displacement curves between 0° and 20°.

In short fibres with no axial misorientation, the equation for push-out force F in short fibres, where A is the fibre surface area and τ_B is the debond stress, is simply: $F = \tau_B \cdot A$.

The misorientation increases the interface area caused by a longer effective length of the fibre. The change in fibre surface area with respect to the angle can be written as: $A = 2\pi r \cdot t / \cos\theta$.

The component of force acting to push-out the fibre is simply $F \cdot \cos\theta$. Combining these equations, the force required to debond and push-out a fibre from a matrix is:

$$F = \tau_B \cdot 2\pi r \cdot \frac{t}{(\cos\theta)^2}. \tag{4.4.7}$$

However, this analytical expression based on simple geometry does not provide sufficient correction in debond force compared to the FEM simulations, suggesting a change in the fibre push-out mechanisms with increasing angle (see Fig. 4.17). The discrepancy is related to the assumption that force is uniform in the fibre for the analytical approximation and that debonding occurs instantaneously along the interface.

In this geometric adjustment, the interface-normal components of force are assumed to cancel out, i.e. the compressive force on one side is balanced by the tensile force opposite. This assumption is applicable in the frictional sliding portion of the experiment, as shown by the small variation in this part of the curves in Fig. 4.16; however, the initiation of debonding is a fracture mechanics process where a tensile component is not equivalent to a compressive component.

With increasing misorientation, the force propagation of the push-out causes a tensile and a compressive load on the opposite sides of the fibre (see Fig. A.2), decreasing and increasing the shear stress respectively when the micro-cracks are formed and altering the crack formation. A complete diagram of this is shown in Fig. A.3, showing the different crack propagation from the compressed and the tensile side. Despite these differences in crack initiation and propagation mechanisms, the variation in the debond force with the angle of misorientation is small compared to other experimental effects (being the damage formation quasi-instantaneous), and the change in push-out friction is minimal. Therefore, the model parameters adjustment shown in Fig. 4.7 can be valid even if the fibres were slightly misoriented.

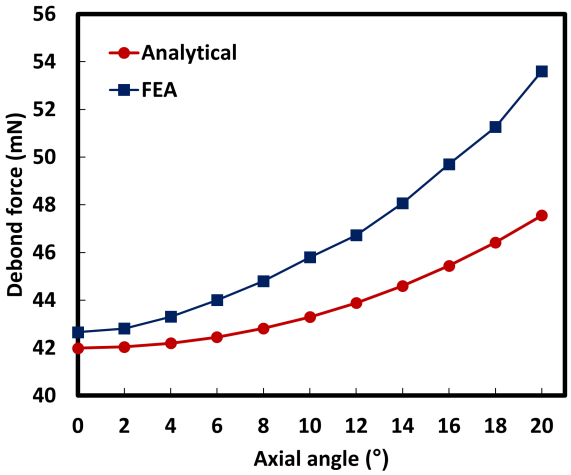

Figure 4.17: Effect of axial angle on debond force comparing FEM and analytical approximations.

4.4.7 Parametric study – taper

The effect of fibre taper on debond stress and pushout friction gradient for the same four cross-sectioned fibres is shown in Fig. 4.18. In this case, the value for taper is the average angle of the sides of the fibre. This is calculated from $tan^{-1}(\frac{r_{top}-r_{bottom}}{L})$ where r_{top} is half the measured width at the top of a fibre and r_{bottom} is half the measured width at the bottom of a fibre, and L is the gauge length of the fibre measured from cross-sections made at approximately the diametric plane of the fibre. Negative angles are referred to as negative taper, and positive angles are referred to as positive taper. Fibre B3, which has the most prominent negative taper measured from the FIB cross-section, is the only test with a negative friction

gradient following debonding, as shown in Fig. 4.6 (b). In the cross-sectioned plane, fibre A2 has a slightly negative taper, however, the mechanical response during the test gives a positive friction gradient shown in Fig. 4.6 (d), while the fibres A1 and B2 which have measurable positive taper also have positive friction gradients. Based on experimental results in Fig. 4.18, fibre taper appears to have no discernible effect on debond stress, i.e. the peak force in the experiment; fibre B3 with large negative taper has similar debond stress to the other fibres. Regarding the friction, the taper does appear to have a large effect on the gradient of the shear stress component after debonding; fibre B3 has a negative gradient showing decreasing shear stress during pushout whereas the other fibres have a positive gradient even when displacement is taken into account in the shear stress calculation.

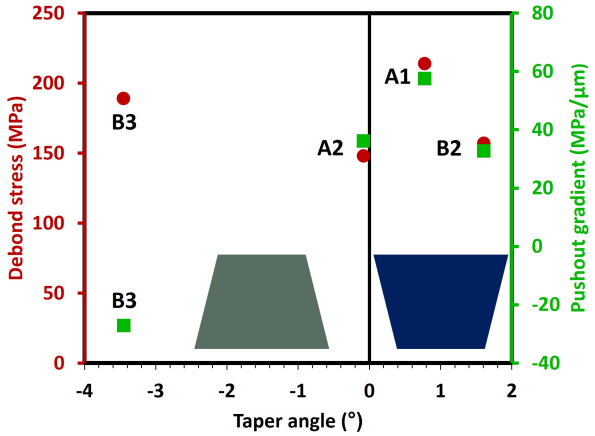

Figure 4.18: Effect of fibre taper on debond stress (red circles) and pushout gradient (green squares). Definitions of negative and positive taper are indicated by the shapes.

To investigate the taper effect further, FEM simulations were implemented in Abaqus using axisymmetric CAX4 elements. In these models, the fibre is 4 μm long with 4 μm maximum radius at the top of the fibre, while the radius at the bottom varies from 4 to 3.6 μm, corresponding to a range of fibre taper angles from 0° to 10°. The debond stress was set to a high value τ_s = 300 MPa to appreciate the load drop compared with the load increase caused by the taper effect, no clamping stress was applied during the force-displacement comparison of the fibres (Fig. 4.20) to clearly differentiate the effect of fibre taper compared to other causes of friction (roughness, thermal stress or defects). The remaining cohesive properties are the same as the fibres modelled during the experimental simulations (Toughness $G_I = 2.5$ J/m^2, $G_{II} = 10.5$ J/m^2 and Coulomb friction μ = 0.15). This is a simplified case to isolate the role of fibre taper - an analysis of taper combined with friction follows beneath.

Fig. 4.19 presents the von Mises, radial (σ_{rr}), and axial (σ_{zz}) stress distributions in the cross-sectional plane during the frictional push-out phase. The first column shows a positively tapered fibre, while the second and third columns show a parallel fibre without clamping stress.

By analysing the radial (σ_{rr}) and axial (σ_{zz}) stress distributions for the parallel fibre as a baseline case, several mechanical effects are observed:

- Axial Stress Concentrations (σ_{zz}). As shown in Fig.4.19(i) (dark blue), a significant concentration of compressive vertical stress occurs at the contact perimeter between the indenter and the fibre top face. This is attributed to the sharp transition at the indenter's edge, which creates a localised stress concentration where the downward load is first transferred to the fibre. The fibre material is constrained vertically by the indenter and radially by the matrix. This "trapping" effect prevents local deformation, leading to a massive build-up of compressive stress before the load is redistributed axially down the fibre.
- Radial Stress in the Fibre (σ_{rr}). As illustrated in Fig.4.19(h), radial stress varies significantly along the fibre length. At the top of the fibre, radial compression (green) is dominant as the matrix constrains the fibre's natural tendency to expand laterally under the axial load. Conversely, at the bottom of the fibre, where it emerges from the matrix, the absence of lateral support allows for radial expansion (orange/red).
- Matrix Flexure. Under the load of the indenter the entire cross-section of the matrix undergoes bending or "tilting" toward the centre (see Fig.4.19(h)). Due to the matrix's thickness, this rotation stretches the upper outer border (radial tension/red/positive stress) and squeezes the lower outer border (radial compression/green/negative stress), this effect occurs at the edges of the matrix modelled. On the other hand, the region of the matrix close to the fibre is affected by the fibre radial compression, that compress radially the region (yellow).

While these effects are present in both parallel and tapered fibres, they reach a significantly higher magnitude in the tapered case due to the wedging effect of the fibre shape that induces strong normal contact stresses and shear stresses along the interface. In contrast, for the parallel fibre, the friction is just caused by the Poisson expansion, resulting in a limited resistance during the fibre sliding. A comparison of the radial stress in Fig.4.19 (b,h), reveals that the fibre compression, the zone coloured green, corresponds to approximately -6 GPa in the tapered fibre and only about -0.2 GPa in the parallel configuration. In the same way, the von Mises stress is also significantly higher in the tapered fibre. Comparing Fig.4.19 (a,g), the von Mises reaches $\sim$9 GPa (red/orange) in the tapered fibre compared to only $\sim$0.3 GPa (light blue) in the parallel case.

Force-displacement response for the parametric study of various fibre tapers shows that debond force is not affected, in agreement with the experimental results, but the crack propagation and frictional stage are significantly altered (Fig. 4.20). The compressive interfacial forces of the tapered simulation occur after the cohesive damage initiation, and increase the Coulomb friction which affect the toughness value (when

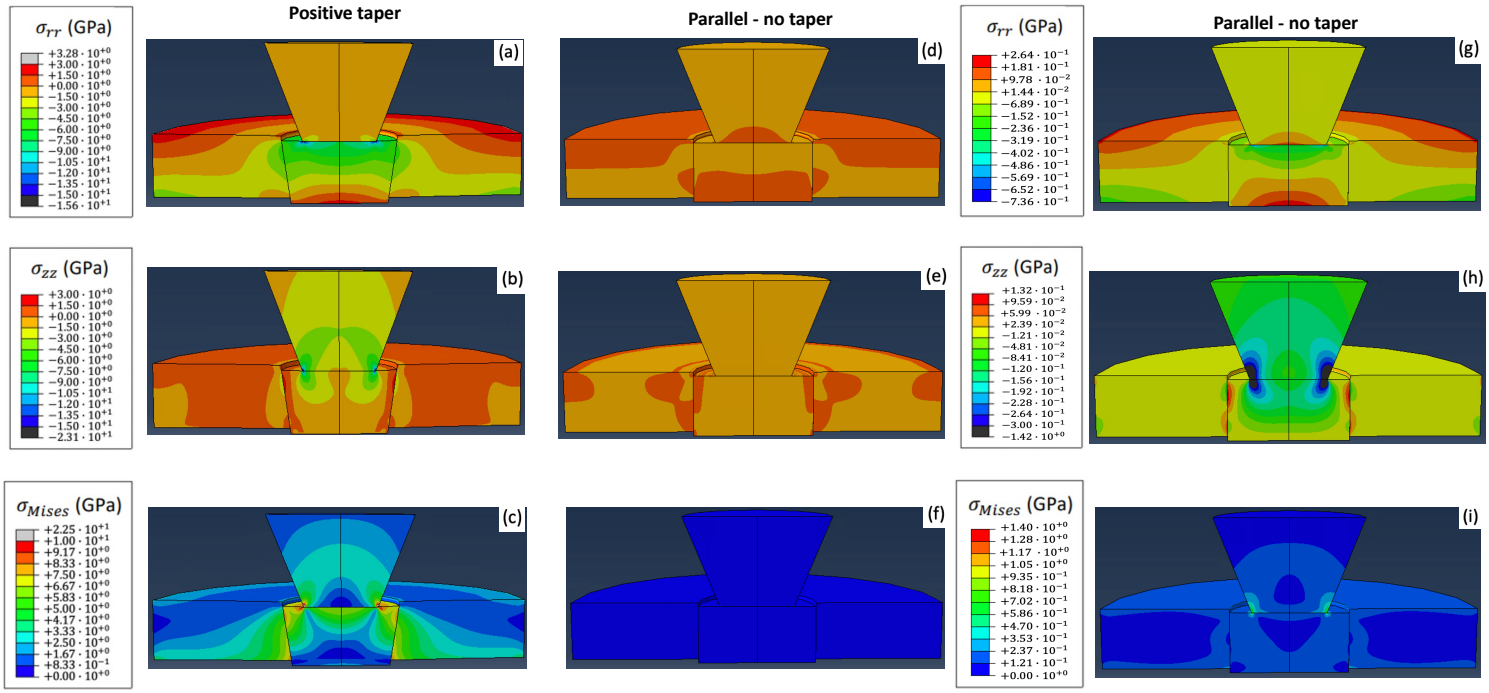

Figure 4.19: Distributions of von Mises, radial σ_{rr}, and axial σ_{zz} stress for pushed-out fibres during the frictional sliding phase. Column (d,e,f) uses the same colour scale as the positive-taper fibre (a,b,c) to facilitate comparison, whereas column (g,h,i) employs a more detailed colour scale to enhance the visualization of stress distributions.

the fracture area is created the friction starts to oppose the crack formation creating a toughening effect). This causes that the load drop after the peak force is smaller and over a larger displacement than the fibre with 0 taper where the force falls to 0 (the radial force was 0 to simplify the analysis). When the crack is formed, the fibre slides respect to the matrix, with increasing misfit of the fibre in the matrix hole, the force to continue push-out increases and can exceed the debonding force, as observed experimentally.

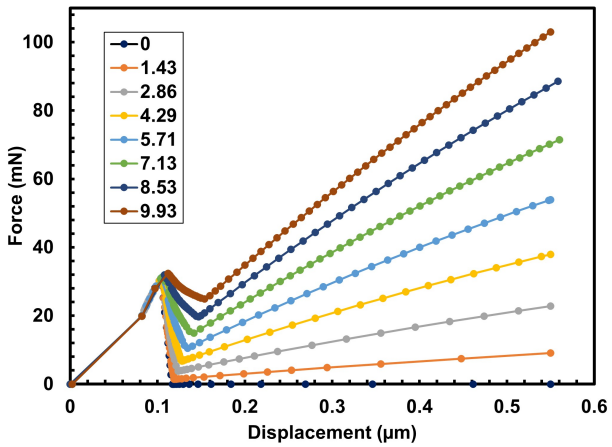

Figure 4.20: Force-displacement curves for a simplified fibre push-out test with varying extents of positive taper in the absence of a radial stress. Each line corresponds to increasing fibre surface angle, each with the bottom radius decreasing by 0.1μm .

The analysis of friction combined with fibre geometry has been studied using shear lag theory [13, 154],

the force due to friction resistance P_{fric} with respect to push-out displacement (u) is defined through the expression:

$$P_{\text{fric}} = C_{\text{Diff}} \frac{A_{\text{top}}\, E_{\text{fibre}}}{v_{\text{fibre}}\, R(u)} \left[\exp\left(\frac{2\mu\Lambda v_{\text{fibre}}\,(t-u)}{(R(u)E_{\text{fibre}})} \right) - 1 \right], \quad \text{where} \quad \Lambda = \frac{E_{\text{fibre}}\, E_{\text{Matrix}}}{E_{\text{Matrix}}\,(1-v_{\text{fibre}}) + E_{\text{fibre}}\,(1+v_{\text{Matrix}})}. \tag{4.4.8}$$

C_{Diff} is an amplitude term, $R(u)$ is the radius of the deformed fibre and L_{fibre} is the length of the fibre.

Eq. (4.4.8) can be modified for fibre taper by substituting the amplitude term $C_{Diff} = k \cdot u$. Where $k = (R_{\text{max}} - R_{\text{min}})/L_{\text{fibre}}$ represents the geometry of the taper for a push-out displacement of u (R_{max} and R_{min} represent the value of the radius at the top and bottom of the fibre respectively). The taper effect also modifies $R(u)$ as the radius of the deformed fibre, which is replaced by $R(u) = R_{max} - k \cdot u$. The area of the top face of the fibre is $A_{top} = \pi R_{max}^2$, E_{fibre} and ν_{fibre} are Young's modulus and Poisson ratio of the fibre, μ is the friction Coulomb coefficient, E_{matrix} and ν_{matrix} are Young's modulus and Poisson ratio of the matrix and t is the thickness of the sample/length of the fibre. The modification results in:

$$P_{\text{fric}} = \frac{k \cdot u \cdot A_{\text{top}}\, E_{\text{fibre}}}{(R_{\text{max}} - k \cdot u) \cdot v_{\text{fibre}}} \left[\exp\left(\frac{2\mu\Lambda v_{\text{fibre}}\,(t-u)}{((R_{\text{max}} - k \cdot u)\, E_{\text{fibre}})} \right) - 1 \right]. \tag{4.4.9}$$

Eq. (4.4.9) does not consider the debond strength or toughness, just the friction post-cracking. In Fig. 4.21, this theoretical model is compared to the FEM simulations of taper fibre push-out with and without cohesive interface for a 3.9 μm bottom radius and 4 μm top radius (positively tapered fibre). Firstly, there is an initial peak and drop in the fibre with cohesive interface showing the effect of crack formation.

During fibre sliding, there is an initial increase in the force due to the taper effect, then a maximum and finally a gradual reduction of the force as the contact area of the fibre-matrix is reduced while the fibre is expelled. There is a good match between Eq. (4.4.9) and the simulations, showing the potential applicability of this equation. Importantly, the friction component is identical whether there is an cohesive bond or not. This indicates that the modification to friction caused by the taper effect is not linked to the interfacial debond stress of a fibre and that the debond stress is still a valid property when experimentally measured from a tapered fibre.

Fibre taper has no apparent effect on debond stress but dominates the friction during the fibre sliding. The variation of the diameter along the fibre axis has previously been shown to have a significant effect on increasing the friction during the push-outs of longer fibres (approx. 50-100 um long), which results in higher sliding force after the crack is completed [13, 154]. However, this force never exceeds the debond force in long fibres, contradicting some short-fibre experiments where the frictional force was greater than the debond force. The explanation is that in longer fibres there are regions with negative tapered shapes compensating the friction produced by the positive tapered regions.

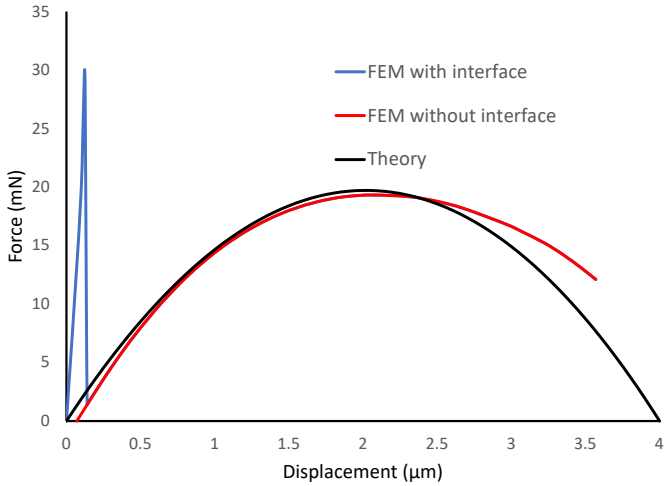

Figure 4.21: Comparison of modified shear-lag theory with FEM for a positively tapered fibre. The force-displacement of FEM with cohesive interface (that experiences a fracture previous to friction) matches with the FEM without interface (only friction provides resistance to fibre sliding) except for the initial peak that corresponds to the interface crack.

4.5 Discussion

4.5.1 Considerations for short fibre push-out testing

The purpose of developing short fibre push-out technique is to be able to acquire mechanical data from ion-irradiated thin SiC layers. These SiC layers are created when using ions to study irradiation damage. Typically, ion irradiation facilities operate at 5 MV accelerating voltage which, depending on ion species, charge stage, and experimental design, can generate damage depths between 0.5 μm - 10 μm in SiC.

Interfacial failure in short fibre push-out tests of SiC_f/SiC composites appears to follow a Weibull distribution of defects; therefore, interface surface area is the more specific parameter to be assessed against, as shown in Fig. 4.3 (b). The trend of debond stress with interfacial area shows that interfacial areas greater than $\sim$200 μm^2 are big enough to be independent of defects. Considering that fibre radius r can easily be measured, a general rule for determining the required gauge length for a test L_f can be written as $L_f > (200\mu m^2)/(2\pi r)$.

The results in this work suggest that a gauge length greater than $\sim$7.5 μm is suitable for assessing bulk mechanical properties, which is within the range of radiation damage (see Fig. 4.3 (b,c)). At this point, the fibres essentially have a reasonable concentration of interface defects that makes the debond stress independent of Weibull size distribution. The upper limit of gauge length (or interface surface area) occurs when there is non-uniform stress on the interface, there is too much fibre swelling, and there is stable crack growth leading to extra friction. Further work may be required to determine this inflexion point of push-out

mechanisms; however, this will be at longer lengths than achievable in ion-irradiated layers.

The Weibull modulus, m=1.71 is low compared to literature values for thick pyrolytic carbon materials, m = 8-11 [155]. This statistical analysis suggests that critical flaws leading to failure are not associated with pyrolytic carbon but with the fibre-PyC interface, which agrees with the microstructural observations for inside debonding of the fibre-matrix interfaces in this work and the literature [67, 10].

The long fibre push-out tests of this work are comparable to the literature. The interfacial debond stress (obtained from Eq. (4.4.4)) was 59.5 $\pm$ 17.5 MPa, close to the 69.4 $\pm$ 14.4 MPa measured by Hussey *et al.* [67] using Tyranno SA3 fibres with PyC interphase and CVI SiC matrix, a very similar material to our work. However, in both cases, Eq. (4.4.4) assumes that the damage initiation is instantaneous across the full surface. Herbretau *et al.* suggest an approach using a modified equation for debond strength based on accounting for crack initiation at the top surface of the sample and propagation along the interface, rather than simply averaging the force across the entire surface area [156]. Using this method, they calculated 160-220 MPa as the debond stress from a Nicalon fibre composite with PyC interphase and CVI SiC matrix [156]. Their value includes the effect of friction and geometry due to swelling during the interface failure. Without their analytical adjustment, the debond stress based on Eq. (4.4.4) is 115-159 MPa (39% lower), showing the importance of fibre swelling. However, this analytical method is still limited to isolating the non-linear friction effects caused by interface rugosity and residual stress. During long fibre push-outs, the fibre swelling increases the non-linear effects, being able to withstand stresses even higher than the interface debond stress, this effect does not occur during crack propagation inside composites, where fibres contract.

Short fibre push-out testing appears to be an appropriate method to directly measure interfacial debond stress without analytical adjustments, as debonding is instantaneous across the entire interface with a known and well-defined fibre length. As this property is a vital input for multi-scale performance models of composites, we consider that it should be measured directly rather than indirectly [157]. Weibull analysis can be used to estimate if the size of the interface area influences the experiment, for example, when the ion irradiation conditions are used with different damage ranges, as long as the fibre remains "short".

4.5.2 Fibre push-out mechanisms and implications

Elucidated by the finite element modelling and experimental characterisation, the micro-fibre push-out mechanism consists of four steps:

1. Elastic loading of the fibre.
2. Damage initiation quasi-homogeneous on the interface of the fibre at peak stress (see Appendix A.5).
3. Crack formation at the bottom of the interface and abrupt propagation (see Appendix A.3).

4. Frictional sliding as the fibre is pushed out.

FEM simulations predict that the fracture forms close to the bottom of the fibre in the micro push-out tests and then propagates to the top(See Fig. A.4). This is caused by the bottom face of the "bridge" being put into tension by slight bending, also reducing the friction in that area, similar to De Meyere *et al.* [72]. Although this happens, changes to Mode I properties do not affect the total load displacement data. Two explanations are possible to justify this: The first one is that the failure is almost instantaneous, indicating that regardless of the crack initiation being on the top or bottom surface, the crack formation is mainly Mode II shear debonding. The second one is the reduced friction in the bottom faces, which causes a reduced Mode II resistance compared with the rest of the interface.

Steps 2, 3, and 4 could not be differentiated in the long fibre push-out tests, as the G200 instrument is load-controlled and there is a displacement jump once the fibre is detached. The in-situ tests conducted in displacement control show a load drop with a second lower peak immediately after initial debonding and frictional sliding. This characteristic double peak could not be replicated in the FEM simulations. The second load peak could be caused by a larger asperity on the fibre surface roughness impinging on an asperity on the matrix surface. This would need a continued force to overcome after some further displacement has occurred after initial debonding. Another explanation may be the spalling of interphase PyC, causing a local barrier to be overcome. This may explain the scratches on the interphase which is seen for all tests regardless of the gradient of the frictional component in step 4.

To model Step 4 (frictional sliding), the simulations require a clamping stress determined by the Coulomb friction coefficient and a surface radial force. This is simple to evaluate if a perfectly parallel fibre is assumed; however, in these short fibre tests, even small tapers in the fibre dominate frictional sliding forces to the extent that the gradient is positive even as the contact length is reduced during push-out, making it necessary to take several measurements to have a reasonable estimation.

During irradiation inside a Fusion reactor, SiC fibres undergo many changes which impact their mechanical performance [143]. Significant degradation of the interphase at high doses is likely to change the debond stress and crack propagation [146, 147]. At high doses, SiC fibres have been observed to shrink and densify while SiC matrices swell and expand, causing a geometric mismatch across the interface [158]. The combination of fibre shrinkage and matrix swelling relieves radial residual stress, reducing the frictional component of SiC fibre composite mechanics. The swelling of high-purity SiC by displacement damage has been extensively characterised in fission reactor conditions, but is likely to be different due to higher transmutation rates in fusion reactor conditions [159, 123, 160]. Fusion transmutation and displacement damage can only be simulated by ion implantation, which requires thin layers. Displacement-controlled

short fibre push-out testing is potentially the most representative method of measuring these properties, and will be used to evaluate ion irradiated SiC_f/SiC composites in future work.

4.6 Conclusions

The technique of short fibre push-out testing has been demonstrated on nuclear grade SiC_f/SiC composites with gauge lengths within the obtainable range of ion implantation experiments. This technique provides new benefits over other micromechanical methods, such as micropillar sliding, as it retains most of the geometric constraints of fibres in a composite component. Additionally, compared to long fibre push-out experiments, it is easier to isolate properties such as debond stress from friction, and it is easier to model with faster and simpler simulations. Drawbacks include the relatively higher cost of FIB sample preparation, being constrained to testing fibres close to the edge of a specimen, defining a "long" or a "short" fibre, and higher sensitivity to local fibre geometry, which is averaged out in long fibre push-out experiments.

Various parameters have been studied using experiments and finite element modelling to ascertain their relative importance and impact on push-out mechanisms and material properties. Debond stress is minimally affected by residual stress, geometric taper in the fibre, or changes in interface properties such as toughness, roughness, or friction coefficient. Axial misorientation of the fibre has no detectable effect within the scatter of experimental measurements; force-displacement response is insensitive to misalignment, whether by sample preparation or fibre orientation differences within a unidirectional tow or woven fabric. However, axial misorientation has a detectable effect on debond stress in simulations for exaggerated angles beyond those obtained in experiments ($>10°$), being greater than the simple analytical adjustment for a tilted geometry. This suggests there is a change in the crack formation mechanism at large misorientation angles, which is not represented by Eq. (4.4.7). Debond stress is therefore a robust value which can be extracted from short fibre push-out experiments and can be used for quantifying changes in fibre-interphase-matrix properties following shallow ion implantation damage, and which cannot be evaluated using long fibre push-out testing.

The crack propagation and friction component of these experiments is affected noticeably by residual stress, interfacial friction (Coulomb) coefficient, and toughness as a property of the interphase. These determine the bulk toughness of the composite component at the crack deflection and fibre pull-out stage of mechanical failure. Different manufacturing methods, interphase deposition techniques or chemistries could be developed to beneficially tailor these properties which can be evaluated using various methods and tested before and after irradiation using the micro push-out technique.

Localised fibre taper has been found to be the dominant factor during the frictional component of micro push-out tests. In long fibre tests, local fibre tapers are averaged out along the length of the fibre; however, at these short gauge lengths, positive and negative tapers do not cancel out. This makes measuring a friction coefficient from these experiments challenging – a micropillar sliding test without geometric constraint is valuable here.

This micromechanical method allows prediction of the load-bearing ability of SiC composites beyond the proportional limit stress after irradiation, i.e. the strength of the fibre-matrix interface during crack bridging and before fibre pull-out mechanisms take effect. The method allows key fibre-matrix mechanical data to be measured and utilised as part of an experimentally informed multi-scale mechanical performance model, which can also be verified by micromechanical testing.

4.7 Statement of Authorship form

Statement of Authorship for joint/multi-authored papers for PGR thesis

To appear at the end of each thesis chapter submitted as an article/paper

The statement shall describe the candidate's and co-authors' independent research contributions in the thesis publications. For each publication there should exist a complete statement that is to be filled out and signed by the candidate and supervisor **(only required where there isn't already a statement of contribution within the paper itself).**

Title of Paper	Progress towards a micro fibre push-out method for measuring fibre-matrix interface properties in SiC composites.
Publication Status	☐Published ☐ Accepted for Publication ☐Submitted for Publication ☐Unpublished and unsubmitted work written in a manuscript style
Publication Details	Leide, A., Martinez-Pechero et al. Progress towards a micro fibre push-out method for measuring fibre-matrix interface properties in SiC composites. Journal of the European Ceramic Society, 117624.

Student Confirmation

Student Name:	Alvaro Martinez Pechero		
Contribution to the Paper	As the second author of the paper, the student's contributions included: • Developing the entire Finite Element fracture models and its theoretical formalism. • Designing and executing all Finite Element modeling simulations, analyzing the results, and comparing them with experimental data and existing literature. • Conducting the parametric study presented in the paper, which involved modifying geometry and crack parameters. • Developing the initial Weibull formalism analysis, which was subsequently refined by Dr. Alex Leide with the inclusion of new experimental measurements. • Co-writing the discussion sections with Dr. Alex Leide. While experimental data was acquired by other authors (led by Dr. Alex Leide), all modeling work was performed by the student under the supervision of Dr. Eralp Demir, Dr. Anna Widdowson, Dr. Yevhen Zayachuk, and Prof. Edmund Tarleton.		
Signature		Date	28th July 2025

Supervisor Confirmation

By signing the Statement of Authorship, you are certifying that the candidate made a substantial contribution to the publication, and that the description described above is accurate.

Supervisor name and title: Professor Edmund Tarleton		
Supervisor comments		
Signature	Date	1st August 2025

This completed form should be included in the thesis, at the end of the relevant chapter.

Chapter 5: Restraining geometrically necessary dislocations to the active slip systems in a crystal plasticity finite element framework

Chapter 5 of the thesis is based on the publication in the International Journal of Plasticity, titled "Restraining geometrically-necessary dislocations to the active slip systems in a crystal plasticity-based finite element framework", Demir, E., Martinez-Pechero, A., Hardie, C., & Tarleton, E. (2024), available at: https://www.sciencedirect.com/science/article/pii/S0749641924001402. For the statement of authorship, refer to Section 5.6.

This chapter introduces the topic of *Metal Deformation* in the thesis. Metals are fundamental materials in fusion energy applications, serving as heat sinks in Tokamaks (e.g., copper detailed in Chapter 6) or as neutron multipliers to enhance tritium breeding (e.g., the beryllium discussed in Chapter 7). In metals, plasticity is a critical deformation mechanism that precedes fracture, and the calculation of geometrically necessary dislocations (GND) is essential for analysing material behaviour under fatigue or pre-fracture strain. This capability stands as one of the key strengths of the OXFORD-UMAT code [18], a project in which the author has been involved throughout his doctoral research.

Restraining geometrically necessary dislocations to the active slip systems in a crystal plasticity finite element framework

5.1 Abstract

Strain gradients have been cast in the form of geometrically necessary dislocations (GND) to relate the length-scale dependence of strength and to determine potential sites for failure initiation. The literature contains various different incompatibility measures, the main ones being the total form ($\nabla \times \boldsymbol{F}_p$), the rate form for large displacements ($\nabla \times \dot{\gamma}^a \boldsymbol{n}^a \boldsymbol{F}_p$), and the slip gradient form ($\nabla \dot{\gamma}^a$). Here, these different approaches are compared rigorously for the first time. Obtaining GND densities when using the total form is a rank-deficit linear problem, solved by singular value decomposition (SVD), known as the Least Squares Minimisation (L2 method). Alternative methods for finding GND densities such as Karush-Kuhn-Tucker (KKT) optimisation are also investigated. Both L2 and KKT methods predict unrealistic GND densities on inactive slip systems leading to excessive strain hardening; even for a single crystal single slip case. Therefore, the restriction of GNDs to the active slip systems by using a threshold based on the total slip is essential. This proposed restriction reveals relatively consistent results for various single-crystal single slip cases including simple shear, uniaxial tension, and four-point bending. In addition, the small numerical differences in slip leads to large discrepancies in the flow stress due to error accumulation, even for strain-gradient-free uniaxial tension, hence a threshold for the GND density increment (2×10^2 m^{-2}) is used in all models to avoid the formation of artificial GND densities. Finally, the proposed method is applied to the evolution of the GND density for a grain inside a polycrystal aggregate having a complex stress state. The total forms that use the curl of the plastic deformation gradient, with the active slip system restriction giving the lowest incompatibility errors suggest that they are the most reliable GND measures.

5.2 Introduction

Strain gradients have been used to account for the length-scale dependence of mechanical strength with various physical origins [161]. GND and strain gradients were used to explain various physical phenomena. For example, GNDs were used to reveal crack initiation and strain localisation sites in a single crystal [162] and in polycrystals [97]. Polycrystal applications include modelling the Hall-Petch grain size effect [163], length scale effect in multiphase steels [164] and martensitic steels [165], understanding shear localisation in high-purity titanium [166], creep in nickel-based superalloys [167], transformation-induced defect formations in dual phase steels [168], tension-compression asymmetry in an aluminium alloy [169]

and modelling of indentation of ion-irradiated materials [170]. The heterogeneity in plastic deformation has been expressed in terms of the geometrically necessary density of dislocation (GND), ρ_{GND}, which is the length of dislocations per unit volume. Similarly, the *statistically stored dislocation* (SSD) density, ρ_{SSD}, accounts for the dislocation with a net Burgers vector of zero. Dislocations contribute to the strength by Taylor's relation $\tau_c \propto \sqrt{\rho_{GND} + \rho_{SSD}}$.

The total deformation in a crystal is predicted by GND density unless there exist voids or gaps in the material. Therefore, plastic or elastic deformation has been used to quantify GNDs [171]. Elastic distortion consists of rotations and elastic strains, both of which can be determined experimentally using electron backscattered diffraction (EBSD) measurements [172]. Therefore, many studies used orientation gradients to quantify GNDs from EBSD maps [173, 174, 175], or elastic strain gradients [176].

Regarding the computational GND calculus, the models can be classified into finite element-based or mesh-free approaches. Finite element GND calculus methods may lead to inaccuracies between elements that may potentially cause instabilities in the GND calculations. To overcome numerical instabilities, the mesh-free methods were used to compute the strain gradient field instead of using conventional finite element shape functions [177, 178]. These methods showed lower mesh dependence but are computationally very expensive and limited to simple geometries.

On the other hand, the finite element GND calculus methods can be classified with respect to the order of the strain gradients. The second or higher-order theories introduced micro stress and the GND density as another field variable [179] to search for a solution with mechanical equilibrium [180, 181]. Second or higher-order theories require additional boundary conditions, such as micro-hard grain boundaries [182], which have not yet been experimentally validated. Therefore, various forms of first-order strain gradient theory and finite element-based calculations have still been widely used as a simple means to introduce length-scale dependence, avoiding making assumptions about the grain boundary behaviour, which is known to be very complex [183, 184, 185].

This study overviews first-order strain gradient computation procedures that aim at finding an accurate measure for GNDs. The numerical procedures are susceptible to produce errors, hence the error sources need to be identified. For example, the widely used least squares solution known as the L2-minimum [171] reveals GNDs on inactive slip systems. Similarly, time integration causes error accumulation that is manifested as erratic GND densities at smaller dimensions. For this reason, various strain gradient approaches are investigated, including different variants of the curl of $\boldsymbol{F}_p$, such as the rate form originally proposed in [186], and slip gradients. Comparison of GND distributions for different boundary conditions, including simple shear, uniaxial tension, and bending, is performed for various 2D and 3D element types with quadrilateral

and linear interpolation functions in order to identify important constraints that are needed to accurately calculate GND densities. Finally, the lattice incompatibility error is quantitatively determined for different GND measures using a realistic polycrystal scenario.

5.3 Modelling

A brief overview of crystal plasticity kinematics is presented followed by constitutive models and the numerical solution method[*]. Next, the derivations for different strain gradient models are revisited in detail to provide a complete reference. Strain gradient explanations include an overview of fundamental definitions: Burgers circuit; definitions of lattice incompatibility measures, including two different total forms, a time rate form, and a slip gradient form.

5.3.1 Crystal plasticity kinematics

The total deformation gradient (which can be obtained from FEM), $\boldsymbol{F}$, is decomposed into its elastic (which contribute to the stress increase through elasticity matrix), $\boldsymbol{F}_e$, and plastic parts (which contribute to the stress increase through dislocation hardening), $\boldsymbol{F}_p$ with the volume remaining constant during plastic deformation:

$$\boldsymbol{F} = \boldsymbol{F}_e \boldsymbol{F}_p, \;\; \det(\boldsymbol{F}_p) = 1. \tag{5.3.1}$$

The total velocity gradient is given by:

$$\boldsymbol{L} = \dot{\boldsymbol{F}} \boldsymbol{F}^{-1}. \tag{5.3.2}$$

The total velocity gradient can be expressed as a sum of its plastic part L_p and elastic part L_e. The plastic velocity gradient can be used to calculate the plastic deformation gradient and it is obtained by the sum of the slip rates with the dyadic product of slip direction, $\boldsymbol{s}^a$, and slip plane normal, $\boldsymbol{n}^a$, in the intermediate configuration[†]:

$$\boldsymbol{L}_p = \sum_a \dot{\gamma}^a \boldsymbol{s}^a \otimes \boldsymbol{n}^a. \tag{5.3.3}$$

And the elastic velocity gradient is obtained by subtracting the plastic from the total component. Slip direction and slip plane normal transform to the deformed reference indicated with the subscript $_e$:

$$\boldsymbol{s}_e^a = \boldsymbol{F}_e \boldsymbol{s}^a, \;\; \boldsymbol{n}_e^a = \boldsymbol{F}_e^{-T} \boldsymbol{n}^a. \tag{5.3.4}$$

[*]The fourth rank tensors are shown with $\mathbb{A}$ or A_{ijkl}, second rank tensors are with capital letters in bold fonts, $\boldsymbol{A}$ or A_{ij}, vectors with small letters in bold fonts, $\boldsymbol{a}$ or a_i, and scalars with regular fonts, a, throughout this study.

[†]Intermediate of relaxed configuration is a non-physical reference frame to account for the shape changes after slip, $\boldsymbol{F}_p$.

The total velocity gradient can also be expressed as the sum of symmetric stretch rate (or rate of deformation), $\boldsymbol{D}$, and anti-symmetric spin tensors (the rate of rotation), $\boldsymbol{\Omega}$:

$$\boldsymbol{L} = \boldsymbol{D} + \boldsymbol{\Omega}. \tag{5.3.5}$$

The total strain rate can be decomposed into its elastic and plastic parts:

$$\boldsymbol{D} = \boldsymbol{D}_e + \boldsymbol{D}_p. \tag{5.3.6}$$

The total slip per slip system is obtained by the net sum of slip rates over time up to the current time step, which is indicated by former time, t, plus the time step, Δt, in incremental solutions:

$$\gamma^a = \int_0^{t+\Delta t} \dot{\gamma}^a \, \mathrm{d}t. \tag{5.3.7}$$

5.3.2 Constitutive laws

Elasticity relates the objective Jaumann rate of stress without rotation, $\overset{\nabla}{\boldsymbol{\sigma}}_e$, to the vectorised form of the elastic deformation rate D_e in the Voigt notation, $\boldsymbol{d}_e$. The subscript e represents the configuration changes resulting from elastic deformation. According to [187]:

$$\overset{\nabla}{\boldsymbol{\sigma}}_e \approx \boldsymbol{C} \cdot \boldsymbol{d}_e. \tag{5.3.8}$$

$\boldsymbol{C}$ is the (6×6) matrix of elastic constants in the deformed configuration, which is obtained by transformation from the crystal reference to the sample or deformed reference using:

$$\boldsymbol{C} = \boldsymbol{R}\boldsymbol{C}_0\boldsymbol{R}^T. \tag{5.3.9}$$

$\boldsymbol{R}$ is a (6×6) special transformation matrix that is constructed to transform the matrix of elastic stiffness constants in Voigt notation [55] which uses components of the crystal to sample transformation matrix, $\boldsymbol{g}_{ij}$. Different from conventional literature, the transformation matrix $\boldsymbol{g}_{ij}$ maps the crystal reference to the material orientation in the deformed configuration, which initially (at $t = 0$) can be defined in terms of the Bunge angles (see Appendix B.1).

The stiffness in the crystal reference is given by Eq. (5.3.10) for a cubic material with three independent

elastic constants C_{11}, C_{12}, and C_{44}:

$$\boldsymbol{C}_0 = \begin{bmatrix} C_{11} & C_{12} & C_{12} & 0 & 0 & 0 \\ C_{12} & C_{11} & C_{12} & 0 & 0 & 0 \\ C_{12} & C_{12} & C_{11} & 0 & 0 & 0 \\ 0 & 0 & 0 & C_{44} & 0 & 0 \\ 0 & 0 & 0 & 0 & C_{44} & 0 \\ 0 & 0 & 0 & 0 & 0 & C_{44} \end{bmatrix}. \tag{5.3.10}$$

The slip rates are computed by Eq. (5.3.11) (Power law slip [188]) using a reference slip rate, $\dot{\gamma}_0$, and a rate sensitivity exponent, n:

$$\dot{\gamma}^a = \dot{\gamma}_0 \left(|\tau^a|/\tau_c^a\right)^n \operatorname{sgn}(\tau^a). \tag{5.3.11}$$

Taylor's relation in Eq. (5.3.12) is used to compute the critical resolved shear stress in the slip system a (τ_c^a) in which τ_c^0, α, G, b^a and ρ_{for}^a represent lattice friction, geometric factor, shear modulus, Burgers vector, and forest dislocation density, respectively. Statistically stored dislocations [189] are ignored in this study to investigate the direct effect of GNDs only on strength:

$$\tau_c^a = \tau_c^0 + \alpha G b \sqrt{\rho_{for}^a}. \tag{5.3.12}$$

Strain hardening due to the dislocation interactions is known to be present. The forest projections of dislocations to other systems are assumed to account for these interactions. Therefore, forest dislocation density is computed using the projection of edge, $\rho_{GND,e}^b$, and screw $\rho_{GND,s}^b$ type of GND densities onto the slip plane normals:

$$\rho_{for}^a = \sum_b \left|\boldsymbol{n}^a \cdot \boldsymbol{t}^b\right| \left|\rho_{GND,e}^b\right| + \left|\boldsymbol{n}^a \cdot \boldsymbol{s}^b\right| \left|\rho_{GND,s}^b\right|, \tag{5.3.13}$$

where $\boldsymbol{t}^b$ is the cross product of slip direction and slip plane normal:

$$\boldsymbol{t}^b = \boldsymbol{s}^b \times \boldsymbol{n}^b. \tag{5.3.14}$$

5.3.3 Strain-gradient models

Total form, rate form, and the small strain measures are investigated that are all based on the plastic part of the deformation gradient. For the total form, the solution for GND densities is obtained by four different methods including; projection onto all slip systems via L2 minimisation (giving the minimum dislocation line length), the Karush-Kuhn-Tucker (KKT) optimality condition, the projection onto GND densities re-

stricted to active slip systems only, and finally the same restricted solution with an additional correction accounting for geometry changes due to plastic deformation.

The curl of a second rank tensor is computed according to Eq. (5.3.15) in which ε_{irs} represents the Levi-Civita symbol. This corresponds to the same curl definition as in [190] and the "curl3" definition in [93]. The derivation of Eq. (5.3.15) is revisited in [17]:

$$(\nabla \times \boldsymbol{T})_{ij} = \varepsilon_{irs}\, T_{js,r}. \tag{5.3.15}$$

Burgers circuit

The Burgers circuit is a geometric tool used to define the magnitude and direction of the lattice distortion caused by a dislocation. In a continuum framework, compatibility is satisfied for the total deformation F_{tot}. However, lattice incompatibility arises from plastic deformation and must therefore be evaluated in a configuration where elastic distortions are removed. In this work, the incompatibility of plastic deformation is defined with respect to the intermediate stress-free configuration F_p, obtained by unloading the elastic deformation F_e from the total deformation F_{tot} (see Fig. 5.1).

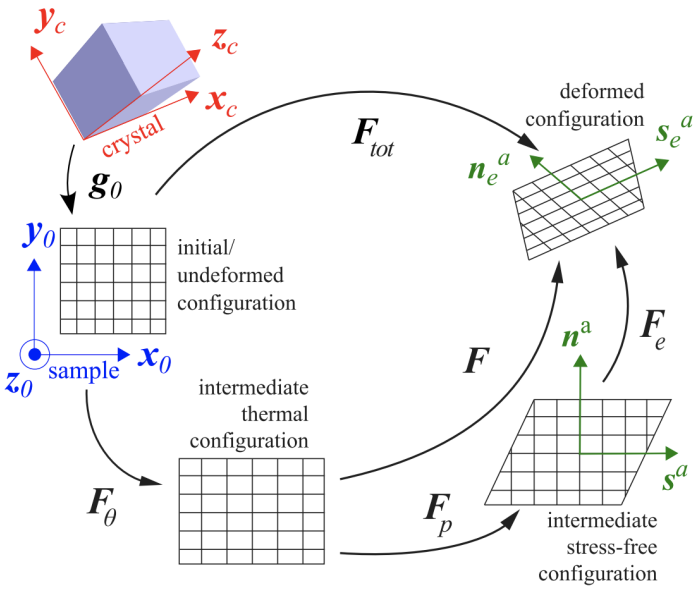

Figure 5.1: Multiplicative decomposition of total deformation [18].

The Burgers circuits are therefore constructed in this intermediate configuration. Fig. 5.2 shows the Burgers circuit around edge and screw type dislocations, the sign conventions of dislocations is indicated for a given slip gradient in a deforming single crystal lattice. A positive shear gradient for a single slip case is accommodated by a negative edge dislocation (see Fig. 5.2(a)) and a positive shear gradient leading to a negative left-handed screw dislocation [191] (see Fig. 5.2(b)).

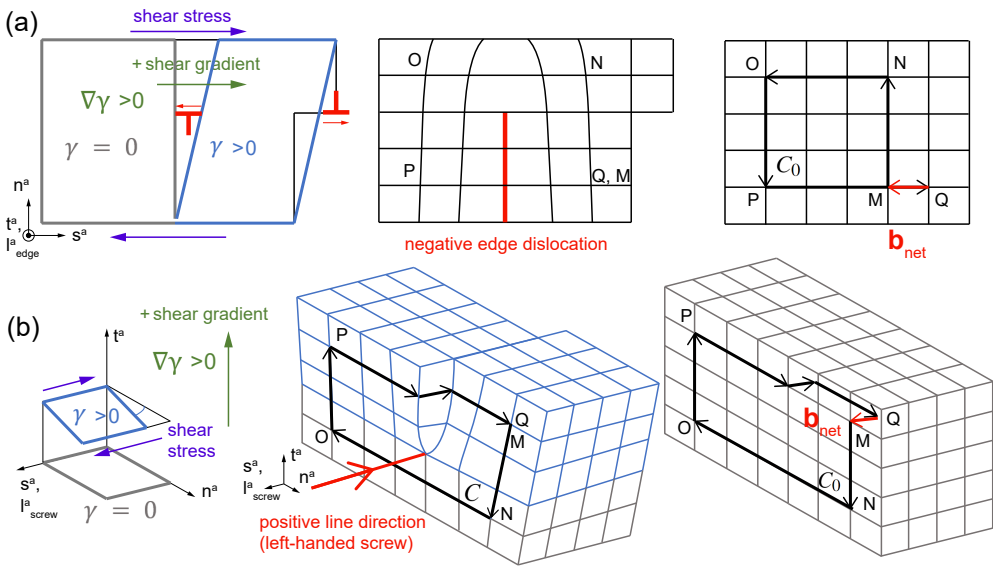

Figure 5.2: GND sign convention for a positive shear gradient, $+\nabla\gamma$, resulting in a (a) negative edge dislocation and (b) negative screw dislocation (left-handed screw). The Burger's circuits are indicated with the set of points M-N-O-P-Q with the net Burger's vectors of $\boldsymbol{b}_{net}$ anti-parallel to the line direction. $\gamma > 0$ and $\gamma = 0$ represent the sheared and unsheared portions of the lattice.

The Burgers circuit is a line integral about the loop C, revealing the net closure failure, $\boldsymbol{b}_{net}$, for a plastically-deformed lattice in terms of the deformed vectors at the intermediate configuration, $\boldsymbol{Y}$, as shown in Eq. (5.3.16):

$$\boldsymbol{b}_{net} = -\oint_C \mathrm{d}\boldsymbol{Y}. \tag{5.3.16}$$

The same incompatibility can be computed in the undeformed configuration, C_0 in terms of the undeformed vectors, $\boldsymbol{X}_0$, by change of basis[‡]:

$$\boldsymbol{b}_{net} = -\oint_{C_0} \boldsymbol{F}_p \, \mathrm{d}\boldsymbol{X}_0. \tag{5.3.17}$$

$\boldsymbol{F}_p$ maps the undeformed vectors, $\mathrm{d}\boldsymbol{X}_0$, to the intermediate or microstructural configuration with:

$$\mathrm{d}\boldsymbol{Y} = \boldsymbol{F}_p \, \mathrm{d}\boldsymbol{X}_0. \tag{5.3.18}$$

Using Stokes theorem, the line integral is converted to an area integral with the area normal $\boldsymbol{r}_0$ and curl operation as:

$$\boldsymbol{b}_{net} = -\int_{S_0} (\nabla \times \boldsymbol{F}_p)^T \cdot \boldsymbol{r}_0 \, \mathrm{d}S_0. \tag{5.3.19}$$

Alternatively, [190] expresses a different form of incompatibility by considering the changes in the area normals with plastic deformation in the integral Eq. (5.3.19) at the microstructural configuration using the change of basis according to Nanson's relation ($\boldsymbol{r}\,\mathrm{d}S = \det(\boldsymbol{F})\,\boldsymbol{F}^{-T}\,\boldsymbol{r}_0\,\mathrm{d}S_0$) and considering isochoric plasticity ($\det(\boldsymbol{F}_p) = 1$) which takes the form:

[‡]The quantities at the undeformed lattice are denoted with the subscript '0'.

$$\boldsymbol{b}_{net} = -\int_S (\nabla \times \boldsymbol{F}_p)^T \cdot \boldsymbol{F}_p^T \, \boldsymbol{r} \, \mathrm{d}S. \tag{5.3.20}$$

Nye tensor

The lattice incompatibility needs to be fulfilled by dislocations that are called geometrically necessary dislocations (GNDs) unless there is a discontinuity like a crack or void.

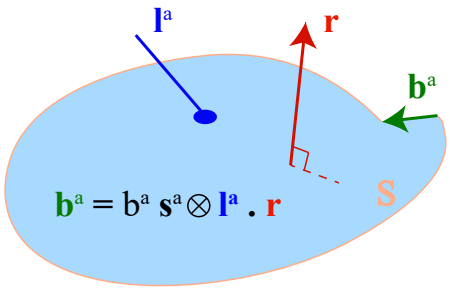

Figure 5.3: A dislocation line, $\boldsymbol{l}^a$, penetrating through an arbitrary area normal, $\boldsymbol{r}$, of a surface S at the microstructural or intermediate configuration.

Nye defined the dislocation tensor as the dislocation lines, $\boldsymbol{l}^a$, that pierce through an arbitrary area normal, $\boldsymbol{r}$, contributing as much as their projected Burgers vector, b^a, [19] as schematically shown in Fig. 5.3. Note that the line direction is along the slip direction, $\boldsymbol{s}^a$ and transverse direction, $\boldsymbol{t}^a$, for screw and edge dislocations, respectively, giving a net Burgers vector of $\boldsymbol{b}_{net}$ at the microstructural configuration:

$$\boldsymbol{b}_{net} = \int_S \left(\sum_a \rho^a_{GND} \, b^a \, \boldsymbol{s}^a \otimes \boldsymbol{l}^a \right) \cdot \boldsymbol{r} \, \mathrm{d}S. \tag{5.3.21}$$

Total form

The incompatibility measure obtained from the Burgers circuit, Eq. (5.3.19), shall be satisfied by Nye's tensor in Eq. (5.3.21) which gives:

$$\boldsymbol{b}_{net} = -\int_{S_0} (\nabla \times \boldsymbol{F}_p)^T \cdot \boldsymbol{r}_0 \mathrm{d}S_0 = \int_S \left(\sum_a \rho^a_{GND} \, b^a \, \boldsymbol{s}^a \otimes \boldsymbol{l}^a \right) \cdot \boldsymbol{r} \, \mathrm{d}S. \tag{5.3.22}$$

Ignoring the changes in the area with plastic deformation ($\boldsymbol{r}_0 \mathrm{d}S_0 = \boldsymbol{r} \, \mathrm{d}S$) and cancelling out the integrals on both sides, gives the overall incompatibility measure:

$$\boldsymbol{\Lambda} = -(\nabla \times \boldsymbol{F}_p)^T = \sum_a \rho^a_{GND} \, b^a \, \boldsymbol{s}^a \otimes \boldsymbol{l}^a, \tag{5.3.23}$$

Eq. (5.3.24) shows the same expression in index notation. Please note the negative sign and the transpose to match the dislocation convention of Nye's tensor:

$$\Lambda_{ji} = -\varepsilon_{irs} F_{p\,js,r} = \sum_a \rho^a_{GND}\, b^a\, s^a_j\, l^a_i. \tag{5.3.24}$$

Considering changes in the area normal or the dislocation flux [190]:

Alternatively, the changes in the area normal vector and the area shall be considered for large deformations as in Eq. (5.3.20). Therefore, setting the incompatibility measure equal to Nye's tensor in Eq. (5.3.21) gives:

$$\boldsymbol{b}_{net} = -\int_S (\nabla \times \boldsymbol{F}_p)^T \cdot \boldsymbol{F}_p^T\, \boldsymbol{r}\, \mathrm{d}S = \int_S \left(\sum_a \rho^a_{GND}\, b^a\, \boldsymbol{s}^a \otimes \boldsymbol{l}^a \right) \cdot \boldsymbol{r}\, \mathrm{d}S. \tag{5.3.25}$$

Cancelling out the integrals on both sides gives the overall incompatibility measure in Eq. (5.3.26). A detailed derivation can also be found in [192]:

$$\boldsymbol{\Lambda}' = -(\nabla \times \boldsymbol{F}_p)^T\, \boldsymbol{F}_p^T = \sum_a \rho^a_{GND}\, b^a\, \boldsymbol{s}^a \otimes \boldsymbol{l}^a, \tag{5.3.26}$$

or in index notation:

$$\Lambda'_{ji} = -\varepsilon_{mrs} F_{p\,js,r} F_{p\,im} = \sum_a \rho^a_{GND}\, b^a\, s^a_j\, l^a_i. \tag{5.3.27}$$

The incompatibility tensor can be written as the sum of dislocation families; screws and edges:

$$\boldsymbol{\Lambda} = \sum_a \rho^a_{GND,e}\, b^a\, \boldsymbol{s}^a \otimes \boldsymbol{t}^a + \rho^a_{GND,s}\, b^a\, \boldsymbol{s}^a \otimes \boldsymbol{s}^a. \tag{5.3.28}$$

Therefore, the solution for the dislocation densities, $\{\boldsymbol{\varrho}_{GND}\}$, of the linear problem in Eq. (5.3.29) is needed:

$$\{\boldsymbol{\Lambda}\} = [\boldsymbol{A}]\, \{\boldsymbol{\varrho}_{GND}\}. \tag{5.3.29}$$

There are 18 dislocation densities for face-centred-cubic materials; 12 edge and 6 screw dislocations and there are more families for other crystal structures. However, the incompatibility tensor has 9 known components, the coefficient matrix, $[\boldsymbol{A}]$, therefore has a size of 9 by 18 for FCC materials, so the solution is not unique. In this paper, three different solution techniques for GND densities are investigated (the solution method used for GND models 1-c and 1-d is the same), which are explained in the following.

- **GND model 1-a:** L2 minimisation

  The incompatibility measure for model 1-a is the total form that relies on the curl of the plastic deformation gradient, Eq. (5.3.23). Once the incompatibility is computed, the GND density is obtained by calculating the right-pseudo inverse of $\boldsymbol{A}$ [93], which has full column rank ($r = 9$). This is equivalent to L2 minimisation, or least-squares fitting to solve Eq. (5.3.29). The inversion is necessary to solve for the linear equation, which is underdetermined:

$$\{\boldsymbol{\varrho}_{GND}\} = [\boldsymbol{A}]^+\, \{\boldsymbol{\Lambda}\}. \tag{5.3.30}$$

where,

$$[\boldsymbol{A}]^{+} = [\boldsymbol{A}]^{T} \left([\boldsymbol{A}] \, [\boldsymbol{A}]^{T} \right)^{-1}. \tag{5.3.31}$$

As shown in Eq. (5.3.30), the right pseudo inverse is applied on the left, thus, this calculation provides the projection of the incompatibility onto the row space, i.e., the incompatibility accommodated by the GND geometry defined in the $[\boldsymbol{A}]$ matrix.

- **GND model 1-b:** KKT optimisation

  In this model, the total form of the incompatibility in Eq. (5.3.23) is used and minimised using KKT optimality criterion.

  The L2 functional, C, is defined as in Eq. (5.3.32), which is a function of GND density, $\boldsymbol{\varrho}_{GND}$, and a vector, $\boldsymbol{\lambda}$, containing penalty factors of the Lagrange multiplier:

$$C(\boldsymbol{\varrho}_{GND}, \boldsymbol{\lambda}) = \boldsymbol{\varrho}_{GND}^{T} \, \boldsymbol{\varrho}_{GND} + \boldsymbol{\lambda}^{T} \left(\boldsymbol{A} \, \boldsymbol{\varrho}_{GND} - \boldsymbol{\Lambda} \right). \tag{5.3.32}$$

  The KKT optimality criteria gives:

$$\frac{\partial C(\boldsymbol{\varrho}_{GND}, \boldsymbol{\lambda})}{\partial \, \boldsymbol{\varrho}_{GND}} = \boldsymbol{0}. \tag{5.3.33}$$

$$\frac{\partial C(\boldsymbol{\varrho}_{GND}, \boldsymbol{\lambda})}{\partial \boldsymbol{\lambda}} = \boldsymbol{0}. \tag{5.3.34}$$

  Substituting Eq. (5.3.34) into Eq. (5.3.32) gives:

$$2\boldsymbol{\varrho}_{GND} + \boldsymbol{\lambda}^{T} \, \boldsymbol{A} = \boldsymbol{0}. \tag{5.3.35}$$

$$\boldsymbol{A} \, \boldsymbol{\varrho}_{GND} - \boldsymbol{\Lambda} = \boldsymbol{0}. \tag{5.3.36}$$

  Using the simple identity; $\boldsymbol{\lambda}^{T} \, \boldsymbol{A} = \boldsymbol{A}^{T} \, \boldsymbol{\lambda}$, Eq. (5.3.37) is obtained:

$$\begin{bmatrix} 2\boldsymbol{I} & \boldsymbol{A}^{T} \\ \boldsymbol{A} & \boldsymbol{0} \end{bmatrix} \begin{Bmatrix} \boldsymbol{\varrho}_{GND} \\ \boldsymbol{\lambda} \end{Bmatrix} = \begin{Bmatrix} \boldsymbol{0} \\ \boldsymbol{\Lambda} \end{Bmatrix}. \tag{5.3.37}$$

  Therefore, the solution for the GND density in Eq. (5.3.30) is obtained by simply inverting the coefficient matrix:

$$[\boldsymbol{B}] = \begin{bmatrix} 2\boldsymbol{I} & \boldsymbol{A}^{T} \\ \boldsymbol{A} & \boldsymbol{0} \end{bmatrix}^{-1}. \tag{5.3.38}$$

  This has two conditions for invertibility [193]:

1. The stacked matrix $\begin{bmatrix} 2\boldsymbol{I} \\ \boldsymbol{A} \end{bmatrix}$ has linearly independent columns; which is guaranteed given the identity matrix.
2. The matrix $\boldsymbol{A}$ has linearly independent rows.

For example, the square coefficient matrix in Eq. (5.3.37), has a size of $18+9=27$ for FCC materials, has full rank, and hence can be inverted to find GND densities. The size of the coefficient matrix gets larger as the number of slip systems increases, reducing the computational efficiency, a downside of the KKT approach.

- **GND model 1-c:** *Restricted solution to the active slip systems*

  In this model, the total form in Eq. (5.3.23) is used as the incompatibility measure. The $\boldsymbol{A}$ matrix is reduced to include the GND geometries of only active slip systems, defined with the limit condition on the absolute value of the cumulative slip, $|\gamma^a|$, which was found as 10^{-10} s^{-1}:

$$[\boldsymbol{A}] = \sum_a \begin{cases} \rho^a_{GND}\, b^a\, \boldsymbol{s}^a \otimes \boldsymbol{l}^a, & \text{if } |\gamma^a| > 10^{-10}, \\ 0, & \text{otherwise.} \end{cases} \tag{5.3.39}$$

  Due to the activation of a few slip systems, this often results in a rank-deficient matrix, which requires a generalised pseudo-inverse obtained by SVD. Here $[\boldsymbol{A}]$ is decomposed into its orthogonal matrices $[\boldsymbol{U}]$, $[\boldsymbol{V}]$, and a diagonal matrix $[\boldsymbol{S}]$:

$$[\boldsymbol{A}] = [\boldsymbol{U}]\,[\boldsymbol{S}]\,[\boldsymbol{V}]^T. \tag{5.3.40}$$

  which is inverted by transposing $[\boldsymbol{U}]$, $[\boldsymbol{V}]$ and the reciprocal of the diagonal terms of $\boldsymbol{S}$:

$$[\boldsymbol{A}]^+ = [\boldsymbol{V}]\,[\boldsymbol{S}]^{-1}\,[\boldsymbol{U}]^T. \tag{5.3.41}$$

  This generalised pseudo-inverse calculates the projection of the incompatibility onto GND densities of the active slip systems only.

- **GND model 1-d:** *Restricted solution to the active slip systems considering configurational changes*

  The incompatibility measure considering configuration changes [190] is used in this model as defined in Eq. (5.3.26). The GNDs are obtained using the same method outlined in GND model 1-c; constraining the solution to the active slip systems only followed by SVD and inversion. Therefore, the same relations are observed in Eqs. 5.3.39 and 5.3.41 are used to calculate the GNDs of incompatibility by eliminating the columns of $\boldsymbol{A}$ of inactive systems.

Rate form (GND model 2)

The rate form of incompatibility uses the curl of a vector instead of using the curl of a second-rank tensor, which has different forms in the literature [93]. The rate form of the incompatibility is obtained by simply taking the time derivative of Eq. (5.3.23):

$$\dot{\boldsymbol{\Lambda}} = -\left(\nabla \times \dot{\boldsymbol{F}}_p\right)^T. \tag{5.3.42}$$

$\dot{\boldsymbol{F}}_p$ is computed in terms of the plastic velocity gradient, Eq. (5.3.43):

$$\dot{\boldsymbol{F}}_p = \boldsymbol{L}_p \boldsymbol{F}_p. \tag{5.3.43}$$

Substituting Eq. (5.3.3) into Eq. (5.3.43) gives:

$$\dot{\boldsymbol{F}}_p = \left(\sum_a \dot{\gamma}^a \boldsymbol{s}^a \otimes \boldsymbol{n}^a\right) \boldsymbol{F}_p = \sum_a \left(\dot{\gamma}^a \boldsymbol{s}^a \otimes \boldsymbol{n}^a\right) \cdot \boldsymbol{F}_p. \tag{5.3.44}$$

Substituting Eq. (5.3.43) into the incompatibility rate in Eq. (5.3.44) gives:

$$\dot{\boldsymbol{\Lambda}} = -\left\{\nabla \times \left(\sum_a \boldsymbol{s}^a \otimes \dot{\gamma}^a \boldsymbol{n}^a \cdot \boldsymbol{F}_p\right)\right\}^T. \tag{5.3.45}$$

Taking the curl into the summation by considering the definition of the curl in Eq. (5.3.15) gives:

$$\dot{\boldsymbol{\Lambda}} = -\left[\sum_a \left(\nabla \times \dot{\gamma}^a \boldsymbol{n}^a \cdot \boldsymbol{F}_p\right) \otimes \boldsymbol{s}^a\right]^T. \tag{5.3.46}$$

The incompatibility rate measure per slip system becomes:

$$\dot{\boldsymbol{\Lambda}}^a = -\left[\nabla \times \left(\dot{\gamma}^a \boldsymbol{n}^a \cdot \boldsymbol{F}_p\right) \otimes \boldsymbol{s}^a\right]^T. \tag{5.3.47}$$

Taking the transpose gives:

$$\dot{\boldsymbol{\Lambda}}^a = -\boldsymbol{s}^a \otimes \left[\nabla \times \left(\dot{\gamma}^a \boldsymbol{n}^a \boldsymbol{F}_p\right)\right]. \tag{5.3.48}$$

Using Nye's dislocation tensor for edge and screw dislocations gives the incompatibility as:

$$\dot{\boldsymbol{\Lambda}}^a = b^a \dot{\rho}^a_{GND,et} \boldsymbol{s}^a \otimes \boldsymbol{t}^a + b^a \dot{\rho}^a_{GND,en} \boldsymbol{s}^a \otimes \boldsymbol{n}^a + b^a \dot{\rho}^a_{GND,s} \boldsymbol{s}^a \otimes \boldsymbol{s}^a. \tag{5.3.49}$$

Equating the incompatibility rate measures in Eq. (5.3.48) to (5.3.49) gives Eq. (5.3.50) in which $\dot{\rho}^a_{GND,et}$, $\dot{\rho}^a_{GND,en}$, and $\dot{\rho}^a_{GND,s}$ are GND density evolution rates for edge type dislocations along transverse direction,

along slip plane normal, and screw type dislocations along slip direction, respectively:

$$\dot{\boldsymbol{\Lambda}}^a = -\boldsymbol{s}^a \otimes \nabla \times \dot{\gamma}^a \boldsymbol{n}^a \boldsymbol{F}_p = b^a \dot{\rho}^a_{GND,et} \boldsymbol{s}^a \otimes \boldsymbol{t}^a + b^a \dot{\rho}^a_{GND,en} \boldsymbol{s}^a \otimes \boldsymbol{n}^a + b^a \dot{\rho}^a_{GND,s} \boldsymbol{s}^a \otimes \boldsymbol{s}^a. \tag{5.3.50}$$

The edge dislocations along the slip normal ($\dot{\rho}^a_{GND,en}$) are neglected in this study because we assume that edges and screws are restricted to gradients on their glide plane. As the final step, the slip direction vector can be cancelled out on both sides of the equations, giving:

$$-\nabla \times (\dot{\gamma}^a \boldsymbol{n}^a \boldsymbol{F}_p) = b^a \dot{\rho}^a_{GND,e} \boldsymbol{t}^a + b^a \dot{\rho}^a_{GND,s} \boldsymbol{s}^a. \tag{5.3.51}$$

Equivalently in index notation:

$$-\varepsilon_{ijk} \left(\dot{\gamma}^a n^a_l F_{plk}\right)_{,j} = b^a \dot{\rho}^a_{GND,e} t^a_i + b^a \dot{\rho}^a_{GND,s} s^a_i. \tag{5.3.52}$$

Equations for edge and screw families of dislocations are computed using the vector projections and rearranging terms, giving:

$$\dot{\rho}^a_{GND,e} = -\frac{1}{b^a} (\nabla \times \dot{\gamma}^a \boldsymbol{n}^a \boldsymbol{F}_p) \cdot \boldsymbol{t}^a, \tag{5.3.53}$$

$$\dot{\rho}^a_{GND,s} = -\frac{1}{b^a} (\nabla \times \dot{\gamma}^a \boldsymbol{n}^a \boldsymbol{F}_p) \cdot \boldsymbol{s}^a. \tag{5.3.54}$$

The formulations explained here can also be found in [186]. Several different references use the same formulation consistently to quantify GNDs [194, 195].

Slip gradients (GND model 3)

Consider small strains ($|\gamma| \ll 1$). The plastic part of the deformation gradient reduces to:

$$\boldsymbol{F}_p = \sum_a \gamma^a \boldsymbol{s}^a \otimes \boldsymbol{n}^a + \boldsymbol{I}. \tag{5.3.55}$$

Substituting the simplified plastic deformation gradient into Eq. (5.3.23) as the curl of the identity is zero gives:

$$\boldsymbol{\Lambda} = -(\nabla \times \boldsymbol{F}_p)^T = -\left(\nabla \times \sum_a \gamma^a \boldsymbol{s}^a \otimes \boldsymbol{n}^a\right)^T. \tag{5.3.56}$$

The curl operation can be taken inside the sum, giving:

$$\boldsymbol{\Lambda} = -\sum_a \left[\nabla \times (\gamma^a \boldsymbol{s}^a \otimes \boldsymbol{n}^a)\right]^T. \tag{5.3.57}$$

The gradient operation is the sum of the directional derivatives along slip direction, $\boldsymbol{s}^a$, slip plane normal, $\boldsymbol{n}^a$, and line (tangent) direction, $\boldsymbol{t}^a$, Eq. (5.3.58):

$$\nabla\gamma^a = \gamma^a_{,\boldsymbol{s}^a}\boldsymbol{s}^a + \gamma^a_{,\boldsymbol{n}^a}\boldsymbol{n}^a + \gamma^a_{,\boldsymbol{t}^a}\boldsymbol{t}^a. \tag{5.3.58}$$

Substituting the directional derivatives and using the definition of curl in Eq. (5.3.15) to compute the incompatibility gives:

$$\boldsymbol{\Lambda} = -\sum_a \left[\left(\gamma^a_{,\boldsymbol{s}^a}\boldsymbol{s}^a \times \boldsymbol{n}^a\right)\otimes\boldsymbol{s}^a + \left(\gamma^a_{,\boldsymbol{n}^a}\boldsymbol{n}^a \times \boldsymbol{n}^a\right)\otimes\boldsymbol{s}^a + \left(\gamma^a_{,\boldsymbol{t}^a}\boldsymbol{t}^a \times \boldsymbol{n}^a\right)\otimes\boldsymbol{s}^a\right]^T. \tag{5.3.59}$$

The cross-product of slip plane normals with itself ($\boldsymbol{n}^a \times \boldsymbol{n}^a = \boldsymbol{0}$) is zero, which vanishes the effect of slip gradients along the slip plane normal. Substituting $\boldsymbol{t}^a = \boldsymbol{s}^a \times \boldsymbol{n}^a$ reduces Eq. (5.3.59) to:

$$\boldsymbol{\Lambda} = -\sum_a \left(\gamma^a_{,\boldsymbol{s}^a}\boldsymbol{t}^a\otimes\boldsymbol{s}^a - \gamma^a_{,\boldsymbol{t}^a}\boldsymbol{s}^a\otimes\boldsymbol{s}^a\right)^T = \sum_a \gamma^a_{,\boldsymbol{t}^a}\boldsymbol{s}^a\otimes\boldsymbol{s}^a - \gamma^a_{,\boldsymbol{s}^a}\boldsymbol{s}^a\otimes\boldsymbol{t}^a. \tag{5.3.60}$$

Equivalently in index notation:

$$\Lambda_{ij} = \sum_a \gamma^a_{,k}t^a_k s^a_i s^a_j - \gamma^a_{,l}s^a_l s^a_i t^a_j. \tag{5.3.61}$$

Expanding on Eq. (5.3.23), the dislocation tensor is computed considering the edge and screw families of dislocations using:

$$\boldsymbol{\Lambda} = \sum_a \rho^a_{GND,e}\, b^a\, \boldsymbol{s}^a\otimes\boldsymbol{t}^a + \rho^a_{GND,s}\, b^a\, \boldsymbol{s}^a\otimes\boldsymbol{s}^a. \tag{5.3.62}$$

Therefore, the individual dislocation densities per slip system can be computed by equating the incompatibility to the dislocation tensor:

$$b^a\,\rho^a_{GND,e} = -\gamma^a_{,\boldsymbol{s}^a} = -\boldsymbol{\nabla}\gamma^a\cdot\boldsymbol{s}^a. \tag{5.3.63}$$

$$b^a\,\rho^a_{GND,s} = \gamma^a_{,\boldsymbol{t}^a} = \boldsymbol{\nabla}\gamma^a\cdot\boldsymbol{t}^a. \tag{5.3.64}$$

The edge dislocation density is the gradient of slip along the slip direction, Eq. (5.3.65):

$$\rho^a_{GND,e} = -\frac{1}{b^a}\boldsymbol{\nabla}\gamma^a\cdot\boldsymbol{s}^a. \tag{5.3.65}$$

The screw dislocation density is the gradient of slip along the transverse direction, Eq. (5.3.66):

$$\rho^a_{GND,s} = \frac{1}{b^a}\boldsymbol{\nabla}\gamma^a\cdot\boldsymbol{t}^a. \tag{5.3.66}$$

Lattice curvature

The lattice curvature is computed using the incompatibility according to Eq. (5.3.67). This equation ignores elastic strain gradients and computes lattice curvature using total lattice incompatibility obtained by rotations [171]:

$$\boldsymbol{\kappa} = -\boldsymbol{\Lambda}^T + \boldsymbol{I}\,\mathrm{tr}(\boldsymbol{\Lambda})/2 \tag{5.3.67}$$

5.3.4 Summary of GND models

Table 5.1: Summary of equations used in GND models.

		incompatibility measure ($\boldsymbol{\Lambda}$)	coefficient	GND density (ρ_{GND}) edge ($\rho_{GND,e}$)	GND density (ρ_{GND}) screw ($\rho_{GND,s}$)
model 1	**a**	$-(\nabla\times\boldsymbol{F}_p)^T$	$b^a\,\boldsymbol{s}^a\otimes\boldsymbol{l}^a$	$[\boldsymbol{A}^+]\,\{\boldsymbol{\Lambda}\}$	
	b	$-(\nabla\times\boldsymbol{F}_p)^T$	$\begin{bmatrix} 2\boldsymbol{I} & \boldsymbol{A}^T \\ \boldsymbol{A} & \boldsymbol{0} \end{bmatrix}$	$[\boldsymbol{B}]\begin{Bmatrix} \boldsymbol{0} \\ \boldsymbol{\Lambda} \end{Bmatrix}$.	
	c	$-(\nabla\times\boldsymbol{F}_p)^T$	$\sum_a \begin{cases} b^a\,\boldsymbol{s}^a\otimes\boldsymbol{l}^a, & \text{if } \lvert\gamma^a\rvert > 10^{-10} \\ 0, & \text{otherwise} \end{cases}$	$[\boldsymbol{A}]^+\,\{\boldsymbol{\Lambda}\}$	
	d	$-(\nabla\times\boldsymbol{F}_p)^T\,\boldsymbol{F}_p^T$	$\sum_a \begin{cases} b^a\,\boldsymbol{s}^a\otimes\boldsymbol{l}^a, & \text{if } \lvert\gamma^a\rvert > 10^{-10} \\ 0, & \text{otherwise} \end{cases}$	$[\boldsymbol{A}]^+\,\{\boldsymbol{\Lambda}'\}$	
model 2		$-\nabla\times\dot{\gamma}^a\,\boldsymbol{n}^a\,\boldsymbol{F}_p$	N/A	$-\frac{1}{b^a}\,(\nabla\times\dot{\gamma}^a\,\boldsymbol{n}^a\,\boldsymbol{F}_p)\cdot\boldsymbol{t}^a$	$-\frac{1}{b^a}\,(\nabla\times\dot{\gamma}^a\,\boldsymbol{n}^a\,\boldsymbol{F}_p)\cdot\boldsymbol{s}^a$
model 3		$\nabla\gamma^a$	N/A	$-\frac{1}{b^a}\,\boldsymbol{\nabla}\gamma^a\cdot\boldsymbol{s}^a$	$\frac{1}{b^a}\,\boldsymbol{\nabla}\gamma^a\cdot\boldsymbol{t}^a$

Different models relying on the total form (model 1), rate form (model 2), and slip gradients (model 3) are investigated. In addition, four other variants of the total form (model 1) are used to obtain GND densities using; (a) the Least-Squares (L2) minimisation [171], (b) Karush-Kuhn-Tucker (KKT) optimality criterion [193], (c) restrained solution to active slip systems, and (d) incompatibility measure considering deformed areas [190] followed by restrained solution were studied. Table 5.1 shows the summary of the incompatibility measures, the coefficient matrix that needs to be inverted to solve for GNDs, and the expression to compute GND densities corresponding to each model that are used in this study.

5.3.5 Gradient operator (element type specific)

The gradient operator is computed in the undeformed reference using the initial coordinates once at the beginning of the calculations. Gradient calculation is performed by isolating each element of the mesh. This allows calculation of the strain gradients without any special treatment for the grain boundaries. To achieve that, there is only one limiting factor; the number of *integration points* (IPs), q, must be greater than 2 in 2D or 3 in 3D to allow calculation of the directional gradients within the element, respectively.

Table 5.2: Element types and properties.

Abaqus® ID	geometry	dim.	Order of GND interpolation	Number of nodes (p)	Number of IPs (q)	condition
CPS4/CPE4	quadrilateral	2D	linear	4	4	p=q
CPS6/CPE6	triangular	2D	quadratic	6	3	p>q
CPS6/CPE6	triangular	2D	linear	3	3	p=q
CPS8/CPE8	quadrilateral	2D	quadratic	8	9	p<q
CPS8/CPE8	quadrilateral	2D	linear	4	9	p<q
CPS8R/CPE8R	quadrilateral	2D	linear	4	4	p=q
C3D8	hexahedral	3D	linear	8	8	p=q
C3D10	tetrahedral	3D	quadratic	10	4	p>q
C3D10	tetrahedral	3D	linear	4	4	p=q
C3D15	prismatic	3D	quadratic	15	9	p>q
C3D15	prismatic	3D	linear	6	9	p<q
C3D20	hexahedral	3D	quadratic	20	27	p<q
C3D20	hexahedral	3D	linear	8	27	p<q
C3D20R	hexahedral	3D	linear	8	8	p=q

The gradient calculation was performed with three stages. First, the values of the parameter ($\boldsymbol{F}_p$, $\dot{\gamma}^a \boldsymbol{n}^a \boldsymbol{F}_p$, or $\dot{\gamma}^a$) at the IPs is obtained. Second, the parameters are extrapolated to the nodes of the element. Third, gradients at the IPs and element centre are computed using the gradient operators. Fig. 5.4 shows these computation steps schematically. The gradient calculation is performed by calculating the shape function gradients in the isoparametric space, $[\boldsymbol{\nabla N}]$, and then transforming the gradient operator to the physical space by Eq. (5.3.68). $[\boldsymbol{T}]$ is computed at each of the IPs and at the element centre.

$$[\boldsymbol{T}]_{(3\times p)} = [\boldsymbol{J}]^{-T}_{(3\times 3)} [\boldsymbol{\nabla N}]_{(3\times p)} . \tag{5.3.68}$$

The Jacobian is computed using the node coordinates, $\{\boldsymbol{x}\}$, that contain the x, y, z coordinates of each node of an element, Eq. (5.3.69):

$$[\boldsymbol{J}]^{T}_{(3\times 3)} = [\boldsymbol{\nabla N}]_{(3\times p)} \{\boldsymbol{x}\}_{(p\times 3)} . \tag{5.3.69}$$

The overall mapping to compute the gradient is given by $[\boldsymbol{G}]$ Eq. (5.3.70) in which $[\boldsymbol{M}]$ represents the

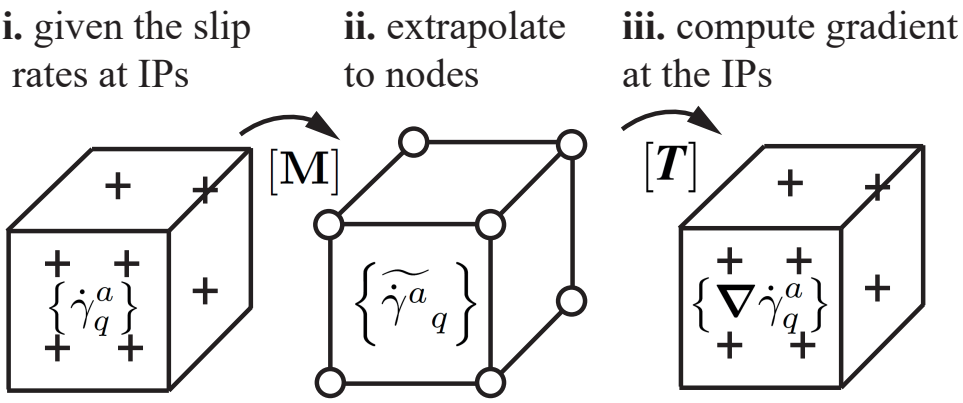

Figure 5.4: General gradient calculation procedure shown only for slip gradients. The same procedure applies to the calculation of the gradient of $\boldsymbol{F}_p$. Subscript 'q' denotes the integration point at which the slip rate is computed, while the superscript ^{a} denotes the corresponding slip system. The symbol $\tilde{}$ indicates nodal variables.

mapping to extrapolate from IPs to nodes:

$$[\boldsymbol{G}]_{(3\times q)} = [\boldsymbol{T}]_{(3\times p)}\,[\boldsymbol{M}]_{(p\times q)} \tag{5.3.70}$$

The gradients are computed at the integration points and the element centroid. In the case of a homogenised solution, the GND density for each IP is then obtained by assigning the centroid value to the IPs.

The extrapolation method varies based on the number of IPs (q) and the number of nodes (p) of an element, which is shown for different types of elements in Table 5.2. $[\boldsymbol{N}]$ represents the matrix containing the interpolation functions of the element, where each row corresponds to an IP (the interpolation functions of each element type are available in [17]). The extrapolation scheme of $[\boldsymbol{N}]$ is described for three cases as follows:

Case (p=q)

The inversion of $[\boldsymbol{N}]$ in Eq. (5.3.71) is possible since $[\boldsymbol{N}]$ is a square matrix of full rank without rank deficiency, hence is invertible:

$$[\boldsymbol{M}]_{(p\times q)} = \left([\boldsymbol{N}]_{(q\times p)}\right)^{-1}. \tag{5.3.71}$$

Case (p <q)

If the total number of nodes is less than the total number of IPs, the solution is overdefined, hence the inversion of $\boldsymbol{N}$ is possible by calculating the left-pseudo inverse. Therefore, the overall inversion mapping

that applies to the variables at the IPs becomes:

$$[\boldsymbol{M}]_{(p\times q)} = \left([\boldsymbol{N}]^T_{(p\times q)}\,[\boldsymbol{N}]_{(q\times p)}\right)^{-1}[\boldsymbol{N}]^T_{(p\times q)}\,. \tag{5.3.72}$$

Case (p >q)

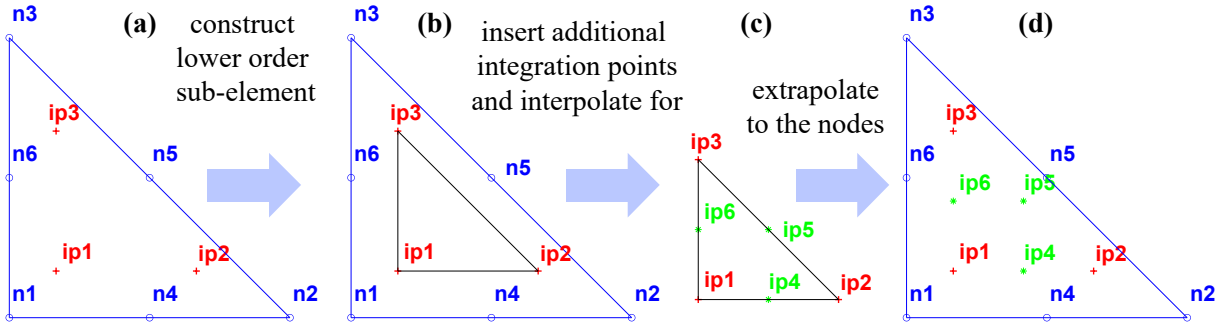

Figure 5.5: Extrapolation method for the case $p > q$, e.g. 6-noded quadratic triangle: (a) Element consisting of 6-nodes and 3-integration points, (b) construction of sub-elements, (c) insertion of additional integration points resembling the nodes of the host element, (d) extrapolation from the integration points to the nodes. An example is shown for CPS6/CPE6 types of element for clarity.

In some quadratic elements, the number of nodes per element is greater than the total number of IPs in that element. In this case, direct extrapolation to the nodes is not possible because of the insufficient number of IP values. For this reason, $p-q$ additional number of IPs are inserted into the host element. A mapping, $[\boldsymbol{O}]$, is used to interpolate the values at these additional IPs while keeping the existing data at the IPs of the host element using the identity matrix, $[\boldsymbol{I}]$. The mapping is defined in Eq. (5.3.73) and uses the sub element interpolation functions, $\overline{[\boldsymbol{N}]}$ which is the shape function of the elements with reduced order (CPS3, CPE3, C3D4, C3D6) of the host element type (CPS6, CPE6, C3D10, C3D15, respectively):

$$[\boldsymbol{O}]_{(p\times q)} = \begin{bmatrix} [\boldsymbol{I}]_{(q\times q)} \\ \overline{[\boldsymbol{N}]}_{(p-q\times q)} \end{bmatrix}. \tag{5.3.73}$$

The interpolation mapping $[\boldsymbol{O}]$ is computed by constructing a sub-element, Fig. 5.5, nodes of which coincide with the integration points of the host element. The position of additional integration points is selected such that the point distribution is the same as the node distribution of the host element.

The total number of nodes of an element and the total number of IPs per element become equal after the application of the mapping $[\boldsymbol{O}]$, while preserving the existing IP data. The mapping for extrapolation, $[\boldsymbol{M}]$, becomes as in Eq. (5.3.74):

$$[\boldsymbol{M}]_{(p\times q)} = \left([\boldsymbol{N}]_{(p\times p)}\right)^{-1}[\boldsymbol{O}]_{(p\times q)}\,. \tag{5.3.74}$$

5.3.6 Numerical method and important constraints

The crystal plasticity solver details can be found elsewhere [48], in which the residual in the solver is based on Cauchy stress using a user-defined subroutine called UMAT. At the end of each time increment, non-local GND calculations are performed using the UEXTERNALDB subroutine of Abaqus®. Therefore, GNDs are updated explicitly at the end of each converged time increment. Fortran files, documentation, and examples are available in the GitHub link with open public access [49].

Most importantly, a constraint on the increment of the GND density is enforced to avoid accumulation of numerical errors. Slight differences in the slip rates can exist, producing artificially large gradients when divided by small numbers at small scales, resulting in low magnitudes of fictitious GND densities. GNDs having a direct effect on CRSS and slip rates amplify those numerical differences further, causing a positive feedback. Therefore, a threshold on the increment of the GND density, which corresponds to physically zero dislocation density (2×10^{-10} μm$^{-2} = 2 \times 10^{2}$ m^{-2}) is employed. This threshold is obtained from strain-gradient-free uniaxial tension, considering various dimensions, which is used to suppress the effect of numerical errors as shown in Eq. (5.3.75):

$$\rho^{a}_{GND} = \rho^{a}_{GNDt} + \begin{cases} \Delta\rho^{a}_{GND}, & \text{if } \left|\Delta\rho^{a}_{GND}\right| > 2 \times 10^{-10}\ \mu\text{m}^{-2} \\ 0, & \text{otherwise} \end{cases} \tag{5.3.75}$$

5.4 Results and Discussion

The GND calculation models were compared simulating a single crystal with FCC symmetry.

The experiments include a uniaxial tension case without strain gradients, simple shear case with linear strain gradient, a uniaxial tension case with geometrically imposed strain gradient, and a four-point bending case.

In addition, a polycrystal with fully active slip systems undergoing large deformation was investigated to determine the difference between L2 restricted calculus (model 1-c and d), the rate form (model 2) and the slip gradient (model 3).

In the single crystal cases examined, the deformed area correction (GND model 1-d), did not give different results compared to the case without the area correction (GND model 1-c) because the deformation is in 2D. The 2D plastic deformation does not change the area normal along the third direction (Z-axis), around which the Burgers' circuit is constructed. For this reason, model 1-d is only discussed for the polycrystal case, excluding the single crystal single slip cases, since it gives the same findings as model 1-c in 2D.

Table 5.3 shows the material parameters used within this study. The critical resolved shear stress (CRSS), τ_c, was selected as 1 MPa to minimise the effect of elastic deformation.

C_{11}	C_{12}	C_{44} (G)	b^a	τ_c^0	α	$\dot{\gamma}_0$	n
170 GPa	124 GPa	75 GPa	2.56×10^{-4} μm	1 MPa	0.25	0.001 s^{-1}	20

Table 5.3: Model parameters used in the simulations.

5.4.1 Strain-gradient-free uniaxial tension (single crystal single slip)

Uniaxial tension of symmetric cube orientation shall reveal zero GND density, $\rho_{GND} = 0$. To test this case, the cube geometry with unit dimensions in micrometres consisting of eight elements with Euler angles of (0°, 0°, 0°) was used. An FCC unit cell was aligned with the sample reference (cube orientation) to avoid single-slip rotations and to avoid complex stress states. All possible slip systems were active in the analysis without any restriction. The cube was loaded up to a uniform tensile strain of 10% with a strain rate of 0.01

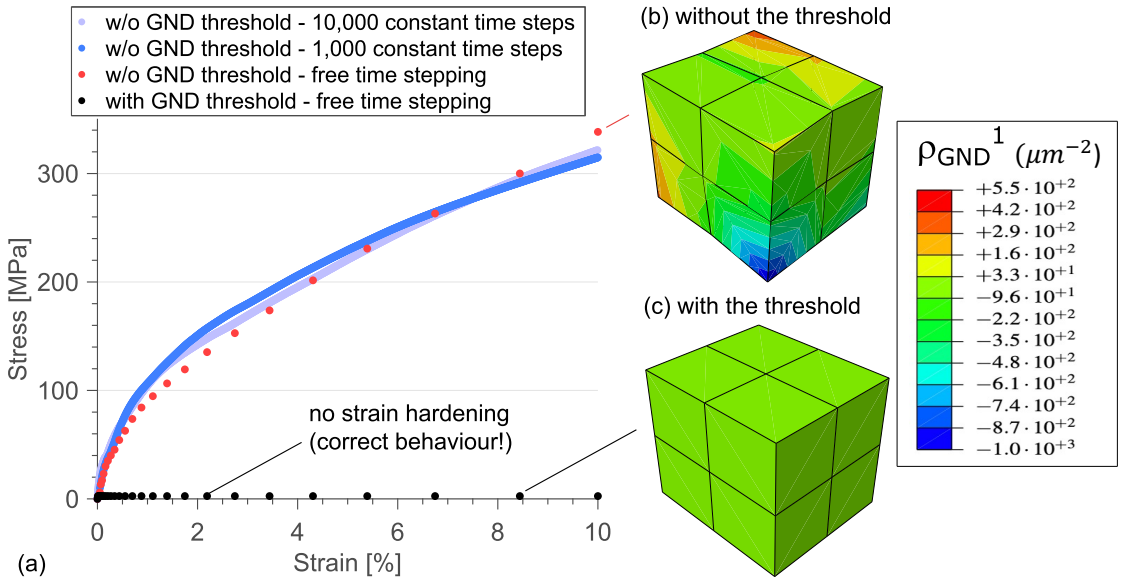

Figure 5.6: (a) Average of the axial stress over the integration points, (b) GND density in slip system - 1 without the threshold, and (c) GND density on slip system - 1 with the threshold. A uniaxial tensile strain of 10% was used with a strain rate of 0.01 s^{-1}. No strain gradient hardening is expected for a uniaxial tension load indicated with the black dots.

s^{-1}. The opposite face was fixed along the loading direction (X-axis), allowing contraction in the other two normal loading directions. The uniaxial loading was simulated in 3D and 2D (plane stress and plane strain) using all of the GND models for all possible element types including quadrilateral, triangular, hexahedral, tetrahedral, and prismatic element geometries and for both quadratic and linear interpolation functions.

Fig. 5.6 shows the results for model 1-c and 3D linear solid brick elements. Fig. 5.6(a) shows the stress-strain behaviour with and without (w/o) using the threshold in Eq. (5.3.75), highlighting the effect of small

numerical errors in the exact solution, $\rho_{GND} = 0$, which accumulate in the gradient calculation, causing a significant difference from an ideally strain-gradient-free case. Either small time steps with 10,000 or 1000 increments or a free time step were used; the error accumulation was no different, suggesting that the source of the error was not the time integration. Similarly, decreasing the convergence tolerances on both the equilibrium solver of Abaqus® and crystal plasticity solver several orders of magnitude from their initial value made no difference in the results. These findings suggest that artificial gradients arise independently of the equilibrium and crystal plasticity solvers. Only the threshold on GND increment could avoid formation of these artifacts, which corresponds to a non-strain hardening case as the expected behaviour for a strain gradient-free uniaxial tensile test. Fig. 5.6 (b) and (c) show the comparison of GND density in an active slip system at the end of loading (10% strain) with and without (w/o) using the threshold, respectively. These findings validate the use of a threshold that acts on the increments of GND.

The procedure was repeated for a larger sample with millimetre dimensions. In this case, these artificial gradients were still present, but with relatively low magnitudes, causing no strain hardening, which validates the size dependence of the proposed approach. Small differences in the slip rates between the integration points were still present, giving rise to small but non-zero amounts of GND density. These small differences amplify over small micrometer dimensions, leading to non-negligible values of the GND density.

The results were exactly the same for all elements and models except in the plane strain case, where the von Mises stress was 2.41 MPa compared to the plane stress case due to a higher constraint in plane strain conditions. This discrepancy arises because the plane strain formulation was designed to restrict displacement in the normal to loading direction in 2D (Z-axis). As a result, using the threshold on the GND increment leads to consistent results regardless of the element type used.

The threshold of 2×10^{-10} μm^{-2} was computed by trial and error. The selected threshold was tested and validated for a range of externally applied strain rates of 0.1 s^{-1}, 0.01 s^{-1}, and 0.001 s^{-1} and also for a range of rate sensitivity exponents, n in Eq. (5.3.11), with values ranging from 0.1, 10 and 100.

5.4.2 Simple shear of a strip

A strip of elements with a height and length of 1 μm and 10 μm, respectively, was used with a strain gradient applied by linearly varying shear displacements applied on the top edge of the strip. It should be noted that, in the presence of a shear gradient, a normal strain/stress component along the shear direction arises as a result of equilibrium which deviates from a simple shear case to a complex case. The shear displacement on the strip was linearly proportional to the position along the X direction, Fig. 5.7 (a), which gradually increases to 10^{-2} μm in the top right corner and was applied over a time duration of 1 s which

corresponds to a maximum strain of 1% and a strain rate of 10^{-2} s^{-1}. The analytical value of the density of GND for this case was calculated by dividing the applied shear stress by the length of the strip and Burgers vector; $10^{-2}\mu m/(10\mu m \times 2.56 \times 10^{-4}\mu m) = -3.9\mu m^{-2}$. The edge dislocation density with a negative sign was obtained for a positive shear gradient along the slip direction, which was as expected [171]. Bunge angles to facilitate single slip were (-135, 35.2, 180) with a CRSS of 1 MPa and the remaining slip systems were deactivated, imposing a high value for CRSS (10^6 MPa). Both plane stress (CPS8) and plane strain (CPE8) elements were investigated.

Mesh convergence

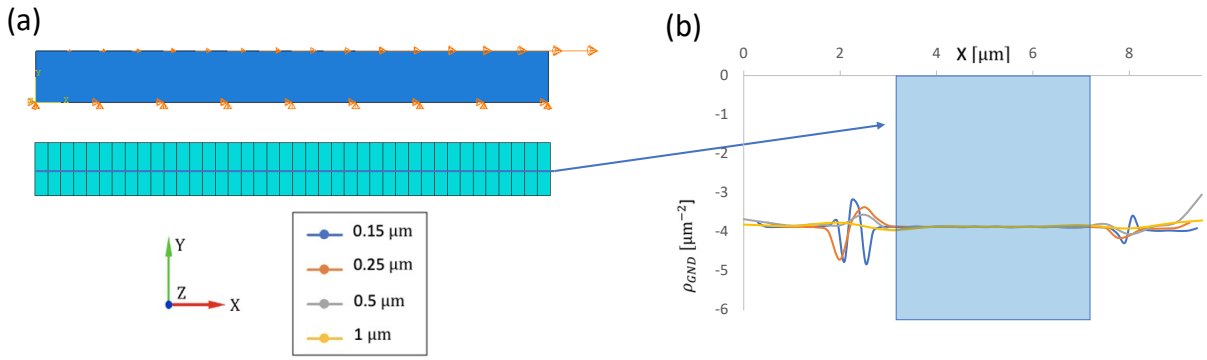

Figure 5.7: (a) Boundary conditions and mesh of strip of elements, (b) GND density distribution in the middle nodes for different mesh sizes of 1, 0.5, 0.25 and 0.15 μm and using GND model 1-c.

To conduct a convergence analysis, the GND density values were measured in the CPS8 elements for different mesh sizes. The density was plotted along the length of the strip (X-direction in Fig. 5.7(a)) using model 1-c for GND calculations.

Fig. 5.7(b) shows the convergence of GND density at the centre nodes of the strip for different mesh sizes. However, fluctuations were present at the two ends of the strip as a result of excessive shear distortions in the first and last elements. The GND density in the centre of the element was approximately the same in all simulations with an average magnitude of -3.85μm^{-2}, which is in excellent agreement with the analytical GND density of -3.9μm^{-2}.

GND model

Different GND models were compared using the same element type and for a converged mesh. Quadratic quadrilateral plane stress elements (C3PS8) with a mesh size of 1 μm were used. Fig. 5.8 shows the GND density in the active slip system. The GNDs on the remaining slip systems vanished for models 1-c, 2 and 3, while non-zero GND values were computed for models 1-a and 1-b for the inactive slip systems. Therefore,

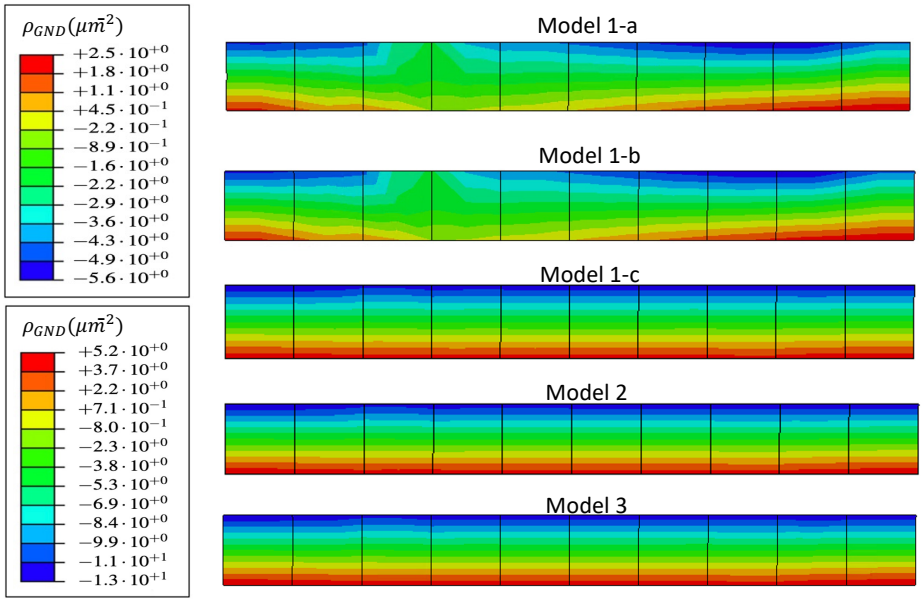

Figure 5.8: Average values of GND density for different GNDs models of the strip under a shear gradient for quadratic plane stress elements (CPS8): model 1-a, model 1-b, model 1-c, model 2, and model 3 after shear strain of $\sim$1% with a strain rate of 10^{-2} s^{-1}. The analytical solution is $\rho = -\frac{1}{b}\nabla\gamma \cdot \boldsymbol{s} = -3.9\mu m^{-2}$.

models 1-a and 1-b reveal nonphysical GND densities on inactive slip systems by either L2 minimisation (model 1-a) or KKT optimisation (model 1-b). Therefore, restriction of the solution of GND densities to the active slip systems, as for model 1-c, is essential to obtain physically relevant results.

The analytical solution for the density of GND reveals: $\rho = -\frac{1}{b}\nabla\gamma \cdot \boldsymbol{s} = -3.9\mu m^{-2}$. The results produced by GND models 1-a and 1-b show the same GND distribution, which is typical for the shear strain gradient, except for some elements. The GND density of models 1-a and 1-b in the middle of the elements was approximately constant having a value of $-1.94\mu m^{-2}$. GND models 1-c, 2, and 3 exhibited a constant GND distribution with $-3.85\mu m^{-2}$. Those were in excellent agreement with the analytical solution than that of the models 1-a and 1-b.

5.4.3 Uniaxial tension with strain gradient

A strain gradient without varying the externally applied load or displacement spatially is also possible by using a gradient geometry. To achieve that, [196] used a uniaxial load that was applied to a material with two slip systems in a double slip configuration. As a result of the varying cross section in the sample geometry, two slip bands formed in a cross shape with decreasing slip intensity as a function of the width of the sample thereby leading to the generation of strain gradients and GNDs.

Fig. 5.9(a) shows the geometry of the model used in this analysis. The tensile force along the Y-axis is uniform. However, varying the area, A, leads to a variation in stress along the Y-direction that results in

a stress/strain gradient. The strain gradient varies approximately according to: $\frac{F}{A} = \sigma = E\varepsilon \rightarrow \frac{-F}{EA^2}\frac{dA}{dy} = \frac{d}{dy}\left(\frac{F}{EA}\right) = \frac{d\varepsilon}{dy}$.

The cross-section area in the test sample was calculated as a function of position at the Y-axis according to: $A = (-2\sqrt{R^2 - y^2} + 2R + a)\,d$ where $y = 0$ was the narrowest location in the cross-section, $R = 12.5$ μm was the radius of curvature of the edges at the sides, $a = 5$ μm was the minimum value of the width, $A = 10$ μm was the maximum value of the width at $y = \pm 7.5$ μm, $d = 1$ μm was the thickness along the Z-axis, and $L = 25$ μmm was the total length.

The total vertical displacement of 0.1 μm was applied in a loading time of 1 s, corresponding to a total strain and a strain rate of 0.5% and 0.005 s^{-1}, respectively. The opposite face was fixed in the Y direction, and one of the corners was fixed in the X direction to prevent lateral displacement of the sample.

The slip system $\langle 1\bar{1}0 \rangle \{111\}$ was oriented with a 45 degrees angle with respect to the loading axis (Y direction) to facilitate single slip, Fig. 5.9(a), thereby giving Bunge angles of (-135, 35.2, -135). The active slip system had a CRSS of 1 MPa, while the remaining slip systems were deactivated by imposing a CRSS of 10^6 MPa. Plane stress quadratic quadrilateral elements (CPS8) were used.

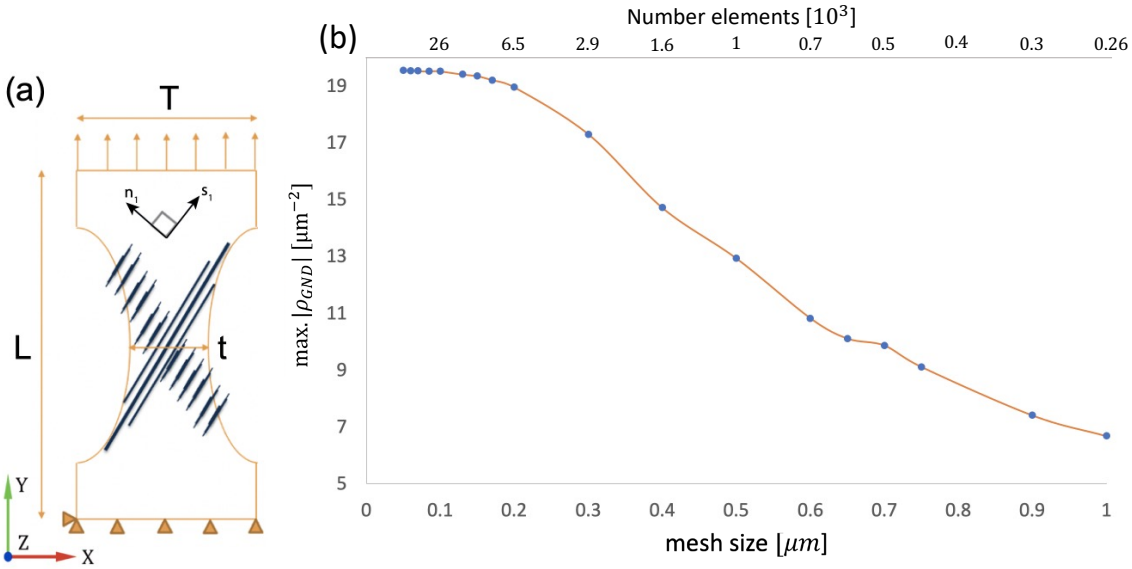

Figure 5.9: Uniaxial tension with a strain gradient sample geometry for quadratic plane stress elements (CPS8) (a) sample geometry and boundary conditions and (b) GND density convergence with mesh refinement.

Mesh convergence

The convergence study was conducted in the 2D model using model 1-c. Fig. 5.9(b) represents the maximum value of the GND density obtained based on the mesh size. The maximum GND density was used

as the measure for the convergence because it occurred at the centre of the sample and was consistently the same for both positive and negative GND bands.

GND density remains unchanged after the mesh size is reduced to 0.2 μm, with a maximum value difference below 1% compared to the finer mesh size of 0.05 μm, Fig. 5.9(b). Therefore, a mesh size of 0.2 μm was selected as the converged mesh and used for the simulations using models 1-c, 2 and 3. However, convergence was not achieved for models 1-a and 1-b for this mesh size. Therefore, the mesh size was $0.5\mu m^2$ for models 1-a and 1-b to give converged results.

Results

Figs. 5.10 illustrates the von Mises stress profile σ_{Mises}, the slip γ and the GND profile of model 1-a, 1-b and 1-c. The material is FCC, characterised by a single active slip system, while the remaining systems remain inactive.

Model 1-a and 1-b exhibited highly irregular profiles for von Mises stress, slip and GNDs. These results were characterised by noise between elements and the mergence of unphysical GNDs in inactive slip systems. This last anomaly is attributed to the optimization process, which minimizes $\sum \rho^2$ but neglects physical constraints such as the CRSS. A detailed analytical explanation of how these GNDs form in materials with a single slip system is provided in Appendix B.2.

The noise observed in the slip and GND maps was investigated in relation to mesh size and the precision/convergence tolerance of the crystal plasticity solver. We conclude that the cause was the interaction between forest hardening (hardening that occurs between slip systems, see Subsec. 5.3.2) and the calculation of GNDs in inactive systems. Further details are available in Appendix B.3. After the elimination of the forest hardening term, we observed that the noise disappears, however, the problem of the apparition of GNDs in inactive slip systems remains.

Figs. 5.10(c,g,j) showed the results of model 1-c. The slip map (g) shows a deformation in the form of a cross-shaped shear band [196]. This geometry arises because the Schmid tensor does not differentiate between the slip direction and normal slip plane; therefore, there is no distinction between a slip band and a kink band [197]. At small deformations, the total slip γ, remains symmetric. However, as strain increases ($\sim$3% of strain), kinematic constraints and rising GND density lead to a loss of the symmetry. The von Mises stress distribution (c) follows a similar cross-shaped profile. While stress concentrations are present at the corners, they remain insufficient to activate further slip systems.

Regarding the GND density (j), we appreciate two equal bands of positive and negative GNDs along one of the diagonals of the slip band with cross-shaped. The amount of slip, γ, was similar in both diagonals,

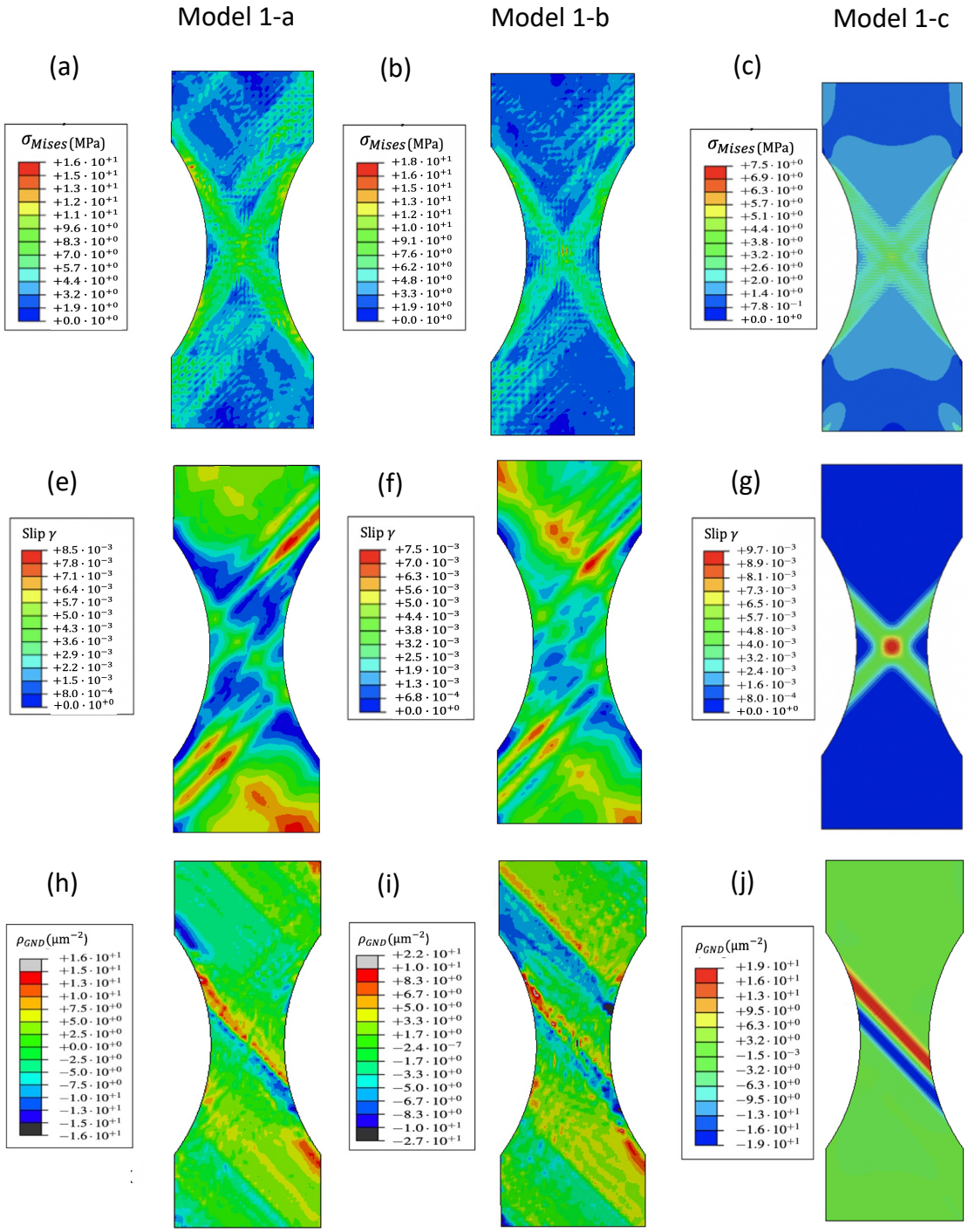

Figure 5.10: Distributions of von Mises stress (a,b,c) total slip (e,f,g) and edge GND density (h,i,j) of the system $\langle 1\bar{1}0\rangle$ $\{111\}$. The results are obtained using models 1-a,1-b,1-c.

but the orientation of the slip gradient was different. Fig. 5.9(a) shows a schematic illustration of the slip distributions. The stress in the centre of the specimen is highest due to the gradient geometry. The distribution of the slip was determined on the basis of the direction of the active slip system, $\boldsymbol{s}^1$ and the stress.

The density of the edge dislocations was calculated analytically using the amount of slip over a path parallel

to the direction of slip, Fig. 5.11(a). The slip gradients ($\rho^a = -\frac{1}{b^a}\nabla\gamma^a \cdot s^a$) were used for the analytical calculation. Fig. 5.11(b) shows the quantity of GND density to compare the analytical solution and that of model 1-c, which was shown in Fig. 5.11(c). The relative difference between the analytical solution and the GND model 1-c did not exceed 17%, as illustrated in Fig. 5.11(d).

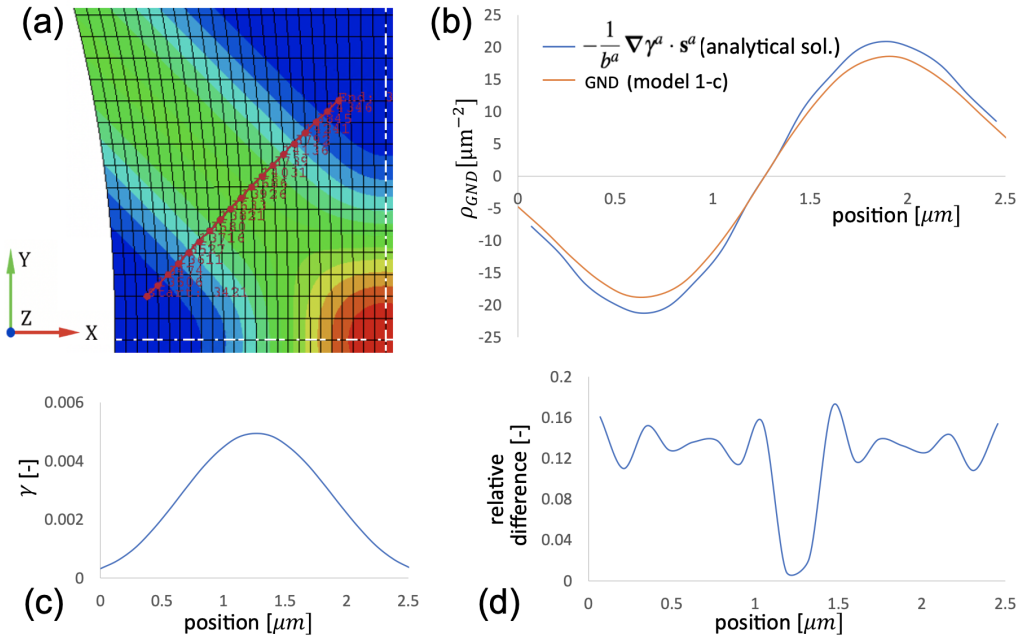

Figure 5.11: (a) Path across the slip band for the GND plots (colour scale is the same as in Fig. 5.10(a)), (b) GND density profile, (c) slip profile along the path, and (d) relative error between theory and model 1-c.

The model 1-c obtained the same GND density map using linear and quadratic interpolation functions. The model 2, and model 3 revealed the same results, showing the two dislocation bands and the slip band with a cross shape. The simulation times for the mesh with 6500 CPS8-type elements (with a mesh size of 0.2 μm) were compared. Models 1-a and 1-b exhibited computation times that are approximately eight times greater than the rest of the models. This was attributed to the GNDs in inactive slip systems that caused excessive strain hardening in the primary system and resulted in poorer convergence behaviour of the crystal plasticity scheme.

5.4.4 Four-point bending

The four-point bending case has been extensively used to investigate the size dependence based on strain gradients because the strain gradient within the beam can be well established in the form of a linear variation toward the neutral axis, which implies a constant density of GND [198, 199]. The finite element model shown schematically in Fig. 5.12 is similar to reference [200]. The half-beam dimensions of length, thickness and width were 200 μm, 20 μm, and 2 μm, respectively. The beam was supported and displacement

loaded by rigid solid bodies (circles or cylinders) at distances of 10 μm and 40 μm from the free end, respectively. Using the symmetry axis normal to the X axis on the left end of the beam (u_x = 0), half of the beam was simulated. The beam displacements were applied over 20 s time intervals, giving a total bending strain of 0.75% and a strain rate of 3.75×10^{-4} s^{-1} for positive/negative bending and straightening. Bunge angles were (-135, 35.2, -135) with respect to the X-Y-Z axis shown in Fig. 5.12 such that the slip system $\langle 1\bar{1}0 \rangle$ $\{111\}$ makes 45 degrees with the neutral axis of the beam and the slip plane normal was perpendicular to the width axis of the beam (Z axis in Fig. 5.12 (a)), thus a single slip can be facilitated. The active slip system had a CRSS of 1 MPa, and the remaining slip systems were deactivated by imposing a CRSS of 10^6 MPa.

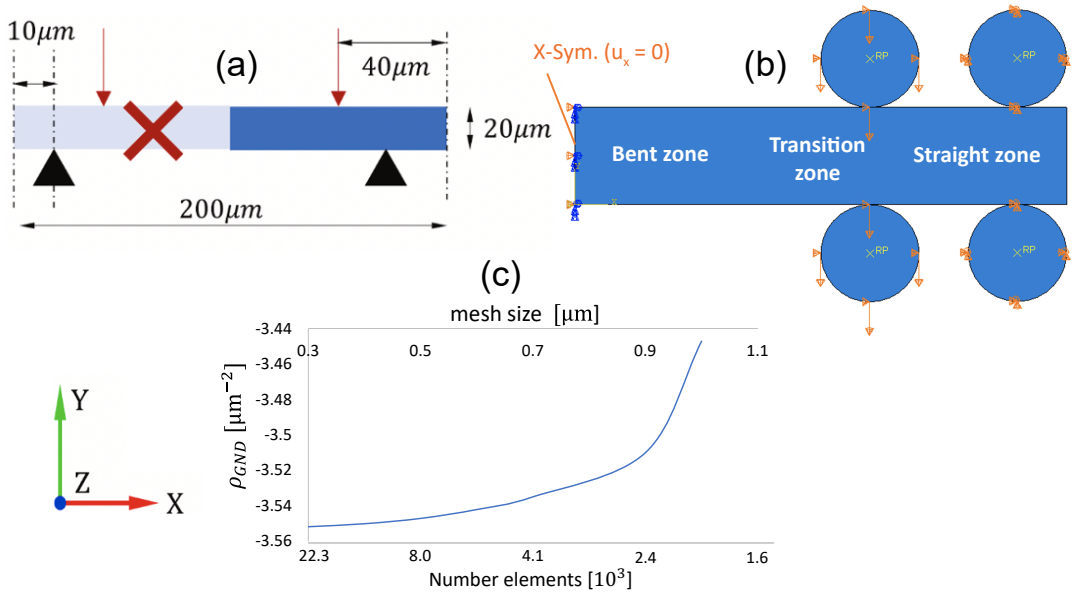

Figure 5.12: Four-point bending (a) beam dimensions and symmetry (the red cross sign indicates the neglected portion of the beam using symmetry), (b) boundary conditions based on [200], and (c) mesh convergence based on model 1-c.

Four-point bending was achieved using rigid bodies with a radius of 10 μm. The deformation was induced through three stages to investigate GND formations after positive bending and straightening, followed by negative bending.

As explained previously, GND formation can be positive or negative; the notation used in all models was based on [171, 200], which defines the slip gradient along the slip direction as a negative edge-type GND.

In the *positive bending* stage, end displacement of u_y = -1 μm was applied in the Y direction using the rigid body located to the top left of Fig. 5.12 (b), while the rigid bodies on the right were fixed. The rigid body on the bottom left also moved with a displacement of u_y = -1.1 μm in the Y direction to prevent contact with the beam.

In the *straightening* stage, the direction of the load was reversed. The rigid body on the bottom left moves with u_y = 1.1 μm when straightening the beam, while the rigid body on the top left moves with u_y = 1.2 μm, disengaging from the beam.

In the *negative bending* stage, the rigid bodies on the left side displace an additional u_y = 1 μm compared to straightening, causing the beam to bend in the opposite direction. The rigid bodies on the right remained fixed along both the X and Y directions throughout the deformation.

Mesh convergence

The convergence study in 2D was conducted for quadratic quadrilateral plane stress elements (CPS8). In this case, the maximum value of the GND density was not taken into account (as was the case in the convergence study of uniaxial strain gradient) because this value occurred at the contact point between the rigid bodies and the beam that is outside of the bent zone. Therefore, the average value of the density of the GND on the left face of the beam (in the bent zone) was used as the convergence measure.

Fig. 5.12(c) shows the average value of the GND densities that were obtained after positive bending, as a function of the element size using model 1-c. The results had approximately 3% difference from each other. Therefore, the mesh size was selected as 0.5 μm for the four-point bending simulations.

Results

The beam was divided into three different zones based on the main characteristics of the deformation, Fig. 5.12(b), similar to the experimental and simulation findings in [199]. The bent zone is the region of greatest interest in four-point bending tests. The straight zone is in between the rigid bodies and does not significantly bend; as a consequence, no significant GNDs were produced with the exception of the contact regions with the rigid bodies. The transition zone exhibits the highest strain gradients and hence the highest GND densities.

Fig. 5.13 shows an overview of von Mises stress, total slip, and GND density distributions calculated using model 1-c for a 2D simulation with 8000 quadratic quadrilateral (CPS8) elements.

After positive bending, the von Mises stress distributions in the bent zone had an expected distribution for bending while local stress concentrations were present at the upper-left and lower-right rigid body contact locations. The slip profile was similar to the one described in the literature [200], with the bent zone being particularly important as the slip increases steadily from bottom to top. This results in a nearly constant GND density in the bent zone that ranges from -3μm^{-2} to -3.7μm^{-2}, the highest variations occur close to the transition zone and in the neutral axis where there is a discontinuity in the GND profile. The

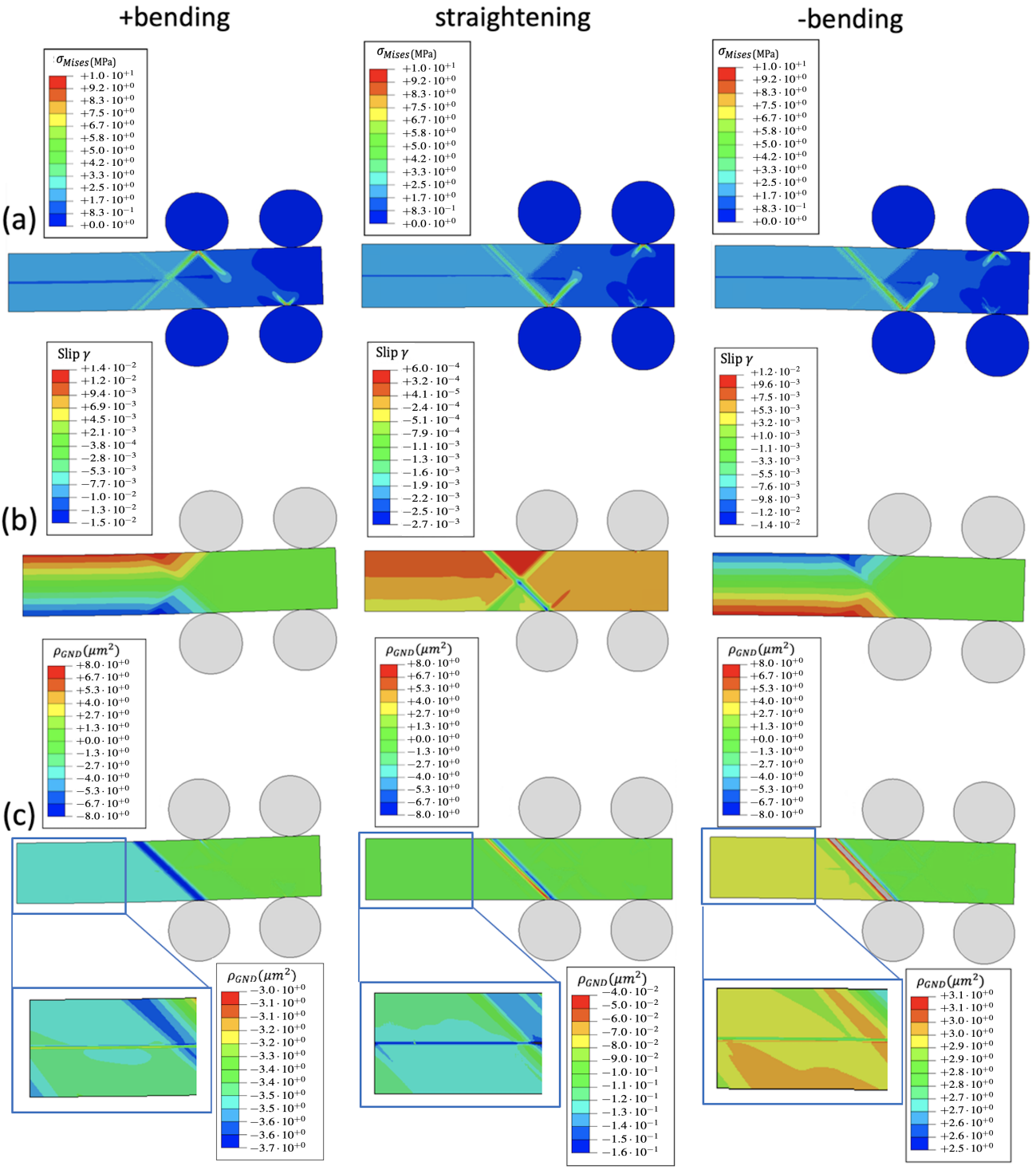

Figure 5.13: (a) von Mises stress, (b) total slip γ, and (c) ρ_{GND} after positive bending (left-most column), straightening (mid-column), and negative bending (right-most column) with a bending strain of 0.75%, strain rate of 3.75×10^{-4} s^{-1} and using model 1-c.

discontinuity arises from the non-slip condition on the neutral axis, while the slip gradient was present due to bending. In the transition zone, a band of negative GNDs with a density of ~-8.06 μm^{-2} was observed, which was related to the change in curvature between the bent and straight zones, where the density of GND

almost vanished because there was no strain gradient.

After the straightening, the calculation of the GND density becomes approximately zero, which indicates recombination of negative GNDs with the accumulating positive GNDs upon straightening. A stress profile similar to positive bending was observed, with the highest concentrations of stress present at the contact locations of the rigid bodies with the beam, specifically the lower left and upper right rigid bodies. The presence of residual stress was observed in the contact region of the lower right rigid body, which was no longer in contact with the beam. Again, the amount of slip was reduced by several orders of magnitude, approaching nearly zero after straightening. Similarly, the GND density in the bent zone had values ranging from -0.04 μm^{-2} to -0.16 μm^{-2}, the lowest value being on the neutral axis (a region particularly difficult to calculate since the slip is 0). However, in the transition zone, the band of negative GNDs did not completely disappear. Instead, a parallel band of positive GNDs was generated with a density of 7 μm^{-2} was generated adjacent to the negative band.

After the negative bending, a positive GND density in the bent zone was expected. The von Mises stress distribution remained similar to that after straightening. The slip profile was also quite similar to that after positive bending, but with the sign reversed. In the transition zone, the negative band of the GNDs was reduced to approximately -5 μm^{-2}, while the positive band increased to almost 15 μm^{-2}. The density of GND in the bent zone ranges from 2.5μm^{-2} to 3.1μm^{-2}. Negative GNDs disappear when the curvature changes. However, in regions where the deformation was higher (such as the transition zone or the contact zone with the rigid bodies), some negative GNDs persist after negative bending.

GND model (2D)

Fig. 5.14 compares the the different GND models after negative bending. Models 1-a and 1-b reveal similar results: von Mises stress, slip and GND bands are oriented along the slip direction and slip plane normal. This forms a noisy pattern and the emergence of GNDs in slip systems that should remain inactive. The bands aligned with the slip direction contain both positive and negative GND densities, with higher values in the regions with more slip γ. The bands in the normal direction exhibit positive GND densities, as expected considering the sign of the curvature. High GND densities are observed at the end of the beam where the curvature was greatest, as well as along the band located between the two leftmost rigid bodies, which is consistent with the other models.

As in the previous case (Uniaxial tension with strain gradient 5.4.3), the noise was caused by a combination of erroneous calculus of GNDs in inactive slip systems and forest hardening (explained in Appendix B.2 and B.3). In Models 1-a and 1-b, the GND densities on inactive slip systems represent 20-30% of the GND

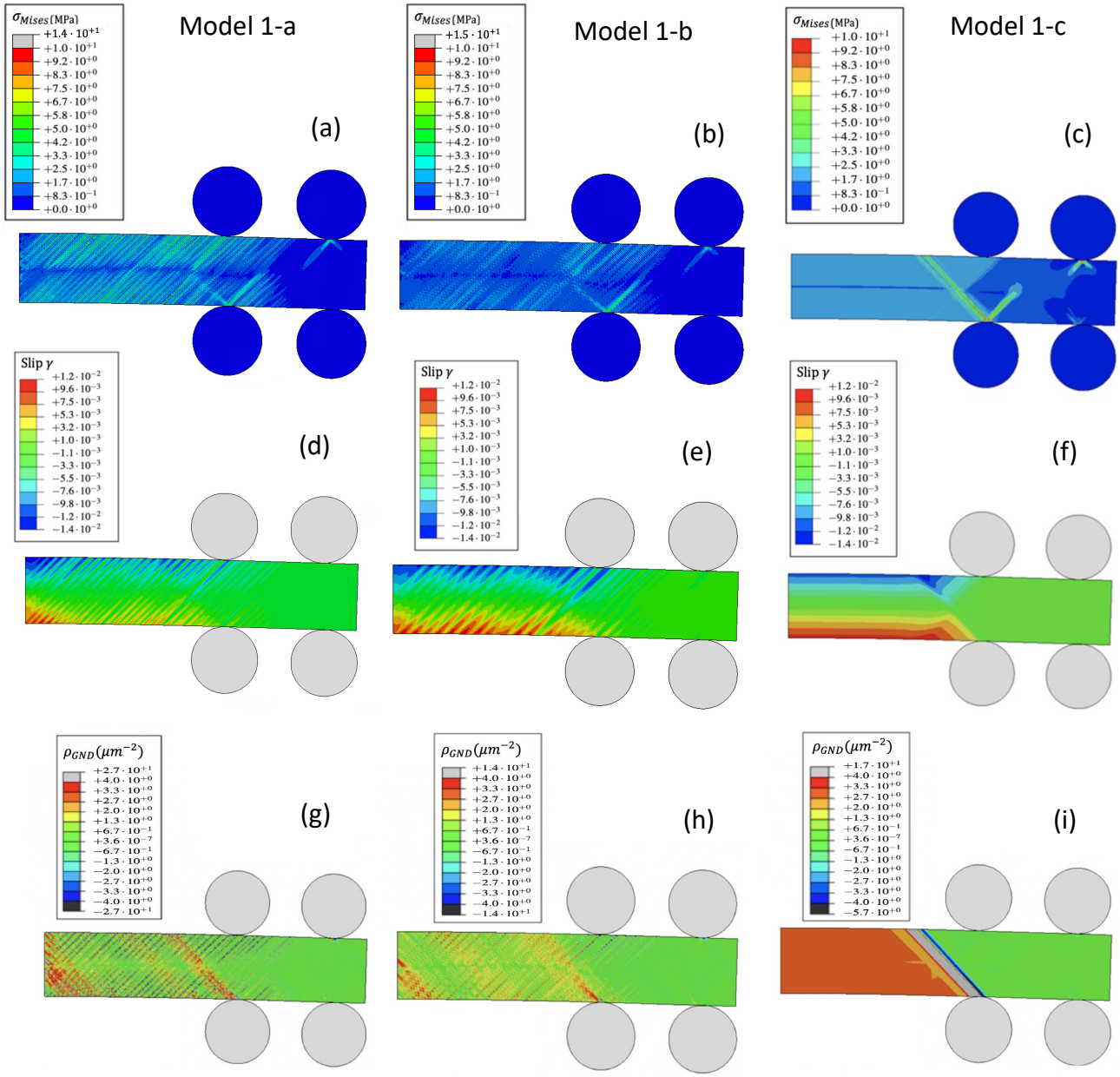

Figure 5.14: Distribution of von Mises stress (a,b,c), slip (e,f,g) and GND density (g,h,i) of the system $\langle 1\bar{1}0 \rangle \{111\}$ after negative bending for different GND models: model 1-a, 1-b, and 1-c.

densities of the active slip systems.

Models 1-c, 2, and 3 give the same 2D GND profile similar to the uniaxial tension case. Path plots of the GND density along the thickness directions (Y-axis) and length directions (X-axis) were included for more detailed comparison. The findings for models 1-a and 1-b are shown separately in Figs. 5.15(b)-(d)-(f) due to noise resulted in these models for clarity.

In Fig. 5.15(a), the horizontal path after the negative bending shows a density of positive GND density in all models (consistent with the curvature). Models 1-a and 1-b exhibited a density profile with oscillations, with the maximum GND density value located at the left face of the beam, which gradually decreases towards

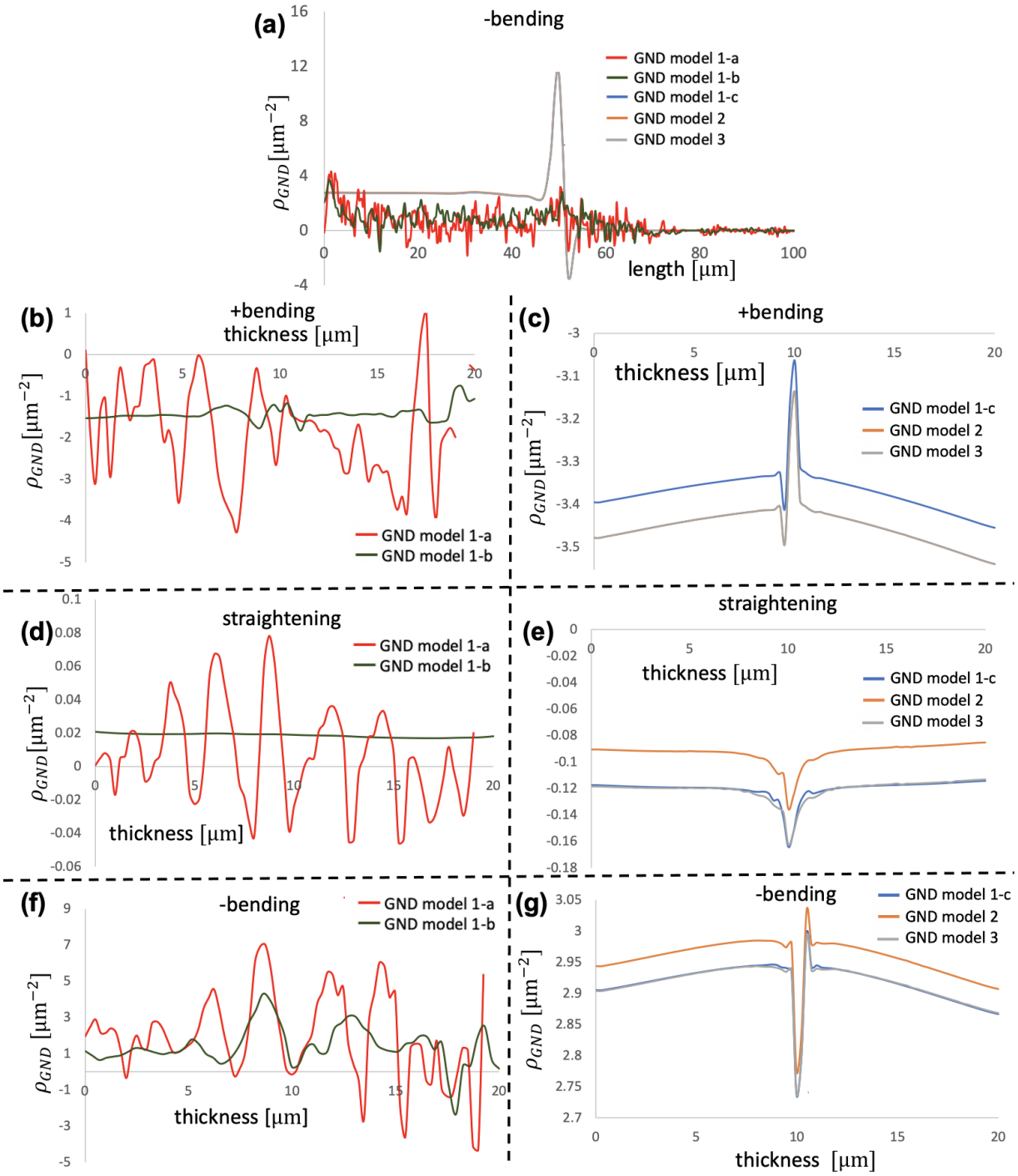

Figure 5.15: GND density vs. (a) length after negative bending for all of the models, (b) thickness for models 1-a and 1-b after positive bending, (c) thickness for models 1-c, 2 and 3 after positive bending, (e) thickness for models 1-a and 1-b after straightening, (f) thickness for models 1-c, 2 and 3 after straightening, (g) thickness for models 1-a and 1-b after negative bending, (h) thickness for models 1-c, 2 and 3 after negative bending.

the zone between the rigid bodies where the beam possesses no curvature. In the transition zone, there was a second peak of positive GND density followed by a decrease until the value reached zero. In models 1-c, 2, and 3, a constant GND density was computed throughout the bent zone until it reached the straight zone.

The transition zones posses two bands with high density of positive and negative GNDs, while the straight zone had zero GND density.

GND density changed its sign to negative values after positive bending, as expected, Fig. 5.15(b) and (c). Model 1-a exhibited a large number of oscillations, even reaching positive values (1 μm^{-2} at thickness position of 17 μm). The GND density obtained from model 1-a differs by 48% with respect to that of models 1-c, 2, and 3. Model 1-b was more consistent, which is consistent with the theory of the four-point bending test, but it still differs by 61% from model 3. In contrast, models 1-c, 2, and 3 show almost constant GND density values that are in perfect agreement with the analytical solution (-3.4 μm^{-2}) within the bent zone. The largest difference was 10% from the average value and occurred at the central axis of the beam where the amount of slip, γ, changed sign, suggesting a possible distortion in the elements in that region. The remaining findings were very similar, revealing a difference in the GND density of less than 2%.

Figs. 5.15(d) and (e) show GND density variations along the thickness direction after straightening. Model 1-a exhibited positive and negative oscillations, while model 1-b shows a constant profile, with both profiles having nearly zero densities. However, models 1-c, 2, and 3 exhibited a low residual constant density of approximately -0.1 μm^{-2}.

Figs. 5.15(f) and (g) show GND densities along the thickness direction after negative bending. Model 1-b revealed an inhomogeneous profile, while it became quite homogeneous after negative bending (Fig. 5.15(b)) and after straightening (Fig. 5.15(d)). This behaviour was attributed to high sensitivity to initial conditions (preexisting GND). The average difference with respect to the model 3 value is 44% for model 1-a and 62% for model 1-b. However, models 1-c, 2, and 3 exhibited almost the same constant value of 2.9 μm^{-2}, which was slightly different from the analytical value of 3.4 μm^{-2}. The analytical value of the GND density was computed on the basis of the slip gradients. GND density annihilates upon load reversal, while leaving a certain amount of residual strain and GND density.

Comparison of 2D and 3D models

A 3D finite element model consisting of 32,000 quadratic hexahedral elements (C3D20) was used to provide a comparison to the plane stress simulations. The GND distributions were similar for 2D and 3D, being nearly homogeneous along the Z-axis, highlighting a good match between 2D and 3D models, Fig. 5.16. However, higher stresses were observed in 3D at the contact zone between the rigid bodies and the bar, and a band of positive and negative GNDs appears in the upper-right corner of the bar. This is related to both the upper and lower rigid bodies that must remain in contact constantly with the specimen to prevent displacements along the Z-axis after positive bending, straightening, and negative bending.

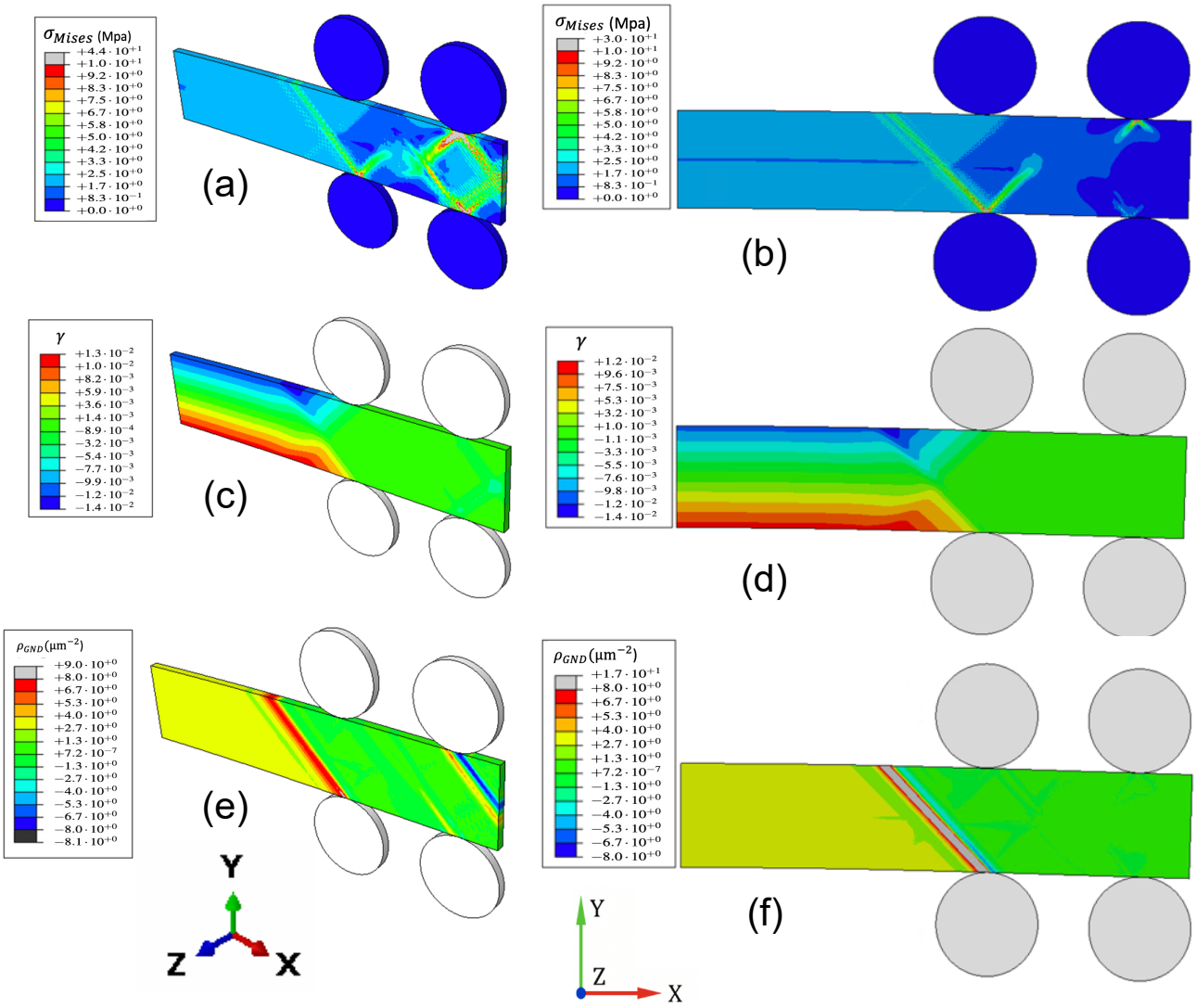

Figure 5.16: von Mises stress distributions in (a) 3D and (b) 2D; total slip in (c) 3D and (d) 2D; GND density in (e) 3D and (f) 2D. GND model 1-c is used in the simulations.

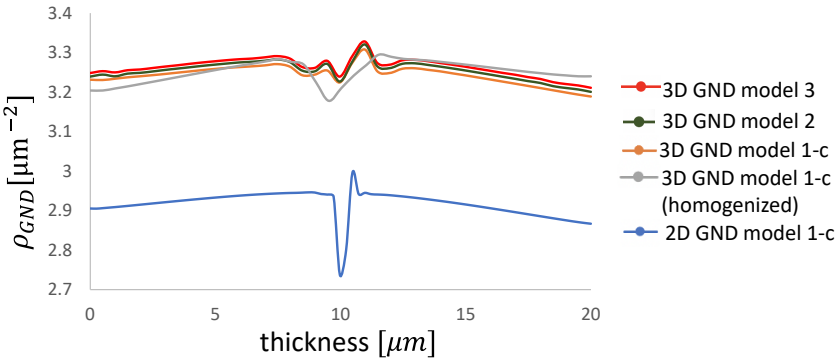

Figure 5.17: GND density along thickness for 2D and 3D simulations using model 1-c.

The bent zone had almost identical GND densities in both the 2D and 3D models. The difference was greater near the rigid bodies. For example, the negative GNDs after positive bending remain during straightening for the 2D model. However, these differences have minimal impact on the bent zone.

Fig. 5.17 shows the GND density along the thickness direction on the left face of the beam after negative bending for the 3D case, including different GND models. The results were compared with the 2D sample using model 1-c. In all cases, a nearly constant profile with an oscillating zone was observed at the neutral axis of the specimen which occurs because of the presence of a slip gradient but no slip. The GND density in the 3D specimen was approximately 10% higher, the difference can be attributed to the selected dimensions, that is, deviation in the boundary conditions can cause different behaviour between 3D and 2D models (plane stress), especially close to the end of the cantilevered beam at which the X-symmetry condition was applied. Fig. 5.17 also compares different GND models in the 3D specimen. The differences were negligible (less than 1%). In addition, there was no significant difference in the computation time between all cases.

Finally, the homogenisation method of the element was studied using model 1-c. In this method, the gradient was computed in the centre of the element instead of separately for IPs. A similar result with approximately 1% difference in the bent zone was obtained when homogenisation was used. The only notable difference was that the homogenised solution exhibited fewer oscillations in the bent zone. Furthermore, no significant improvement in computation time (5% faster) was observed.

5.4.5 Polycrystal

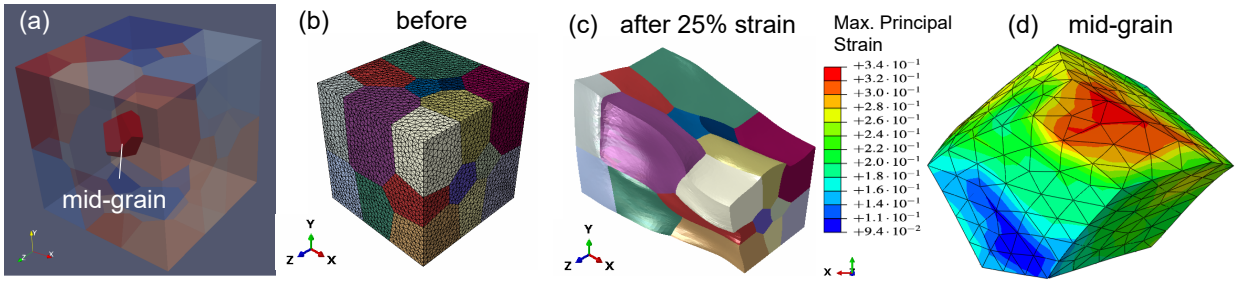

Figure 5.18: (a) Polycrystal RVE with the mid-grain, (b) RVE and mesh before straining, (c) deformed geometry after 25% uniaxial strain, and (d) maximum principal true strain after 25% uniaxial strain for model 1-c (the models 1-d, 2, and 3 are all approximately 0.2% different, hence not included).

In this section, we quantitatively investigate the absolute and relative errors associated with the lattice incompatibility of different models. Numerous studies are in the literature investigating the effect of grain size [201, 163, 202, 203, 204, 205] using various CP-based finite element modelling approaches, but our intention here is slightly different: to examine the evolution of GND in the middle of a *representative volume element* RVE of a polycrystal that possesses realistic stress states.

A polycrystal with 30 grains was generated using NEPER® software [206] and meshed with quadratic tetrahedral elements (C3D10) with four integration points per element. The mesh consisted of 165,968

elements. Each grain contained more than 1000 elements which is consistent with [207], and the grain located in the centre of the RVE (mid-grain) contains 1,308 elements. A uniaxial macroscopic tensile strain of 25% was applied with a strain rate of 2.5×10^{-3} s^{-1}. GNDs were computed using the linear form of the shape functions for GND models 1-c, 1-d, 2, and 3. GND models 1-a and 1-b were excluded from this analysis based on the findings in Subsect. 5.4.1-5.4.4 because they give inconsistent results, resulting in significant strain hardening and convergence issues in case anisotropy in the strain hardening of slip systems was considered as in this study.

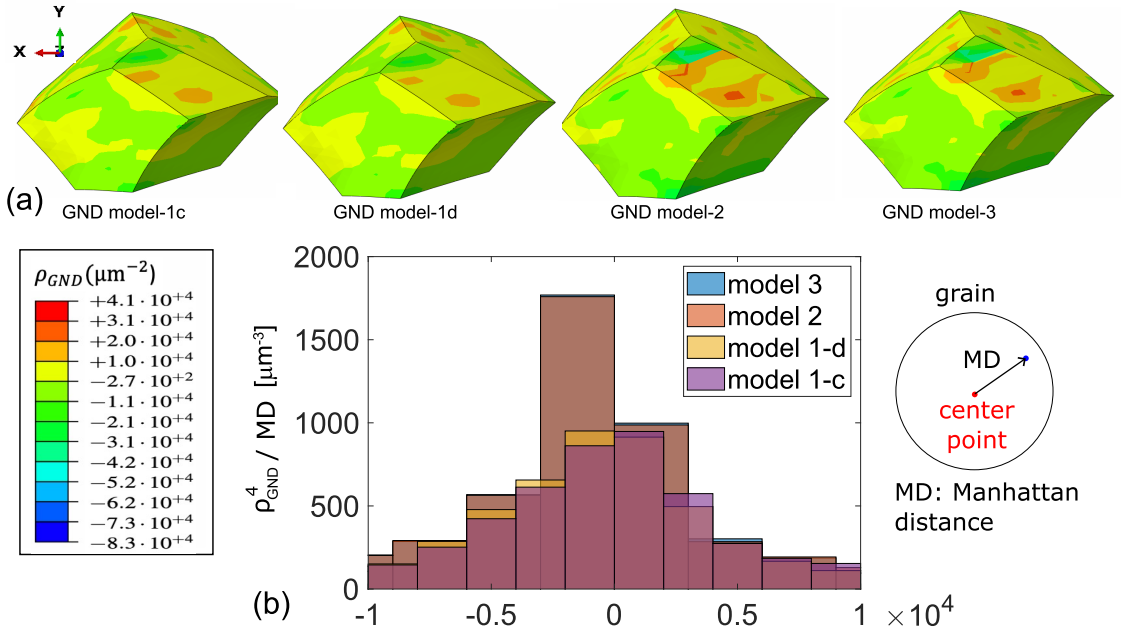

Figure 5.19: Edge dislocation density in the most active slip system (slip system-4), $[110]\,(\bar{1}11)$, in the mid-grain for four different GND models at the end of 25% uniaxial tension: (a) contour plots (legend is shown on the bottom-left corner) and (b) GND density (in the most active slip system, slip system-4) histogram normalised by the Manhattan distance.

Fig. 5.18 shows the polycrystal RVE with the centre grain in which the effect of different GND models was investigated. Simulations were performed using a 2.4 GHz Intel E5-2680 v4 CPU on a total of 20 threads. The simulation durations for models 1-c, 1-d, 2, and 3 were 41.09, 42.11, 37.01, and 37.03 hours, respectively. The simulation time for the total form with and without deformed area correction (e.g., models 1-c and 1-d, respectively) was not significantly different from each other, similar to the simulation time for the models using the rate form and slip gradient (models 2 and 3). However, due to the inversion required to find the density of the GND using the SVD method, models 1-c and 1-d took approximately 14 % longer than both the rate form and the slip gradient models in which the GND densities were obtained from simple vector projections.

Fig. 5.19 is obtained from the distribution of edge type of dislocations on the most active slip system (4th slip system $[01\bar{1}](01\bar{1})$) for comparison. Although the GND density distributions in Fig. 5.19(a) were quite

the same on the surface plots, the GND density at the 5232 integration points of the midgrain had a wide range of scatter. The average GND values were calculated to be 2828, 2643, 3194, and 3102 μm^{-2} for models 1-c, 1-d, 2, and 3, respectively. The difference between model 1d (which considers changes in area / flow with plastic deformation) with respect to model 1c was approximately 20% on average. Similarly, the GND density obtained by the rate form and the slip gradient (models 2 and 3) differs from the total form (model 1-c) by almost 88%. Models 1-c and 1-d reveal the lowest average GND densities in the midgrain which were closest to the minimum energy configuration making them the best approach.

The histogram plot in Fig. 5.19(b) shows the edge type GND density in slip system $[01\bar{1}](01\bar{1})$) normalised by the Manhattan distance. The GND density was normalised by the Manhattan distance to compensate for increasing numbers of integration or data points with increasing distance from the center of the grain to obtain a more representative histogram. The distribution was consistent for the models 1-c and 1-d as well as for models 2 and 3. The higher magnitude of GND density was concluded for models 2 and 3 compared to models 1-c and 1-d, suggesting better findings for models 1-c and 1-d.

The absolute and relative incompatibility errors were obtained by recalculation of incompatibility using the computed by GND densities with Nye's tensor. This error was a result of the effects of SVD inversion for the total forms, the neglected component of GND (edge dislocations along the slip plane normal), the accumulated errors in the rate form and the assumption of small strain for the slip gradients. The higher error in both rate forms is consistent with the findings in [208].

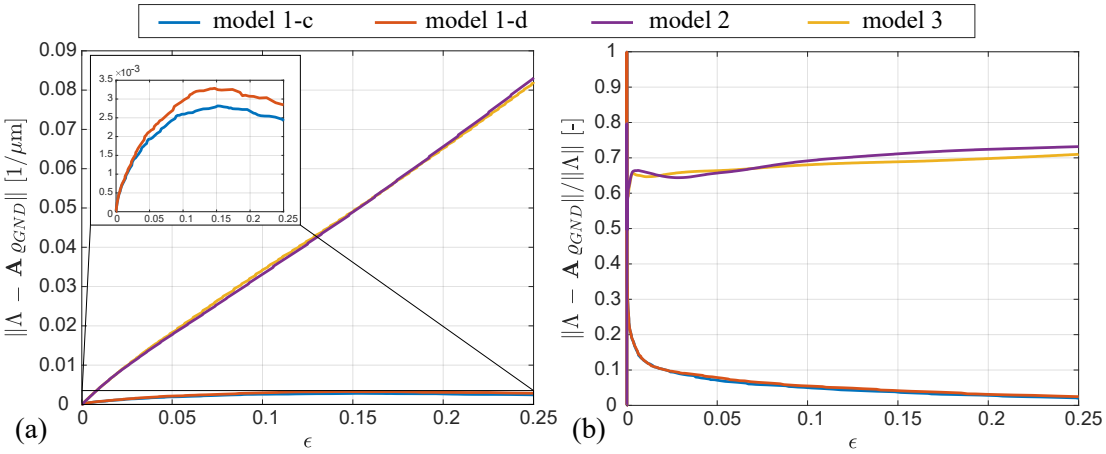

Figure 5.20: Incompatibility error: (a) absolute and (b) relative average over the mid-grain vs. uniaxial strain for total form without area correction (model 1-c) and with area correction (model 1-d), rate form (model 2), and slip gradients (model 3). The relatively lower absolute errors for models 1-c and 1-d are presented within the subplot in part (a).

Fig. 5.20 shows the comparison of the average norm of the incompatibility error that was obtained at all IPs in the mid-grain using GND models 1-c, 1-d, 2, and 3. The absolute and relative errors associated with the rate form (model-2) and the slip gradient model (model-3) were greater relative to the total forms. The

difference was approximately two orders of magnitude higher than that of both total forms (models 1-c and 1-d), which could be linked to the accumulation of numerical errors over time. In addition, neglecting the $\dot{\rho}^{a}_{GND,en}$ term in Eq. (5.3.51) also contributes to this error. However, both total forms using a restricted solution to the active slip systems followed by SVD and inversion reveal relatively low differences, even though the error is averaged over the grain. The area correction reveals an additional 1.5 % absolute error on average with respect to model 1-c while the relative errors were quite close between models 1-c and 1-d. Therefore, in an explicit GND calculation scheme, the total form of incompatibility measure appears to offer superior numerical accuracy rather than the rate forms because the total forms model 1-c or model 1-d reveal the least amount of error, consistently representing the incompatibility.

In Fig. 5.20(b), the relative error originates from the value of unity because of the initial threshold used for the GND densities. There was a small value of incompatibility present initially, which did not exceed the GND density threshold, thereby leaving GND density as zero and giving a relative error of unity (100% error), rather than zero at the start of the analysis.

Fig. 5.20 shows the average results over the mid-grain, which is the most representative location in a polycrystal because it has the most realistic stress state, uninfluenced by the boundary conditions defined at the edge of the FE model. The average error at the integration points becomes approximately zero for model 1-c and model 1-d for some IPs thus these models are most able to capture the incompatibility while providing physically realistic GND densities.

5.5 Conclusions

In this study, we investigate and compare several widely used incompatibility measures and GND calculation procedures in a crystal plasticity-based finite element framework to investigate widely used incompatibility measures. The important conclusions are outlined as follows:

- The total form of incompatibility, $(-\nabla \times \boldsymbol{F}_p)^T$ that has been used to compute GND densities in conjunction with the L2 method revealed GNDs on the inactive slip systems; leading to excessive and erratic strain hardening which also added solution convergence difficulty. The restriction of GNDs only to the active slip systems, followed by SVD and inversion allowed for a more physical calculation of GND density. The other rate form of incompatibility, $-\nabla \times \dot{\gamma}^{a}\, \boldsymbol{n}^{a}\, \boldsymbol{F}_p$, and that based on slip gradients, $\nabla \dot{\gamma}^{a}$, do not have this problem and only reveal GNDs on the active slip systems.

- A small numerical difference in the slip between the material points leads to formation and accumulation of fictitious GND densities. These artificial GNDs lead to misrepresentation of simple cases

such as strain-gradient-free uniaxial tension of cube orientated single crystal under rotation-free symmetric loading. A threshold for the minimum value of the strain gradients is found to be essential for all of the GND methods investigated in this study which was overlooked in previous studies.

- Single crystal and single slip deformation cases of simple shear, uniaxial tension with and without strain gradients, and four-point bending were investigated to test the GND calculation method. The restriction of GND solution to the active slip systems have led to the more physically representative GND densities in all these cases. The total form with solution restricted to active slip systems, followed by SVD and inversion, reveals very similar results to the rate form and the slip gradients at small deformations.

- Polycrystal simulations at large strains revealed significantly lower densities for the total form than the rate form and slip gradients. This is due to the explicit calculation of GNDs for all the methods and incremental calculation leading to the error accumulation over time for the rate forms due to the redundancy in the definition of screw dislocations as explained in [208].

- The incremental forms (rate form and slip gradients) lead to approximately two orders of magnitude higher incompatibility error relative to the total forms. This is due to: one of the GND terms that was neglected in the rate form (model 2), slip gradients (model 3) being only valid for small strains, and the error accumulation due to the nature of the incremental/rate forms (models 2 and 3). The total forms (models 1-c or 1-d) reveal the minimum amount of incompatibility error, making them the best alternative to compute GNDs.

Future studies will involve experimental validation of the theory presented by single-crystal experiments that involve strain gradients, such as microcantilever beam bending and nanoindentation, as well as polycyrstal tests in which strain gradients arise naturally due to anisotropy.

5.6 Statement of Authorship form

Statement of Authorship for joint/multi-authored papers for PGR thesis

To appear at the end of each thesis chapter submitted as an article/paper

The statement shall describe the candidate's and co-authors' independent research contributions in the thesis publications. For each publication there should exist a complete statement that is to be filled out and signed by the candidate and supervisor **(only required where there isn't already a statement of contribution within the paper itself).**

Title of Paper	Restraining geometrically-necessary dislocations to the active slip systems in a crystal plasticity-based finite element framework
Publication Status	☐Published ☐ Accepted for Publication ☐Submitted for Publication ☐Unpublished and unsubmitted work written in a manuscript style
Publication Details	Demir, E., Martinez-Pechero, A., Hardie, C., & Tarleton, E. (2024). Restraining geometrically-necessary dislocations to the active slip systems in a crystal plasticity-based finite element framework. *International Journal of Plasticity*, *178*, 104013.

Student Confirmation

Student Name:	Alvaro Martinez Pechero
Contribution to the Paper	The student is the second author of the article and made significant contributions: • He revised and supported the design of the code framework, assisting the main author, Dr. Eralp Demir, with aspects such as crystal-to-sample rotations, plane-stress elements, slip laws, and convergence issues. • He co-developed the formalism and implementation of the Geometrically Necessary Dislocations (GND) calculus method based on a pseudo-inverse matrix with Dr Eralp Demir. • He designed simulations and the theoretical formalism, and wrote sections to validate the GND calculus methods, including: strain-gradient-free uniaxial tension, simple shear of a strip, uniaxial tension with a strain gradient, and four-point bending. • He identified an issue with GND activation in inactive slip systems based on the simulations he designed, which prompted the team to develop an improved model that restricts GND activity to active slip systems (the last model design was the result of team discussions). Dr. Eralp Demir was responsible for creating the framework, implementing the remaining GND models, and designing the polycrystal simulation. Dr. Chris Hardie and Prof. Edmund Tarleton were responsible for funding, model improvement, and supervising the project.
Signature	Date: 28th July 2025

Supervisor Confirmation

By signing the Statement of Authorship, you are certifying that the candidate made a substantial contribution to the publication, and that the description described above is accurate.

Supervisor name and title: Professor Edmund Tarleton		
Supervisor comments		
Signature	Date	1st August 2025

This completed form should be included in the thesis, at the end of the relevant chapter.

Chapter 6: Modelling the Bauschinger effect in copper during preliminary load cycles

Chapter 6 of the thesis is based on the publication in the Journal Acta Materialia, titled "Modelling the Bauschinger effect in copper during preliminary load cycles", Martinez-Pechero, A., Demir, E., Hardie, C., Zayachuk, Y., Widdowson, A., & Tarleton, E. (2025), available at: https://www.sciencedirect.com/science/article/pii/S1359645425001788. For the statement of authorship, refer to Section 6.9.

This chapter presents an application of Geometrically Necessary Dislocation (GND) theory to copper. GNDs aggregate into complex orientation-dependent dislocation structures that generate internal stress fields. These fields, which impede or assist the motion of other dislocations, result in a strongly anisotropic contribution to material hardening (known as kinematic hardening or Bauschinger effect), where the material's strength depends on the direction of subsequent loading relative to its deformation history.

This research contributes to a core objective of the OXFORD-UMAT project [18]: analysing the fatigue resistance of copper and its alloys for their application in fusion reactors. The cyclic deformation experienced by these components can induce significant kinematic hardening. To better understand this phenomenon, the present study investigates a single-crystal copper micro-cantilever subjected to cyclic bending along different crystallographic directions. By examining the evolution of kinematic hardening during the initial load cycles, we aim to elucidate the mechanisms that form the dislocation structures responsible for fatigue within the crystal.

Modelling the Bauschinger effect in copper during preliminary load cycles

6.1 Abstract

This research utilises established cyclic deformation models to simulate the Bauschinger effect observed in copper monocrystal cantilever experiments during the initial bending and straightening phases. Crystal plasticity finite element simulations employing *Armstrong-Frederick*, *Orowan-Sleeswyk*, and various other backstress models have drawbacks to reproduce the experimental force-displacement curves accurately since they are not able to reproduce the isotropic hardening measured during cantilever straightening. However, the *Armstrong-Frederick* model combined with *Voce-type hardening* and a newly proposed *modified Orowan-Sleeswyk* model has proven to be effective. In this work, we propose a *modified Orowan-Sleeswyk* model, based on recent studies, where not all the geometrically necessary dislocations (GND) recombine during the straightening phase, but instead reorient to achieve a net zero-strain gradient with ongoing hardening during load reversal.

6.2 Introduction

Copper has excellent thermal conductivity and adequate mechanical strength for high thermal stresses, therefore it is often used as a stress-relieving interlayer at the bond interface between the radiation shield and the heat sink in plasma-facing components (PFC) of fusion reactors such as Wendelstein-7X, JET, and ITER [74, 75]. Cyclic heat loads caused by pulsed plasma operations generate a repeated variation in thermal stress in the PFC structure. Under these circumstances, the copper bond layer experiences alternating loads that cause plastic strain accumulation responsible for hardening during deformation (expansion or contraction) or softening when the sense of deformation changes (from expansion to contraction or vice-versa), leading to cycle fatigue of the material [75].

The Bauschinger effect refers to the reduction in yield strength observed when the direction of the applied load is reversed or when the load path is changed [80]. For cyclic deformations, it could explain stress saturation at relatively low stresses, frequently forming persistent slip bands (PSBs) due to extrusions/intrusions that can lead to fatigue cracks [82]. In polycrystals, this effect is well understood and is mainly attributed to polarised dislocations in front of the crystal grain boundaries, as supported by experimental evidence [83, 84].

In single-crystals, the dislocation structures responsible are still under debate [83]. Currently, there are two

main explanations for the Bauschinger effect. The first involves cells formed by dislocations that produce long-range internal stresses (LRIS). This phenomenon was first studied by Mughrabi [86] and Pedersen [209] who proposed a structure called dislocation cell, formed of regions with high yield stress/dislocation densities (cell walls) in combination with lower yield stress/dislocation densities regions (cell interiors); this structure remains nearly invariable during cycles. The second, known as *Orowan-Sleeswyk model*, is based on complex structures of dislocation obstacles which group generally around boundaries, these structures allow movement of dislocations in one direction but not in others until high strain levels are produced [87, 88].

This discussion has remained open for several years, Kassner et al. [89] support the idea of cell structures based on compression and tension experiments on monocrystals of copper, nickel and aluminium but noted that the LRIS were smaller than initially expected and did not discard the idea of the *Orowan-Sleeswyk model*. Levine et al. [82] worked with the compression of monocrystal copper micropillars, measuring low LRIS associated with cell structures and concluding that both models (*Mughrabi* and *Orowan-Sleeswyk*) have importance. The discussion is more complex when we have curvature as during cantilever experiments. The lattice curvature allows the formation of geometrically necessary dislocations (GND) that increase the impact of the *Orowan-Sleeswyk* model. In addition, the interaction of the curvature with extrusions or intrusions in the metal creates slip bands that act as obstacles to the dislocations and are particularly complex to model during the first load cycles [83, 210].

On the other hand, other models have appeared [211, 212] that are not based on dislocations like the two previous ones (*Mughrabi* and *Orowan-Sleeswyk*). These models are based on crystal slip, a much simpler quantity to calculate, reducing the computation time and complexity. These models have been widely used in the literature for polycrystals [213, 214] and monocrystals [215]. They have also been used in combination with the *Orowan-Sleeswyk model* in [84] but in this case, an equation with the same structure as the *Armstrong-Frederick model* is used to model the isotropic hardening (non-softening) and the *Orowan-Sleeswyk model* is responsible for the Bauschinger effect.

Recent studies indicate that the Bauschinger effect and hardening are different during initial load cycles of cantilever experiments [21, 85]. In these studies, a monocrystal copper cantilever undergoes load and straightening cycles. The results showed a more pronounced Bauschinger effect than in polycrystal copper or monocrystal after many cycles, furthermore, isotropic hardening occurred between cycles. Consequently, Ugi et al. [85] illustrates the evolution of GND in a cantilever experiment during initial cycles. The GND distribution contradicts the idea that the structure of the dislocation cell remains constant throughout the full bending/straightening cycle. The GND pile-ups formed during the first bending are converted to a highly

complex structure during the straightening, with the dislocation density being distributed throughout the cantilever base giving rise to the isotropic hardening. Dislocation dynamics simulations provide qualitative information [216], but are computationally expensive for cantilever experiments, making crystal plasticity codes a more practical approach to modelling these types of experiments [17].

Demir et al. [21] presented the Bauschinger effect using a single-crystal copper cantilever. Based on these experimental results, this study has modelled the Bauschinger effect during initial bending/straightening cycles, comparing the results of two well-established model types: the Armstrong-Frederick model [211] combined with hardening laws, and GND-based models [87].

The modelling process used the OXFORD-UMAT code [18] (code available on [49]), which was designed to analyse various types of materials for the Spherical Tokamak for Energy Production reactor. The code incorporates models for plasticity, GND calculus and hardening. The GND calculations follow the method proposed by Demir et al. [17].

6.3 Cantilever Experiment

Demir et al. [21] studied the Bauschinger effect [80] of a monocrystal copper cantilever (25.4×8.64×7.05 μm, Fig. 6.1(b)) consisting of three total cycles of bending and straightening.

The cantilever was produced from a single-crystal copper sample grown in a Bridgman furnace. First, a cylindrical sample with a diameter of 100 μm was crafted using wire electro-discharge grinding and subsequently etched in a 40% HNO3 solution. Finally, focused ion beam (FIB) milling shaped the cantilever beam from this cylindrical specimen, using a 500 pA current at 30 keV to finish all surfaces [21]. The initial Euler angles [217] were ϕ_1 = 260.0°, Φ= 101.1°, ϕ_2 = 248.2° and the corresponding Miller indices were [5 $\bar{2}$ $\bar{1}$] for the longitudinal beam axis (z-axis), [$\bar{4}$ $\bar{1}$1 2] for the transverse direction (y-axis), and [5 2 21] for the loading axis (x-axis) as shown in Fig. 6.1 (b).

The cantilever was bent by a Hysitron$^{\mathbb{R}}$ indenter with a spherical indenter that produced a displacement of 3 μm at a speed of 1 μms^{-1} in displacement-controlled mode. The indentation region was situated at a distance of 17.3 μm from the base. The size of the indented region (approximately 2 μm^3) was much smaller than the bent volume (approximately 180 μm^3), having only a small influence on the strength of the cantilever during deformation.

The bending and straightening process consists of three stages in each cycle: i) the indenter bends the cantilever (bending), ii) the indenter stops applying pressure and gradually releases the load to zero (unloading), and iii) the cantilever is loaded in the reverse direction until its original position (straightening).

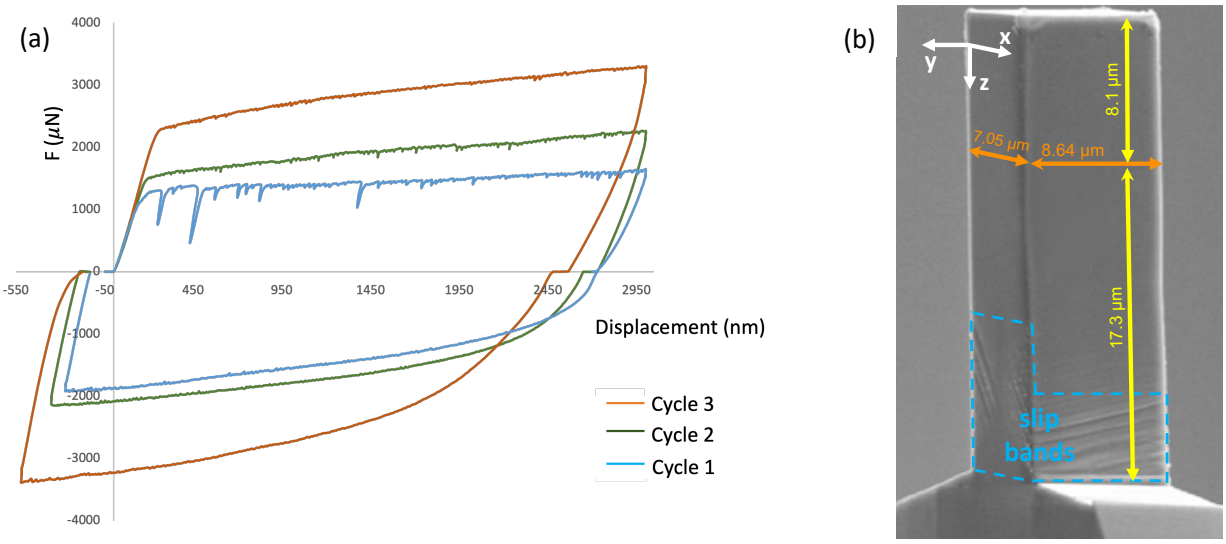

Figure 6.1: (a) Force-displacement bending and straightening cycles of the cantilever experiment [21]. (b) SEM image of the experiment at the end of the first bending straightening cycle, indicating the dimensions of the cantilever. The distances from the base and the top of the cantilever where the indenter was applied are shown in yellow. The areas with slip bands created by active slip systems are shown in blue.

Fig. 6.1(a) illustrates the force-displacement measurements of the experiments in the first three consecutive cycles. There is a notable increase in hardening during bending in successive cycles. There are also drops in force during the 1^{st} bending, which appear as discontinuities in the blue line. These drops are attributed to the formation of slip bands (see slip bands in Fig. 6.1(b)), which cause a plastic displacement of the cantilever with less resistance than usual. Once formed, these slip bands act as obstacles to dislocations, contributing to increase the hardening [210].

During the straightening process, the reverse yield strength is significantly lower than the yield strength observed during bending. Demir et al. [21] estimates a stress reduction of 73% (1^{st} cycle), 76% (2^{nd} cycle) and 83% (3^{rd} cycle) relative to the bending yield stress. This observed reduction in the yield strength during straightening is due to internal backstresses that support the load reversal. They arise from sets of GND accumulated during forward bending that disappear (through the glide in the reverse direction which causes the annihilation with dislocations of the opposite sign) as the cantilever returns to the original position.

6.4 Crystal plasticity framework

A detailed description of the crystal plasticity simulation code used in this study (OXFORD-UMAT) can be found in [18]. The code was applied in combination with the finite element software Abaqus [42], while the specific methodology for GND calculation is outlined in [17]. This section presents an overview of the

crystal plasticity kinematics and constitutive laws governing slip behaviour in the material.

6.4.1 Crystal plasticity kinematics

The deformation gradient in a crystal under stress can be defined by $\boldsymbol{F}_{tot} = \boldsymbol{F}_e \boldsymbol{F}_p$, where $\boldsymbol{F}_e$ is the mechanical elastic deformation gradient, $\boldsymbol{F}_p$ the plastic deformation gradient.

The mechanical elastic deformation gradient $\boldsymbol{F}_e$ is calculated using the Jaumann stress rate [187] in combination with a method which uses the total deformation components minus the plastic deformation components (explained in [18]).

The plastic deformation gradient $\boldsymbol{F}_p$ is calculated from the plastic velocity gradient $\boldsymbol{L}_p$, which is the sum of the slip rates $\dot{\gamma}^a$ times the Schmid tensor $\boldsymbol{S}^a$ of each slip system ^{a}, which is the dyadic product $\boldsymbol{s}^a \otimes \boldsymbol{n}^a$, where $\boldsymbol{s}^a$ is the slip direction and $\boldsymbol{n}^a$ the slip plane normal of the plastically deformed lattice [218]:

$$\boldsymbol{L}_p = \dot{\boldsymbol{F}}_p \boldsymbol{F}_p^{-1} = \sum_a \dot{\gamma}^a \, \boldsymbol{s}^a \otimes \boldsymbol{n}^a = \sum_a \dot{\gamma}^a \, \boldsymbol{S}^a. \tag{6.4.1}$$

However, the slip system undergoes elastic deformations, transforming the slip and normal direction to a deformed configuration $(\boldsymbol{n}_e^a, \boldsymbol{s}_e^a)$:

$$\boldsymbol{s}_e^a = \boldsymbol{F}_e \, \boldsymbol{s}^a; \quad \boldsymbol{n}_e^a = \boldsymbol{F}_e^{-T} \, \boldsymbol{n}^a = \boldsymbol{n}^a \, \boldsymbol{F}_e^{-1}. \tag{6.4.2}$$

The rotation, $\boldsymbol{g}_{ij}$, is applied to use the experiment reference frame during calculations (Bunge convention), where ϕ_1, Φ, and ϕ_2 represent the Euler angles [51], for further details see Appendix B.1. The temporal evolution of the crystal orientation is computed by updating $\boldsymbol{g}_{ij}$ from an initial time t to a subsequent time $t + \Delta t$, where Δt represents the discrete time increment. This update can be expressed as:

$$\boldsymbol{g}_{ij,(t+\Delta t)} = \boldsymbol{g}_{ij} = (\boldsymbol{I} + \boldsymbol{\Delta\Omega}_e \Delta t) \, \boldsymbol{g}_{ij,t}. \tag{6.4.3}$$

Using the orientation rates according to [219]: $\dot{\boldsymbol{g}}_{ij} = \boldsymbol{\Delta\Omega}_e \, \boldsymbol{g}_{ij,t}$.

In which $\boldsymbol{\Delta\Omega}_e$ is the elastic spin obtained by subtracting the plastic spin from the total spin:

$$\boldsymbol{\Delta\Omega}_e = \boldsymbol{\Delta\Omega} - \boldsymbol{\Delta\Omega}_p; \quad \begin{cases} \boldsymbol{\Delta\Omega}_p = \sum_a \boldsymbol{W}^a \dot{\gamma}^a \\ \boldsymbol{\Delta\Omega} = \dfrac{\boldsymbol{L} - \boldsymbol{L}^T}{2} \end{cases} \tag{6.4.4}$$

$$\boldsymbol{W}^a = \frac{1}{2} \left(\boldsymbol{s}_e^a \otimes \boldsymbol{n}_e^a - \boldsymbol{n}_e^a \otimes \boldsymbol{s}_e^a \right). \tag{6.4.5}$$

where $\boldsymbol{W}^a$ is the antisymmetric matrix of the Schmid tensor, and $\dot{\gamma}^a$ is the slip rate, which is determined by various plastic models. $\boldsymbol{L}$ is the velocity gradient of the total strain, defined by $\boldsymbol{L} = \dot{\boldsymbol{F}}\boldsymbol{F}^{-1}$.

The set of equations is solved through a semi-implicit algorithm implemented in a user-defined material subroutine (OXFORD-UMAT [18]) for the finite element software Abaqus, which uses the Forward-Gradient algorithm [52] to obtain the approximate initial and backup solution for the Cauchy stress.

6.4.2 Constitutive laws

The constitutive laws depend on the elasticity and the slip rate responsible for the plasticity (see Eq. (6.4.1)). Elasticity theory relates the rotation-free objective Jaumann rate of stress, $\overset{\nabla}{\boldsymbol{\sigma}}$ [220], to the elastic deformation rate $\boldsymbol{d}_e$, writing the 4^{th} rank elasticity tensor $\mathbb{C}$ for the deformed configuration [187] in Voigt notation:

$$\overset{\nabla}{\boldsymbol{\sigma}} = \mathbb{C} : \boldsymbol{d}_e; \quad \mathbb{C} = \boldsymbol{R}\mathbb{C}_0\boldsymbol{R}^T. \tag{6.4.6}$$

where $\mathbb{C}$ is a 6×6 matrix obtained by applying the rotation matrix $\boldsymbol{R}$ to the elastic stiffness constant $\mathbb{C}_0$ [55], thus adjusting it from the crystalline reference to the experimental one (see Appendix B.1). The stiffness constant $\mathbb{C}_0$ for a face-centred cubic material (FCC) such as copper is given by three elastic constants C_{11}, C_{12}, C_{44} [221]

The slip rates of the slip system "a" are calculated using the hyperbolic-sine law [48], where α and β were assumed to be constants adjusted according to [221], τ^a_{eff} is the effective resolved shear stress (RSS) in each slip system, and τ^a_c the critical resolved shear stress (CRSS), which depends on the initial *Statistically Stored Dislocations* (SSD) density and needs to be calibrated:

$$\dot{\gamma}^a = \alpha \sinh(\beta\left(\left|\tau^a_{eff}\right| - \tau^a_c\right))\,\mathrm{sign}(\tau^a_{eff}). \tag{6.4.7}$$

in which the effective RSS is given by the RSS, τ^a, minus the backstress term, χ^a:

$$\tau^a_{eff} = \tau^a - \chi^a. \tag{6.4.8}$$

The prefactors of the slip law are computed based on physical parameters according to:

$$\alpha = \rho_m b^2 \nu_0 \exp\left(-\frac{\Delta F}{K_B T}\right); \quad \beta = \frac{\Delta V^a}{K_B T}. \tag{6.4.9}$$

The model parameters for crystal orientation, elastic constants, and the slip law are given in the table below:

parameter	definition	unit	value [221]
ϕ_1	Undeformed Euler angle 1	Degrees	260
Φ	Undeformed Euler angle 2	Degrees	101.1
ϕ_2	Undeformed Euler angle 3	Degrees	248.2
C_{11}	Elastic constant 1	MPa	$168{\cdot}10^3$
C_{12}	Elastic constant 2	MPa	$121.4{\cdot}10^3$
C_{44}	Elastic constant 3	MPa	$75.4 \cdot 10^3$
α	constant value	1/s	10^{-5}
β	constant value	1/MPa	0.2
ΔF	activation energy for slip	eV	0.5
ν_0	attempt frequency	1/s	10^{11}
ΔV	Activation volume	b^3	50
b	Burgers vector	μm	$2.56 \cdot 10^{-4}$
ρ_m	mobile dislocation density	μm^{-2}	0.5
K_B	Boltzmann constant	$\text{eV}{\cdot}\text{K}^{-1}$	$8.61 \cdot 10^{-5}$
T	Temperature	K	300

6.5 GND model

Heterogeneity in crystal deformation causes the formation of *Geometrically Necessary Dislocations* (GND), responsible for hardening and backstress (lower yield strength during cantilever straightening) [87, 95].

GND density (ρ_{GND}) [171] is the sum of the length of dislocations per unit volume that is obtained by the lattice incompatibility in the crystalline structure. GND density is calculated according to the formula [19]:

$$\boldsymbol{\Lambda} = -\left(\nabla \times \boldsymbol{F}_p\right)^T \boldsymbol{F}_p^T = \sum_a \rho^a_{GND} b^a \boldsymbol{s}^a \otimes \boldsymbol{l}^a = \sum_a (\rho^a_{GND,edge} b^a \boldsymbol{s}^a \otimes \boldsymbol{t}^a + \rho^a_{GND,screw} b^a \boldsymbol{s}^a \otimes \boldsymbol{s}^a). \tag{6.5.1}$$

Where $\boldsymbol{\Lambda}$ is the Nye tensor that represents lattice incompatibility, b^a is the length of the Burgers vector of the slip system ^{a}, $\boldsymbol{l}^a$ is the dislocation line. Note that the line direction is the slip direction $\boldsymbol{s}^a$, and transverse direction $\boldsymbol{t}^a$, for screw and edge dislocations, respectively.

GND density was calculated from the lattice incompatibility in Eq. (6.5.1), considering only active slip systems and using singular value decomposition to solve the system (model 1-d of Chapter 5) [17].

6.6 Modelling Bauschinger effect

Various models have been proposed based on slip γ or GND to model the Bauschinger effect [82, 86, 87, 211, 85], (see scheme in Fig. 6.2).

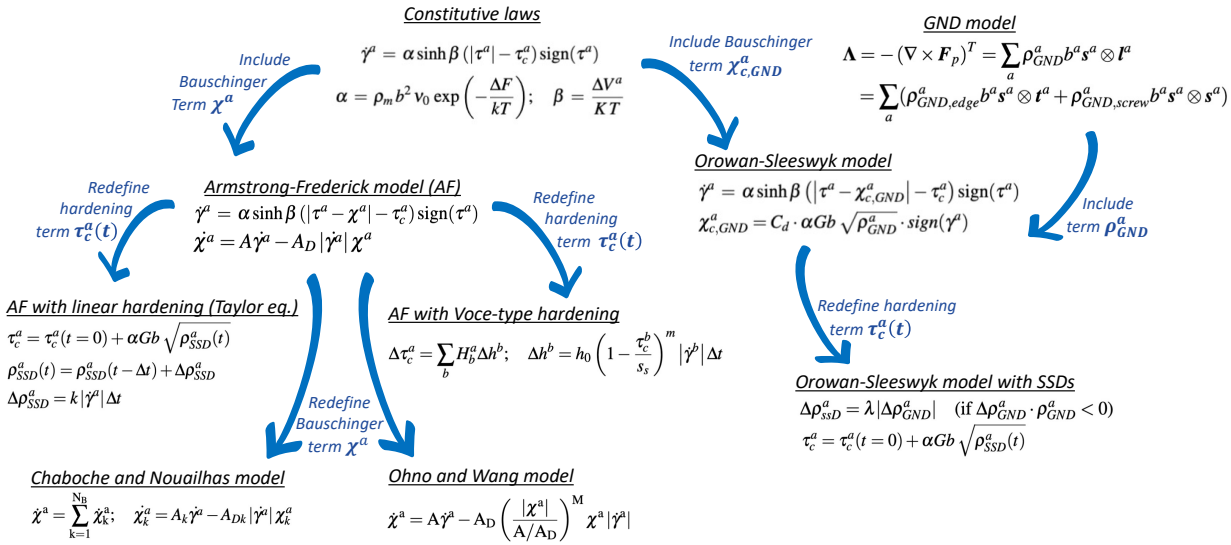

Figure 6.2: Scheme of the models analysed in this study.

6.6.1 Armstrong-Frederick model

The *Armstrong-Frederick* (*A-F*) model is a phenomenological model that integrates the concepts of proportional hardening and saturation into the backstress term χ^a in Eq. (6.4.8), providing greater precision during cyclic loading:

$$\dot{\chi}^a = A\dot{\gamma}^a - A_D\,|\dot{\gamma}^a|\,\chi^a. \tag{6.6.1}$$

where $\dot{\chi}^a$ represents the backstress rate, $\dot{\gamma}^a$ is the slip rate, A and A_D are parameters associated with direct hardening and dynamic recovery respectively that need to be adjusted [84]. The backstress χ^a evolves quasi-linear at the beginning of deformation, curving progressively until a saturation value of A/A_D.

The *A-F* model was first applied to crystal plasticity by [90] and was later adopted by other researchers in their own crystal plasticity frameworks. Several variations have been proposed, such as the *Chaboche* model (see Eq. (6.6.2)) [91] that introduced a combination of linear and non-linear hardening terms or the *Ohno-Wang* model (see Eq. (6.6.3)) [92]:

$$\dot{\chi}^{\mathrm{a}} = \sum_{\mathrm{k}=1}^{\mathrm{N_B}} \dot{\chi}^{\mathrm{a}}_{\mathrm{k}}; \quad \dot{\chi}^a_k = A_k\dot{\gamma}^a - A_{Dk}\,|\dot{\gamma}^a|\,\chi^a_k \quad \text{where } A_{Dk} = 0 \text{ for only linear hardening terms.} \tag{6.6.2}$$

$$\dot{\chi}^{\mathrm{a}} = \mathrm{A}\dot{\gamma}^{\mathrm{a}} - \mathrm{A_D} \left(\frac{|\chi^{\mathrm{a}}|}{\mathrm{A}/\mathrm{A_D}}\right)^{\mathrm{M}} \chi^{\mathrm{a}}\,|\dot{\gamma}^{\mathrm{a}}|. \tag{6.6.3}$$

All these models are empirical and were applicable to the macroscopic length scale to capture the Bauschinger effect and cyclic ratcheting, but they are not expected to capture the underlying mechanisms at a lower length scale [84]. Sect.6.7.1 demonstrates how these models present important limitations to capture the

level of observed hardening during the first cycles of deformation [21]. To overcome this limitation, we combine *A-F type* models with *linear SSD hardening* or *Voce-type hardening* models that include isotropic hardening during bending and straightening without contributing to backstress.

A-F combined with linear SSD hardening

The critical resolved shear stress (CRSS) is defined by the Taylor equation [95] that depends on the dislocation density and τ_c^0, which is the initial strength or friction stress:

$$\tau_c^a = \tau_c^0 + \alpha G b \sqrt{\rho_{SSD}^a}. \tag{6.6.4}$$

The evolution of *statistically stored dislocation (SSD)* density is given by [97]:

$$\dot{\rho}_{SSD}^a = k \left| \dot{\gamma}^a \right|. \tag{6.6.5}$$

where τ_c^a is the CRSS on slip system a, ρ_{SSD}^a is the SSD density, G is the shear modulus, α and k are geometrical parameters being $\alpha = 0.25$ and k needs to be adjusted.

A-F combined with Voce-type hardening

Voce-type hardening [222, 56] is an experimentally-based hardening model composed of a hardening rate and a saturation term. It also considers latent hardening interactions between slip systems:

$$\Delta\tau_c^a = \sum_b H_b^a \Delta h^b; \quad \Delta h^b = h_0 \left(1 - \frac{\tau_c^b}{s_s}\right)^m \left| \dot{\gamma}^b \right| \Delta t. \tag{6.6.6}$$

where h_0 is the hardening rate, s_s is the saturation slip strength that represents the saturation of hardening, m is the hardening exponent and H_b^a is the hardening interaction matrix of the slip system^b in the slip system^a. In our models, the Voce-type hardening is used to represent the linear hardening observed experimentally. Given that Demir et al. [21] did not observe any decrease in the hardening during the initial cycles, we assumed $s_s \gg \tau_c^b$ i.e. $\tau_c^b / s_s \approx 0$, simplifying the expression to:

$$\Delta\tau_c^a = \sum_b H_b^a \Delta h^b; \quad \Delta h^b = h_0 \left| \dot{\gamma}^b \right| \Delta t. \tag{6.6.7}$$

6.6.2 Orowan-Sleeswyk model

The *Orowan-Sleeswyk* model [87, 88] proposes a Taylor's hardening relation to represent the kinematic hardening produced by GND:

$$\chi^a = C_d \cdot \alpha G b \sqrt{\rho^a_{GND}} \cdot P^{aa} \cdot \text{sign}(\dot{\gamma}^a) = C_d \cdot \alpha G b \sqrt{\rho^a_{GND}} \cdot \text{sign}(\gamma^a). \tag{6.6.8}$$

$$\text{where } P^{aa} = \text{sign}(\dot{\gamma}^a) \cdot \text{sign}(\gamma^a)$$

where C_d denotes a geometric factor that requires adjustment, $\alpha = 0.25$ is a geometrical factor, G the shear modulus, b the Burgers vector magnitude and ρ^a_{GND} the GND density.

P^{aa} is the reversibility term [96] to determine the sign of χ^a respect to the sign of the resolved shear stress τ^a. P^{aa} is positive (χ^a causes kinematic hardening) when both signs of accumulated slip γ^a and slip rate $\dot{\gamma}^a$ are the same, and negative (χ^a causes kinematic softening) otherwise. The overall sign of χ^a is:

$$\text{sign}(\chi^a) = P^{aa} \cdot \text{sign}(\tau^a) = P^{aa} \cdot \text{sign}(\dot{\gamma}^a) = \text{sign}(\gamma^a) \tag{6.6.9}$$

In contrast to the mathematical approach of the *A-F* model, *Orowan-Sleeswyk* model tries to apply our knowledge of dislocation structures. According to Mughrabi et al. [86], two explanations for hardening and softening can be found due to GND. i) GND obstacles are dislocation cell walls, and the hardening results from interactive forces between the walls and the mobile dislocations, while the initial drop in the yield strength occurs as a consequence of the glide of the GND during the reverse loading, which produces some relaxation of the dislocations cell walls and the plasticity generated in the interior of the cell. ii) The pile-up of GND in certain regions during deformation causes stress on the slip systems and prevents further slip (strain hardening). For a cantilever, the region corresponds to the neutral axis of the cantilever. During the reverse loading, the backstress induced by the dislocations previously formed facilitates the transition towards equilibrium, contributing to the observed softening.

SSD modification in the Orowan-Sleeswyk model

The examination of load/straightening experimental curves for the cantilever (see Sect.6.3) reveals an excessive increase in hardening during the straightening process, despite the anticipated reduction in yield stress caused by backstress.

HR-ESBD measurements on the monocrystal copper cantilever [85] found the creation of complex dislocation structures, caused by changes in the direction of some of the GND that remain instead of recombining

during straightening. In this article, we attribute to these dislocations the excess of hardening generated.

This study proposes to consider these dislocations as responsible for the unexpected hardening observed by [21] during initial cycles. Because developing a dislocation dynamics code to calculate the new orientation of the GND could be complex and computationally expensive, an alternative was to approximate them as randomly oriented and transform these GND into SSD.

$$\Delta\rho^{a}_{SSD} = \lambda|\Delta\rho^{a}_{GND}| \quad (\text{if } \Delta\rho^{a}_{GND}\cdot\rho^{a}_{GND} < 0). \tag{6.6.10}$$

where $\Delta\rho_{SSD}$ is the change of SSD density, $\Delta\rho_{GND}$ is the change of GND density, λ is the percentage of GND density converted to SSD density. The SSD density increment causes hardening through the Taylor hardening (see Eq. (6.6.4)).

6.6.3 Finite Element Method (FEM)

The bending and straightening of the cantilever were simulated using the finite element method. The x-axis displacement was applied over two lines of nodes on opposite faces of the cantilever at 17.3 μm from the base (see Fig. 6.3(a)). The line of nodes were used instead of simulating the indenter to simplify the calculations after finding similar results in the comparative study of Appendix C.1.

The following boundary conditions were imposed on the model during the successive cycles:

1. Bending obtained by displacing the cantilever -3μm along the x-axis in the indentation region during 3 seconds (as in Demir et al. [173]).
2. 3 seconds rest by deactivating the load.
3. Straightening obtained by displacing the cantilever 3μm along the x-axis in the opposite direction in the indentation region during 3 seconds.
4. 3 seconds rest by deactivating the load.

15,600 quadratic tetrahedral elements (C3D20) were applied in simulations. For further details about convergence, see Appendix C.2. The parameters of the Bauschinger models were adjusted using the Nelder-Mead optimisation algorithm [15]. The optimisation minimises a distance function between the force-displacement values obtained from experimental data and those derived from simulations [13]. Nelder-Mead was chosen among other optimisation methods due to its simplicity of use by not requiring mathematical derivatives of the distance function and its rapid convergence in a limited number of iterations, a crucial factor given the computationally intensive nature of FEM simulations.

The parameter values p_i used to adjust the models are defined by:

$$p_i = \arg\min_{p_i} \left(\sum_{cycles} \frac{\int \mid F_{FEM}(u,p_i) - F_{EXP}(u) \mid du}{\int \mid F_{EXP}(u) \mid du} \right). \tag{6.6.11}$$

where F_{FEM} is the force obtained in the model, F_{EXP} is the force measured experimentally, and u is the displacement of the indenter or the displacement of the nodes in the case of the FEM model.

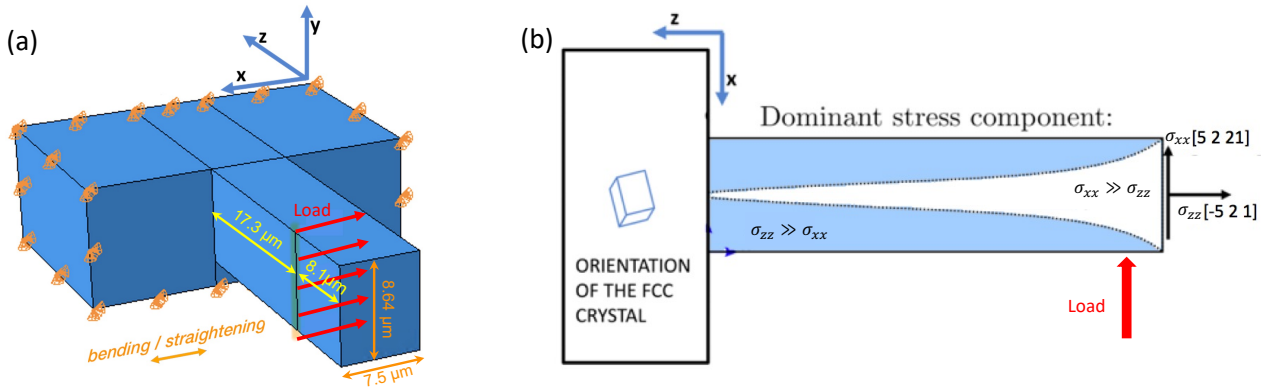

Figure 6.3: (a) Boundary conditions for the FEM model during bending/straightening (in yellow, distances from the base and the top of the cantilever where the indenter was applied, in orange, dimensions of the base, in green, line of nodes where the load was applied, in red, direction of the load). (b) Diagram showing load orientation respect to FCC crystal. The dominant stress component along the cantilever is also indicated.

6.7 Results and Discussion

This section presents the results derived from the Bauschinger models applied to the cantilever experiment. The results obtained from the *Armstrong-Frederick* based models are detailed in Subsect. 6.7.1, while the results from the GND-based models are in Subsect. 6.7.2.

As mentioned in *Cantilever Experiment* (Sect. 6.3), slip bands are formed during the 1^{st} bending due to the activation of dislocation sources [223], but their impact during formation is extremely complex. For this reason, our analysis focuses on the subsequent 2^{nd} and 3^{rd} cycles, where no additional slip bands are created. Once the most suitable models are selected and their parameters adjusted, they are applied to the 1^{st} cycle, trying to estimate the impact associated with the slip bands' formation.

6.7.1 Armstrong Frederick based models

A-F relate the slip to the hardening and backstress, the accumulated slip γ for a slip system is defined through the Schmid factor and the CRSS (τ_c) of the slip system [218].

Fig. 6.3(b) shows the initial vector components of the stress during cantilever modelling (σ_z =[$\bar{5}$ 2 1], σ_x=[5

2 21], on crystal coordinates). We can observe how the tensile load σ_z dominates σ_x as we approach the cantilever base (blue zone).

Appendix C.3 includes the table with each slip system (n^a, s^a), their Schmid factor, and Fig. C.4 shows the accumulated slip γ during the 2^{nd} bending, demonstrating that the main slip occurs in the two slip systems with the highest Schmid factor, which are shown in more detail in Fig. 6.4 for the 2^{nd} and 3^{rd} cycle (slip system $(1\bar{1}1)[10\bar{1}]$ with Schmid factor 0.49, and slip system $(\bar{1}11)[101]$ with Schmid factor 0.43).

Furthermore, in Fig. 6.1(b), we can identify two different directions in the slip bands, which seems to confirm the result of our model with two clear main slip systems as responsible for the formation of the hardening and backstress.

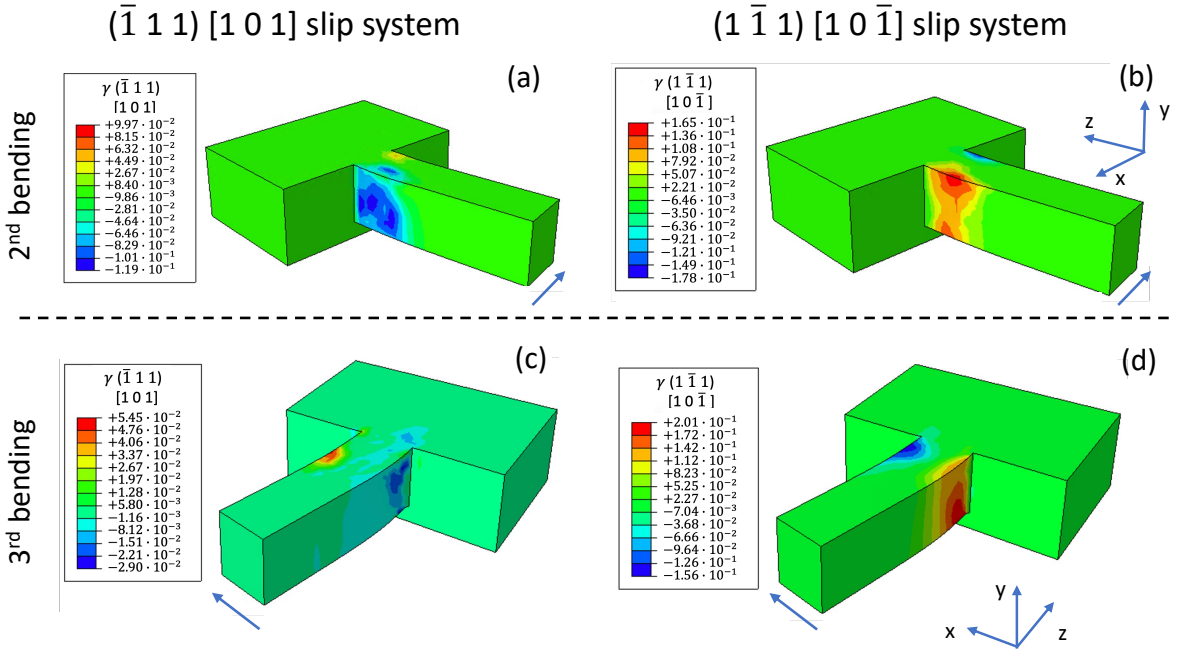

Figure 6.4: (a) The slip accumulated γ in the $(\bar{1}11)[101]$ slip system after 2^{nd} bending. (b) γ in $(1\bar{1}1)[10\bar{1}]$ after 2^{nd} bending. (c) γ in $(\bar{1}11)[101]$ after 3^{rd} bending. (d) γ in $(1\bar{1}1)[10\bar{1}]$ after 3^{rd} bending.

Table 6.1 includes the parameters that have been calibrated for the *A-F* models using the Nelder-Mead optimisation algorithm (Subsect.6.6.3). Given that copper has a face-centred cubic structure with symmetry in its crystalline lattice, the properties are uniform across the different slip systems. The initial CRSS $\tau_c^0 =$ 43 MPa was adjusted to be the same for all models, this value takes into account all the previous hardening suffered in the previous deformation (1^{st} cycle and sample treatment), explaining why it deviates from the values of the literature (19-25 MPa [224]).

Fig. 6.5 compares the force-displacement profiles of the 2^{nd} and 3^{rd} bending/straightening cycles of the *A-F* models with the experimental data. The initial *A-F* model (green curves), defined by Eq. (6.6.1),

Bauschinger model	Hardening model	Parameters adjusted
A-F with saturation Eq. (6.6.1)	None	$A = 2050$ MPa$\cdot s^{-1}$, $A_D = 30 s^{-1}$
A-F with no saturation Eq. (6.6.1)	None	$A = 2050$ MPa$\cdot s^{-1}$, $A_D = 0 s^{-1}$
A-F Eq. (6.6.1)	Linear Eq. (6.6.5)	$A = 1030$ MPa$\cdot s^{-1}$, $A_D = 25 s^{-1}$, $k = 1970 \mu m^{-2}$
A-F with no saturation Eq. (6.6.1)	Voce-type Eq.(6.6.7)	$A = 1150$ MPa$\cdot s^{-1}$, $h_0 = 400$ MPa, $A_D = 0 s^{-1}$, $\tau_c^b / s_s = 0$

Table 6.1: Parameters adjusted for the A-F models.

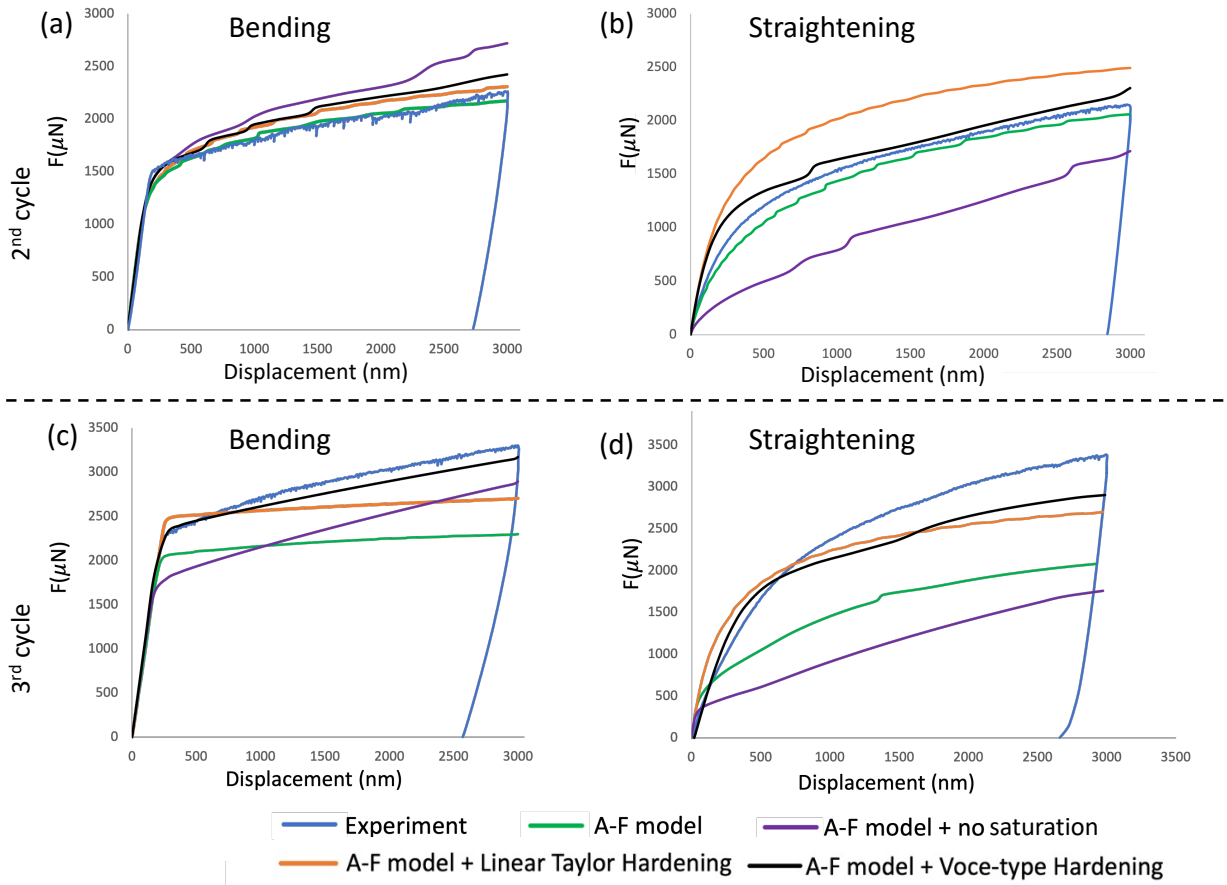

Figure 6.5: Comparison of experimental data with A-F type models.

exhibits favourable agreement with the experimental data (blue curves) during the bending/straightening of the 2^{nd} cycle (Fig. 6.5(a, b)), but there is a notable absence of hardening during the 3^{rd} cycle (Fig. 6.5(c, d)). This limitation is attributed to the saturation term A_D, which maintains the value of χ^a constant once it reaches $\chi^a = A/A_D$. While the *A-F* model can be effective in simulating cyclic fatigue experiments, it proves inadequate for initial cycles characterised by large strains in opposite directions without saturation. This limitation is evident in our case, where there is isotropic hardening between cycles.

Similar behaviour was observed in the model proposed by *Ohno and Wang* (presented in Subsect.6.6.1), which differs mainly in the curvature of the force-displacement representation (depends on the exponent "*M*" of the Eq. (6.6.3)) until it stabilises at $\chi^a = A/A_D$ and then remains constant.

A-F model without saturation ($A_D = 0$) is represented in (purple curves). The notable increase in hardening

during 2^{rd} bending (Fig. 6.5(a)) results in an excessive softening of the 2^{rd} straightening (Fig. 6.5(b)). Furthermore, there is no curvature in the force-displacement graph, which is similar during the 2^{rd} and 3^{rd} cycles. This similarity between cycles demonstrates the cyclic nature of the model, which is unable to capture the increased hardening during the 3^{rd} cycle.

The Chaboche model [91] aggregates various backstresses $\chi^{\mathrm{a}}_{\mathrm{k}}$, derived from both the Armstrong-Frederick (A-F) model with and without saturation.

$$\dot{\chi}^{\mathrm{a}} = \sum_{\mathrm{k}=1}^{\mathrm{N_B}} \dot{\chi}^{\mathrm{a}}_{\mathrm{k}}; \quad \dot{\chi}^{a}_{k} = A_k \dot{\gamma}^{a} - A_{Dk} |\dot{\gamma}^{a}| \chi^{a}_{k} \quad \text{where } A_{Dk} = 0 \text{ for some } \dot{\chi}^{a}_{k}. \tag{6.7.1}$$

The results would reflect a mixture of the green and purple curves. In Fig. 6.5(c), the experimental force-displacement slope during the 3^{rd} bending closely resembles that obtained during the 2^{nd} bending. The Chaboche model is expected to exhibit a steeper slope compared to the A-F model during the 3^{rd} bending. However, this slope would not be similar to that obtained during the 2^{nd} bending, as certain backstresses χ^{a}_{k} become saturated during the 2^{nd} cycle, resulting in some $\dot{\chi}^{\mathrm{a}}_{\mathrm{k}} = 0$.

Another approach was to combine *A-F* models with *Linear Taylor hardening* (orange curves, Subsect.6.6.1). Although the 2^{nd} bending cycle (Fig. 6.5(a)) demonstrates good agreement with the experimental data, a reduction of the backstress term, χ^{a}, was necessary during the calibration of the model to avoid excessive hardening. However, this reduction in χ^{a} in conjunction with linear hardening produces a higher yield strength during the 2^{nd} straightening compared to experimental data. Furthermore, the 3^{rd} bending cycle exhibits insufficient hardening compared to the experiment, since the linear Taylor hardening is proportional to $\sqrt{\rho^{a}_{SSD}} \propto \sqrt{\gamma^{a}}$ (see Eq. (6.6.4) and (6.6.5)).

With the A-F models without saturation, the same shape was observed between the 2^{nd} and 3^{rd} cycles (bending and straightening); however, the saturation of the force-displacement curve during straightening was less than the experimental curves, and there was no hardening between cycles. The introduction of linear Taylor hardening increases the curvature of the force-displacement curves during the straightening of the cantilever, but it does not provide enough hardening during the 3^{rd} bending.

Finally, the *A-F* model was combined with *Voce-type hardening* without saturation (black curves, Subsect.6.6.1, Eq. (6.6.7)). The results agree well with the experiment, demonstrating the necessity of including hardening in *A-F* models.

Clarification is necessary about the saturation of the *Voce-type hardening*. Although in our parameterisation there is no saturation ($A_D = 0$ in Eq. (6.6.1) and $\tau_c/s_s \to 0$ in Eq. (6.6.6)), saturation is necessary for fatigue experiments of many cycles [91, 75]. The saturation is negligible for the slip, γ^{a}, accumulated during

the first cycles (A/A_D and s_s are much higher than the stresses reached during the experiments), but it is necessary to recalculate it once there are more cycles with more slip accumulation.

6.7.2 Orowan-Sleeswyk models

The GND densities of the two most active slip systems $(\bar{1}11)[101]$ and $(1\bar{1}1)[10\bar{1}]$ during the simulations are shown in Fig. 6.6. They were calculated by solving the Nye tensor in its matrix form (see Sect.6.5), the results show the highest concentration in the base of the cantilever, since it is the region where the curvature is the highest.

During the 2^{nd} bending, it can be observed how a slip band of positive GND is formed in both slip systems (see Fig. 6.6(a, b)). Applying the formulation of Dai et al. [186] for small strains, we can check the sign of the edge GND using an analytical expression.

$$\rho^a_{GND,e} = -\frac{1}{b^a}\nabla\gamma^a \cdot \boldsymbol{s}^a. \tag{6.7.2}$$

For ($\bar{1}$ 1 1)[1 0 1], the direction of $\nabla\gamma^a$ is along -x (see Fig. 6.4(a)) that corresponds to [$\bar{5}$ $\bar{2}$ $2\bar{1}$] in the crystal system for the Euler angles ϕ_1 = 260.0°, Φ= 101.1° and ϕ_2 = 248.2° [21]:

$$\text{sign}(\rho^a_{GND,e}) = -\nabla\gamma^a \cdot \boldsymbol{s}^a = -[\bar{5}\ \ \bar{2}\ \ 2\bar{1}] \cdot [1\ \ 0\ \ 1] = +\tag{6.7.3}$$

For (1 $\bar{1}$ 1)[1 0 $\bar{1}$], the direction of $\nabla\gamma^a$ is +x (see Fig. 6.4(a, b)) that corresponds to [5 2 21]:

$$\text{sign}(\rho^a_{GND,e}) = -\nabla\gamma^a \cdot \boldsymbol{s}^a = -[5\ \ 2\ \ 21] \cdot [1\ \ 0\ \ \bar{1}] = +\tag{6.7.4}$$

The same procedure can be used for the sign of GND during the 3^{rd} bending, in this case, $\rho_{GND} < 0$.

Fig. 6.6 shows a high concentration of GND at the base of the cantilever during the 2^{nd} and 3^{rd} bending cycles, reaching densities of $\sim \pm 130\mu m^{-2}$ for ($\bar{1}$ 1 1)[1 0 1] and $\sim \pm 160\mu m^{-2}$ for (1 $\bar{1}$ 1)[1 0 $\bar{1}$]. The maximum total value of GND (the sum of all GND) is $\sim |10^3|\mu m^{-2}$, a value of the same order of magnitude as the values obtained through *kernel average misorientation* (KAM) images [21]. During 2^{nd} and 3^{rd} straightening, the GND density was very low. This happens because the GND is calculated from the plastic strain gradient, $\boldsymbol{F_p}$, and when the cantilever returns to its original position, the strain disappears.

Fig. 6.7 shows the force-displacement curves for the Orowan-Sleewyck model with and without SSD modification during the 2^{nd} and 3^{rd} cycles of the experiment.

The golden curve represents the force-displacement obtained from the Orowan-Sleeswyk model. There is a good match with the experimental data during the 2^{nd} bending Fig. 6.7(a) presenting slightly low yield stress but reaching the maximum force measured experimentally. However, during the 2^{nd} straightening

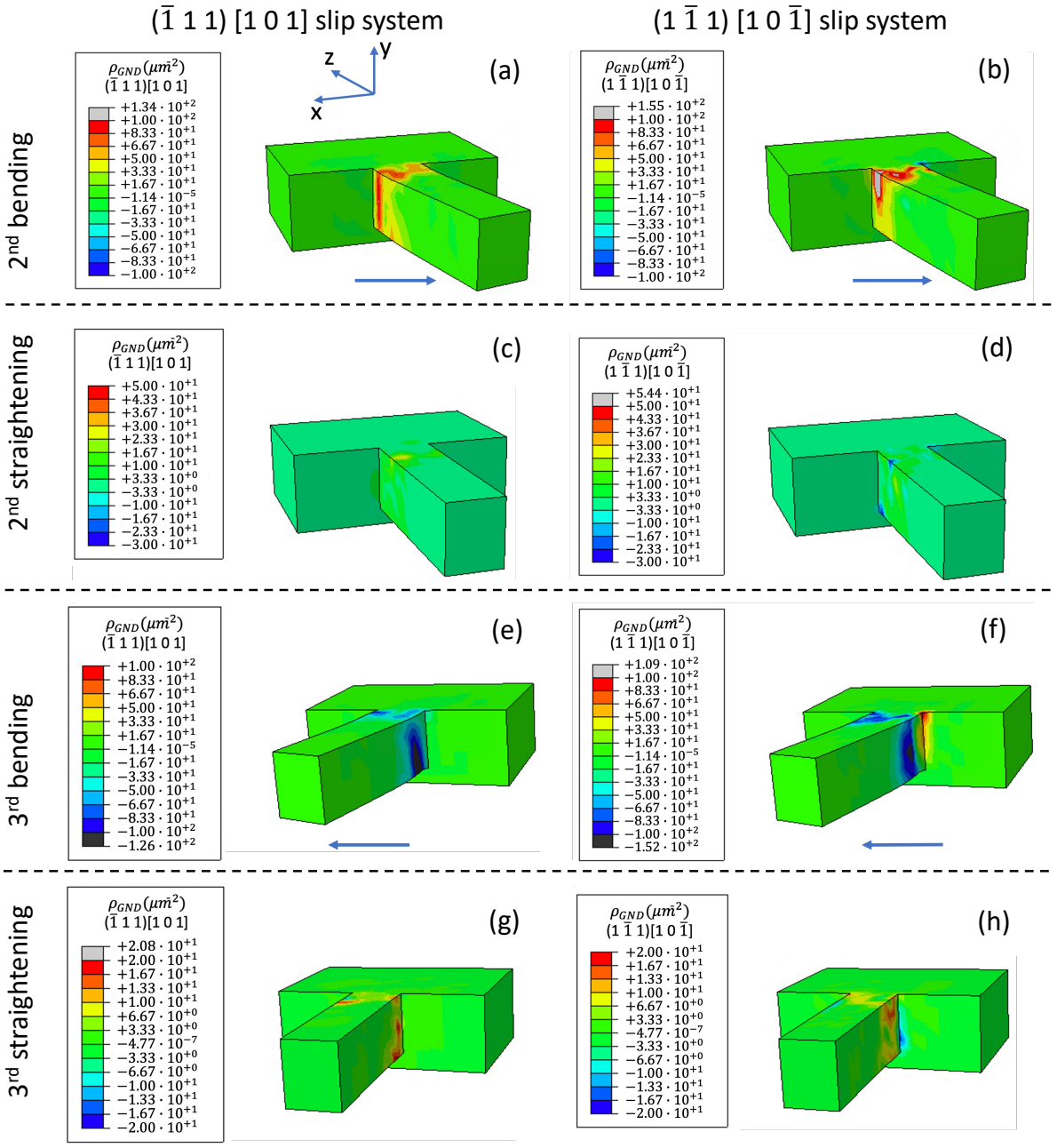

Figure 6.6: Edge GND profiles of the two more active slip systems (1̄ 1 1)[1 0 1] and (1 1̄ 1)[1 0 1̄] after the 2^{nd} and 3^{rd} cycles. The colour scale is adjusted in the straightening figures (c,d,g,h) where the GND density is smaller and difficult to appreciate the distribution compared with the bending scale.

(Fig. 6.7(b)), we observed a lower strain hardening than experiments and the maximum force reached is approximately the initial yield value presented in curve Fig. 6.7(a), which is expected since this force occurs when the beam is straight and $\rho_{GND} \sim 0\ \mu m^{-2}$.

The 3^{rd} cycle is shown in Fig. 6.7(c) (bending) and Fig. 6.7(d) (straightening), the shape of the curve is similar to the 2^{nd} cycle with slightly more hardening during bending and more Bauschinger during straightening, these shapes are reasonable since the deformation is similar but in opposite direction. The slightly

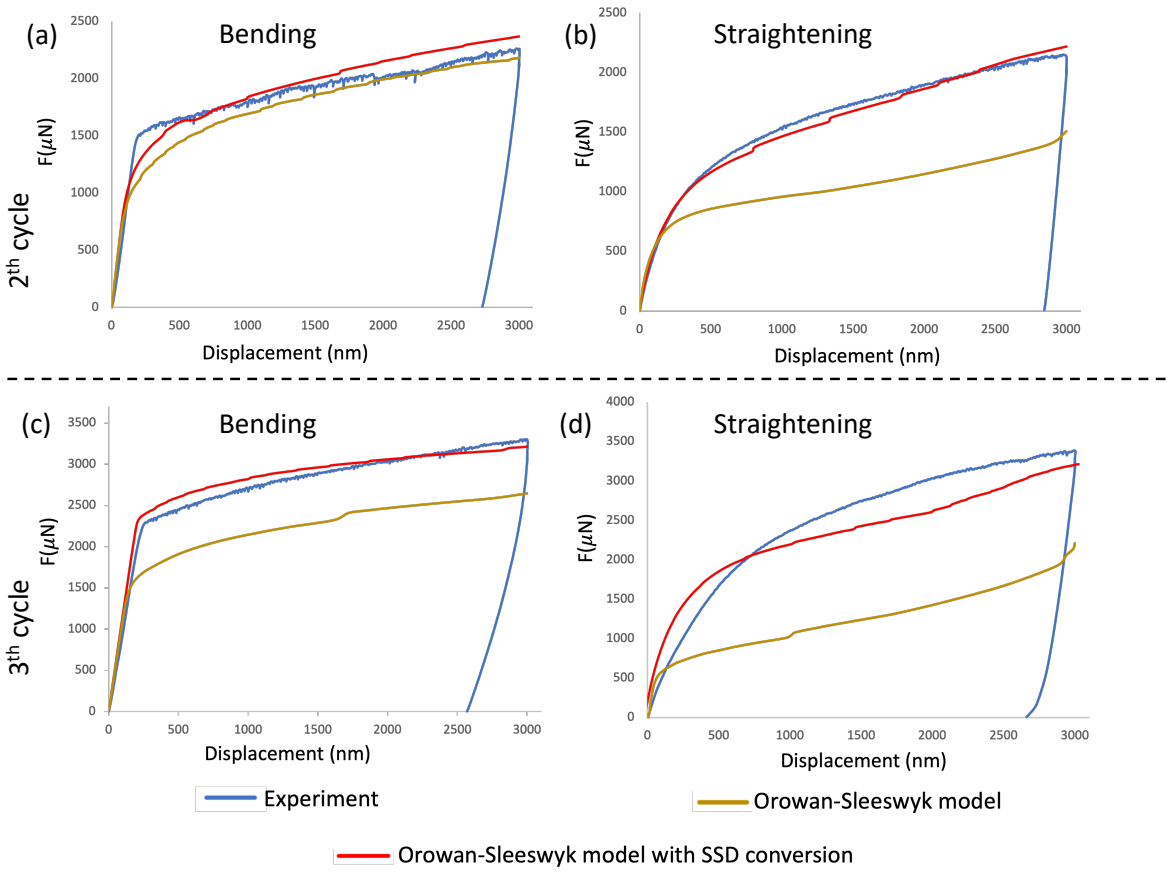

Figure 6.7: Comparison of experimental data with Orowan-Sleeswyck model without and with SSD.

higher hardening can be attributed to the GNDs that remain in the corners after the previous cycle.

Table 6.2 includes the parameters that have been adjusted using the Nelder-Mead optimisation algorithm (Subsect.6.6.3). The *Orowan-Sleeswyk* models were calibrated with a geometrical factor $C_d = 3.6$ (see Eq. (6.6.8)). For comparison, the value reported by Sleeswyk with a low carbon steel alloy [88, 94] was $C_d \sim 10$. In both cases the material was FCC and there were bands (slip for copper and Lüdder for steel) with $\rho_{GND} \sim 10^3 \mu m^2$ around them. Nevertheless, the model seems incomplete when we compare straightening curves with the experiment, which presents an excessive hardening not explained by the Orowan-Sleeswyk formula (see Eq. (6.6.8)).

We examined the possibility that dislocations do not disappear during straightening. Ugi et al. [85] did HR-ESBD measurements of the monocrystal copper cantilever, and they observed that during straightening some GND changed their orientation, forming complex structures whose contribution to kinematic hardening ~ 0 (because dislocations do not have a clear orientation). In general, only $\sim 25\%$ GND were recombined instead of total recombination, as shown by the Orowan-Sleeswyk model combined with the GND calculus model (see Sect. 6.5).

Orowan-Sleeswyk model with SSD (red curves) includes a representation of the previously mentioned com-

GND model	Parameters adjusted
Orowan-Sleeswyk Eq. (6.6.8)	$C_d = 3.6$
Orowan-Sleeswyk Eq.(6.6.8) with SSD Eq.(6.6.10)	$C_d = 3.6$ and $\lambda = 0.72$

Table 6.2: Parameters adjusted for the different GND models.

plex dislocation structures. As discussed in Subsect. 6.6.2, we approximate these structures as an increase in the SSD density, giving a random orientation to these GND when they change. The hardening produced by the SSD increment is given by Taylor equation (see Eq. (6.6.4)). The percentage of GND density converted to SSD density during straightening was adjusted to 72% (parameter λ), a value close to the $\sim 75\%$ GND that remains after straightening in the experiment described in [85].

The force-displacement profile shows good agreement with the experimental data (Fig. 6.7) that reproduce the hardening expected during straightening. The highest mismatch is presented in the 3^{rd} straightening, where the experimental slope is lower than the rest of the straightening cases; the reason that we found most probable comes from the indentation process, which is not perfectly perpendicular after 3 consecutive cycles and requires an adaptation of the cantilever to the indenter shape, reducing the stiffness of the structure.

6.7.3 Modelling bending/straightening 1^{st} cycle

Once the parametrisation of the models was adjusted for the 2^{nd} and 3^{nd} cycles, where slip bands are completely formed, they were applied to the 1^{st} cycle to estimate the impact associated with the slip band formation process. The models and parameters applied were those that have proven capable of reproducing the Bauschinger effect during initial cycles: *A-F combined with Voce-type* model and *"modified" Orowan-Sleeswyk model by SSD density conversion*. For modelling the 1^{st} cycle only the parameter CRSS was changed to 30 MPa, which differs from the 43 MPa of the 2^{nd} cycle. The increase in the 2^{nd} cycle is due to the hardening during the 1^{st} cycle.

Fig. 6.8(a) presents the force-displacement results from the 1^{st} bending. Experiment results show less hardening ($\sim 540\mu N$) than simulations ($\sim 950\mu N$ for Orowan-Sleeswyk + SSD conversion and $\sim 1100\mu N$ for A-F+Voce). The experimental curve also exhibits several drops or discontinuities, with the largest drop $\sim 1000\mu N$. These drops, attributed to slip bands formation (see Fig. 6.1b), appear responsible for the different stress-strain response in 1^{st} cycle compared to the 2^{nd} and 3^{rd}. Confirming this hypothesis, our simulations, which do not include the slip bands effect, show similar hardening in the 1^{st},2^{nd} and 3^{rd} cycles. Once formed, the slip bands act as obstacles to dislocations [210], increasing the hardening of posterior cycles.

Fig. 6.8(b) presents the force-displacement results from the straightening process. The absence of drops

indicates that the slip bands formation mainly occurs during the bending of 1^{st} cycle. These results discard the hypothesis that the force drops are due to cantilever adaptation to the indenter, as the cantilever must also adapt during the 1^{st} straightening to the indenter on the opposite beam face. The experimental data and simulations show good agreement.

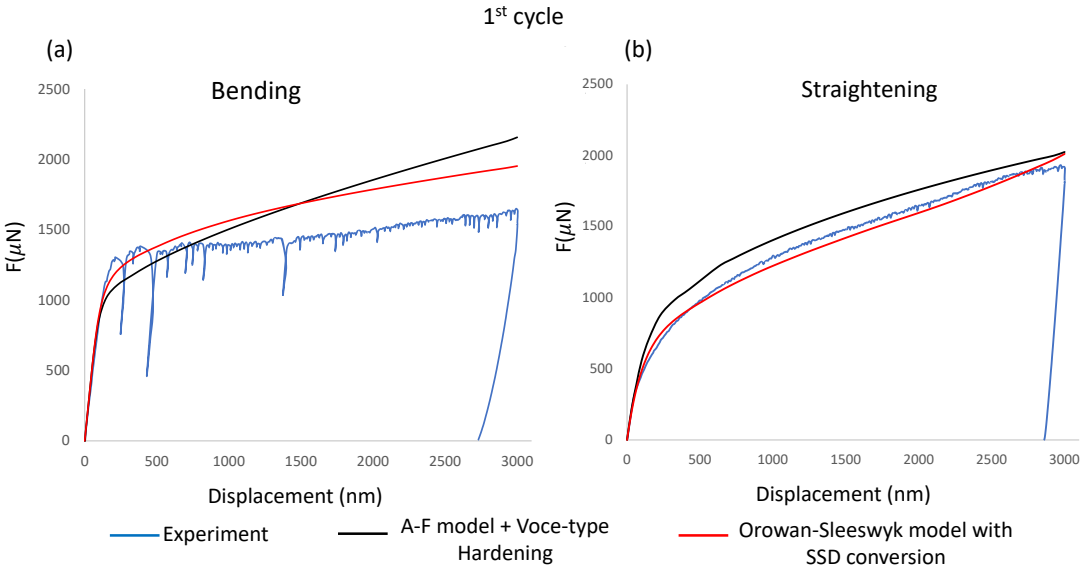

Figure 6.8: Comparison of 1st cycle experimental data with "modified" Orowan-Sleeswyck + SSD conversion and A-F model + Voce type hardening.

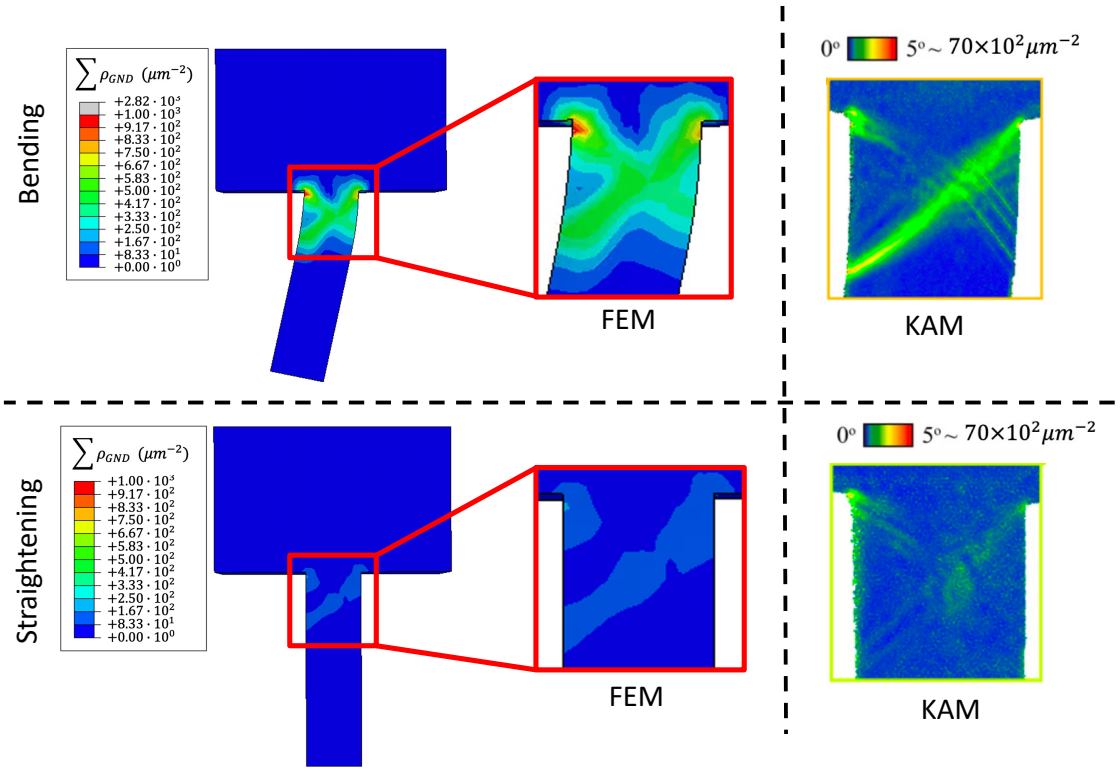

Figure 6.9: Comparison of maps of total GND density between simulations and experimental estimations based on KAM analysis based on three nearest neighbours [173] after the 1^{st} cycle.

The effect of slip bands on total GND distribution is analysed by comparing simulated GND density (Fig. 6.9) with experimental estimations from KAM analysis [173]. KAM data was calculated from the misorientation gradient of each EBSD data point of the Cu cantilever relative to its first, second and third nearest neighbour points. It measures local lattice curvature, and thus, GND density. The calculation of the GND density from the lattice curvature, as described in [173], uses elastic rotation gradients to determine the incompatibility of the lattice (valid only for small deformations [93]), employing L1 minimisation to identify 9 unknown GND densities that accommodate a given lattice curvature. In contrast, our model uses the plastic deformation gradient F_p and a restricted solution for 18 possible GND densities described in [17].

Fig. 6.9 shows an "X-shape" GND distribution in both simulations and KAM analysis. The simulations exhibit a more uniform distribution across the cantilever, while the KAM analysis reveals higher concentrations within the slip bands. During straightening, both simulations and KAM analysis show a significant reduction in GND density at the cantilever's corners and edges. The KAM image shows high GND concentrations due to the slip bands, but it is noteworthy that the KAM analysis is designed for small strains.

Although slip bands were not directly simulated, the model reproduces a very similar GND distribution, suggesting it represents a state preceding the abrupt slips observed, believing it could be obtained experimentally using a lower strain rate. While the geometric effect of the slip bands in Eq. (6.6.8) and Eq. (6.6.10) is evident, the current lack of activation of dislocation sources [223] prevents separating this effect from the constants C_d and λ.

We conclude that our models still have room for improvement. It represents a step towards creating shape and size-independent models (due to the use of GND), but requires considering dislocation sources to model and predict GND concentration.

6.7.4 Comparison of A-F model with Voce-type hardening and Orowan-Sleeswyk model with SSD

The force-displacement profiles of both models demonstrate that the two alternatives are able to reproduce the Bauschinger effect during initial cycles (Fig. 6.5, Fig. 6.7).

The *Orowan-Sleeswyk* model with SSD conversion introduces the physical concept of dislocations such as GND and SSD and their evolution. These models allow us to better understand the internal processes in the material for more complex experiments or other materials. On the other hand, the *A-F with Voce-type hardening* is based on a mathematical approach that considers the relationships between stress, slip γ, and different parameters that need adjustment.

The *Orowan-Sleeswyk* model requires solving Nye's dislocation tensor, making it computationally more

complex and prone to convergence issues (especially at the corners), while the *A-F* model performs better for coarser meshes and is more practical if the goal is to model material fatigue over multiple cycles.

Numerous studies corroborate that hardening saturates after several cycles or higher strains [75, 91]. During the initial cycles, there was no saturation, so adjustment of the saturation parameters in the *A-F model with Voce-type hardening* was not necessary ($A_D \sim 0$ in Eq. (6.6.1) and $\tau_c/s_s \sim 0$ in Eq. (6.6.6)). However, in a cyclic regimen, the *A-F with Voce-type hardening* requires calibration of the saturation parameters. In contrast, the modified *Orowan-Sleeswyk* model does not need additional parameters since the hardening and Bauschinger effect are proportional to $\sqrt{\rho_{GND}}$, attenuating the slope for higher values of ρ_{GND}.

6.7.5 Improvement to the *Orowan-Sleeswyk* model with SSD after multiple cycles

We propose enhancements to the *Orowan-Sleeswyk* model with SSD conversion, incorporating strain rate influence, slip bands effects and cracking due to fatigue accumulation. These enhancements are derived from a literature review and require validation through additional multi-cycle cantilever experiments.

- *Strain rate influence*: Comparing the experiments of the data used in Demir et al. [21] and Ugi et al. [85], the load rate was different. In Demir et al., the load rate was 1 $\mu m s^{-1}$ for a 25.4×8.64×7.05 μm cantilever, while in Ugi et al. the load rate was 5 nms^{-1} for a 20.6×5.0×5.0 μm cantilever. The difference in the strain rate might be responsible for less isotropic hardening during the straightening in Ugi et al. since there is more time for the dislocations to recombine.

  However, this lower strain rate also led to fewer slip band formations in the Ugi et al. cantilever, occurring only at the cantilever's corner. Slip bands play an important role as dislocation obstacles increasing the strain hardening during the initial cycles but also in dislocation recombination by reducing hardening after multiple cycles (reaching dislocation density saturation) and initiating fatigue cracks, as shown in [225, 226].

  The SSD conversion mechanism (see Eq. (6.6.10)) should be positively correlated with the strain rate, however, it also should be positively correlated with any dislocation saturation term derived from slip band formation.

- *Slip Bands effects*: Essmann et al. [227] identified slip bands in single-crystal copper during uniaxial loading fatigue experiments and subsequently proposed the EGM model [225] to explain the slip bands formation, dislocation recombination, and crack development over multiple loading cycles. The formation of slip bands is attributed to the interaction between strain with material extrusions and intrusions. During the initial loading cycles, the dislocation structure exhibits a disorganised pattern, resulting in an accumulation of dislocations over consecutive cycles. This process reaches

saturation after approximately 50 cycles, in which steady-state cyclic deformation is established due to dislocation recombination within the slip bands, achieving a balance between dislocation multiplication and recombination [228].

During steady-state, dislocations form intricate clusters called "veins" outside the slip bands, similar to structures observed in the early cycles. Within the slip bands, edge dislocation density varies, forming high-density and low-density areas known as "cells". The cell characteristics may differ in cantilevers compared to uniaxial loading experiments due to curvature effects, which create distinct tensile and compressive regions separated by a neutral axis.

Modelling dislocation recombination through slip bands can be achieved by incorporating an attenuation term inside Eq. (6.6.10). However, accurate local strain prediction after multiple cycles requires modelling slip bands, including both dislocation sources (extrusions and intrusions) [223] and the recombination mechanisms that occur inside the slip bands [229].

- *Cracking due to fatigue accumulation*: Strain accumulation within slip bands leads to crack initiation when edge dislocations from separate slip systems recombine. The extrusions or intrusions must be left over, debilitating the structure [228]. Cracks can form at the interface between slip bands and the surrounding material or in the rugosity that is formed in the surface of the material due to slip bands [225]. In polycrystals, cracks might also occur at crystal interfaces [230]. In cantilevers, the neutral axis of curvature acts as a dislocation barrier, functioning similarly to polycrystal interfaces.

In summary, understanding strain rate effects on fatigue accumulation, slip bands and crack formation is crucial for enhancing the *Orowan-Sleeswyk* model with SSD conversion. The literature shows that loading rate variations affect slip band formation and dislocation behaviour, which are crucial for crack development. Additional cantilever experiments with extended cycles are needed to validate these proposed improvements and expand our understanding of dislocation processes.

6.8 Conclusions

In this study, we applied well-established models in cyclic deformations to reproduce the Bauschinger effect observed in a copper monocrystal cantilever experiment during the initial bending and straightening cycles. These models were implemented with the OXFORD-UMAT Crystal Plasticity Finite Element code; files, documentation, and examples are available in the GitHub link with open public access [49]. The principal findings are as follows.

- The *Armstrong-Frederick (A-F)* model and their variants (*Chaboche, Ohno and Wang*) failed to repli-

cate the experimental data. The parameters necessary to attenuate the straightening phase result in excessive saturation during subsequent cantilever bending, reaching a point where the resistance no longer increases. While these models are very useful for understanding multiple deformation cycles, they are not suitable for reproducing the initial cycles.

- The combination of *A-F* with *Voce-type hardening* models has proven effective in simulating the initial cycles. The results reveal the confluence of two forms of hardening: the reversible type represented by the *A-F* model, which arises during bending and contributes to the Bauschinger effect, and the irreversible type represented by the *Voce-type hardening* model.
- The *Orowan-Sleeswyk* model failed to replicate the experimental data. Although the hardening is appropriate during the bending, the values obtained during the straightening are well below the experimental results. This discrepancy can be attributed to the near-zero density of geometrically necessary dislocations (GND) when the cantilever is straight, as per the GND formulation.
- In this study, we propose to enhance the *Orowan-Sleeswyk* model by integrating the conversion of certain GND into statistically stored dislocations (SSD). This alternative has proven to be effective in simulating the initial cycles. According to recent research suggesting that a percentage of GND do not recombine during the straightening phase, but rather reorient, leading to increased hardening, our innovation involves considering that a percentage of the GND density reduced is converted to SSD density and incorporating it into the model.
- Both models: *A-F with Voce-type hardening* and *Orowan-Sleeswyk with SSD* are valid alternatives with similar accuracy to reproduce the hardening and Bauschinger effect during the initial cycles. Some of the most significant differences are: *Orowan-Sleeswyk with SSD* allows us to better understand the internal physical mechanisms of the material and is easier to adjust because there are no saturation parameters as the kinematic hardening is proportional to the square root of the GND density, however, it is more computationally complex and prone to convergence issues. On the other hand, *A-F with Voce-type hardening* works better with coarser meshes but it is complicated to adjust several saturation parameters that vary after several cycles or big strains.
- Future research derived from this study should focus on two main areas: Studying how slip bands formation affects the hardening and Bauschinger effect across initial and posterior cycles, and investigating the impact of GND and SSD in polycrystalline materials. Additional cantilever experiments with extended cycles are necessary to validate and expand our understanding of dislocation dynamics.

6.9 Statement of Authorship form

Statement of Authorship for joint/multi-authored papers for PGR thesis

To appear at the end of each thesis chapter submitted as an article/paper

The statement shall describe the candidate's and co-authors' independent research contributions in the thesis publications. For each publication there should exist a complete statement that is to be filled out and signed by the candidate and supervisor **(only required where there isn't already a statement of contribution within the paper itself).**

Title of Paper	Modelling the Bauschinger effect in copper during preliminary load cycles
Publication Status	☐Published ☐ Accepted for Publication ☐Submitted for Publication ☐Unpublished and unsubmitted work written in a manuscript style
Publication Details	Martinez-Pechero, A., Demir, E., Hardie, C., Zayachuk, Y., Widdowson, A., & Tarleton, E. (2025). Modelling the Bauschinger effect in copper during preliminary load cycles. *Acta Materialia*, *289*, 120886.

Student Confirmation

Student Name:	Alvaro Martinez Pechero		
Contribution to the Paper	The student is the corresponding author and was responsible for writing the document, analyzing experimental data, creating Finite Element models and the mathematical formalism, processing results, conducting the literature review, and formulating conclusions. The remaining authors performed the experimental measurements (Dr Eralp Demir), supervised the work, obtained the funding, provided support and advice for the modeling, and reviewed the writing.		
Signature		Date	28th July 2025

Supervisor Confirmation

By signing the Statement of Authorship, you are certifying that the candidate made a substantial contribution to the publication, and that the description described above is accurate.

Supervisor name and title: Professor Edmund Tarleton		
Supervisor comments		
Signature 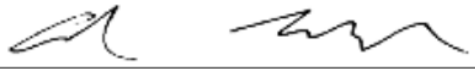	Date	1st August 2025

This completed form should be included in the thesis, at the end of the relevant chapter.

Chapter 7: Single-Crystal Beryllium Cracking: A Crystal Plasticity XFEM Model

Chapter 7 of the thesis is a preprint article that we hope to publish in the coming months with title "Single-Crystal Beryllium Cracking: A Crystal Plasticity XFEM Model", Martinez-Pechero, A., Kuksenko S., J. Long, D., Demir, E., Hewitt, L., Hardie, C., Zayachuk, Y., Widdowson, A., & Tarleton, E. (2025).

This chapter presents the integration of the cohesive zone model (CZM) and extended finite element method (XFEM) with the OXFORD-UMAT Crystal Plasticity code. In this formulation, CZM governs crack initiation and propagation, while XFEM determines the crack trajectory.

The coupled approach is applied to simulate fracture in notched single-crystal beryllium cantilevers. The work constitutes a final integration of the techniques developed throughout this thesis and is used to analyse a highly anisotropic HCP material where plasticity is strongly dependent on crystallographic direction. This anisotropy directly influences crack initiation and propagation behaviour. The final outcome is a Crystal Plasticity code that unifies models for fatigue or kinematic hardening, GND density calculation, and fracture mechanics, enabling the simulation of complex material experiments used in the nuclear industry.

Single-Crystal Beryllium Cracking: A Crystal Plasticity XFEM Model

7.1 Abstract

This study analyses and models single-crystal beryllium cracking, motivated by its importance in fusion reactors for tritium production. Determining the mechanical properties of beryllium is challenging due to its toxicity and small grain size. For this work, notch cantilever experiments were conducted at different crystal orientations, yielding force-displacement curves.

Crystal-Plasticity Extended Finite Element Method (CP+XFEM) models were employed to successfully reproduce fracture behaviour and propagation. The models incorporate a unified criterion that combines plasticity with Mode I and Mode II fracture. This work extends the OXFORD-UMAT code by integrating fracture treatment.

The study characterises the fracture properties of single-crystal beryllium, revealing a significant difference between Mode I and Mode II fracture initiation stresses. This anisotropy explains the orientation-dependent maximum failure stress observed in the experiments. The findings provide insights into beryllium's mechanical behaviour at the microscale, contributing to the understanding of its performance in fusion reactors.

7.2 Introduction

Beryllium (Be) has distinct mechanical and physical properties, such as low density, good radiation resistance, high strength, and excellent heat conductivity, making it suitable for harsh environments and crucial for nuclear applications such as fusion or fission [231, 232].

Be is considered a potential candidate for the construction of the first protection wall of fusion reactors [231] and plays a crucial role in the production of tritium, an essential fuel for fusion reactors that is scarce in nature.

One method of generating tritium is through the reaction of lithium with the neutrons produced during the fusion process, but this process yields only one tritium atom per captured neutron and consumes another tritium atom to produce that neutron (having important neutron losses). To overcome this limitation, Be has been proposed as a neutron multiplier, as shown in the following chemical reaction [22].

$$^{9}\mathrm{Be} + \mathrm{n} \rightarrow 2\alpha + 2\mathrm{n}' - 2.5\mathrm{MeV} \tag{7.2.1}$$

The *breeding blanket*, located behind the first wall and composed of Be and Li pebbles, is responsible for capturing the neutrons produced by the fusion reaction to produce tritium and convert their kinetic energy into heat for power generation [233]. The ITER prototype *Helium-Cooled Ceramic Breeder Blanket (HCCB)* utilises this design within a SiC structure cooled by He at $600/900^{o}C$ [22]. Extreme temperatures and cooling processes cause the structure to expand and contract, generating high stress that can lead to cracking due to the inherent brittleness of Be and SiC. Consequently, studying the cracking properties of these materials is essential to ensure the structural integrity and avoid the formation of Be dust, which is highly toxic [234].

Be is a *hexagonal close-packed* (HCP) material with a c/a ratio of 1.567 at room temperature [54]. The plasticity of HCP is influenced by the crystal orientation of grains, the grain size [99], and the presence of defects in the material [100]. The two primary mechanisms for plasticity are *slip* and *twinning*. *Slip* occurs when atoms slide along specific crystalline planes [101], while *twinning* involves the crystal lattice splitting into two separate mirror-image parts at the crystalline boundaries [235].

The fracture process in Be is complex to study due to the significant role of slip plasticity, which is dependent on crystal orientation. This article focuses on the fracture properties of Be single-crystals, excluding the effects of grain boundaries such as crystal twinning.

For this analysis, several experiments have been conducted using an indenter to apply pressure on notched cantilevers at different crystal orientations. Depending on the alignment of the basal slip system relative to the cantilever tension, distinct fracture behaviours were observed.

Based on the data of these experiments, the main objectives of this study are: a) Determine a fracture propagation criterion and investigate its dependence on crystal orientation, b) Create an *Extended Finite Element Method* (XFEM) model coupled with the OXFORD-UMAT crystal plasticity code [18] to model the full deformation process from plastic slip to completed fracture.

7.3 Cantilever experiments

The fracture properties of single-crystal Be are challenging to determine due to its small grain size and the toxicity of the dust formed during fracture, which can cause long-term health effects. A classical method for measuring fracture toughness involves fracturing a pre-notched cantilever. Di Maio et al. [109] used a *Focused Ion Beam* (FIB) to create a pre-cracked micro cantilever from a bulk specimen. Then, by applying nano-indentation, the material's toughness is obtained from the load-displacement curves.

We applied the FIB technique to produce the same cantilever geometry for Be single-crystals along different crystal orientations and used a Crystal Plasticity *Finite Element Model* (CPFEM) to determine the Be properties through the force-displacement response of each indentation.

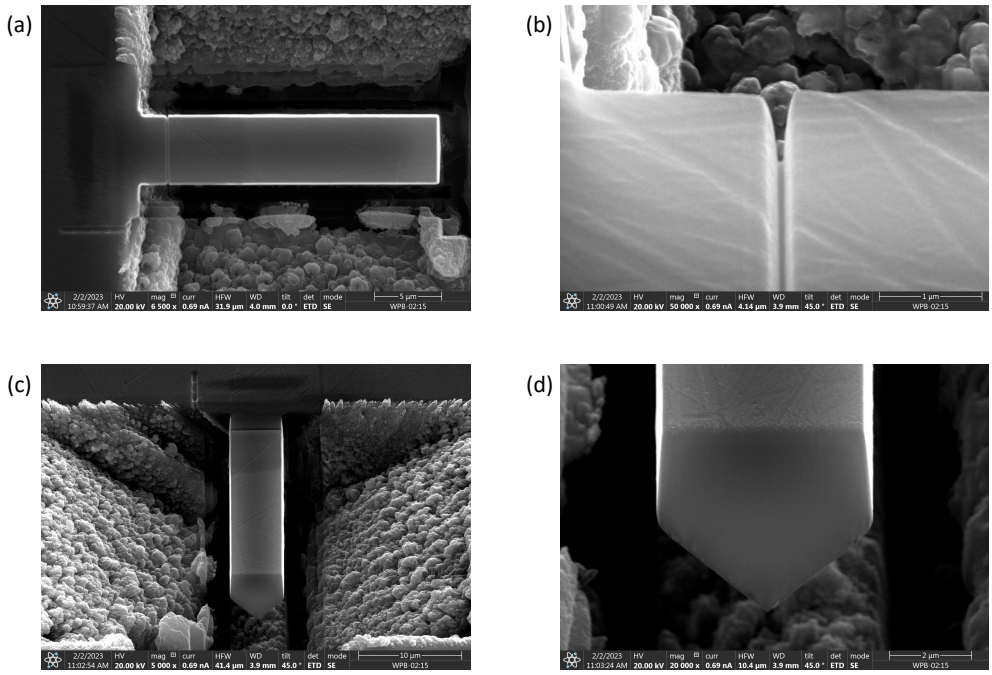

Figure 7.1: SEM images from different angles of Cantilever 1.

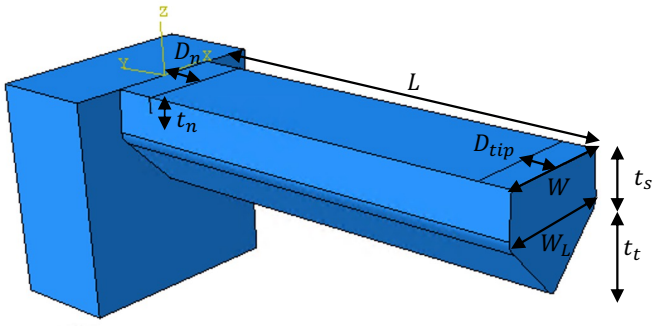

Figure 7.2: Scheme of cantilever dimensions used in Table 7.1.

The load was applied through a displacement-controlled Berkovich indenter [105] at 5 nm/s. The geometry of the cantilevers is illustrated schematically in Fig. 7.2. The corresponding dimensions, summarised in Table 7.1, were measured from SEM images as Fig. 7.1.

#	L (μm)	W (μm)	W_L (μm)	t_s (μm)	t_t (μm)	D_{tip} (μm)	D_n (μm)	t_n (μm)	Euler Angles(°)
1	22.20	4.86	5.22	3.19	3.05	1.90	1.95	0.90	(146.7, 102.1, 6.3)
2	20.61	5.28	5.52	2.41	3.07	2.00	2.20	0.65	(171.5, 103.7, 45.4)
3	21.77	4.30	4.55	2.65	2.7	1.82	2.15	0.90	(88.1, 60.4, 28.9)

Table 7.1: Dimensions of the cantilever (see nomenclature in Fig. 7.2), and Euler angles.

Consistent with literature [236, 237], the fracture process exhibited a crack path perpendicular to the normal

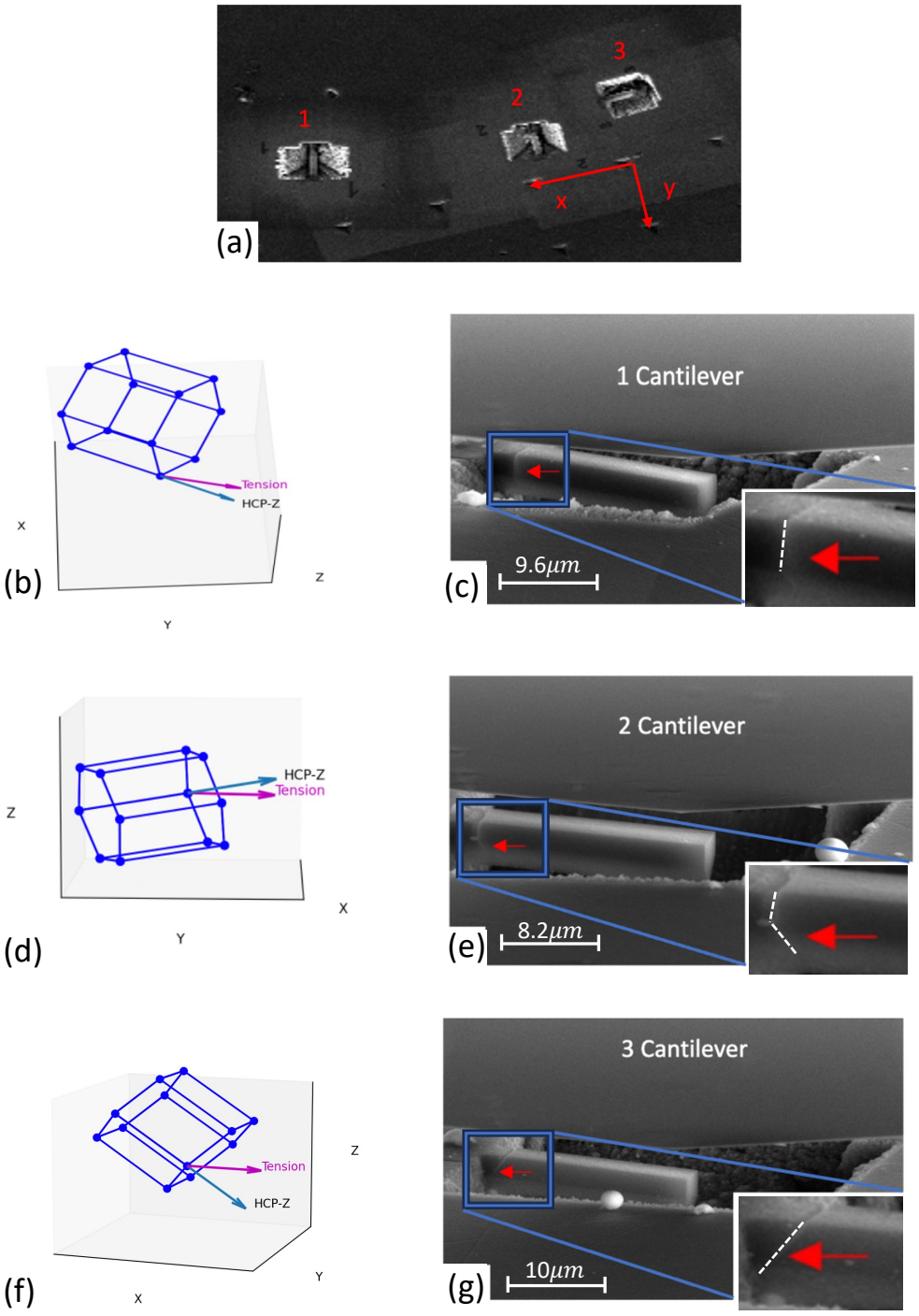

Figure 7.3: (a) SEM images of the three cantilevers with their xyz orientation. (b,d,f) Crystal orientation of cantilevers 1-2-3. (c,e,g) Crack path of cantilevers 1-2-3.

of the slip system plane with the highest Schmid factor. In HCP materials like Be, this corresponds to the basal slip systems (see Fig. 7.3 (c, e, g)).

Fig. 7.4 shows the force-displacement responses of the notched cantilevers. A voltage drift that increases over time affects the measurements in the load cell of the indenter, resulting in a time-increasing error. This drift was calculated by fitting a linear relation of the load-time data during the indenter approach to the cantilever and after indenter unloading. The corrected force-displacement curves are the uncorrected force-displacement curves minus their drifts. The uncorrected force-displacement curves and the drifts are presented in Appendix D.1.

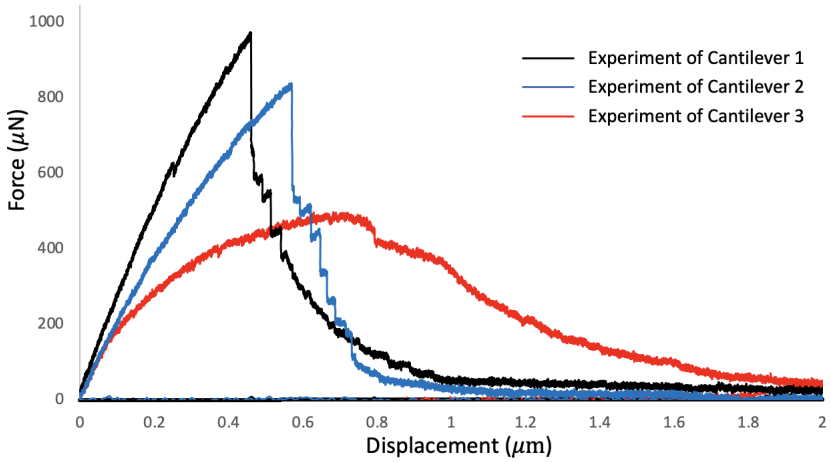

Figure 7.4: Force-displacement curves of the cantilever experiments.

#	[1 0 0](0 0 1)	$[1\bar{2}\ \sqrt{3}/2\ 0](0\ 0\ 1)$	$[1\bar{2}\ \sqrt{\bar{3}}/2\ 0](0\ 0\ 1)$
1	0.18	0.23	0.05
2	0.12	0.24	0.11
3	0.44	0.41	0.03

Table 7.2: Schmid factor of the different basal slip systems concerning the tension stress.

Cantilever 3 (C3) presents a higher Schmid factor relative to the applied tensile force compared to C1 and C2 (see Table 7.2), which aligns with the force-displacement curves showing greater plasticity in C3.

During the crack initiation, the peak force is significantly lower in C3. Given the similar dimensions of all three cantilevers, this indicates that C3 has lower *Crack Initiation Stress* than C1 and C2.

Regarding fracture completion, C3 presents a larger displacement prior to complete fracture. We cannot experimentally determine which portion of this increased resistance is attributed to plasticity and which is related to the fracture process. To overcome these experimental limitations, we use FEM simulations that integrate representations of plasticity and fracture to gain a clearer understanding of their respective contributions.

7.4 Modelling

Crystal Plasticity can simulate the plastic deformation of HCP materials, and the *Extended Finite Element Method (XFEM)* can model the fracture without the need for remeshing during crack propagation. This study extends the *OXFORD-UMAT code* to a Crystal Plasticity Extended Finite Element Modelling (CP+XFEM) framework to model crack propagation in Be (a detailed description of the OXFORD-UMAT code can be found in [18]).

7.4.1 Crystal plasticity framework

This section presents an overview of the crystal plasticity kinematics and constitutive laws governing slip behaviour in Be*.

Crystal plasticity kinematics

The deformation gradient in a crystal under stress can be defined by $\boldsymbol{F_{tot}} = \boldsymbol{F_e F_p}$, where $\boldsymbol{F_e}$ is the mechanical elastic deformation gradient and $\boldsymbol{F_p}$ the plastic deformation gradient.

The mechanical elastic deformation gradient $\boldsymbol{F_e}$ can be calculated by $\boldsymbol{F_e} = I + \varepsilon_e$, where I is the identity matrix and ε_e is the elastic strain which depends on the total strain minus the plastic strain $\varepsilon_e = \varepsilon - \varepsilon_p$.

The plastic deformation gradient $\boldsymbol{F_p}$ is calculated from the plastic velocity gradient $\boldsymbol{L_p}$, which is the sum of the slip rates $\dot{\gamma}^a$ times the Schmid tensor $\boldsymbol{S^a}$ of each slip system ^{a}, which is the dyadic product $\boldsymbol{s^a} \otimes \boldsymbol{n^a}$, where $\boldsymbol{s^a}$ is the slip direction and $\boldsymbol{n^a}$ the slip plane normal [218]:

$$\boldsymbol{L_p} = \dot{\boldsymbol{F}}_p \boldsymbol{F}_p^{-1} = \sum_a \dot{\gamma}^a \, \boldsymbol{s^a} \otimes \boldsymbol{n^a} = \sum_a \dot{\gamma}^a \, \boldsymbol{S^a}. \tag{7.4.1}$$

However, the slip system undergoes elastic deformations, transforming the slip and normal direction to a deformed configuration $(\boldsymbol{n_e^a}, \boldsymbol{s_e^a})$:

$$\boldsymbol{s_e^a} = \boldsymbol{F_e} \, \boldsymbol{s^a}; \quad \boldsymbol{n_e^a} = \boldsymbol{F_e^{-T}} \, \boldsymbol{n^a} = \boldsymbol{n^a} \, \boldsymbol{F_e^{-1}}. \tag{7.4.2}$$

The rotation, $\boldsymbol{g}_{ij}$, is applied to transform the experiment reference frame during calculations (Bunge convention), where ϕ_1, Φ, and ϕ_2 are the Euler angles [51] (see Appendix B.1 for further details). The temporal evolution of the crystal orientation is computed by updating $\boldsymbol{g}_{ij}$ from an initial time t to a subsequent time

*Throughout this study, the second rank tensors are with capital letters in bold fonts, $\boldsymbol{A}$ or A_{ij}, vectors with small letters in bold fonts, $\boldsymbol{a}$ and scalars with regular fonts, a.

$t+\Delta t$, where Δt is the discrete time increment. This update can be expressed as

$$\boldsymbol{g}_{ij} = \boldsymbol{g}_{ij,(t+\Delta t)} = (\boldsymbol{I} + \boldsymbol{\Delta\Omega_e}\,\Delta t)\,\boldsymbol{g}_{ij,t} \implies \dot{\boldsymbol{g}}_{ij} = \frac{\boldsymbol{g}_{ij,(t+\Delta t)} - \boldsymbol{g}_{ij,t}}{\Delta t} = \boldsymbol{\Delta\Omega_e}\,\boldsymbol{g}_{ij,t}. \tag{7.4.3}$$

Where $\boldsymbol{\Delta\Omega}_e$ is the elastic spin obtained by subtracting the plastic spin from the total spin:

$$\boldsymbol{\Delta\Omega_e} = \boldsymbol{\Delta\Omega} - \boldsymbol{\Delta\Omega_p}; \quad \begin{cases} \boldsymbol{\Delta\Omega_p} = \sum_a \boldsymbol{W}^a \dot{\gamma}^a \\ \boldsymbol{\Delta\Omega} = \dfrac{\boldsymbol{L} - \boldsymbol{L}^T}{2} \end{cases} \tag{7.4.4}$$

$$\boldsymbol{W^a} = \frac{1}{2}\left(\boldsymbol{s_e^a} \otimes \boldsymbol{n_e^a} - \boldsymbol{n_e^a} \otimes \boldsymbol{s_e^a}\right), \tag{7.4.5}$$

where $\boldsymbol{W}^a$ is the antisymmetric matrix of the Schmid tensor, and $\dot{\gamma}^a$ is the slip rate, which is determined by the slip constitutive law. $\boldsymbol{L}$ is the velocity gradient of the total strain, defined by $\boldsymbol{L} = \dot{\boldsymbol{F}}\boldsymbol{F}^{-1}$.

The equations set are solved through a semi-implicit algorithm implemented within a user-defined material subroutine (OXFORD-UMAT, [17]) for the finite element software Abaqus. This code utilises the Forward-Gradient algorithm [52] to obtain the approximate initial solutions for the Cauchy stress.

Constitutive laws

The constitutive laws are determined by the elasticity and the slip rate governing plastic deformation (see Eq. (7.4.1)). Elasticity theory relates the rotation-free objective Jaumann rate of stress, $\overset{\nabla}{\boldsymbol{\sigma}}$ [220], to the elastic deformation rate, $\boldsymbol{d}_e$. This relationship is expressed using the 4^{th} elasticity tensor, $\mathbb{C}$, for the deformed configuration in Voigt notation [187]:

$$\overset{\nabla}{\boldsymbol{\sigma}} = \mathbb{C} : \boldsymbol{d}_e; \quad \mathbb{C} = \boldsymbol{R}\mathbb{C}_0\boldsymbol{R}^T. \tag{7.4.6}$$

Where $\mathbb{C}$ is a 6×6 matrix obtained by applying the rotation matrix $\boldsymbol{R}$ to the elastic stiffness constant $\mathbb{C}_0$ [55], thus adjusting it from the crystalline reference to the experimental one (see Appendix B.1). For Be, a HCP material, we used the following elastic constants to represent the elastic anisotropy: E_1 = E_2 = 289 GPa, E_3 = 335 GPa, G_{12}=138 GPa, G_{13} = G_{23}=162 GPa and ν_{12} = 0.09, ν_{13} = ν_{23}= 0.04 [101, 232]

The plasticity is determined by the slip rate law, denoted by $\dot{\gamma}$. We apply the sinh formula from [48], which has been previously applied to Be in [105] with the model parameters presented in Table 7.3.

$$\dot{\gamma}^a = \alpha \sinh\left(\beta\left(|\tau^a| - \tau_c^a\right)\right) \mathrm{sign}(\tau^a) \tag{7.4.7}$$

$$\alpha = \rho_m b^2 \nu_0 \exp\left(-\frac{\Delta F}{K_B T}\right); \quad \beta = \frac{\Delta V}{K_B T} \tag{7.4.8}$$

parameter	definition	unit	values
$b_{<a>}$	burgers vector length	nm	0.228
$b_{<c+a>}$	burgers vector for $< c+a >$ systems	nm	0.424
ΔF	activation energy for slip	eV/mol	0.216
ν_0	attempt frequency	1/s	10^{11}
K_B	Boltzmann constant	$\text{eV}\cdot\text{K}^{-1}$	$8.617 \cdot 10^{-5}$
T	Temperature	K	293
ρ_m	mobile dislocation density	$1/\mu m^2$	$2 \cdot 10^{-3}$
ΔV	Activation Volume	b^3	20

Table 7.3: Parameters used to determine the plasticity of Be.

In HCP crystals, there are 3 basal, 3 prismatic and 24 pyramidal slip systems [102]. The burgers vector length is equal to the length of one edge of the hexagonal base $< a >$ for the basal, prismatic and 6 of the pyramidal slip systems. The remaining 18 pyramidal slip systems have a burgers vector length of $\sqrt{c^2+a^2}$, where c is the height of the hexagonal prism.

According to the literature [105, 103, 104], the 6 second-order pyramidal slip systems are sufficient to reproduce the plasticity in the $< c >$ direction, avoiding the computational cost of simulating all 24 pyramidal systems. We tested both cases, applying the same *Critical Resolved Shear Stress* (CRSS) for all the pyramidal slip systems, and found no significant differences. The negligible difference can be attributed to the high CRSS of the pyramidal slip systems compared to the basal and prismatic systems (further details in Subsect. Slip Hardening model).

The constants ΔF, ν_0, K_B were obtained from the literature [105], and $T = 293\ K$ represents room temperature. The constants ρ_m and ΔV were adjusted using the force-displacement curves from the Be cantilever experiments. Kuksenko et al. [105] reports $\rho_m = 3 \cdot 10^{-3} \mu\text{m}^{-2}$ and a dislocation density-dependent ΔV, we use a constant value of $\Delta V = 20 \cdot b^3$, similar to other HCP plasticity studies to simplify the adjustment process and avoid convergence issues [107, 238, 97, 20].

Slip Hardening model

The CRSS τ_c^a on slip system a is defined by the Taylor hardening equation [95]:

$$\tau_c^a = \tau_c^{0,a} + Gb\sqrt{\rho^a}. \tag{7.4.9}$$

Where ρ^a is the dislocation density, G is the shear modulus and $\tau_c^{0,a}$ is the initial strength of CRSS. The $\tau_c^{0,a}$

values are: τ_c=15.2 MPa for $<a>$ basal, τ_c= 67.7 MPa for $<a>$ prismatic, and τ_c=172.5 MPa for $<c+a>$ second-order pyramidal slip systems [103]. The mobility of the 18 remaining $<c+a>$ systems is lower according to dislocation models [104], and they are neglected.

The dislocation evolution law was formulated based on the total dislocation density, rather than the forest dislocations, as in [101]. This approach simplifies the incorporation of additional effects beyond forest hardening, such as kinematic hardening [20] and debris dislocation dynamics [101].

During this study, we used the Kocks-Mecking hardening [239] as evolution law, with an initial dislocation density of $\rho_O = 1.25\mu\text{m}^{-2}$, consistent with the value $\rho_O = 1.0\mu\text{m}^{-2}$ reported by [105].

$$\dot{\rho^a} = \left(\frac{k_1}{b^a} \sqrt{\sum H_{a,b}\rho^b} - k_2\rho^a \right) \dot{\gamma^a}. \tag{7.4.10}$$

The interaction matrix $H_{a,b}$, which defines the latent hardening between slip systems, was assigned an interaction coefficient of $H_{a,b} = 1.0$ for all a, b, similar to the value used in [240]. The parameters k_1 and k_2 were calibrated using the Nelder-Mead optimisation method through successive FEM Abaqus simulations [13]. The objective function used to optimize the parameter values was defined as:

$$D = \sum_{Cant} \frac{\int \mid F_{FEM}(u) - F_{EXP}(u) \mid du}{\text{N}_{Cant} \int \mid F_{EXP}(u) \mid du}, \tag{7.4.11}$$

where F_{FEM} and F_{EXP} are the modelled and experimental forces during the indentation process until crack propagation begins, u is the indenter displacement, and N_{Cant} is the number of cantilevers experiments modelled.

The parameter k_1 was calibrated to 1.03 within a search domain of $0.1 \leq K_1 \leq 3$, with a sensitivity range of $0.94 \leq K_1 \leq 1.13$ corresponding to an additional 10% error. The parameter k_2 was calibrated to 1000 within a search domain of $0 \leq K_2 \leq 3000$, with a sensitivity range of $950 \leq K_2 \leq 1090$ corresponding to an additional 10% error.

7.4.2 Extended Finite Element Method (XFEM)

Modelling cracks using the traditional finite element method requires the mesh to conform to geometric discontinuities with significant refinement near the crack tip. This process becomes more complex when dealing with a progressing crack because the mesh must be continuously updated.

The *EXtended Finite Element Method (XFEM)*, introduced by Belytschko et al. [23], overcomes these challenges by incorporating additional functions to represent discontinuities or singularities while preserving

the sparsity and symmetry of the finite element framework.

The enrichment functions include a *"crack-tip"* function, capturing the behaviour near the crack tip, and a *"crack-jump"*function representing the displacement jump across the crack [42]. The displacement of the nodes of the elements, $\boldsymbol{u}$, is given by:

$$\boldsymbol{u} = \sum_{I=1}^{N} N_I(x) \left[\boldsymbol{u}_I + H(x)\boldsymbol{a}_I + \sum_{\alpha=1}^{4} F_\alpha(x)\boldsymbol{b}_I^\alpha \right], \tag{7.4.12}$$

where $N_I(x)$ and $\boldsymbol{u}_I$ are the standard shape and displacement FEM functions applicable to all elements in the model. The term $H(x)\boldsymbol{a}_I$ represents the jump enrichment for elements crossed by the crack, $\boldsymbol{a}_I$ is the enriched degree of freedom vector in the nodes of the elements and $H(x)$ the *"crack-jump"* function. Similarly, $\sum_{\alpha=1}^{4} F_\alpha(x)\boldsymbol{b}_I^\alpha$ represents the tip enrichment for elements in the crack tip, $\boldsymbol{b}_I^\alpha$ is the nodal enriched degree of freedom vector and $F_\alpha(x)$ the associated elastic asymptotic "crack-tip" function (see Fig. 7.5(a)).

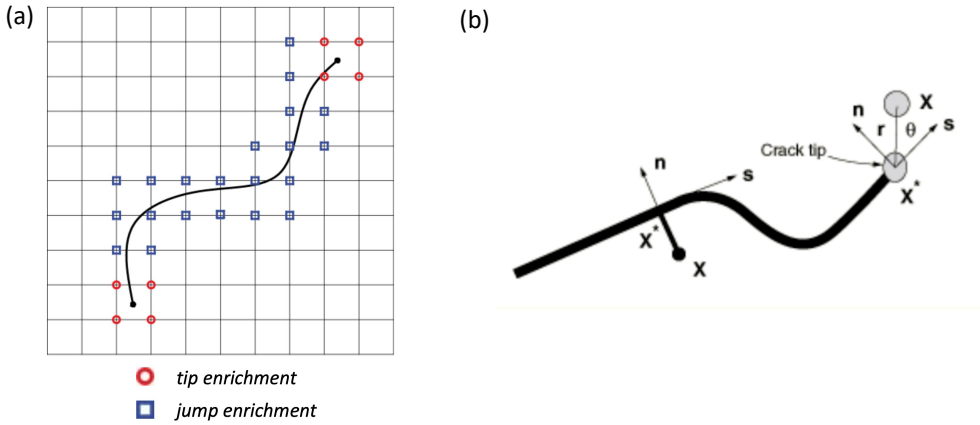

Figure 7.5: (a) Crack propagation and enrichment of the different elements. (b) Illustration of normal and tangential coordinates for a smooth crack [42].

The *"crack-jump"* function $H(x)$ is a step function, where x is a Gauss point, x^* is the point on the crack closest to x, and n is the unit outward normal to the crack at x.

$$H(\mathrm{x}) = \begin{cases} 1 \text{ if } (\boldsymbol{x} - \boldsymbol{x}^*) \cdot \boldsymbol{n} \geq 0 \\ -1 \text{ otherwise} \end{cases} \tag{7.4.13}$$

The *"crack-tip"* function $F_\alpha(x)$ is designed to accurately model the stress singularity that develops at the crack tip. This function uses a polar coordinate system (r, θ), where the origin is located at the crack tip and the angle $\theta = 0$ corresponds to the tangent to the crack at the tip (see Fig. 7.5(b)):

$$F_\alpha(x) = \left[\sqrt{r}\sin\frac{\theta}{2}, \sqrt{r}\cos\frac{\theta}{2}, \sqrt{r}\sin\theta\sin\frac{\theta}{2}, \sqrt{r}\sin\theta\cos\frac{\theta}{2}\right], \tag{7.4.14}$$

To model discontinuities and cohesive behaviour, special "phantom" nodes are added alongside the real nodes. Initially, each phantom node is connected to its corresponding real node. When the material damage initiation criterion is satisfied, the nodes begin to separate according to a cohesive law (degradation of the element stiffness matrix) until the damage completion criterion is accomplished. When the cohesive strength drops to zero, indicating the crack propagates through the element, the phantom and real nodes separate, splitting the element into two, each with both real and phantom nodes [241].

XFEM is integrated with the OXFORD-UMAT code through the Abaqus UDMGINI Library [42], where the crack direction (normal vector of the crack surface) and propagation are specified according to the criteria explained in the following sections.

Crack direction criteria

The cracks propagate along the basal plane of the HCP crystal structure of Be (0 0 1), similar to the crack direction observed in the experiments and literature [98, 242, 236, 237, 243].

The propensity for cracking along the basal plane is attributed to its reduced toughness and cohesive strength compared to other planes within the HCP structure [242, 244]. Although the literature has reported cracks in the prismatic planes [236], cracks typically initiate in the basal direction and tend to deviate to other slip planes after reaching a length of $\sim 50\mu$m. This deviation was not observed in our cantilever experiments, where the cracks were $<5\mu$m.

The OXFORD-UMAT code is designed to evaluate crack propagation along multiple planes in a crystal structure. It evaluates the damage initiation criteria (see Eq. (7.4.15)) for each slip plane, and the crack propagation follows the plane that first satisfies these criteria.

Crack propagation criteria

The crack propagation process is based on the cohesive bilinear law [41] and structured in three stages: damage initiation, damage progression, and damage completion. These stages are described in detail in the following paragraphs.

Damage Initiation: Initially, the stress-strain response of the material is obtained from the OXFORD-

UMAT code until the stress in the element reaches the damage initiation criterion represented by:

$$\sqrt{\left(\frac{\langle \tau_n \rangle}{\sigma_I^{\max}}\right)^2 + \left(\frac{\tau_s}{\sigma_{II}^{\max}}\right)^2} = 1, \qquad \langle \tau_n \rangle = \tau_n \text{ if } \tau_n > 0 \quad \text{or} \quad \langle \tau_n \rangle = 0 \text{ if } \tau_n < 0, \tag{7.4.15}$$

where σ_I^{max} and σ_{II}^{max} are the cohesive strengths for Mode I and II (Mode III is ignored for this model, assuming that twisting is not possible in a cantilever crack). While Mode I represents the theoretical cleavage strength (the force required to separate atomic planes), Mode II is influenced by basal plane slip, which occurs because the stress exceeds the CRSS and generates dislocations that weaken the crystal structure.

The normal stress responsible for Mode I cracking, τ_n, is calculated by projecting the traction stress, $\boldsymbol{\tau}$ (representing the stress acting on the basal plane) onto the direction of normal base plane ($\boldsymbol{n}$) to isolate the mode I stress component (the opening mode). This traction stress is previously calculated by projecting also the stress tensor $\boldsymbol{\sigma}_{ij}$ onto the normal basal plane. Simplifying this process, we obtain:

$$\tau_n = \boldsymbol{\tau} \cdot \boldsymbol{n} = (\boldsymbol{\sigma}_{ij} \cdot \boldsymbol{n}) \cdot \boldsymbol{n} = \boldsymbol{n} \cdot \boldsymbol{\sigma}_{ij} \cdot \boldsymbol{n} \tag{7.4.16}$$

The shear traction τ_s responsible for Mode II is calculated by subtracting the normal component $\boldsymbol{\tau}_n = \tau_n \cdot n$ from the traction stress $\boldsymbol{\tau}$ (assuming that Mode III is negligible).

$$\tau_s = |\boldsymbol{\tau} - \boldsymbol{\tau}_n| = |(\boldsymbol{\sigma}_{ij} \cdot \boldsymbol{n}) - (\boldsymbol{n} \cdot \boldsymbol{\sigma}_{ij} \cdot \boldsymbol{n}) \cdot \boldsymbol{n}| \tag{7.4.17}$$

The results should be similar to the *Ultimate Tensile Stress* value (UTS, maximum stress that a material reaches before its resistance is reduced). Jones et al. [242] obtained UTS= 0.31-0.59 GPa, but in experiments with polycrystals, Lee et al. [245] reported an average fracture stress of 1.97 GPa for single-crystal, but the fracture was obtained from compression. Attempts to find more recent experimental data for Be single crystals have been unsuccessful, opening the door to future lines of research in this field.

The parameters were adjusted by Nelder-Mead optimisation over Abaqus simulations[20]. The distance function D between the modelling results and the experimental values is determined by Eq. 7.4.11 and it is calculated during the full bending process until the fracture is completed.

The parameter σ_I^{max} was optimised to 1.91 GPa within a search domain of 0.1 GPa $\leq \sigma_I^{max} \leq$ 3GPa, the sensitivity range is 1.65 GPa $\leq \sigma_I^{max} \leq$2.33 GPa corresponding to an additional 10% error. The parameter σ_{II}^{max} was optimised to 0.34 GPa, within a search domain of 0.1 GPa $\leq \sigma_I^{max} \leq$ 3GPa, the sensitivity range is 0.29 GPa $\leq \sigma_I^{max} \leq$0.4 GPa.

The difference between the values ($\sigma_I^{max} \approx 5 \cdot \sigma_{II}^{max}$) is due to the anisotropy of HPC materials, with Mode

II more susceptible to dislocation movement.

Damage Progression: Once the cohesive damage has been initiated, the material's resistance is affected by the damage variable D, which is 0 at damage initialisation and increases linearly to 1 upon reaching the damage completion criterion. The damage progression is calculated by Eq. (7.4.18), where $\hat{\tau}_n$ and $\hat{\tau}_s$ represent the normal and shear components when the cohesive region (region that is suffering the crack formation) is undamaged.

$$\tau_n = \begin{cases} (1-D)\hat{\tau}_n; & \tau_n > 0, \\ \hat{\tau}_n; & \tau_n \leq 0, \end{cases} \qquad (7.4.18)$$
$$\tau_s = (1-D)\hat{\tau}_s;$$

Damage Completion: The damage completion criteria is defined by Eq. (7.4.19),

$$G = G_I + G_{II}, \qquad (7.4.19)$$

where $G_I = \int \tau_n d\delta_n$ and $G_{II} = \int \tau_s d\delta_s$ are the energetic work of fracture.

The toughness was calibrated through Nelder-Mead optimization method to $G = 8.5\ \mathrm{J}/m^2$, the optimisation process was performed simultaneously with G, σ_I^{max} and σ_{II}^{max} throughout the entire cantilever bending process using the distance function defined by Eq.7.4.11.

The search domain was $1\ \mathrm{J}/m^2 \leq G \leq 20\mathrm{J}/m^2$ and the sensitivity range was $5.3\ \mathrm{J}/m^2 \leq G \leq 11.4\ \mathrm{J}/m^2$ corresponding to an additional 10% error between modelling and experimental data. The toughness value is consistent with $G = 6-10\ \mathrm{J}/m^2$ reported in the literature for single crystals experiments [242, 244].

7.4.3 Boundary conditions, mesh, and Indenter Modelling

A fully clamped boundary condition was applied to the base of the cantilevers, constraining all translational degrees of freedom (U1=U2=U3=0) to simulate a rigid fixture (the cantilevers are embedded inside a material). The loading protocol consisted of a prescribed vertical displacement applied to a line of nodes on the superior surface at the distal end of the beam, as illustrated in the Fig. 7.6. This displacement was ramped linearly at a quasi-static rate of 5 nm/s. The simulation proceeded until a maximum displacement of 1 μm was reached for C1, C2, and 2 μm for C3.

The continuum was discretised using first-order, eight-node linear brick elements (C3D8). The mesh density was selected to ensure adequate resolution of stress and strain gradients while maintaining computational

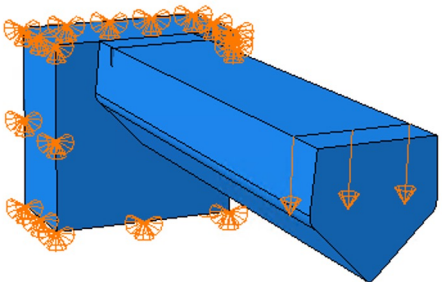

Figure 7.6: Boundary conditions of cantilever 1, similar to cantilever 2 and 3.

efficiency. The resulting models consisted of C1=62,653, C2=40,280 and C3=39476 elements.

Modelling cantilever experiments using a line of element nodes instead of simulating the full geometry and behaviour of the Berkovich indenter is a simplification that facilitates model convergence and significantly reduces computational costs. Appendix D.2 verifies that incorporating the Berkovich indenter into the model does not significantly alter the results.

In this work, we adopted a line of nodes because the current version of the OXFORD-UMAT code does not support the combination of XFEM and the particularities of the indenter contact during fracture modelling. This limitation will be addressed in future versions.

7.5 Modelling Results

Fig. 7.7 shows the force-displacement curves obtained from experiments and CP+XFEM simulations. The results demonstrate strong agreement between the model and the experiments, capturing the distinct mechanical responses dictated by crystallographic orientation.

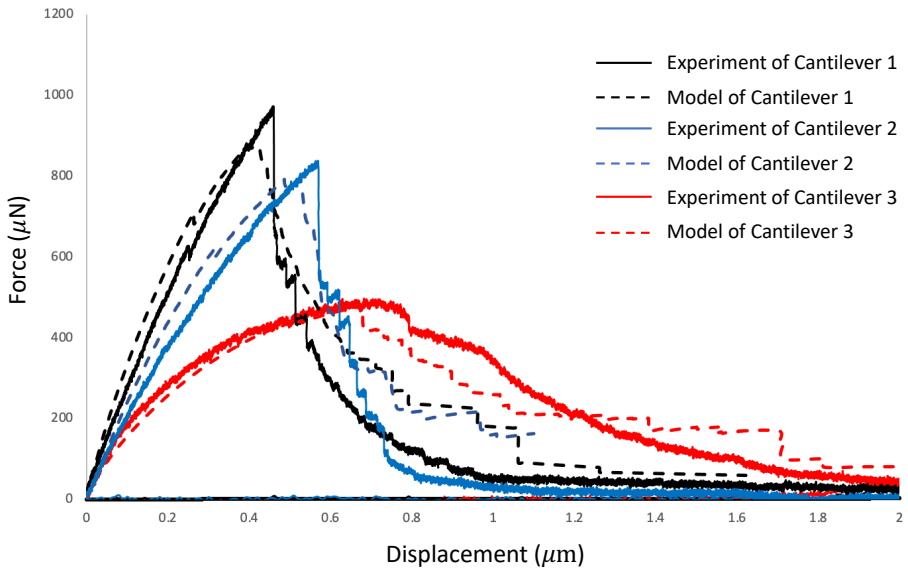

Figure 7.7: Force–Displacement of the model versus experimental data.

During the stage prior to peak force, C1 and C2 exhibit a brittle behaviour, characterised by a near-linear elastic response with minor load drops indicative of small, stable crack initiations before reaching the maximum force. Conversely, C3 exhibits a significantly more ductile behaviour, with a pronounced non-linear response preceding the peak load. This increased ductility is attributed to its crystallographic orientation, which results in a higher Schmid factor for the basal slip system relative to the tensile stress experienced by the cantilever (see Table 7.2). The model predicts the maximum force for each case, with deviations between experimental and modelled peak forces of C1=197μN (11%), C2=41μN (5%), and C3=5μN (1%).

The model also accurately replicates the post-fracture behaviour observed in the experiments. For the more brittle C1 and C2, the force drops abruptly after the peak load, indicating rapid, uncontrolled crack propagation. In contrast, C3 exhibits a more gradual failure, consistent with significant plastic flow from the active slip system, accommodating deformation and allowing for more controlled crack growth. While the models successfully reproduce the onset and general trend of these force drops, the simulated fracture propagation manifests as a distinct step-wise or "staircase" pattern. This is a known numerical artefact of the discrete crack advancement within the XFEM framework, associated with the crack propagation into discrete elements instead of a continuous medium [23].

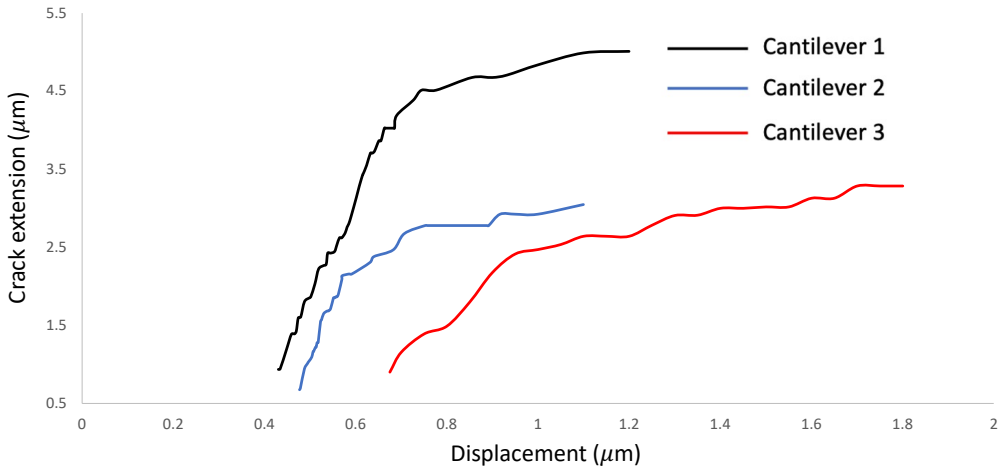

Figure 7.8: Crack propagation versus the displacement in the XFEM simulations.

Fig. 7.8 illustrates the evolution of the crack extension relative to the indenter displacement. The crack is evaluated based on fully broken finite elements (zero stiffness). For each increment in the displacement, the crack front is defined by the set of newly broken elements located furthest from the preceding crack front (or the initial notch) along the propagation direction. Since the front may exhibit small irregularities, the crack extension is determined by averaging the crack front positions across the entire cantilever width (see Fig. 7.2).

The onset of crack extension corresponds to the notch depth, 0.9 μm for C1 and C3, and 0.65 μm for C2.

However, the indenter displacement at crack initiation was more similar between C1 and C2 (0.43 μm and 0.48 μm, respectively), than for C3 0.68 μm. This 50% increase for C3 is attributed to enhanced plastic dissipation, driven by a much higher Schmid factor with respect to the tension of the C3 crystallographic orientation.

Crack propagation remained stable throughout the entire indenter displacement. Crack initiation and the highest growth rates occurred immediately after the peak load was reached. As the crack advanced, the reduction in the remaining ligament area led to a progressive loss of bending stiffness, analogous to the behaviour observed in double cantilever beam (DCB) experiments [246]. This increasing flexibility competes with the rising stress intensity factor at the crack tip, which would typically trigger instability under load control experiments. However, as outlined in the experimental design by Di Maio et al. [109], the reduction in ligament area ensures stable crack growth in displacement-controlled experiments, as it is reproduced by the simulation.

Fig. 7.9 illustrates the spatial distribution of cumulative plastic slip in the cantilevers at the point of maximum load, which occurs at displacements of C1=0.42 μm, C2=0.5 μm, and C3=0.68 μm (see Fig. 7.7). The simulations show that the most active slip systems are [1 0 0](0 0 1) and [1$\bar{2}$ $\sqrt{3}$/2 0](0 0 1), which is consistent with the slip systems exhibiting the highest Schmid factors in the experimental measurements of Table 7.2. The results reveal significant slip concentrations localised around the notch and at the bottom corner of the cantilever root, consistent with expectations for a notched, pentagonal cross-section cantilever, as these regions are most vulnerable to deformation [109]. In agreement with the Table 7.2, C3 exhibits substantially more plasticity than C1 and C2, and the primary active slip system in C3 is [1 0 0](0 0 1), while it is [1$\bar{2}$ $\sqrt{3}$/2 0](0 0 1) in C1 and C2.

The Von Mises stress maps of the cantilevers are plotted in Fig. 7.10. The stress state of the cantilevers is illustrated when the crack has not yet initiated (the displacement load is 0.25 μm in C1, C2 and C3), when the force response is maximum (C1=0.42 μm, C2=0.5 μm, C3=0.68 μm) and when the crack is close to be completed (C1=C2=1.00 μm, C3=2.00 μm). The completion of the crack dividing the cantilevers into 2 pieces results impossible, as a drop of the force to 0.0 makes the simulation unstable with convergence problems.

In the initial loading phase, previous to the fracture (*No Fracture row* of Fig. 7.10), all three cantilevers exhibit a stress concentration at the base of the cantilever, where it joins the bulk substrate. The highest stresses are localised at the corner of the cantilever and at the notch tip. The stress field around the notch displays the characteristic "half butterfly-shaped" pattern, which is the typical stress distribution around a sharp notch in an elastic material [247, 32]. Away from this region of high stress concentration, the

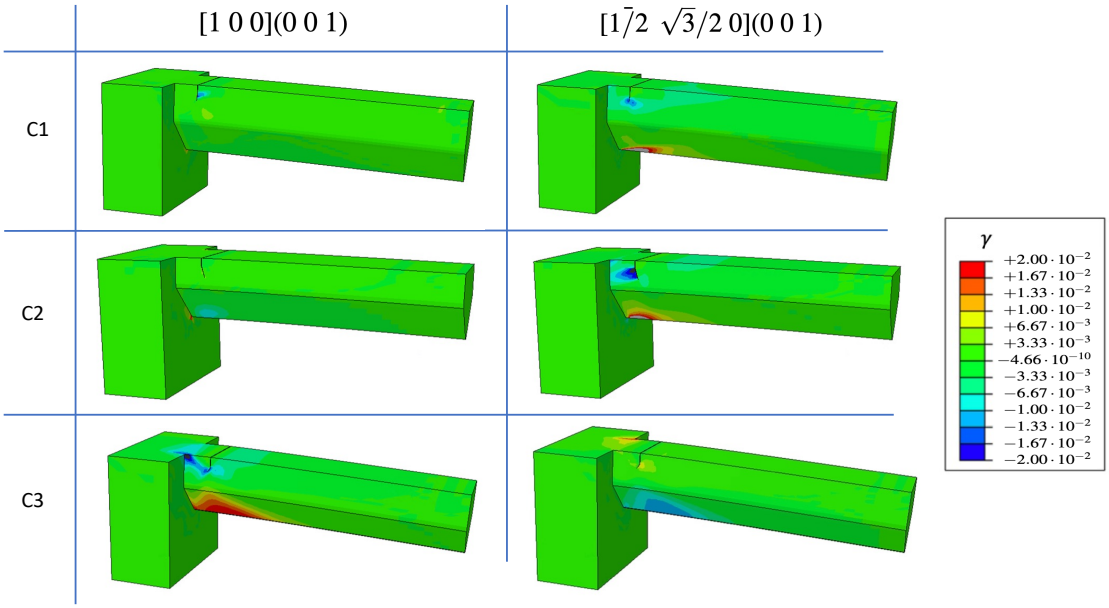

Figure 7.9: Slip map of the cantilevers for the most active slip systems during the maximum force.

remainder of the cantilever beam experiences significantly lower stress levels.

At the peak force (*Max Force row* of Fig. 7.10), the fracture has initiated in the three cantilevers, the stress fields are now more intense and have evolved due to the combined effects of crack initiation and plasticity. While some semblance of the initial elastic stress distribution remains, the dominant feature is the reorientation of the high-stress region in the notch, which is strongly influenced by the underlying crystal anisotropy. In C1, this reorientation is difficult to discern because the direction of highest stress aligns closely with the cantilever's longitudinal axis. However, in cantilevers C2 and C3, the influence of crystal orientation is pronounced. The bands of high stress are now oriented diagonally, as indicated by the red arrows. The orientation of this stress band is opposite for C2 and C3, aligning in each case with the direction perpendicular to the basal slip plane of the hexagonal crystal. This indicates that plastic deformation caused by basal slip attenuates the stress in the slip direction, leaving the perpendicular stress component.

Upon fracture completion (*Fracture completed row* of Fig. 7.10), the crack clearly propagates along the basal plane. The resulting fracture path closely resembles the SEM micrographs presented in Fig. 7.3 (c, e, g). These results align well with the predictions of other CP+XFEM studies [107, 238], which also show the fracture surface to be perpendicular to the normal direction of the most activated slip plane, and with literature on Be, which strongly indicates that the crack follows the basal plane. Analysis of the crack reveals notch opening but no discernible shear displacement of the cantilever relative to the base, suggesting that Mode I (opening mode) dominates the final stage of fracture completion, even though Mode II (sliding mode) strongly influences damage initiation.

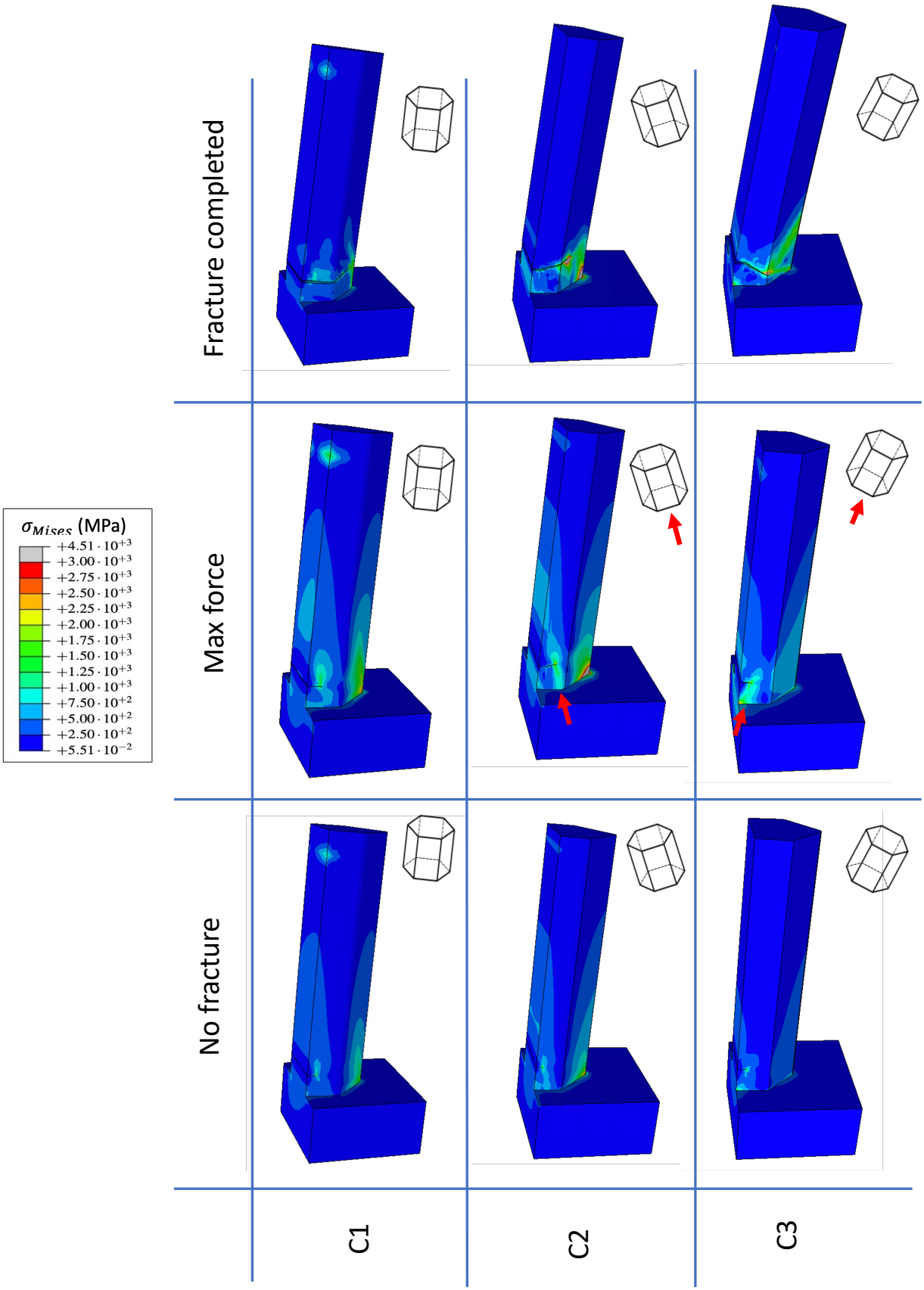

Figure 7.10: Von Mises stress maps of the cantilevers: before the fracture is initiated, during the maximum force and after the fracture is completed.

7.5.1 Parameter Sensitivity

A parameter sensitivity analysis was conducted to assess the impact of parameters on the resulting force-displacement curves. The parameters investigated were the toughness (G, calibrated to 8.5 J/m^2), the Mode I Crack Initiation Stress ($\sigma_I^{max} = 1.91$ GPa), and the Mode II Crack Initiation Stress (σ_{II}^{max}= 0.34 GPa), as defined in in Eq. (7.4.15) and Eq. (7.4.19). The results of this sensitivity study, focusing on variations above and below the values used in the adjusted model, are presented in Fig. 7.11 for C3, which is characterised by a low peak force and a high degree of plasticity.

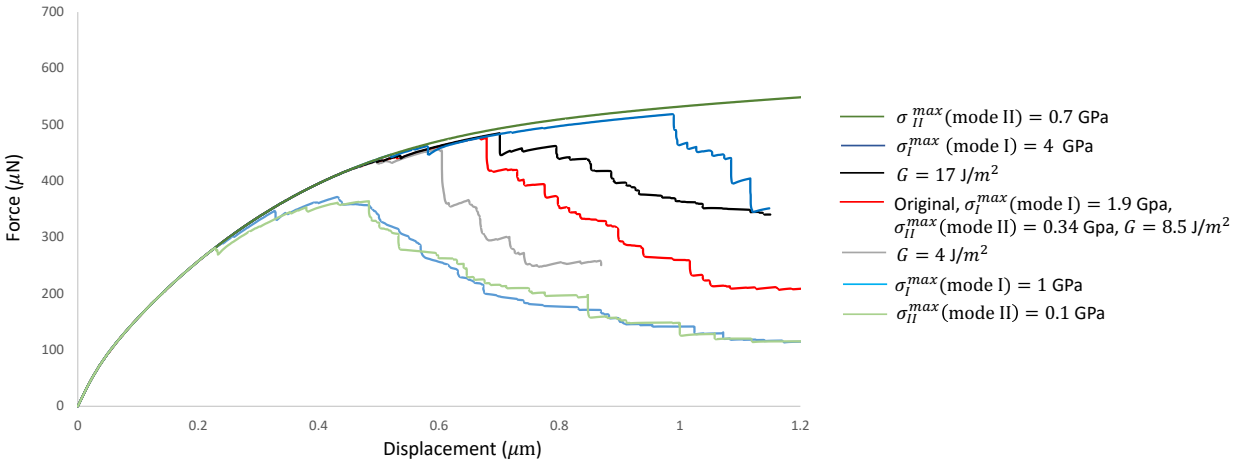

Figure 7.11: A parametric study on the force-displacement response of the Cantilever 3 Model.

- **Toughness (G):** The toughness primarily governs the post-failure behaviour of the cantilever. It has little influence on the peak force since the crack initiates slightly earlier than the cantilever reaches the peak stress, but it dictates the rate of force reduction during crack propagation. A higher toughness value ($G = 17\,\mathrm{J/m^2}$) leads to a more gradual decrease in force (a more ductile failure), while a lower toughness ($G = 4\,\mathrm{J/m^2}$) results in a sharp drop in force (brittle fracture).
- **Mode I Crack Initiation Stress (σ_I^{max}):** The Mode I crack initiation stress determines the maximum stress the elements can sustain before failure begins. A higher $\sigma_I^{\max}$ value (e.g., 4 GPa) directly corresponds to a higher peak force on the curve, signifying a greater resistance to crack initiation under tension. Conversely, a lower value (e.g., 1 GPa) results in a lower peak force and earlier failure initiation. Regarding the cantilever's force decrease, a lower/higher damage initiation stress leads to a more gradual/sharp decrease in force (ductile/brittle failure) to satisfy the damage completion (see Eq. (7.4.19)).
- **Mode II Crack Initiation Stress ($\sigma_{II}^{\max}$):** The Mode II crack has a similar effect to Mode I in Eq. (7.4.15). However, the shear stress increase with the strain is not governed by elasticity as Mode I (opening of the basal plane), the stress-strain relation is governed by the SSD hardening of Eq. (7.4.9)

which implies a much lower growth of stress with respect to strain. A higher $\sigma_{II}^{\max}$ (e.g., 0.7 GPa) allows the material to sustain a much higher shear strain. For a pure Mode II crack, the strain could be theoretically infinite if $\sigma_{II}^{\max}$ is bigger than the saturation stress of the Kocks-Mecking Eq. (7.4.10). In that scenario, the stress couldn't grow further and remains below the fracture initiation stress.

In contrast, a lower $\sigma_{II}^{\max}$ (e.g., 0.1 GPa) has a similar effect than decreasing $\sigma_{I}^{\max}$. This is because strain hardening is closer to the elastic regime, which is the regime that dominates Mode I. In case $\sigma_{II}^{\max} < \tau_c$, the behaviour between Mode I and Mode II would be the same.

The influence of crystal orientation is critical in the failure mode. C3 has the highest Schmid factors (see Table 7.2), increasing the influence of Mode II in crack initiation because the stress tensor has a higher shear projection on the basal plane. On the other hand, the Schmid factor in C1 and C2 is smaller, which leads to a smaller contribution of Mode II in Eq. (7.4.15). As $\sigma_{I}^{\max} > \sigma_{II}^{\max}$, C1 and C2 require a much higher stress state to damage initiation, resulting in higher peak forces and a more abrupt drop.

In conclusion, the observed differences in the force-displacement curves can be attributed to the influence of Mode II stress on the fracture initiation process and the role of plasticity in the evolution of shear stress. Furthermore, the parametric sensitivity analysis of this study is consistent with those reported in other cohesive zone modelling investigations [16].

7.6 Conclusions

This study extends the OXFORD-UMAT Crystal Plasticity Finite Element code (developed through a collaboration between UKAEA and Prof. Edmund Tarleton's group) by incorporating XFEM models to simulate fracture behaviour and crack propagation in three single-crystal beryllium cantilever experiments with distinct crystallographic orientations. The OXFORD-UMAT code is available via open public access in GitHub [49] with the files, documentation, and examples of simulations. The principal findings are as follows.

- During the experiments, fracture stress exhibited a strong dependence on crystallographic orientation. The crack follows the basal plane in all the experiments as reported in the literature, and the cantilever oriented for a greater Schmidt factor achieved a lower peak stress and required a larger displacement to reach complete fracture.
- The crystal plasticity-extended finite element method (CP+XFEM) model successfully reproduced the force-displacement response of the cantilevers by integrating plasticity and fracture mechanics in a compact and efficient framework using only a few parameters. The model also accurately captured

the fracture propagation along the basal plane, paving the way as a valuable tool to investigate other possible scenarios.

- During the simulations, the fracture properties of single-crystal Be were characterised. This revealed a significant disparity between the Mode I (elastic) and Mode II (plastic) fracture initiation stresses. This difference explains why the maximum failure stress is dependent on crystal orientation; a change in orientation alters the proportion of Mode I and Mode II contributions to the fracture. Consequently, cantilevers with similar dimensions and different orientations exhibited markedly different peak forces. The model was optimally calibrated with a fracture toughness of $G = 8.5\text{J/m}^2$, and crack initiation stresses of $\sigma_{\text{I}}^{\text{max}} = 1.91$ GPa and $\sigma_{\text{II}}^{\text{max}} = 0.34$ GPa, these values are consistent with those reported in the literature [242, 244, 245].
- Future research derived from this study should focus on three primary areas. (1) *Exploring Alternative Fracture Mechanisms*: A validation of the current model with new cantilever experimental data is needed and an investigation into pyramidal or prismatic slip systems. While their contribution may be negligible when basal slip is active, these systems could become the dominant failure mechanism in specific crystal orientations. (2) *Understanding Irradiation Damage*: The effect of irradiation on Be should be studied, particularly how void-induced reductions in plasticity alter the fracture properties. (3) *Modelling Polycrystalline Behaviour*: The single-crystal properties characterised in this work could be used as a basis for developing predictive models of polycrystalline Be. Given that the existing literature reports significantly reduced crack initiation stress and toughness for polycrystals, future work should investigate how crack propagation is influenced by grain boundaries.

Chapter 8: Thesis Conclusions and Future Work

8.1 Conclusions

This thesis, entitled ***"Modelling Micromechanical Damage of Fusion Reactor Materials"***, uses computational Finite Element Models (FEM) to study fracture processes in ceramic and metallic materials used in fusion reactors. Given the complexity of these processes, which involve various phenomena within the material's atomic structure, this work focuses on isolating and studying specific aspects (a-d):

(a) Estimating fracture properties of ceramic SiC fibre-reinforced composite with a PyC interphase.

(b) Modelling plasticity in metals based on the calculus of geometrically necessary dislocations (GNDs), dislocation structures necessary for the deformation and responsible of hardening or softening.

(c) Modelling the Bauschinger effect during preliminary load cycles, applied to the practical case of copper.

(d) Modelling a Single-Crystal Beryllium Cracking, where it is modelled the effect of plasticity and fracture from the onset of deformation until the fracture is complete.

The computational models used in this thesis provide an effective way to simulate the complete damage process (from initial deformation to fracture). These models can isolate the effects of specific material properties, bypassing the need for experiments that can be costly, time-consuming, complex, or physically impossible to conduct. Furthermore, their frameworks allow quick adaptation to other materials and do virtual experiments, being used by the UKAEA to characterise different materials for the STEP Fusion Reactor, such as the ceramic structure of the blanket, joining alloys or the first-wall.

While this work has focused on materials for fusion reactors, the nature of the developed models allows for their application to a wide range of engineering challenges, such as characterising fibre composites used in other industries, like aerospace or automotive, or modelling any mechanical deformation inside metals.

By combining these modelling techniques with experimental data, this work provides important insights into the fracture process and dislocations, with their consequent changes in mechanical properties. The main conclusions are discussed below, grouped according to the points outlined above (a–d):

(a) SiC fibre-reinforced composite with PyC interphase

This work studies how the PyC interphase can protect SiC fibres from crack propagation. The fracture process at the surface where the PyC interphase connects with the SiC fibre (known as *interface*) was characterised using push-out experiments on isolated fibres.

These experiments were complemented with FEM simulations of models that generate virtual push-out experiments, providing easily understandable 3D representations of fracture evolution. By using cohesive zone modelling (CZM) coupled with friction is reproduced the experimental results and a more detailed analysis of the failure process. FEM modelling in combination with optimisation algorithms provides a valuable alternative to experimental data for characterising the properties of SiC composites.

The following conclusions were drawn from this study.

- Push-out experiments and corresponding simulations were performed on both long (80-100 μm) and short fibres (5-10 μm), revealing differences in their fracture behaviour:
  - Fracture Process: While long fibres exhibited a gradual fracture process that initiates at the top and propagates downward, short fibres showed a quasi-instantaneous damage initiation across the entire *interface*, followed by abrupt fracture propagation.
  - Frictional Forces: The bonded lower section of long fibres induces additional radial expansion in the fibres, or "swelling", which increases the frictional forces during fibre sliding. Conversely, short fibres exhibit significantly less swelling, resulting in reduced Coulomb friction (similar to the behaviour of the composite during a fracture propagation).
  - Interfacial Debonding: Short fibres allowed for the isolation of the interfacial debond from other non-linear frictional effects like roughness, a capability not possible with long fibres, where the Coulomb friction complicates the calculation of the interfacial debond stress and the other non-linear frictional effects.
- Short fibres are sensitive to the presence of defects in the *interface*. As discussed in the study, determining the optimum length requires a balance: Long enough to mitigate the impact of the defects in the *interface* and short enough to enable a quasi-instantaneous crack formation.
- Debond stress during FEM simulations was minimally affected by the tapered geometry of the fibre or changes in the *interface* properties like toughness, roughness, or friction coefficient. Additionally, axial misorientation of the fibre had no detectable effect within the range of experimental measurements. Therefore, debond stress can be considered a robust value which can be extracted from short fibre push-outs.

- Crack propagation and consequent friction were affected noticeably by the radial stress, Coulomb friction coefficient, and toughness of the PyC interphase. Fibre taper geometry was found to be the dominant factor during the frictional component of short fibre push-out simulations. In contrast, long fibres do not have a taper geometry; their diameter widens and narrows along the fibre's length, which avoids this effect.

(b) Modelling plasticity in metals based on GNDs

Following the study of cracks in the fibre interface of ceramic materials like SiC, this research now focuses on modelling plasticity in metals as a foundational step for future studies that will combine the effects of plasticity and fracture.

The OXFORD-UMAT FEM code was developed to model the plastic deformation of metals relevant for the operation of the STEP fusion reactor. The plasticity is governed by the formation of dislocations within the crystal structure. This dislocation formation, which is influenced by strain, is ultimately responsible for structural failure. To capture this phenomenon, several methods for calculating *geometrically necessary dislocation* (GND) densities based on strain gradients were included, with the following conclusions:

- A reliable, well-documented, and flexible tool for calculating GNDs has been developed, being open access to the scientific community [18].
- Based on the literature, several methods for calculating GNDs using strain gradients were implemented and evaluated using various deformation cases, including simple shear, uniaxial tension, four-point bending, and polycrystals with large strain, with the following results:
  - *Total form of incompatibility* $(-\nabla \times \boldsymbol{F}_p)^T$: When it is solved by L2 and KKT methods, it reveals erroneously GNDs on inactive slip systems, a problem with significant effect in anisotropic materials. This led to erratic strain hardening, causing solution convergence difficulties. Nevertheless, a more realistic calculation was achieved by restricting the GND solution to the active slip systems and then applying *singular value decomposition* (SVD).
  - *Rate form of incompatibility* $(-\nabla \times \dot{\gamma}^a \boldsymbol{n}^a \boldsymbol{F}_p)$, and *Based on slip gradient*, $(\nabla \dot{\gamma}^a)$: do not suffer from erroneous GNDs on inactive slip systems. However, in polycrystal simulations with large strains, both methods predicted higher GND densities than the previously established "*Total form restricted to active slip systems*" and an error approximately two orders of magnitude greater. This discrepancy is attributed to the substantial error accumulation, which is caused by neglecting terms in the formulation of these methods that become significant at large strains.
  - The results lead us to establish the "*Total form restricted to active slip systems*" as the default

calculation method in the OXFORD-UMAT code.

(c) Modelling Bauschinger effects during preliminary load cycles

The Bauschinger effect, or kinematic hardening, refers to the reduction in a material's yield stress when the direction of applied loading is reversed. To study this effect, the calculus of GND within the OXFORD-UMAT code proved to be an essential tool for creating models that help to simulate and understand different scenarios.

In a fusion reactor, copper is an important material that serves as both a heat sink and a stress-relief layer, making it prone to cyclic fatigue induced by alternating thermal and mechanical loads. These repeated loading conditions can ultimately result in material failure. In this study, different kinematic hardening models were tested to reproduce the Bauschinger effect observed in a copper monocrystal cantilever experiment during the initial bending and straightening cycles. The following conclusions were drawn from the study:

- Slip-based kinematic hardening models: Models such as the *Armstrong-Frederick* model and its variants (*Chaboche, Ohno-Wang*), failed to replicate the experimental data for the initial loading cycles. The parameters needed to capture the unbending phase caused premature hardening saturation during subsequent bending. While suitable for multi-cycle simulations, these models are inadequate for capturing initial loading cycles. To address this limitation, the *Armstrong-Frederick* model was combined with *Voce-type* isotropic hardening. This approach successfully simulated the initial cycles by capturing the confluence of two distinct mechanisms: reversible kinematic hardening from the *Armstrong-Frederick* model, and irreversible isotropic hardening from the *Voce-type* model.
- GND-based kinematic hardening models: These models offer a more physical explanation of kinematic hardening. While the *Orowan-Sleeswyk* model accurately captured hardening during cantilever bending, it significantly underestimated the hardening during the straightening phase. This discrepancy can be attributed because the model predicts a near-zero density of GNDs when the cantilever is straight. To address this limitation, we propose an enhancement to this model that incorporates the conversion of some GNDs into statistically stored dislocations (SSDs). This modification is based on recent research suggesting that a percentage of GNDs do not fully recombine during unbending but instead reorient into structures that do not contribute to the strain gradient but do contribute to subsequent hardening.
- Both models: *Armstrong-Frederick with Voce-type hardening* and *Orowan-Sleeswyk with SSD* are valid alternatives with similar accuracy to reproduce the hardening and Bauschinger effect during the initial loading cycles. While the *Orowan-Sleeswyk with SSD* allows better understanding of the inter-

nal physical mechanisms of the cooper, it is more computationally complex and prone to convergence issues than the *Armstrong-Frederick and Voce-type hardening model*.

(d) Modelling fracture in Single-Crystal Beryllium

This work successfully modelled the combined effects of plasticity and fracture in single-crystal beryllium from the onset of deformation to complete fracture. Beryllium is a crucial material in fusion reactors due to its role in tritium production, but its brittleness and the toxicity of the dust formed during its fracture are potential issues that need to be addressed.

The study focused on three distinct single-crystal beryllium cantilever experiments with different crystallographic orientations, as beryllium's fracture behaviour is complex and highly dependent on slip plasticity and crystal orientation. A summary of the key findings is as follows:

- The work extends the OXFORD-UMAT code, an open-access tool available to the scientific community, into a Crystal Plasticity Extended Finite Element framework (CP+XFEM), enabling efficient fracture modelling without the need for remeshing.
- CP+XFEM models successfully reproduced the force-displacement response of the cantilevers by integrating plasticity and fracture mechanics in a compact and efficient way using a few parameters.
- The simulations revealed a significant disparity between the initiation stresses for Mode I (elastic) and Mode II (plastic) fracture, which explains the material's strong orientation-dependent failure. A change in crystal orientation alters the relative contributions of Mode I and Mode II, leading to markedly different peak forces for cantilevers of identical dimensions. The model's ability to capture this complex behaviour, in addition to accurately reproducing the overall force-displacement response and crack propagation along the basal plane, validates it as a compact and efficient predictive tool.

8.2 Future work

This thesis is composed of modelling studies of materials used in the nuclear industry. The following section outlines potential research directions to guide future projects building on the work presented here.

- The work on SiC_f/SiC composites presented in Chapters 3 and 4 should be extended to elucidate the effect of irradiation on the fibre–matrix interface and its implications for composite mechanical performance. In particular, irradiation is expected to significantly alter debonding stress, fibre residual stress, and crack propagation mechanisms. Furthermore, future FEM studies should focus on more complex and realistic configurations using the interface properties obtained from the thesis. These

include crack bridging by intact fibres, the interaction and failure of multiple fibres, and the influence of fibre distributions (e.g. density, orientation, and clustering). Such extensions will enable predictive modelling of damage accumulation and failure in structural ceramic composites.

- The GND research (Chapter 5) should proceed with experimental validation of the calculation method developed in this thesis. Single-crystal experiments designed to introduce controlled strain gradients, such as microcantilever and nanoindentation experiments, are required. These results could be analysed via Kernel Average Misorientation (KAM) techniques to estimate the GND densities and evaluate their role in size effects and hardening behaviour. In parallel, investigations should be extended to polycrystalline materials, where strain gradients arise naturally due to elastic and plastic anisotropy between grains. Coupling these experiments with crystal plasticity modelling will enable the quantification of the relative contributions of GNDs and SSDs in more realistic microstructures.
- While Chapter 6 demonstrates how GNDs can be applied to model the Bauschinger effect in single-crystal copper, it also provides a foundation for investigating how slip band formation influences hardening and backstress throughout both initial and subsequent loading cycles. Understanding the evolution of these mechanisms over increasing cycles is essential for developing physically-informed models of cyclic plasticity. Additional microcantilever experiments involving extended cyclic loading histories are necessary to validate and expand the proposed interpretations of dislocation dynamics, ultimately enhancing predictive capabilities for structural materials under cyclic fatigue.
- The framework presented in Chapter 7 establishes a CP+XFEM approach for modelling fracture in beryllium single-crystal cantilevers. Firstly, the identified fracture mechanisms should be further validated through experiments on cantilevers with additional crystal orientations, focusing on the role of pyramidal and prismatic slip systems. While basal slip often dominates, alternative slip systems may become critical in specific loading configurations, significantly influencing fracture behaviour. Secondly, the effect of irradiation on beryllium plasticity and fracture remains largely unexplored. Future studies should investigate how irradiation-induced defects, such as voids, reduce plasticity and alter crack initiation and propagation. This is particularly relevant in nuclear environments, where irradiation damage is unavoidable. Finally, the single-crystal properties characterised in this work serves as a basis for developing predictive models of polycrystalline beryllium. Given that existing literature reports significantly lower crack initiation stresses and toughness in polycrystals, future work should explicitly investigate the role of grain boundaries in crack propagation and failure.

Appendix A: Short fibre push-outs

A.1 Experimental indenter tip effects

Fig. A.1(a) shows an SEM image of the flat punch tip used for push-out testing. The nominally 5 µm diameter flat tip has a rounded square shape in reality and appears to be slightly concave rather than flat. Surface contamination or debris can be seen on the tip. Considering the extremely low loads for the testing here, the tip shape is unlikely to have a significant effect, and no evidence of plastic deformation or indentation was observed in the surfaces of pushed-out fibres.

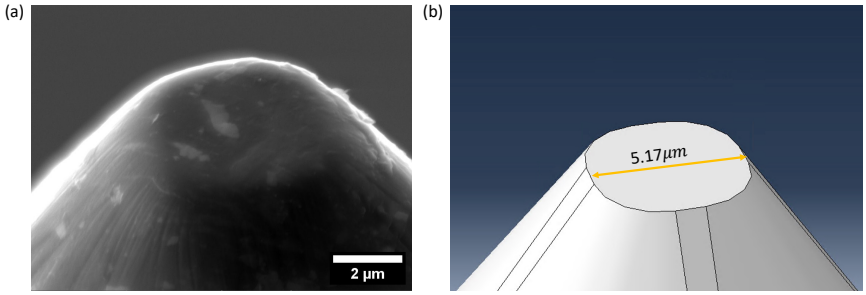

Figure A.1: (a) SEM image of flat punch tip used for the experiments. (b) Flat tip in the FEA model.

A.2 Axial misorientation geometry

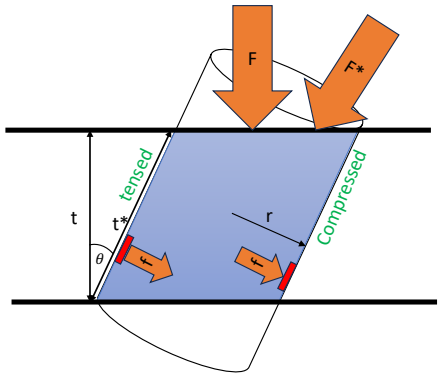

Figure A.2: Schematic of axial misorientation geometry.

Fig. A.3 shows the complete debonding of a fibre misoriented by 20° through the cohesive damage D. This magnitude is 0 when the area is unaffected by damage and 1 when it is completely debonded (see Eq. (4.3.3)). While the damage initiates in the compressed side, indicated by the red arrow, the friction slows

down the sliding (mode II crack) compared with the tensile side. The crack initiated at the tensile side propagates to the compressed side, but the friction slows down the process compared to a 0° short-fibre.

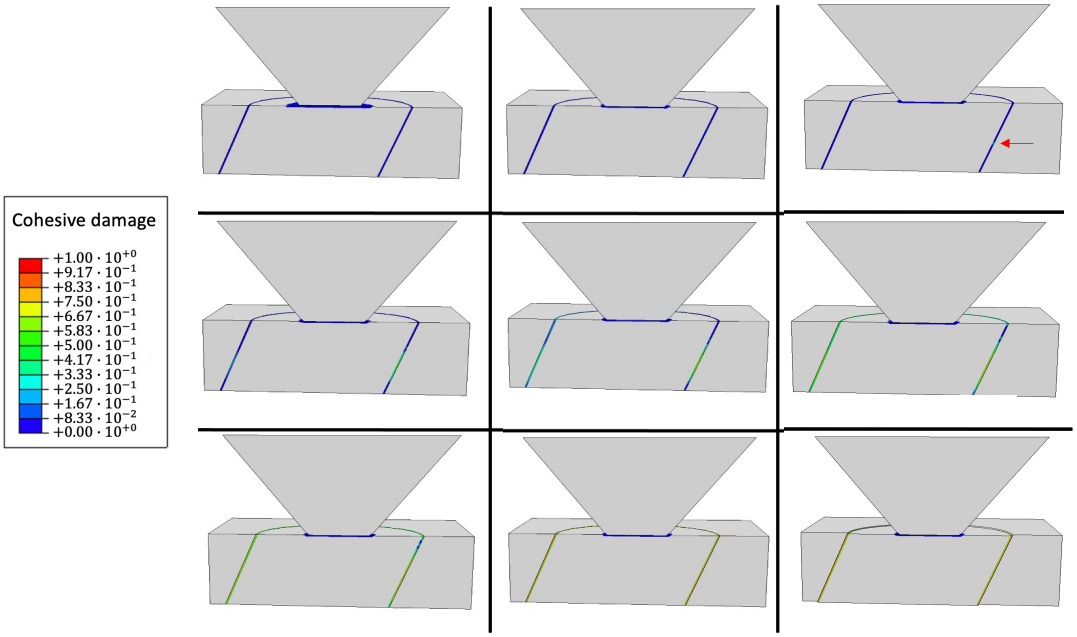

Figure A.3: Failure process of a fibre with an axial misorientation of 20°. The variable shown is the cohesive damage D defined in Eq. (4.3.3). The red arrow indicates the point where the crack has been initiated.

A.3 Failure process of a short fibre

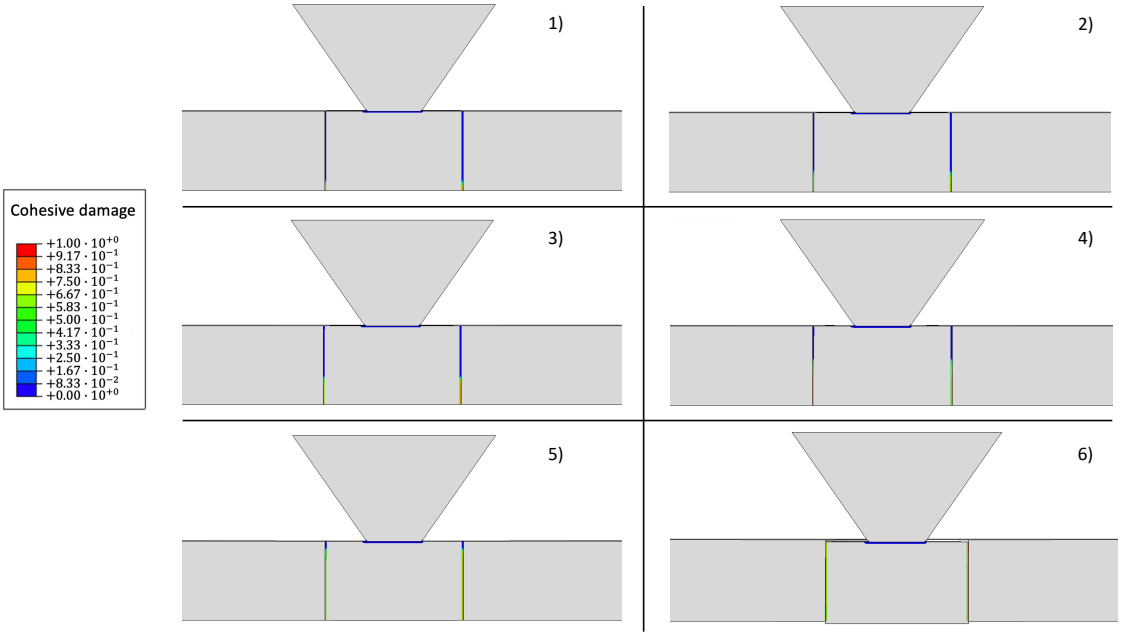

Figure A.4: Failure process of a short fibre. The variable D is the cohesive damage defined in Eq. (4.3.3). The crack propagates from the bottom to the top face, as it was observed experimentally in [72].

A.4 Mesh of the fibre-push out model.

The optimization of model parameters to best represent experimental results is an iterative process conducted through the following steps:

- Parameter Selection: Initial tentative values are selected for each parameter within their respective valid ranges.
- Mesh Determination: Based on these values, the optimal mesh size is determined by applying Eq. (A.4.1). This formula ensures a mesh fine enough to prevent cases where a coarse discretization could alter the fracture results, while remaining large enough to minimize computational time, which is typically the bottleneck in the optimisation.
- Simulation: The simulation is executed using the selected parameters and the established mesh resolution.
- Error Quantification: The discrepancy (distance) between the numerical model output and the experimental data is calculated.
- Heuristic Optimisation: The parameters optimisation process continues with a new set of parameters determined by Nelder-Mead method, a heuristic approach that avoids an exhaustive search of the entire parameter space.

According to Turon et al. [248], the mesh size must be sufficiently small to ensure that the cohesive length, l_{cz}, is captured by 3-5 elements. The cohesive length is the characteristic distance ahead of a crack tip over which fracture processes occur in a material. This zone represents the area where cohesive forces act to resist the separation of crack surfaces. In [248], several definitions from the literature describe the cohesive length in the following form:

$$\text{element size} = \frac{l_{cz}}{5}; \quad l_{cz} = ME^* \frac{G_c}{(\sigma^{\max})^2} \quad \text{where } \frac{1}{E_*} = \frac{1}{2}\left(\frac{1}{E_{PyC}} + \frac{1}{E_{Fibre}}\right), \tag{A.4.1}$$

where G_c is the mode II toughness of the interface which governs the fracture mode during the crack propagation across the interface, the debond stresses are $\sigma^{\max}$=86.9, 116 and 158 MPa for fibres F6, B4 and B2 respectively, calculated using Eq.4.4.4 at the peak push-out force. The elastic modulus of the interface was estimated as E^*= 37 GPa [141] based on the elastic modulus of the PyC interface E_{PyC}=20 GPa and the fibre E_{Fibre}=365 GPa [13]. The parameter M varies in the literature but generally ranges from 0.21 to 1. A conservative value of 0.21 was adopted here.

This formulation guarantees CZM convergence and is conservative with respect to fracture. However, this

formula might lead to a very coarse mesh if the optimiser explores high toughness values. For example, at the upper limit of the exploration space 40 J/m^2 $\rightarrow l_{cz} = 41.1\mu$m $\rightarrow$ element size = 8.2μm for fibre F6. To overcome this issue, a maximum characteristic mesh size of 0.5μm was imposed; the mesh is determined by Eq.A.4.1 unless it exceeds this limit. This ensures that the remainder of the model is not adversely affected by a fracture whose mesh requirements are very coarse for the rest of the model.

After optimisation, the toughness was adjusted to G_c=10.5J/m^2, that corresponds to $l_{cz} = 11.07, 6.06$ and 3.2 μm, which results in a seed=2.21, 1.21 and 0.65 μm for fibres F6, B4 and B2, respectively. These seeds were large than the maximum seed established during the optimisation process 0.5μm, providing a margin of safety regarding the CZM convergence.

Finally, once the adjustment was completed, we verified convergence using a smaller seed of 0.2μm. Fig. A.5(a) shows the mesh seed applied to the fibre F6. Fig. A.5(b) illustrates the matrix, Fig. A.5(c) shows the fibre, and Fig. A.5(d) depicts the indenter. The seed sizes generate simulations with 235,862, 325,915 and 212,003 elements for fibres F6, B4 and B2, respectively.

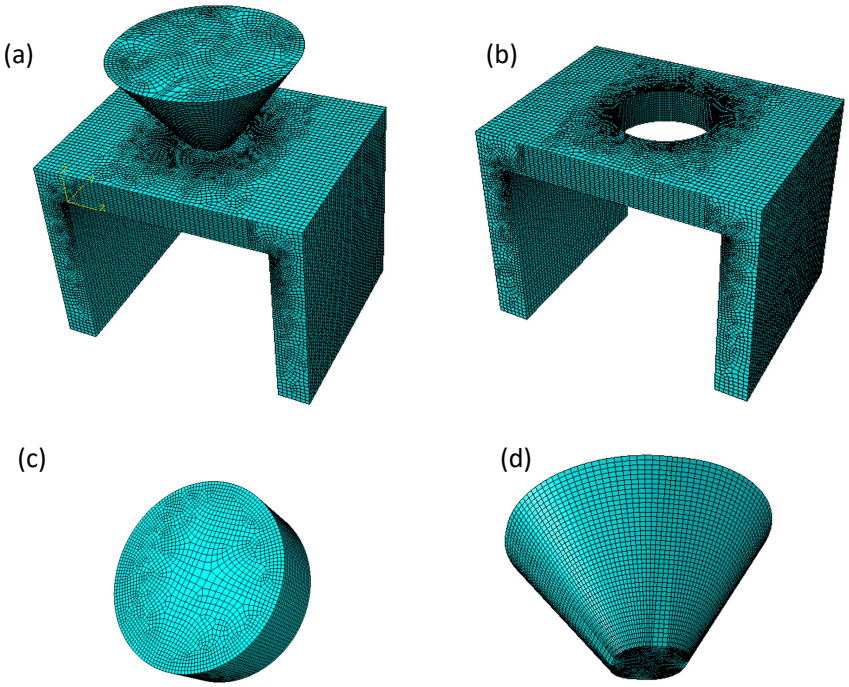

Figure A.5: Mesh of the different components of fibre push-out simulation F6.

A.5 Shear stress over the interface of Fibre F6

In short fibres, the distribution of shear stress exhibits a more uniform behaviour compared to that in long fibres. Utilising the software Abaqus, it is possible to visualise shear stress along the interface of fibre F6 as an example (represented by cohesive contact). The provided image represents the condition at the onset of damage, which occurs very close to the point of damage completion due to the rapid progression of this process.

The variation in colour observed within the stress profile arises from the positioning of the x=0 plane in the middle of the fibre; this causes the change of direction of the X-coordinate and therefore it changes the sign of shear stress.

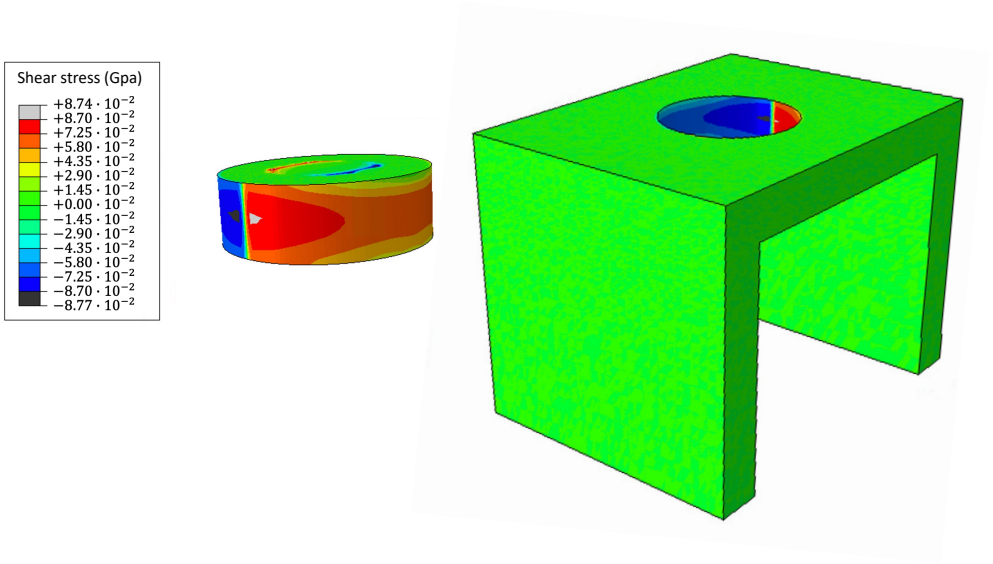

Figure A.6: Shear stress over the interface of fibre F6.

As illustrated, the shear stress distribution exhibits a high degree of uniformity, with more than 75% of the contact area reaching values close to the debond stress threshold of 87 MPa prior to crack initiation. It is important to note that the distribution is not perfectly homogeneous, primarily due to the geometric configuration of the fibre's experimental bridge shape. This introduces minor inhomogeneities in the stress field; however, these variations are negligible when compared to the stress profiles typically observed in long fibre specimens [13].

Appendix B: Restaining GNDs to active slip systems

B.1 Crystal to sample transformation

The transformation from the crystal reference frame to the sample reference frame is defined by the transformation matrix $\boldsymbol{g}_{ij}$. The matrix $\boldsymbol{g}_{ij}$ is computed using the three Bunge angles $(\varphi_1, \Phi, \varphi_2)$.

$$\boldsymbol{g}_{ij} = \begin{bmatrix} \cos\varphi_1\cos\varphi_2 - \sin\varphi_1\sin\varphi_2\cos\Phi & \sin\varphi_1\cos\varphi_2 - \cos\varphi_1\sin\varphi_2\cos\Phi & \sin\varphi_2\sin\Phi \\ -\cos\varphi_1\sin\varphi_2 - \sin\varphi_1\cos\varphi_2\cos\Phi & -\sin\varphi_1\sin\varphi_2 + \cos\varphi_1\cos\varphi_2\cos\Phi & \cos\varphi_2\sin\Phi \\ \sin\varphi_1\sin\Phi & -\cos\varphi_1\sin\Phi & \cos\Phi \end{bmatrix}^T . \tag{B.1.1}$$

The transformation of the elastic matrix from the crystal reference $\mathbb{C}_0$ to the elasticity matrix in the deformed configuration $\mathbb{C}$ is given by $\mathbb{C} = [\boldsymbol{R}]\,[\mathbb{C}_0]\,[\boldsymbol{R}]^T$, where $[\boldsymbol{R}]$ is a special 6×6 transformation matrix constructed from the crystal to the sample transformation matrix (g_{ij}) [55]

$$[\boldsymbol{R}] = \begin{bmatrix} (g_{11})^2 & (g_{12})^2 & (g_{13})^2 & 2g_{11}g_{12} & 2g_{13}g_{11} & 2g_{12}g_{13} \\ (g_{21})^2 & (g_{22})^2 & (g_{23})^2 & 2g_{21}g_{22} & 2g_{23}g_{21} & 2g_{22}g_{23} \\ (g_{31})^2 & (g_{32})^2 & (g_{33})^2 & 2g_{31}g_{32} & 2g_{33}g_{31} & 2g_{32}g_{33} \\ g_{11}g_{21} & g_{12}g_{22} & g_{13}g_{23} & g_{11}g_{22}+g_{12}g_{21} & g_{13}g_{21}+g_{11}g_{23} & g_{12}g_{23}+g_{13}g_{22} \\ g_{31}g_{11} & g_{32}g_{12} & g_{33}g_{13} & g_{11}g_{32}+g_{12}g_{31} & g_{13}g_{31}+g_{11}g_{33} & g_{12}g_{33}+g_{13}g_{32} \\ g_{21}g_{31} & g_{22}g_{32} & g_{23}g_{33} & g_{22}g_{31}+g_{21}g_{32} & g_{21}g_{33}+g_{23}g_{31} & g_{22}g_{33}+g_{23}g_{32} \end{bmatrix} . \tag{B.1.2}$$

B.2 Emergence of GNDs in inactive slip systems using L^2

In models involving a single slip system, such as the "uniaxial tension with strain gradient" or "4-point bending test" cases, it was observed GNDs in non-activated slip systems with $\tau_C^0 \geq 1000$ GPa. In this section, a theoretical example will study the limits of L^2 method in high anisotropic crystal geometries, and how it can be solved with slip system restrictions.

The L^2 minimization approach (pseudoinverse matrix A^+) seeks the solution that minimizes $\sum \rho^2$. This

solution tends to distribute or smear the dislocation density across all available slip systems. While this method has shown good results similar to L^1 [93] in the calculus of total GND density of complex deformation modes such as nano-indentation of BCC tungsten, those scenarios involve severe multi-axial stress gradients. Such gradients naturally compel the simultaneous activation of numerous slip systems, which effectively masks the method's inherent tendency to over-distribute density among inactive systems.

For applications requiring higher microstructural fidelity of the dislocation hardening, the L^2 formulation can be enhanced by restricting the interaction matrix $\mathbf{A}$ in the Nye tensor equation to the subset of physically active systems where the apparition of GNDs is physically more probable. This "restricted" approach is computationally efficient in the reduced matrix and is particularly advantageous in strongly anisotropic materials where a standard geometric projection might otherwise populate "hard" slip systems (e.g., pyramidal modes in HCP materials) to satisfy the lattice curvature.

However, this restriction must be applied with caution; by limiting the solution space *"a priori"*, one risks ignoring systems with low Schmid factors that may be locally actived by steep gradients or similar Critical Resolved Shear Stresses (CRSS). Consequently, while the unrestricted L^2 method remains a robust and unbiased tool for estimating global defect quantities, restricting the slip basis offers a refined strategy for capturing the behaviour in anisotropic crystals. It serves as a valid tool for improving models of hardening, fatigue or other GND effects in materials where the active systems can be identified with confidence.

In this section, we analyse a theoretical case of a FCC material in which a single slip system $\langle 1\bar{1}0\rangle$ $\{111\}$ is significantly weaker (lower CRSS) than the remaining systems. The applied deformation causes the slip to evolve linearly along the x-direction, thus $\gamma = ax$. A similar analysis can be applied to the KKT method. Considering $L^p(t) = \dot{F}^p(t)(F^p)^{-1} = \dot{\gamma}(t)s \otimes n$ and assuming $s = (1,-1,0)$ and $n = (1,1,1)$ are constant (low rotation) and 0,0,0 as Euler angles. Integrating we obtain:

$$F^p(t) = \exp(\gamma(x)s \otimes n), \tag{B.2.1}$$

where just one slip system is contributing to the strain gradient. Assuming low slip $\gamma(x)^2 \sim 0$ and that $s \cdot n = 0$ thus $(s \otimes n)^2 = 0$. If we do Taylor expansion we get:

$$F^p(t) = I + \gamma(x)s \otimes n = I + ax \begin{pmatrix} 1 \\ -1 \\ 0 \end{pmatrix} \otimes \begin{pmatrix} 1 \\ 1 \\ 1 \end{pmatrix} = \begin{pmatrix} 1+ax & ax & ax \\ -ax & 1-ax & -ax \\ 0 & 0 & 1 \end{pmatrix} \tag{B.2.2}$$

Calculating the Nye tensor:

$$\Lambda_{ij} = -\left(\nabla \times \mathbf{F}_p\right)^T = a \begin{pmatrix} 0 & 1 & -1 \\ 0 & -1 & 1 \\ 0 & 0 & 0 \end{pmatrix}; \quad \text{vec}(\Lambda) = \begin{Bmatrix} \Lambda_{11} \\ \Lambda_{12} \\ \Lambda_{13} \\ \Lambda_{21} \\ \Lambda_{22} \\ \Lambda_{23} \\ \Lambda_{31} \\ \Lambda_{32} \\ \Lambda_{33} \end{Bmatrix} = \begin{Bmatrix} 0 \\ a \\ -a \\ 0 \\ -a \\ +a \\ 0 \\ 0 \\ 0 \end{Bmatrix} \tag{B.2.3}$$

The incompatibility tensor can be written as the sum of dislocation families: screws and edges.

$$\boldsymbol{\Lambda} = \sum_a \rho^a_{GND,e} b^a s^a \otimes \boldsymbol{t}^a + \rho^a_{GND,s} b^a s^a \otimes s^a \tag{B.2.4}$$

Resulting in a final equation:

$$\{\boldsymbol{\Lambda}\} = [\boldsymbol{A}]\,\{\boldsymbol{\varrho}_{GND}\}\,. \tag{B.2.5}$$

Where A is:

$$\mathbf{A} = b \begin{pmatrix} 0.29 & 0.29 & -0.29 & -0.29 & -0.29 & 0.00 & 0.29 & \mathbf{0.29} & -0.29 & 0.00 & 0.00 & 0.00 & 0.50 & 0.50 & \mathbf{0.50} & 0.50 & 0.00 & 0.00 \\ 0.58 & 0.58 & -0.29 & 0.29 & 0.29 & 0.00 & -0.58 & \mathbf{0.29} & 0.58 & 0.00 & 0.00 & 0.00 & 0.00 & 0.00 & \mathbf{-0.50} & 0.50 & 0.00 & 0.00 \\ 0.29 & -0.29 & -0.58 & -0.58 & 0.58 & 0.00 & 0.29 & \mathbf{-0.58} & -0.29 & 0.00 & 0.00 & 0.00 & -0.50 & 0.50 & \mathbf{0.00} & 0.00 & 0.00 & 0.00 \\ 0.00 & 0.00 & 0.29 & -0.29 & -0.29 & -0.58 & 0.00 & \mathbf{-0.29} & 0.00 & 0.58 & -0.58 & -0.58 & 0.00 & 0.00 & \mathbf{-0.50} & 0.50 & 0.00 & 0.00 \\ 0.00 & 0.00 & 0.29 & 0.29 & 0.29 & -0.29 & 0.00 & \mathbf{-0.29} & 0.00 & -0.29 & -0.29 & 0.29 & 0.00 & 0.00 & \mathbf{0.50} & 0.50 & 0.50 & 0.50 \\ 0.00 & 0.00 & 0.58 & -0.58 & 0.58 & 0.29 & 0.00 & \mathbf{0.58} & 0.00 & 0.29 & -0.29 & 0.29 & 0.00 & 0.00 & \mathbf{0.00} & 0.00 & 0.50 & -0.50 \\ -0.29 & 0.29 & 0.00 & 0.00 & 0.00 & -0.58 & 0.29 & \mathbf{0.00} & 0.29 & 0.58 & 0.58 & 0.58 & -0.50 & 0.50 & \mathbf{0.00} & 0.00 & 0.00 & 0.00 \\ -0.58 & 0.58 & 0.00 & 0.00 & 0.00 & -0.29 & -0.58 & \mathbf{0.00} & -0.58 & -0.29 & 0.29 & -0.29 & 0.00 & 0.00 & \mathbf{0.00} & 0.00 & 0.50 & -0.50 \\ -0.29 & -0.29 & 0.00 & 0.00 & 0.00 & 0.29 & 0.29 & \mathbf{0.00} & 0.29 & 0.29 & 0.29 & -0.29 & 0.50 & 0.50 & \mathbf{0.00} & 0.00 & 0.50 & 0.50 \end{pmatrix} \tag{B.2.6}$$

The matrix was created using the slip systems in the following order:

In this case the activate slip system is the Sys #8: $s = (1,-1,0)$ and $n = (1,1,1)$ (see Table B.1). This type of slip would generate edge and screw dislocations that corresponds to columns 8 and 15 of matrix A. However, the L^2 method is unable to distinguish which specific slip systems are active and calculates GNDs based solely on the F_p (see B.2.7).

$$\mathbf{A}^+ = \mathbf{A}^T \left(\mathbf{A}\mathbf{A}^T\right)^{-1}; \quad \text{thus } \{\boldsymbol{\varrho}_{GND}\} = [\boldsymbol{A}]^+ \{\boldsymbol{\Lambda}\}. \tag{B.2.7}$$

Sys #	Slip normal	Slip direction	Transverse direction
1	(1, -1, 1)	[1, 0, -1]	[1, 2, 1]
2	(-1, 1, 1)	[1, 0, 1]	$[1,2,-1]$
3	(1, 1, -1)	$[1,-1,0]$	$[-1,-1,-2]$
4	(-1, 1, 1)	[1, 1, 0]	$[-1,1,-2]$
5	(1, -1, 1)	[1, 1, 0]	[-1, 1, 2]
6	(1, -1, 1)	[0, 1, 1]	$[-2,-1,1]$
7	(1, 1, -1)	[1, 0, 1]	$[1,-2,-1]$
8	**(1, 1, 1)**	**[1,-1,0]**	**[1, 1, -2]**
9	(1, 1, 1)	$[1,0,-1]$	$[-1,2,-1]$
10	(1, 1, -1)	[0, 1, 1]	$[2,-1,1]$
11	(-1, 1, 1)	[0, 1, -1]	$[-2,-1,-1]$
12	(1, 1, 1)	$[0,1,-1]$	[-2, 1, 1]

Table B.1: Order of slip systems, with the active slip system highlighted.

$$\mathbf{A}^{+}=\frac{1}{b}\begin{pmatrix}
0.19 & 0.27 & 0.13 & 0.00 & 0.00 & 0.00 & -0.13 & -0.27 & -0.19\\
0.19 & 0.27 & -0.13 & 0.00 & 0.00 & 0.00 & 0.13 & 0.27 & -0.19\\
-0.19 & -0.13 & -0.27 & 0.13 & 0.13 & 0.27 & 0.00 & 0.00 & 0.00\\
-0.19 & 0.13 & -0.27 & -0.13 & 0.13 & -0.27 & 0.00 & 0.00 & 0.00\\
-0.19 & 0.13 & 0.27 & -0.13 & 0.13 & 0.27 & 0.00 & 0.00 & 0.00\\
0.00 & 0.00 & 0.00 & -0.27 & -0.13 & 0.13 & -0.27 & -0.13 & 0.13\\
0.19 & -0.27 & 0.13 & 0.00 & 0.00 & 0.00 & 0.13 & -0.27 & -0.19\\
0.19 & 0.13 & -0.27 & -0.13 & -0.13 & 0.27 & 0.00 & 0.00 & 0.00\\
-0.19 & 0.27 & -0.13 & 0.00 & 0.00 & 0.00 & 0.13 & -0.27 & 0.19\\
0.00 & 0.00 & 0.00 & 0.27 & -0.13 & 0.13 & 0.27 & -0.13 & 0.13\\
0.00 & 0.00 & 0.00 & -0.27 & -0.13 & -0.13 & 0.27 & 0.13 & 0.13\\
0.00 & 0.00 & 0.00 & -0.27 & 0.13 & 0.13 & 0.27 & -0.13 & -0.13\\
0.28 & 0.00 & -0.23 & 0.00 & 0.00 & 0.00 & -0.23 & 0.00 & 0.28\\
0.28 & 0.00 & 0.23 & 0.00 & 0.00 & 0.00 & 0.23 & 0.00 & 0.28\\
0.28 & -0.23 & 0.00 & -0.23 & 0.28 & 0.00 & 0.00 & 0.00 & 0.00\\
0.28 & 0.23 & 0.00 & 0.23 & 0.28 & 0.00 & 0.00 & 0.00 & 0.00\\
0.00 & 0.00 & 0.00 & 0.00 & 0.28 & 0.23 & 0.00 & 0.23 & 0.28\\
0.00 & 0.00 & 0.00 & 0.00 & 0.28 & -0.23 & 0.00 & -0.23 & 0.28
\end{pmatrix} \tag{B.2.8}$$

This matrix is limited in high anisotropic materials as this example (which is a theoretical scenario). For example if we analyse the edge dislocation of Sys #1 ($s=(1,0,-1)$ and $n=(1,-1,1)$) which correspond to column 1 of $\mathbf{A}^{+}$:

$$\rho_{GND}^{1,edge}=0.19\cdot\Lambda_{11}+0.27\cdot\Lambda_{12}+0.13\cdot\Lambda_{13}+0.0\cdot\Lambda_{21}+0.0\cdot\Lambda_{22}+0.0\cdot\Lambda_{23}-0.13\cdot\Lambda_{31}-0.27\cdot\Lambda_{32}-0.19\cdot\Lambda_{33} \tag{B.2.9}$$

Using Eq.B.2.3, we obtain a GND value of $\rho_{GND}^{1,edge}=0.14a/b$, which is very different from zero despite the system is inactive.

If the L^2 method is restricted to the formulation used in Model 1-c (see Eq. 5.3.39), the matrix $\mathbf{A}$ is reduced

to columns 8 and 15, getting the solution: $\rho_{GND}^{8,edge} = 1.72a/b$ and $\rho_{GND}^{15,screw} = -a/b$ (see Eq. B.2.10).

$$\begin{pmatrix} \rho_{GND}^{8,edge} \\ \rho_{GND}^{15,screw} \end{pmatrix} = \mathbf{A}^{+} \cdot \Lambda = \frac{1}{b} \begin{pmatrix} 0.29 & 0.29 & -0.57 & -0.29 & -0.29 & 0.57 & 0.00 & 0.00 & 0.00 \\ 0.50 & -0.50 & 0.00 & -0.50 & 0.50 & 0.00 & 0.00 & 0.00 & 0.00 \end{pmatrix} \cdot \begin{pmatrix} 0 \\ a \\ -a \\ 0 \\ -a \\ a \\ 0 \\ 0 \\ 0 \end{pmatrix} \tag{B.2.10}$$

The L^2 model is based on the minimization of $\sum \rho^2$, but remains agnostic to physical restrictions. Incorporating these restrictions allowed us to increase the accuracy in the simulations or get a more probable solution, particularly in cases where a few slip systems dominate due to crystal orientation or sample geometry.

B.3 Noise analysis of L2 and KKT models

While the theoretical analysis in Appendix B.2 explains the reason of GNDs on inactive slip systems, it does not explain the noise observed in the GND maps. We have identified this noise as a couple effect arising from the emergence of GNDs on inactive slip systems interacting with forest hardening (hardening that occurs between slip systems, see section 5.3.2). Together, these factors induce an unphysical stress state that leads to numerical instability in the solver.

An extensive investigation into the precision and convergence tolerances for stress and slip updates within the algorithm of the model yielded no significant reduction in the noise. Similarly, mesh refinement failed to significantly mitigate the noise. The noise disappears when we disable the hardening formulations, yielding GND profiles comparable to models 1-c, 2, and 3. Likewise, the noise also disappears when GNDs on inactive slip systems are explicitly suppressed, even when forest hardening is retained.

Fig. B.1 compares the edge GND profiles for three slip systems (one active and two inactive slip systems) in the 4-point bending case. The comparison evaluates the activation and deactivation of hardening using the unrestricted L^2 model versus the restricted L^2 approach (the KKT model yielded results similar to L^2). The results demonstrate the conclusions mentioned previously.

On the other hand, as evidence that the mesh size does not significantly mitigate the noise, Fig. B.2 illustrates the noise across different mesh sizes for L^2 and KKT models. Similar banding patterns occur regardless of the level of mesh refinement.

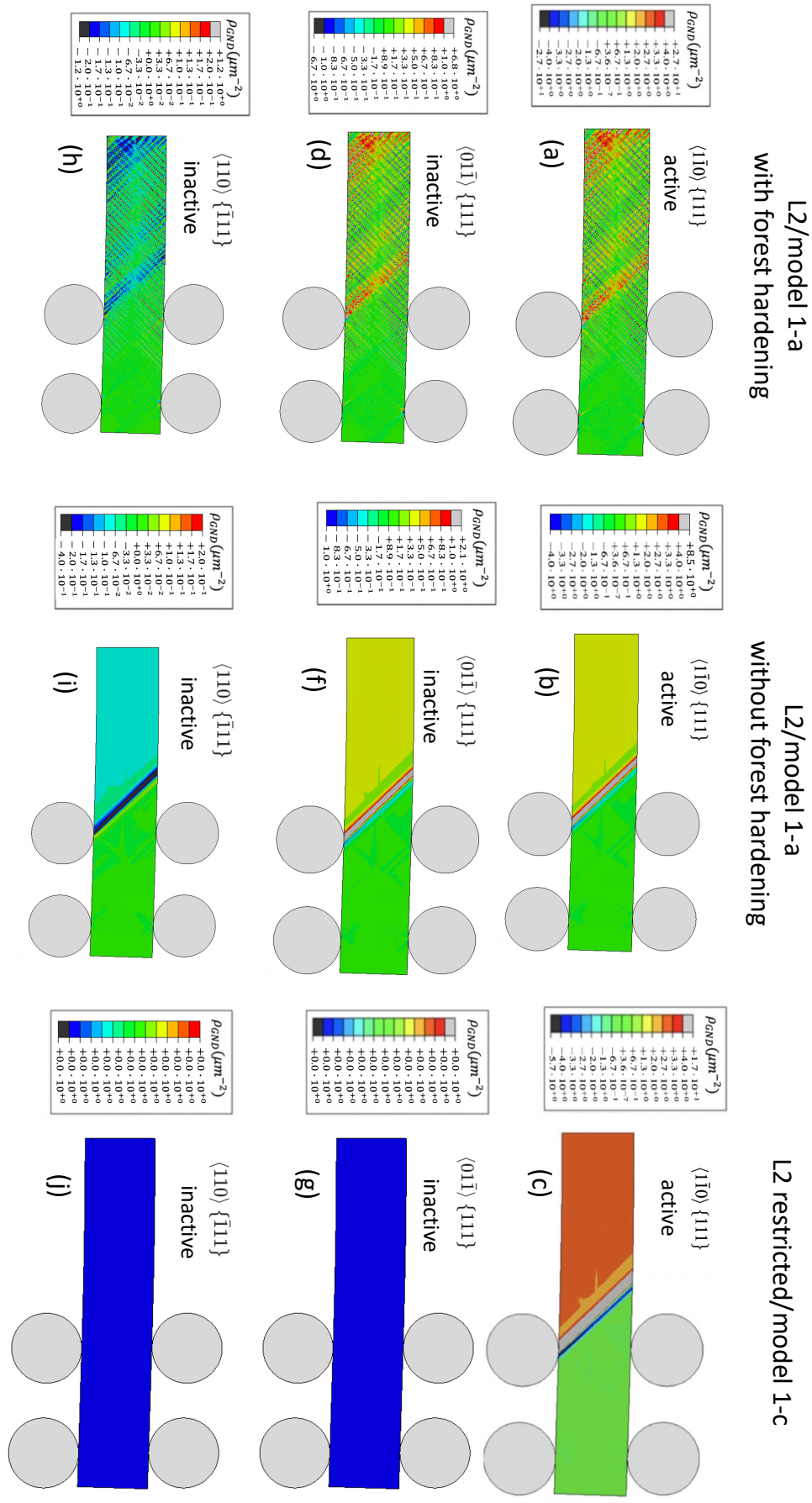

Figure B.1: GND profiles of L^2 models with/without forest hardening and with/without restriction to only active slip systems

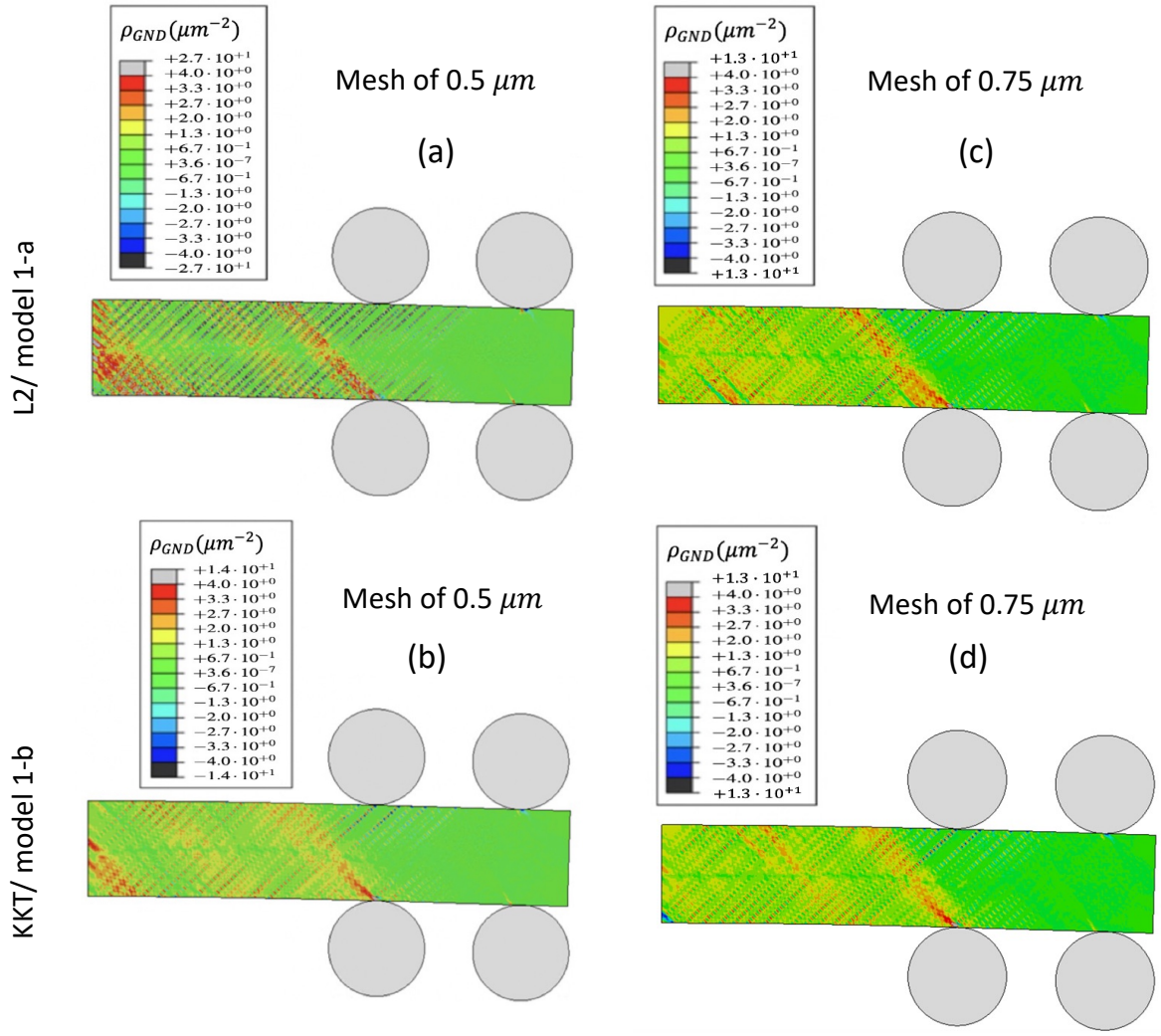

Figure B.2: GND profiles of L^2 or KKT models for a mesh of 0.5 μm and 0.75 μm.

Appendix C: Modelling Bauschinger effect

C.1 Comparison of Node Line and Indenter of Copper

In this section, we analyse whether incorporating the indenter into the model significantly alters the results compared to a line of element nodes (Node Line) as a substitute for the indenter. Modelling the indenter provides a more accurate representation of the contact mechanics, including stress distributions and potential deformation of both the indenter and the material being tested. However, Demir et al. [21] determined that the volume affected by the indenter contact is very small (2 μm^3) compared to the deformed volume of the cantilever (180 μm^3), suggesting that its effect can be neglected.

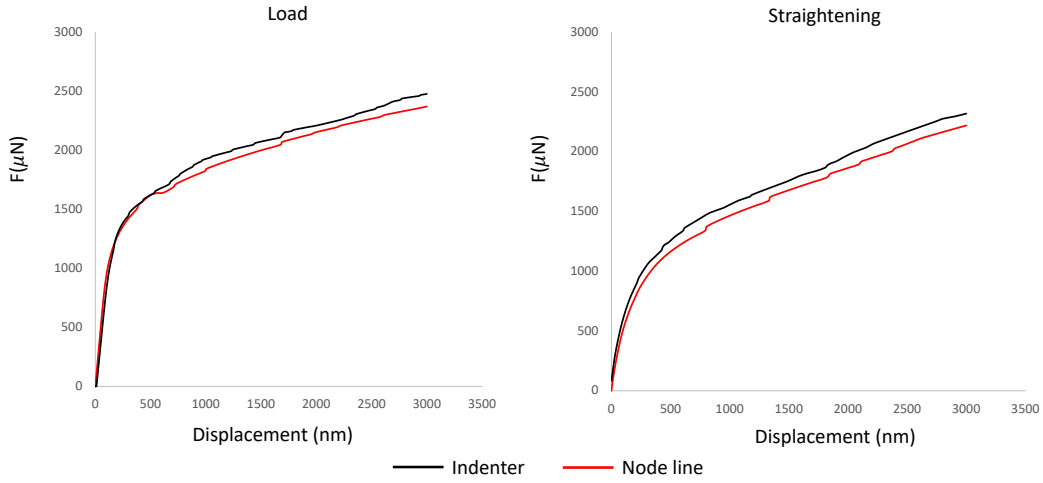

Figure C.1: Comparison of force-displacement using a line of nodes or an indenter during the 2^{nd} cycle.

In our models, the indenter was represented with a spherical tip of approximately $5\mu m$ of radius. In Abaqus, the contact was modelled with "hard normal" and "rough friction". Fig. C.1 compares the force-displacement responses of modelling the indenter and using the Node Line representation. The results demonstrate minimal differences between the two loading methods.

The spherical indenter exhibited slightly higher resistance, potentially due to its contact point of 1.5 μm of radius. This contact point generates less torque and promotes greater force dissipation in the contact area compared to the distributed load of the Node Line, thus requiring more force to achieve equivalent displacement.

Fig. C.2 presents the stress profiles of the indenter and the Node Line. The continuous Node Line applies

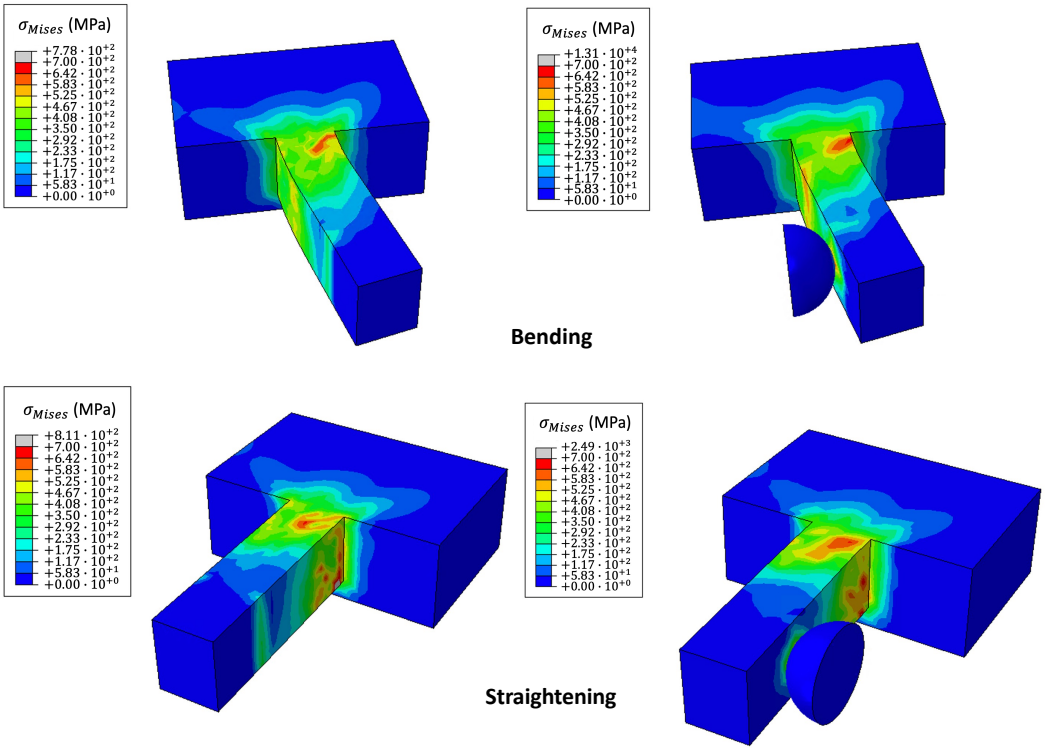

Figure C.2: Stress profile of the cantilever after the 2^{nd} cycle with Node Line (left) and Indenter (right).

a distributed load, which creates a larger moment arm relative to the cantilever's fixed end. In contrast, the spherical indenter applies a concentrated force, resulting in a smaller effective lever arm. This localised pressure in the contact region induces higher local stress concentrations, as evidenced by peak stress values that are nearly two orders of magnitude compared to those observed in the Node Line simulations (as indicated by the maximum values on the colour gradient scale in Fig. C.2).

Using an indenter instead of a Node Line causes convergence issues in simulations when the indenter detaches from the sample, typically occurring between cycles. This may be due to the "rough friction" contact, which may not effectively handle the sliding of the indenter during unloading. As a result, the Node Line is a more practical approach for modelling the cycles with a reduced loss of precision.

C.2 Convergence study of Copper

Fig. C.3 illustrates the convergence study of the cycles for different mesh sizes:

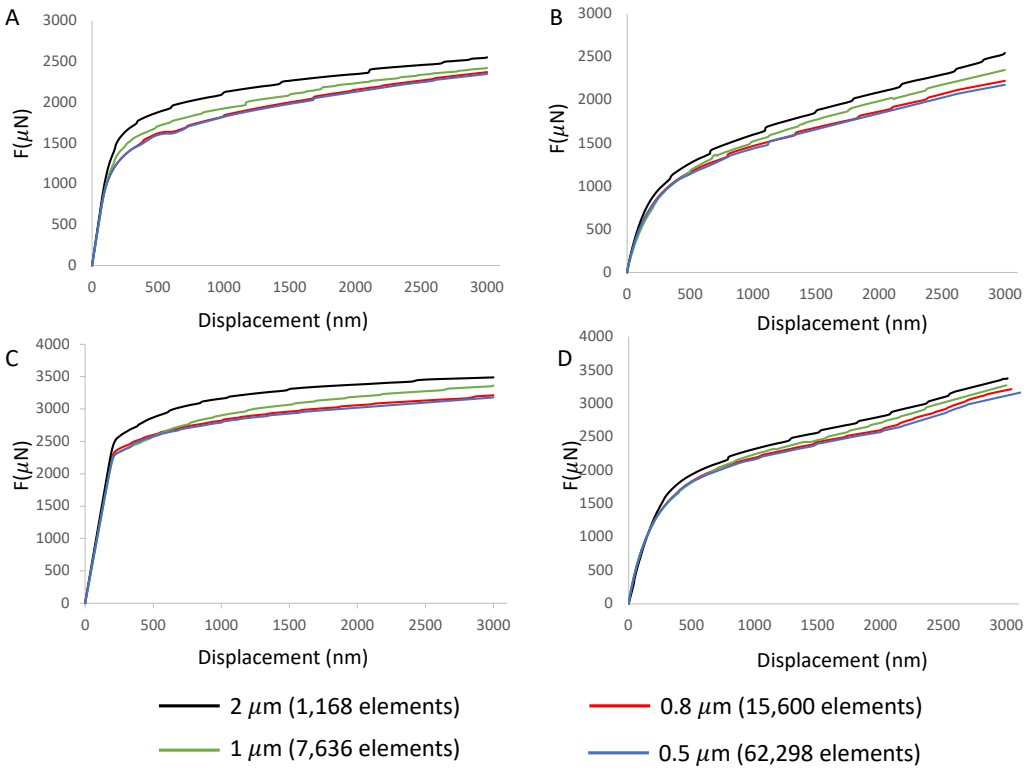

Figure C.3: Convergence study for 2^{nd} and 3^{rd} cycles.

C.3 Slip systems activation of Copper

The activation of the slip systems depends on the Schmid factor m and CRSS. The Schmid factor (m) for a stress σ is given by the product $m = (\sigma \cdot s^a) \cdot (\sigma \cdot n^a)/(|\sigma \cdot s^a| \cdot |\sigma \cdot s^a|)$, where n^a and s^a are the normal and slip direction of the slip system, respectively. The calculation of the Schmid factor for the main stress component σ_z in the cantilever experiment (see Fig. 6.3(b)) is presented in Table C.1:

Slip normal	**Slip direction**	**Schmid factor respect to $\sigma_z = [\bar{5}, 2, 1]$**
$(1, \bar{1}, 1)$	$[1, 0, \bar{1}]$	0.49
$(\bar{1}, 1, 1)$	$[1, 0, 1]$	-0.43
$(1, 1, \bar{1})$	$[1, \bar{1}, 0]$	0.38
$(\bar{1}, 1, 1)$	$[1, 1, 0]$	-0.32
$(1, \bar{1}, 1)$	$[1, 1, 0]$	0.24
$(1, \bar{1}, 1)$	$[0, 1, 1]$	-0.24
$(1, 1, \bar{1})$	$[1, 0, 1]$	-0.21
$(1, 1, 1)$	$[1, \bar{1}, 0]$	-0.19
$(1, 1, 1)$	$[1, 0, \bar{1}]$	0.16
$(1, 1, \bar{1})$	$[0, 1, 1]$	-0.16
$(\bar{1}, 1, 1)$	$[0, 1, \bar{1}]$	0.1
$(1, 1, 1)$	$[0, 1, \bar{1}]$	-0.02

Table C.1: Schmid factors of slip systems respect to $\sigma_z = [\bar{5}, 2, 1]$.

The Schmid factor is higher in slip systems (1 $\bar{1}$ 1) [1 0 $\bar{1}$] and ($\bar{1}$ 1 1) [1 0 1]. In Fig. C.4, we can observe the

amount of slip after applying the second bending. We can see how γ decreases in subsequent slip systems, being almost imperceptible compared to the two main ones. The explanation for this occurrence is that the plasticity generated by the slip of (1 $\bar{1}$ 1) [1 0 $\bar{1}$] and ($\bar{1}$ 1 1) [1 0 1] induces stress relaxation, preventing the activation of subsequent slip systems. For this reason, we focus our analysis of slip and dislocations only on the first two (see Fig. 6.4 and Fig. 6.6).

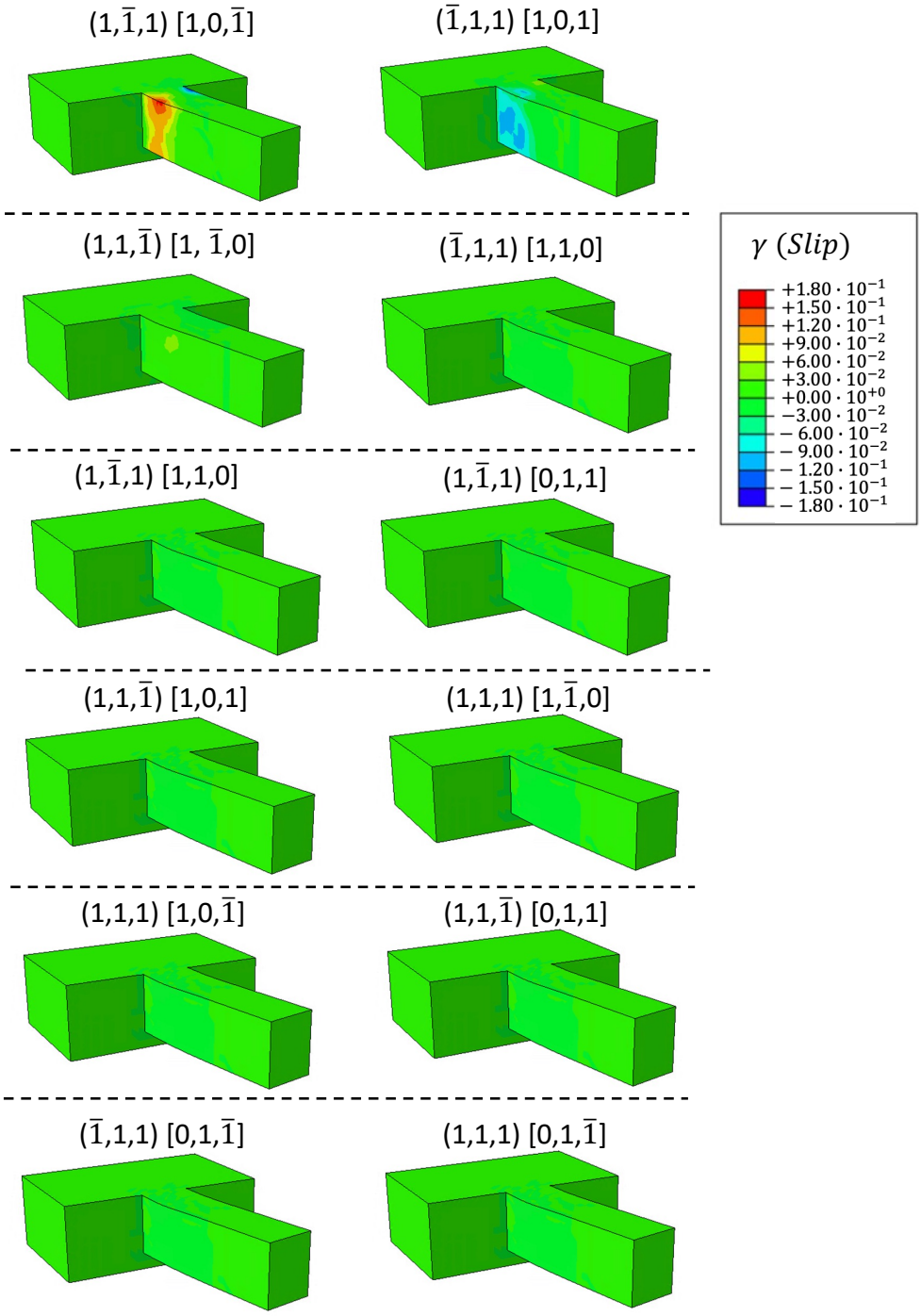

Figure C.4: Accumulated slip γ after the 2^{nd} bending of all the slip systems.

Appendix D: Single-Crystal Beryllium Cracking: A Crystal Plasticity XFEM Model

D.1 Corrections of the force-displacement experimental curves of Beryllium cantilevers

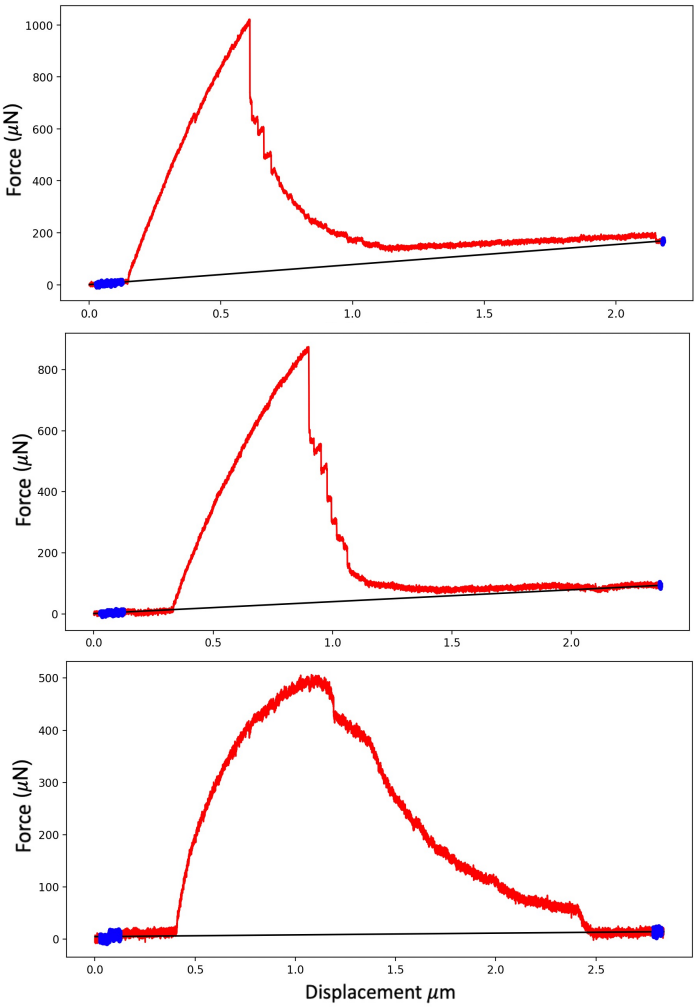

Figure D.1: The drift in the experimental force-displacement curves of the three cantilevers was corrected by fitting a linear interpolation to the contact and decohesion phases and subtracting this baseline from the raw data (see Section Cantilever experiments). The red curve represents the raw data, while the blue line represents the linear interpolation.

D.2 Berkovich indenter effect in Beryllium

As discussed in the article, the simulation of cantilever experiments employed a line of element nodes due to restrictions in the current release of the OXFORD-UMAT code when coupled with XFEM and contact with a Berkovich indenter. These limitations will be addressed in forthcoming versions.

This section examines the potential influence of including the Berkovich indenter in the model during the pre-cracking phase. The observed incompatibility between OXFORD-UMAT and XFEM only occurs during crack initiation and subsequent propagation.

Modelling the Berkovich indenter provides a more accurate representation of the contact mechanics, including stress distributions and potential deformation of both the indenter and the material. The Berkovich indenter contact was modelled with "hard normal" property and a friction coefficient of μ=0.15 [249].

Fig. D.2(a) compares the force-displacement responses obtained by modelling the indenter versus using the Node Line representation. The results demonstrate minimal differences between the two loading methods. The Berkovich indenter exhibited slightly higher resistance, potentially due to its reduced contact point compared to the load of the Node Line. This concentrated contact generates less torque and promotes greater force dissipation in the contact area, thus requiring more force to achieve equivalent displacement.

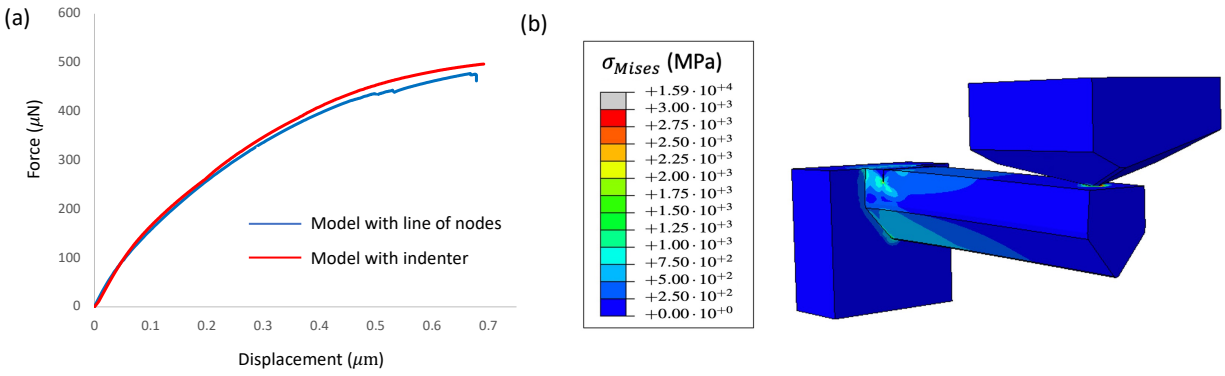

Figure D.2: (a) Modelling Force-Displacement in cantilever 3: Line Load vs. Berkovich Indenter. (b) Von Mises stress profile using the Berkovich indenter after a displacement.

Fig. D.2(b) presents the stress profiles of the Berkovich indenter after applying 0.25μm displacement to the indenter trip, where the Von Mises stress maps are visually identical to the Node Line simulation of Fig. 7.10 (C3 - Max Force).

References

[1] Fatih Birol. Key world energy statistics. *International Energy Agency*, 2017.

[2] IT Chapman, SC Cowley, and HR Wilson. The spherical tokamak for energy production: theme issue introduction, 2024.

[3] William D. Gunter and Robert A. Hubbs. Revised weizsäcker semiempirical formula for diffuse nuclear surfaces. *Phys. Rev.*, 113:1697–1697, Mar 1959. doi: 10.1103/PhysRev.113.1697.4. URL https://link.aps.org/doi/10.1103/PhysRev.113.1697.4.

[4] H.-S. Bosch and G.M. Hale. Improved formulas for fusion cross-sections and thermal reactivities. *Nuclear Fusion*, 32(4):611, apr 1992. doi: 10.1088/0029-5515/32/4/I07. URL https://dx.doi.org/10.1088/0029-5515/32/4/I07.

[5] Markus J Aschwanden and Markus J Aschwanden. The quiet-sun corona. *New Millennium Solar Physics*, pages 219–259, 2019.

[6] Wetson M Stacey. *Fusion: An Introduction to the Physics and Technology of Magnetic Confinement Fusion*. John Wiley and Sons, 2010.

[7] Francis F. Chen. *Introduction to Plasma Physics and Controlled Fusion Volume I*. Plenum Press New York and London, 1965.

[8] R. Gonzalez-Arrabal, A. Rivera, and J. M. Perlado. Limitations for tungsten as plasma facing material in the diverse scenarios of the european inertial confinement fusion facility hiper: Current status and new approaches. *Matter and Radiation at Extremes*, 5(5):055201, 2020. doi: 10.1063/5.0010954.

[9] Lee W. G. Morgan. *Inertial Confinement Fusion Neutronics. Phd Thesis*. University of York, 2012.

[10] Yevhen Zayachuk, Phani Karamched, Christian Deck, Peter Hosemann, and David E.J. Armstrong. Linking microstructure and local mechanical properties in SiC-SiC fiber composite using micromechanical testing. *Acta Materialia*, 168:178–189, 2019. ISSN 1359-6454.

[11] G Pintsuk, S Brezinsek, J W Coenen, A Huber, M Rubel, A Widdowson, and JET Contributors. Metallography and mechanical parameters of plasma-exposed plasma-facing materials and components. *Physica Scripta*, 2020(T171):014042, mar 2020. doi: 10.1088/1402-4896/ab4d72.

[12] Barenblatt G.I. The formation of equilibrium cracks during brittle fracture: general ideas and hypothesis, axially symmetric cracks. *Appl Math Mech*, 23:623–636, 1959.

[13] Alvaro Martinez-Pechero, Yevhen Zayachuk, Anna Widdowson, David EJ Armstrong, and Edmund Tarleton. Obtaining sic fibers–pyc interfacial properties through push-out fem models. *Journal of the European Ceramic Society*, 44(2):784–794, 2024.

[14] G. Lin, P.H. Geubelle, and N.R. Sottos. Simulation of fiber debonding with friction in a model composite push-out test. *International Journal of Solids and Structures*, 38(46):8547–8562, 2001. ISSN 0020-7683.

[15] J.A. Nelder and R. Mead. A simplex method for function minimization. *The Computer Journal*, 7: 308–313, 1965. ISSN 0010-4620. doi: https://doi.org/10.1093/comjnl/7.4.308.

[16] Alex Leide, Alvaro Martinez-Pechero, George Clark, Christopher Bearcroft, Oriol Gavalda-Diaz, Stuart Robertson, Eralp Demir, Yevhen Zayachuk, Anna Widdowson, Edmund Tarleton, et al. Progress towards a micro fibre push-out method for measuring fibre-matrix interface properties in sic composites. *Journal of the European Ceramic Society*, page 117624, 2025.

[17] Eralp Demir, Alvaro Martinez-Pechero, Chris Hardie, and Edmund Tarleton. Restraining geometrically-necessary dislocations to the active slip systems in a crystal plasticity-based finite element framework. *International Journal of Plasticity*, 178:104013, 2024.

[18] Eralp Demir, Alvaro Martinez-Pechero, Chris Hardie, and Edmund Tarleton. Oxford-umat: An efficient and versatile crystal plasticity framework. *International Journal of Solids and Structures*, 307:113110, 2025.

[19] John F Nye. Some geometrical relations in dislocated crystals. *Acta metallurgica*, 1(2):153–162, 1953.

[20] Alvaro Martinez-Pechero, Eralp Demir, Chris Hardie, Yevhen Zayachuk, Anna Widdowson, and Edmund Tarleton. Modelling the bauschinger effect in copper during preliminary load cycles. *Acta Materialia*, 289:120886, 2025.

[21] Eralp Demir and Dierk Raabe. Mechanical and microstructural single-crystal bauschinger effects: Observation of reversible plasticity in copper during bending. *Acta Materialia*, 58(18):6055–6063, 2010.

[22] S. Nishio et al. Improved tokamak concept focusing on easy maintenance. *Fusion Engineering and Design*, 41(1):357–364, 1998. ISSN 0920-3796. doi: https://doi.org/10.1016/S0920-3796(98)00119-7. URL https://www.sciencedirect.com/science/article/pii/S0920379698001197.

[23] Nicolas Moës, John Dolbow, and Ted Belytschko. A finite element method for crack growth without remeshing. *International Journal for Numerical Methods in Engineering*, 46(1):131–150, 1999. doi: https://doi.org/10.1002/(SICI)1097-0207(19990910)46:1⟨131::AID-NME726⟩3.0.CO;2-J.

[24] Robert Kerr, Sergio Lozano-Perez, David EJ Armstrong, Martin S Meier, Michael P Moody, Yevhen Zayachuk, and Anna Widdowson. Cracking and void formation in bulk w components manufactured for jet iter-like wall. *IEEE Transactions on Plasma Science*, 2024.

[25] G. R. Irwin. Analysis of Stresses and Strains Near the End of a Crack Traversing a Plate. *Journal of Applied Mechanics*, 24(3):361–364, June 2021. ISSN 0021-8936. doi: 10.1115/1.4011547. URL https://doi.org/10.1115/1.4011547.

[26] A.A. Griffith. The phenomena of rupture and flow in solids. *Philosophical Transactions of the Royal Society of London Series A*, (221):163–198, 1921.

[27] C. E. Inglis. Stresses in a plate due to the presence of cracks and sharp corners. *SPIE Milestone Series*, (137):3–17, 1913.

[28] I. N. Sneddon. Integral transform methods—circular cracks. *Mechanics of fracture*, (1):350–363, 1973.

[29] Anders Klarbring J.R. Barber. *Plasticity and fracture*, volume 244. Solid Mechanics and Its Applications, 2018.

[30] G. R. Irwin. Structural aspects of brittle fracture. *Appl Mater Res*, (3):65–81, 1964.

[31] J.R. Rice. A path independent integral and the approximate analysis of strain concentration by notches and cracks. *Journal of Applied Mechanics*, 35:379–386, 1968.

[32] T.L. Anderson. *Fracture Mechanics: Fundamentals and Applications, Fourth Edition (4th ed.)*.

[33] A. T. Travesa. *PhD Thesis. Simulation of delamination in composites under quasi-static and fatigue loading using cohesive zone models*.

[34] Krueger. *The virtual crack closure technique: history, approach and applications*. 2002.

[35] E.F. Rybicki and M.F. Kanninen. A finite element calculation of stress intensity factors by a modified crack closure integral. *Engineering Fracture Mechanics*, 9(4):931–938, 1977. ISSN 0013-7944. doi: https://doi.org/10.1016/0013-7944(77)90013-3. URL https://www.sciencedirect.com/science/article/pii/0013794477900133.

[36] D.S. Dugdale. Yielding of steel sheets containing slits. *Journal of the Mechanics and Physics of Solids*, 8(2):100–104, 1960. ISSN 0022-5096. doi: https://doi.org/10.1016/0022-5096(60)90013-2. URL https://www.sciencedirect.com/science/article/pii/0022509660900132.

[37] A. Hillerborg, M. Modéer, and P.-E. Petersson. Analysis of crack formation and crack growth in concrete by means of fracture mechanics and finite elements. *Cement and Concrete Research*, 6 (6):773–781, 1976. ISSN 0008-8846. doi: https://doi.org/10.1016/0008-8846(76)90007-7. URL https://www.sciencedirect.com/science/article/pii/0008884676900077.

[38] G. Davies U. Mi, M. Crisfield. Progressive delamination using interface elements. *Journal of Composite Materials*, 32:1246–1272, 1998.

[39] Viggo Tvergaard and John W. Hutchinson. The relation between crack growth resistance and fracture process parameters in elastic-plastic solids. *Journal of the Mechanics and Physics of Solids*, 40(6): 1377–1397, 1992. ISSN 0022-5096. doi: https://doi.org/10.1016/0022-5096(92)90020-3. URL https://www.sciencedirect.com/science/article/pii/0022509692900203.

[40] A. Needleman. *An analysis of decohesion along an imperfect interface*. Springer Netherlands, 1990. ISBN 978-94-017-2444-9. doi: 10.1007/978-94-017-2444-9_2. URL https://doi.org/10.1007/978-94-017-2444-9_2.

[41] Giulio Alfano. On the influence of the shape of the interface law on the application of cohesive-zone models. *Composites Science and Technology*, 66(6):723–730, 2006. ISSN 0266-3538. doi: https://doi.org/10.1016/j.compscitech.2004.12.024. URL https://www.sciencedirect.com/science/article/pii/S0266353804003641. Advances in statics and dynamics of delamination.

[42] Michael Smith. *ABAQUS/Standard User's Manual, Version 6.14*. Dassault Systèmes Simulia Corp, United States, 2022.

[43] James R Rice and Andy L Ruina. Stability of steady frictional slipping. 1983.

[44] E Buet, C Sauder, D Sornin, S Poissonnet, J-N Rouzaud, and C Vix-Guterl. Influence of surface fibre properties and textural organization of a pyrocarbon interphase on the interfacial shear stress of sic/sic minicomposites reinforced with hi-nicalon s and tyranno sa3 fibres. *Journal of the European Ceramic Society*, 34(2):179–188, 2014.

[45] Giulio Alfano and Elio Sacco. Combining interface damage and friction in a cohesive-zone model. *International Journal for Numerical Methods in Engineering*, 68(5):542–582, 2006.

[46] Alireza Golahmar, Christian F Niordson, and Emilio Martinez-Paneda. A phase field model for high-cycle fatigue: Total-life analysis. *International Journal of Fatigue*, 170:107558, 2023.

[47] S.A. Silling. Reformulation of elasticity theory for discontinuities and long-range forces. *Journal of the Mechanics and Physics of Solids*, 48(1):175–209, 2000. ISSN 0022-5096. doi: https://doi.org/10.1016/S0022-5096(99)00029-0. URL https://www.sciencedirect.com/science/article/pii/S0022509699000290.

[48] FPE Dunne, D Rugg, and A Walker. Lengthscale-dependent, elastically anisotropic, physically-based hcp crystal plasticity: Application to cold-dwell fatigue in ti alloys. *International Journal of Plasticity*, 23(6):1061–1083, 2007.

[49] Edmund Tarleton. Github link for crystal plasticity code, 2023. https://github.com/TarletonGroup/CrystalPlasticity [Accessed: 2023-10-18].

[50] Dan Zhao, Yi-Guo Zhu, Ping Hu, and Wan-Xi Zhang. A new integration algorithm for finite deformation of thermo-elasto-viscoplastic single crystals. *Acta Mechanica Sinica*, 29(5):709–717, 2013.

[51] Akhtar S Khan and Sujian Huang. *Continuum theory of plasticity*. John Wiley & Sons, 1995.

[52] Y Huang. A user-material subroutine incorporating single crystal plasticity in the abaqus finite element program. *Harvard University: Cambridge, Massachusetts*, 1991.

[53] J. F. Smith and C. L. Arbogast. Elastic constants of single crystal beryllium. *Journal of Applied Physics*, 31(1):99–102, 1960. doi: 10.1063/1.1735427.

[54] Ali Hedayat, Ali Khounsary, and Farzad Mashayek. Thermo-mechanical properties of silicon, germanium, diamond, beryllium and silicon carbide for high heat load x-ray optics applications. In *Advances in X-Ray/EUV Optics and Components VII*, volume 8502, pages 167–188. SPIE, 2012.

[55] Walter L Bond. The mathematics of the physical properties of crystals. *The Bell System Technical Journal*, 22(1):1–72, 1943.

[56] Surya R Kalidindi, Curt A Bronkhorst, and Lallit Anand. Crystallographic texture evolution in bulk deformation processing of fcc metals. *Journal of the Mechanics and Physics of Solids*, 40(3):537–569, 1992.

[57] Argon A.S. Kocks, U.F. *Thermodynamics and Kinetics of Slip*. Prog. Mater. Sei., Pergarnon Press., 1975.

[58] M.A. Meyers, D.J. Benson, O. Vöhringer, B.K. Kad, Q. Xue, and H.-H. Fu. Constitutive description of dynamic deformation: physically-based mechanisms. *Materials Science and Engineering: A*, 322 (1):194–216, 2002. ISSN 0921-5093. doi: https://doi.org/10.1016/S0921-5093(01)01131-5. URL https://www.sciencedirect.com/science/article/pii/S0921509301011315.

[59] A. Manonukul, F.P.E. Dunne, and D. Knowles. Physically-based model for creep in nickel-base superalloy c263 both above and below the gamma solvus. *Acta Materialia*, 50(11):2917–2931, 2002. ISSN 1359-6454. doi: https://doi.org/10.1016/S1359-6454(02)00119-2. URL https://www.sciencedirect.com/science/article/pii/S1359645402001192.

[60] Steven J. Zinkle and Nasr Ghoniem. Operating temperature windows for fusion reactor structural materials. *Fusion Engineering and Design*, 51:55–71, 2000.

[61] Y. Katoh, L.L. Snead, C.H. Henager, T. Nozawa, T. Hinoki, A. Iveković, S. Novak, and S.M. Gonzalez de Vicente. Current status and recent research achievements in SiC/SiC composites. *Journal of Nuclear Materials*, 455(1):387–397, 2014. ISSN 0022-3115. Proceedings of the 16th International Conference on Fusion Reactor Materials (ICFRM-16).

[62] Aljaž Ivekovic, Sasa Novak, Goran Drazic, Darina Blagoeva, and Sehila Gonzalez de Vicente. Current status and prospects of SiCf/SiC for fusion structural applications. *Journal of the European Ceramic Society*, 33(10):1577–1589, 2013. ISSN 0955-2219.

[63] J. A. DiCarlo, N.P.Bansal, and J.Lamon. Advances in SiC/SiC Composites for Aero-Propulsion. 2014.

[64] S. Yajima, J. Hayashi, M. Omori, and K. Okamura. Development of a silicon carbide fibre with high tensile strength. *Nature*, 261(5562):683–685, June 1976. doi: 10.1038/261683a0.

[65] A.A. Campbell and T.D. Burchell. 3.11 - radiation effects in graphite. In R. J.M. Konings and R. E. Stoller, editors, *Comprehensive Nuclear Materials (Second Edition)*, pages 398–436. Elsevier, 2020. doi: 10.1016/B978-0-12-803581-8.12055-7.

[66] Joey Kabel, Peter Hosemann, Yevhen Zayachuk, David E. J. Armstrong, Takaaki Koyanagi, Yutai Katoh, and Christian Deck. Ceramic composites: A review of toughening mechanisms and demonstration of micropillar compression for interface property extraction. *Journal of Materials Research*, 33(4):424–439, 2018. doi: 10.1557/jmr.2017.473.

[67] A. Hussey, R. De Meyere, C. Deck, D.E.J. Armstrong, and Y. Zayachuk. Statistically sound application of fiber push-out method for the study of locally non-uniform interfacial properties of SiC-SiC fiber composites. *Journal of the European Ceramic Society*, 40(4):1052–1056, 2020. ISSN 0955-2219.

[68] Dinesh K. Shetty. Shear-lag analysis of fiber push-out (indentation) tests for estimating interfacial friction stress in ceramic-matrix composites. *J. of the American Ceramic Society*, 71(2):C-107–C-109, 1988. doi: https://doi.org/10.1111/j.1151-2916.1988.tb05843.x. URL https://ceramics.onlinelibrary.wiley.com/doi/abs/10.1111/j.1151-2916.1988.tb05843.x.

[69] P. Lawrence. Some theoretical considerations of fibre pull-out from an elastic matrix. *Journal of Materials Science*, 135:102817, 1972. ISSN 1573-4803. doi: https://doi.org/10.1007/BF00549541.

[70] LB Greszczuk. Theoretical studies of the mechanics of the fiber-matrix interface in composites. 1969.

[71] Francis Rebillat, Jacques Lamon, Roger Naslain, Edgar Lara-Curzio, Mattison K Ferber, and Theodore M Besmann. Properties of multilayered interphases in sic/sic chemical-vapor-infiltrated composites with “weak” and “strong” interfaces. *Journal of the American Ceramic Society*, 81(9): 2315–2326, 1998.

[72] Robin MG De Meyere, Kay Song, Louise Gale, Stephen Harris, Ian M Edmonds, Thomas J Marrow, Eduardo Saiz, Finn Giuliani, David EJ Armstrong, and Oriol Gavaldà-Diaz. A novel trench fibre push-out method to evaluate interfacial failure in long fibre composites. *Journal of Materials Research*, 36:2305–2314, 2021.

[73] TR Barrett, G Ellwood, G Perez, M Kovari, M Fursdon, F Domptail, S Kirk, L Boccaccini, and J-H You. Plasma facing components for the european demo: advances in engineering designs. In *29th Symposium on Fusion Technology (SOFT 2016)*, 2016.

[74] Manfred Lipa, A Durocher, R Tivey, Th Huber, B Schedler, and J Weigert. The use of copper alloy cucrzr as a structural material for actively cooled plasma facing and in vessel components. *Fusion engineering and design*, 75:469–473, 2005.

[75] J-H You and M Miskiewicz. Material parameters of copper and cucrzr alloy for cyclic plasticity at elevated temperatures. *Journal of Nuclear Materials*, 373(1-3):269–274, 2008.

[76] I Sriyantika, D D'Addona, et al. 3d-printed pure copper: Density and thermal treatments effects. In *Procedia CIRP*, volume 96, pages 239–244. Elsevier, 2021.

[77] Anton Hohenwarter and Reinhard Pippan. Fracture and fracture toughness of nanopolycrystalline metals produced by severe plastic deformation. *Philosophical Transactions of the Royal Society A: Mathematical, Physical and Engineering Sciences*, 373(2038):20140366, 2015.

[78] HM Ledbetter and ER Naimon. Elastic properties of metals and alloys. ii. copper. *Journal of physical and chemical reference data*, 3(4):897–935, 1974.

[79] Stefanie Japel, Beate Schwager, Reinhard Boehler, and Marvin Ross. Melting of copper and nickel at high pressure: The role of d electrons. *Physical Review Letters*, 95(16):167801, 2005.

[80] Xiaoyu Hu, Chao Wei, Harold Margolin, and Said Nourbakhsh. The bauschinger effect and the stresses in a strained single crystal. *Scripta metallurgica et materialia*, 27(7):865–870, 1992.

[81] P Lukáš and L Kunz. Role of persistent slip bands in fatigue. *Philosophical magazine*, 84(3-5): 317–330, 2004.

[82] Lyle E Levine, Mark R Stoudt, Adam Creuziger, Thien Q Phan, Ruqing Xu, and Michael E Kassner. Basis for the bauschinger effect in copper single crystals: changes in the long-range internal stress with reverse deformation. *Journal of Materials Science*, 54:6579–6585, 2019.

[83] Marlene W Kapp, Christoph Kirchlechner, Reinhard Pippan, and Gerhard Dehm. Importance of dislocation pile-ups on the mechanical properties and the bauschinger effect in microcantilevers. *Journal of Materials Research*, 30(6):791–797, 2015.

[84] Ritwik Bandyopadhyay, Sven E Gustafson, Kartik Kapoor, Diwakar Naragani, Darren C Pagan, and Michael D Sangid. Comparative assessment of backstress models using high-energy x-ray diffraction microscopy experiments and crystal plasticity finite element simulations. *International journal of plasticity*, 136:102887, 2021.

[85] Dávid Ugi, Kolja Zoller, Kolos Lukács, Zsolt Fogarassy, István Groma, Szilvia Kalácska, Katrin Schulz, and Péter Dusán Ispánovity. Irreversible evolution of dislocation pile-ups during cyclic microcantilever bending. *Materials & Design*, 238:112682, 2024.

[86] H Mughrabi. Dislocation wall and cell structures and long-range internal stresses in deformed metal crystals. *Acta metallurgica*, 31(9):1367–1379, 1983.

[87] E Orowan. Internal stresses and fatigue in metals. In *Proceedings of the Symposium on Internal Stresses and Fatigue in Metals, Detroit*, 1959.

[88] AW Sleeswyk, MR James, DH Plantinga, and WST Maathuis. Reversible strain in cyclic plastic deformation. *Acta Metallurgica*, 26(8):1265–1271, 1978.

[89] ME Kassner, Peter Geantil, and Lyle E Levine. Long range internal stresses in single-phase crystalline materials. *International Journal of Plasticity*, 45:44–60, 2013.

[90] Laurent Meric, Philippe Poubanne, and Georges Cailletaud. Single crystal modeling for structural calculations: part 1—model presentation. 1991.

[91] JL Chaboche and D Nouailhas. Constitutive modeling of ratchetting effects—part i: experimental facts and properties of the classical models. 1989.

[92] N Ohno and J-D Wang. Kinematic hardening rules with critical state of dynamic recovery, part ii: application to experiments of ratchetting behavior. *International journal of plasticity*, 9(3):391–403, 1993.

[93] Suchandrima Das, Felix Hofmann, and Edmund Tarleton. Consistent determination of geometrically necessary dislocation density from simulations and experiments. *International Journal of Plasticity*, 109:18–42, 2018.

[94] AW Sleeswyk and DJ Verel. The rate-determining process in luders band growth. *Scripta metallurgica*, 6(8):677–679, 1972.

[95] Geoffrey Ingram Taylor. Plastic strain in metals. *J. Inst. Metals*, 62:307–324, 1938.

[96] Irene J Beyerlein and Carlos N Tomé. Modeling transients in the mechanical response of copper due to strain path changes. *International Journal of Plasticity*, 23(4):640–664, 2007.

[97] Bo Chen, Jun Jiang, and Fionn PE Dunne. Microstructurally-sensitive fatigue crack nucleation in ni-based single and oligo crystals. *Journal of the Mechanics and Physics of Solids*, 106:15–33, 2017.

[98] MW Perra and I Finnie. Fracture toughness of a high-strength beryllium at room temperature and 300 c. *Journal of Materials Science*, 12:1519–1526, 1977.

[99] Jae-Hwan Kim and Masaru Nakamichi. Effect of grain size on the hardness and reactivity of plasma-sintered beryllium. *Journal of Nuclear Materials*, 453(1):22–26, 2014. ISSN 0022-3115. doi: https://doi.org/10.1016/j.jnucmat.2014.06.019. URL https://www.sciencedirect.com/science/article/pii/S0022311514003766.

[100] A.S. Pokrovsky, S.A. Fabritsiev, R.M. Bagautdinov, and Yu.D. Goncharenko. High-temperature beryllium embrittlement. *Journal of Nuclear Materials*, 233-237:841–846, 1996. ISSN 0022-3115. doi: https://doi.org/10.1016/S0022-3115(96)00027-X. URL https://www.sciencedirect.com/science/article/pii/S002231159600027X.

[101] Marko Knezevic, Irene J. Beyerlein, Donald W. Brown, Thomas A. Sisneros, and Carlos N. Tomé. A polycrystal plasticity model for predicting mechanical response and texture evolution during strain-path changes: Application to beryllium. *International Journal of Plasticity*, 49:185–198, 2013. ISSN 0749-6419. doi: https://doi.org/10.1016/j.ijplas.2013.03.008. URL https://www.sciencedirect.com/science/article/pii/S0749641913000788.

[102] Zebang Zheng, Daniel S Balint, and Fionn PE Dunne. Rate sensitivity in discrete dislocation plasticity in hexagonal close-packed crystals. *Acta Materialia*, 107:17–26, 2016.

[103] Donald William Brown, IJ Beyerlein, Thomas A Sisneros, Bjorn Clausen, and CN Tomé. Role of twinning and slip during compressive deformation of beryllium as a function of strain rate. *International Journal of Plasticity*, 29:120–135, 2012.

[104] Mark C Messner, Moono Rhee, Athanasios Arsenlis, and Nathan R Barton. A crystal plasticity model for slip in hexagonal close packed metals based on discrete dislocation simulations. *Modelling and Simulation in Materials Science and Engineering*, 25(4):044001, 2017.

[105] Viacheslav Kuksenko, Steve Roberts, and Edmund Tarleton. The hardness and modulus of polycrystalline beryllium from nano-indentation. *International Journal of Plasticity*, 116:62–80, 2019. ISSN 0749-6419. doi: https://doi.org/10.1016/j.ijplas.2018.12.008. URL https://www.sciencedirect.com/science/article/pii/S0749641918306260.

[106] David Wilson, Weifeng Wan, and Fionn PE Dunne. Microstructurally-sensitive fatigue crack growth in hcp, bcc and fcc polycrystals. *Journal of the Mechanics and Physics of Solids*, 126:204–225, 2019.

[107] Daniel J Long and Fionn PE Dunne. On the mechanistic driving force for short fatigue crack path. *Journal of the Mechanics and Physics of Solids*, 179:105368, 2023.

[108] Y Sakaguchi Otsuka. Strain field measurement around the crack tip in ni-base superalloy using digital image correlation. *Transactions of the JSME (in Japanese)*, 84(866), 2018.

[109] D Di Maio and SG Roberts. Measuring fracture toughness of coatings using focused-ion-beam-machined microbeams. *Journal of materials research*, 20(2):299–302, 2005.

[110] R Haswell, DW McComb, and W Smith. Preparation of site-specific cross-sections of heterogeneous catalysts prepared by focused ion beam milling. *Journal of microscopy*, 211(2):161–166, 2003.

[111] Warren Carl Oliver and George Mathews Pharr. An improved technique for determining hardness and elastic modulus using load and displacement sensing indentation experiments. *Journal of materials research*, 7(6):1564–1583, 1992.

[112] H Chan, SG Roberts, and J Gong. Micro-scale fracture experiments on zirconium hydrides and phase boundaries. *Journal of Nuclear Materials*, 475:105–112, 2016.

[113] Earl A. Gulbransen and Sven A. Jansson. The high-temperature oxidation, reduction, and volatilization reactions of silicon and silicon carbide. *Oxidation of Metals*, 4:181–201, 1972.

[114] C.H. Carter Jr., R.F. David, and J. Bentley. Kinetics and mechanisms of high-temperature creep in silicon carbide: I, reaction-bonded. *Journal of the American Ceramic Society*, 67(6):409–417, 1984.

[115] Hideaki Kikuchi, Rajiv K. Kalia, Aiichiro Nakano, Priya Vashishta, Paulo S. Branicio, and Fuyuki Shimojo. Brittle dynamic fracture of crystalline cubic silicon carbide (3C-SiC) via molecular dynamics simulation. *Journal of Applied Physics*, 98(10):103524, 2005. doi: 10.1063/1.2135896.

[116] Erich Fitzer and Dieter Hegen. Chemical vapor deposition of silicon carbide and silicon nitride—chemistry's contribution to modern silicon ceramics. *Angewandte Chemie International Edition in English*, 18(4):295–304, 1979.

[117] Francis Rebillat, Jacques Lamon, Roger Naslain, Edgar Lara-Curzio, Mattison K. Ferber, and Theodore M. Besmann. Interfacial bond strength in SiC/C/SiC composite materials, as studied by single-fiber push-out tests. *Journal of the American Ceramic Society*, 81(4):965–978, 2005. doi: https://doi.org/10.1111/j.1151-2916.1998.tb02434.x.

[118] Emilien Buet, James Braun, and Cédric Sauder. Influence of texture and thickness of pyrocarbon coatings as interphase on the mechanical behavior of specific 2.5 d sic/sic composites reinforced with hi-nicalon s fibers. *Coatings*, 12(5):573, 2022.

[119] C.P. Deck, H.E. Khalifa, B. Sammuli, T. Hilsabeck, and C.A. Back. Fabrication of SiC–SiC composites for fuel cladding in advanced reactor designs. *Progress in Nuclear Energy*, 57:38–45, 2012. ISSN 0149-1970. Nuclear Materials: Selected articles from the E-MRS 2011 Spring Meeting.

[120] Zhichao Ma, Hongwei Zhao, Xijie Du, Mingxing Zhou, Xiaoxi Ma, Changyi Liu, and Luquan Ren. Evaluation of nanoindentation load-depth curve of mems bridge structures by calculating the critical elastic-plastic bending deflections. *Applied Surface Science*, 434:1–10, 2018. ISSN 0169-4332. doi: https://doi.org/10.1016/j.apsusc.2017.10.106.

[121] William B. Hillig. Melt infiltration approach to ceramic matrix composites. *Journal of the American Ceramic Society*, 71(2):C-96–C-99, 1988.

[122] Frank H. Gern and Richard Kochendörfer. Liquid silicon infiltration: description of infiltration dynamics and silicon carbide formation. *Composites Part A: Applied Science and Manufacturing*, 28 (4):355–364, 1997. ISSN 1359-835X.

[123] Lance L Snead, Takashi Nozawa, Yutai Katoh, Thak-Sang Byun, Sosuke Kondo, and David A Petti. Handbook of sic properties for fuel performance modeling. *Journal of nuclear materials*, 371(1-3): 329–377, 2007.

[124] M.E. Sawan, N.M. Ghoniem, L. Snead, and Y. Katoh. Damage production and accumulation in SiC structures in inertial and magnetic fusion systems. *Journal of Nuclear Materials*, 417(1):445–450, 2011. ISSN 0022-3115. Proceedings of ICFRM-14.

[125] Wilfried Gauthier, Frédéric Pailler, Jacques Lamon, and Rene Pailler. Oxidation of silicon carbide fibers during static fatigue in air at intermediate temperatures. *Journal of the American Ceramic Society*, 92(9):2067–2073, 2009.

[126] Kohei Morishita, Shojiro Ochiai, Hiroshi Okuda, Toshihiro Inshikawa, Mitsuhiko Sato, and Tadanobu Inoue. Fracture Toughness of a Crystalline Silicon Carbide Fiber (Tyranno-SA3). *Journal of the American Ceramic Society*, 89(8):2571–2576, 2006.

[127] Robin MG De Meyere, Louise Gale, Stephen Harris, Ian M Edmonds, Thomas J Marrow, and David EJ Armstrong. Optimizing the fiber push-out method to evaluate interfacial failure in sic/bn/sic ceramic matrix composites. *Journal of the American Ceramic Society*, 104(6):2741–2752, 2021.

[128] Rongqiao Wang, Jiangbo Han, Jianxing Mao, Dianyin Hu, Xi Liu, and Xiaojun Guo. A molecular dynamics based cohesive zone model for interface failure under monotonic tension of 3d four direction SiCf/SiC composites. *Composite Structures*, 274:114397, 2021. ISSN 0263-8223. doi: https://doi.org/10.1016/j.compstruct.2021.114397.

[129] Z.Cedric Xia and John W. Hutchinson. Mode II fracture toughness of a brittle adhesive layer. *International Journal of Solids and Structures*, 31(8):1133–1148, 1994. ISSN 0020-7683. doi: https://doi.org/10.1016/0020-7683(94)90168-6.

[130] Ronald J. Kerans and Triplicane A. Parthasarathy. Theoretical analysis of the fiber pullout and pushout tests. *Journal of the American Ceramic Society*, 74(7):1585–1596, 1991.

[131] N Chandra and H Ghonem. Interfacial mechanics of push-out tests: theory and experiments. *Composites Part A: Applied Science and Manufacturing*, 32(3):575–584, 2001. ISSN 1359-835X.

[132] Philippe H Geubelle and Jeffrey S Baylor. Impact-induced delamination of composites: a 2D simulation. *Composites Part B: Engineering*, 29(5):589–602, 1998. ISSN 1359-8368. doi: https://doi.org/10.1016/S1359-8368(98)00013-4.

[133] Sachin Joglekar. Nelder-Mead Optimization technique. https://codesachin.wordpress.com/2016/01/16/nelder-mead-optimization/, 2016.

[134] Suchandrima Das, Hongbing Yu, Kenichiro Mizohata, Edmund Tarleton, and Felix Hofmann. Modified deformation behaviour of self-ion irradiated tungsten: A combined nano-indentation, HR-EBSD and crystal plasticity study. *International Journal of Plasticity*, 135:102817, 2020. ISSN 0749-6419. doi: https://doi.org/10.1016/j.ijplas.2020.102817.

[135] J. Kabel, Y. Yang, M. Balooch, C. Howard, T. Koyanagi, K.A. Terrani, Y. Katoh, and P. Hosemann. Micro-mechanical evaluation of SiC-SiC composite interphase properties and debond mechanisms. *Composites Part B: Engineering*, 131:173–183, 2017. ISSN 1359-8368. doi: https://doi.org/10.1016/j.compositesb.2017.07.035. URL https://www.sciencedirect.com/science/article/pii/S1359836817311502.

[136] Oriol Gavalda-Diaz, Riccardo Manno, Antonio Melro, Giuliano Allegri, Stephen R Hallett, Luc Vandeperre, Eduardo Saiz, and Finn Giuliani. Mode i and mode ii interfacial fracture energy of sic/bn/sic cmcs. *Acta Materialia*, 215:117125, 2021.

[137] WM Mueller, Judith Moosburger-Will, Markus GR Sause, M Greisel, and S Horn. Quantification of crack area in ceramic matrix composites at single-fiber push-out testing and influence of pyrocarbon

fiber coating thickness on interfacial fracture toughness. *Journal of the European Ceramic Society*, 35(11):2981–2989, 2015.

[138] N Carrère, E Martin, and J Lamon. The influence of the interphase and associated interfaces on the deflection of matrix cracks in ceramic matrix composites. *Composites Part A: Applied Science and Manufacturing*, 31(11):1179–1190, 2000. ISSN 1359-835X.

[139] M. Sakai, R. C. Bradt, and D.B. Fischbach. Fracture toughness anisotropy of a pyrolytic carbon. *Mater Sci*, 21:1491–1501, 1986.

[140] AG Evans and FW Zok. The physics and mechanics of fibre-reinforced brittle matrix composites. *Journal of Materials science*, 29:3857–3896, 1994.

[141] C Liang and JW Hutchinson. Mechanics of the fiber pushout test. *Mechanics of materials*, 14(3): 207–221, 1993.

[142] Matthew R. Begley and John W. Hutchinson. *The Mechanics and Reliability of Films, Multilayers and Coatings*. Cambridge University Press, United Kingdom, 2022.

[143] Yutai Katoh and Lance L Snead. Silicon carbide and its composites for nuclear applications–historical overview. *Journal of Nuclear Materials*, 526:151849, 2019.

[144] Bei Yang, Xingui Zhou, and Yuxin Chai. Mechanical properties of sicf/sic composites with pyc and the bn interface. *Ceramics International*, 41(5, Part B):7185–7190, 2015. ISSN 0272-8842. doi: https://doi.org/10.1016/j.ceramint.2015.02.041. URL https://www.sciencedirect.com/science/article/pii/S0272884215002606.

[145] Justine Delage, Eduardo Saiz, and Nasrin Al Nasiri. Fracture behaviour of sic/sic ceramic matrix composite at room temperature. *Journal of the European Ceramic Society*, 42(7):3156–3167, 2022. ISSN 0955-2219. doi: https://doi.org/10.1016/j.jeurceramsoc.2022.01.060. URL https://www.sciencedirect.com/science/article/pii/S0955221922000863.

[146] Takashi Nozawa, Takaaki Koyanagi, Yutai Katoh, and Hiroyasu Tanigawa. High-dose, intermediate-temperature neutron irradiation effects on silicon carbide composites with varied fiber/matrix interfaces. *Journal of the European Ceramic Society*, 39(8):2634–2647, 2019.

[147] Alejandro G Perez-Bergquist, Takashi Nozawa, Chunghao Shih, Keith J Leonard, Lance L Snead, and Yutai Katoh. High dose neutron irradiation of hi-nicalon type s silicon carbide composites, part 1: Microstructural evaluations. *Journal of Nuclear Materials*, 462:443–449, 2015.

[148] EB Callaway, PG Christodoulou, and FW Zok. Deformation, rupture and sliding of fiber coatings in ceramic composites. *Journal of the Mechanics and Physics of Solids*, 132:103673, 2019.

[149] E. Buet, C. Sauder, S. Poissonnet, P. Brender, R. Gadiou, and C. Vix-Guterl. Influence of chemical and physical properties of the last generation of silicon carbide fibres on the mechanical behaviour of sic/sic composite. *Journal of the European Ceramic Society*, 32(3):547–557, 2012. ISSN 0955-2219. doi: https://doi.org/10.1016/j.jeurceramsoc.2011.09.023. URL https://www.sciencedirect.com/science/article/pii/S0955221911004912.

[150] JJ Petrovic. Weibull statistical fracture theory for the fracture of ceramics. *Metallurgical Transactions A*, 18:1829–1834, 1987.

[151] C Sauder, A Brusson, and J Lamon. Influence of interface characteristics on the mechanical properties of hi-nicalon type-s or tyranno-sa3 fiber-reinforced sic/sic minicomposites. *International Journal Of Applied Ceramic Technology*, 7(3):291–303, 2010.

[152] W Yang, A Kohyama, T Noda, Y Katoh, T Hinoki, H Araki, and J Yu. Interfacial characterization of cvi-sic/sic composites. *Journal of nuclear materials*, 307:1088–1092, 2002.

[153] T Hinoki, W Zhang, A Kohyama, S Sato, and T Noda. Effect of fiber coating on interfacial shear strength of sic/sic by nano-indentation technique. *Journal of Nuclear materials*, 258:1567–1571, 1998.

[154] Triplicane A Parthasarathy, Douglas R Barlage, Paul D Jero, and Ronald J Kerans. Effect of interfacial roughness parameters on the fiber pushout behavior of a model composite. *Journal of the American Ceramic Society*, 77(12):3232–3236, 1994.

[155] William F Skerjanc and Blaise P Collin. Assessment of material properties for triso fuel particles in parfume. Technical report, Idaho National Lab.(INL), Idaho Falls, ID (United States), 2018.

[156] M Herbreteau, S Jouannigot, P Weisbecker, A Coradi, and E Martin. A new push-out procedure for the evaluation of interfacial properties of sic/sic composites. In *ECCM15-15TH European Conference On Composite Materials, Venice, Italy*, pages 2–4, 2012.

[157] Yang Chen and James Marrow. Effect of irradiation swelling on the mechanical properties of unidirectional sic/sic composites: A numerical investigation at microstructural level. *Journal of Nuclear Materials*, 569:153918, 2022. ISSN 0022-3115. doi: https://doi.org/10.1016/j.jnucmat.2022.153918. URL https://www.sciencedirect.com/science/article/pii/S0022311522004044.

[158] Sosuke Kondo, Tatsuya Hinoki, Makoto Nonaka, and Kazumi Ozawa. Irradiation-induced shrinkage of highly crystalline sic fibers. *Acta Materialia*, 83:1–9, 2015.

[159] MTP Rigby-Bell, AJ Leide, V Kuksenko, CJ Smith, G Zilahi, L Gale, T Razzell, J Wade-Zhu, and DJ Bowden. The response of silicon carbide composites to he ion implantation and ramifications for use as a fusion reactor structural material. *Journal of the European Ceramic Society*, 43(16): 7390–7402, 2023.

[160] ME Sawan, Yutai Katoh, and Lance Lewis Snead. Transmutation of silicon carbide in fusion nuclear environment. *Journal of Nuclear Materials*, 442(1-3):S370–S375, 2013.

[161] NA Fleck, GM Muller, Mike F Ashby, and John W Hutchinson. Strain gradient plasticity: theory and experiment. *Acta Metallurgica et materialia*, 42(2):475–487, 1994.

[162] Nikoletta G Prastiti, Yilun Xu, Daniel S Balint, and Fionn PE Dunne. Discrete dislocation, crystal plasticity and experimental studies of fatigue crack nucleation in single-crystal nickel. *International Journal of Plasticity*, 126:102615, 2020.

[163] William A Counts, Michael V Braginsky, Corbett C Battaile, and Elizabeth A Holm. Predicting the hall–petch effect in fcc metals using non-local crystal plasticity. *International journal of plasticity*, 24(7):1243–1263, 2008.

[164] Hao Lyu, Annie Ruimi, and Hussein M Zbib. A dislocation-based model for deformation and size effect in multi-phase steels. *International Journal of Plasticity*, 72:44–59, 2015.

[165] Fengwei Sun, Edward D Meade, and Noel P O'Dowd. Strain gradient crystal plasticity modelling of size effects in a hierarchical martensitic steel using the voronoi tessellation method. *International Journal of Plasticity*, 119:215–229, 2019.

[166] Chaoyi Zhu, Veronica Livescu, Tyler Harrington, Olivia Dippo, George T Gray III, and Kenneth S Vecchio. Investigation of the shear response and geometrically necessary dislocation densities in shear localization in high-purity titanium. *International Journal of Plasticity*, 92:148–163, 2017.

[167] Soran Birosca, Gang Liu, Rengen Ding, Jun Jiang, Thomas Simm, Chris Deen, and Mark Whittaker. The dislocation behaviour and gnd development in a nickel based superalloy during creep. *International Journal of Plasticity*, 118:252–268, 2019.

[168] A Ramazani, K Mukherjee, A Schwedt, P Goravanchi, U Prahl, and W Bleck. Quantification of the

effect of transformation-induced geometrically necessary dislocations on the flow-curve modelling of dual-phase steels. *International Journal of Plasticity*, 43:128–152, 2013.

[169] Fengwei Sun, Shengxun Wang, and Qingge Xie. Role of particles and lattice rotation in tension–compression asymmetry of aluminium alloys. *International Journal of Plasticity*, 159:103464, 2022.

[170] Xiazi Xiao, Lirong Chen, Long Yu, and Huiling Duan. Modelling nano-indentation of ion-irradiated fcc single crystals by strain-gradient crystal plasticity theory. *International Journal of Plasticity*, 116:216–231, 2019.

[171] A Arsenlis and DM Parks. Crystallographic aspects of geometrically-necessary and statistically-stored dislocation density. *Acta materialia*, 47(5):1597–1611, 1999.

[172] Angus J Wilkinson, Graham Meaden, and David J Dingley. High-resolution elastic strain measurement from electron backscatter diffraction patterns: New levels of sensitivity. *Ultramicroscopy*, 106 (4-5):307–313, 2006.

[173] Eralp Demir, Dierk Raabe, Nader Zaafarani, and Stefan Zaefferer. Investigation of the indentation size effect through the measurement of the geometrically necessary dislocations beneath small indents of different depths using ebsd tomography. *Acta Materialia*, 57(2):559–569, 2009.

[174] Peter Joachim Konijnenberg, Stefan Zaefferer, and Dierk Raabe. Assessment of geometrically necessary dislocation levels derived by 3d ebsd. *Acta Materialia*, 99:402–414, 2015.

[175] Wyatt A Witzen, Andrew T Polonsky, Tresa M Pollock, and Irene J Beyerlein. Three-dimensional maps of geometrically necessary dislocation densities in additively manufactured ni-based superalloy in718. *International Journal of Plasticity*, 131:102709, 2020.

[176] Jun Jiang, T Ben Britton, and Angus J Wilkinson. The orientation and strain dependence of dislocation structure evolution in monotonically deformed polycrystalline copper. *International Journal of Plasticity*, 69:102–117, 2015.

[177] Haiming Zhang and Xianghuai Dong. Physically based crystal plasticity fem including geometrically necessary dislocations: numerical implementation and applications in micro-forming. *Computational Materials Science*, 110:308–320, 2015.

[178] Xuefeng Tang, Zhizhou Wang, Xinyun Wang, Lei Deng, Mao Zhang, Pan Gong, Junsong Jin, and MW Fu. Unraveling size-affected plastic heterogeneity and asymmetry during micro-scaled defor-

mation of cp-ti by non-local crystal plasticity modeling. *International Journal of Plasticity*, 170: 103733, 2023.

[179] Morton E Gurtin. On the plasticity of single crystals: free energy, microforces, plastic-strain gradients. *Journal of the Mechanics and Physics of Solids*, 48(5):989–1036, 2000.

[180] LP Evers, WAM Brekelmans, and MGD1115 Geers. Non-local crystal plasticity model with intrinsic ssd and gnd effects. *Journal of the Mechanics and Physics of Solids*, 52(10):2379–2401, 2004.

[181] Mitsutoshi Kuroda and Viggo Tvergaard. A finite deformation theory of higher-order gradient crystal plasticity. *Journal of the Mechanics and Physics of Solids*, 56(8):2573–2584, 2008.

[182] Habib Pouriayevali and Bai-Xiang Xu. Decomposition of dislocation densities at grain boundary in a finite-deformation gradient crystal-plasticity framework. *International Journal of Plasticity*, 96: 36–55, 2017.

[183] XD Zan, X Guo, GJ Weng, and G Chen. Nanoindentation study of δ-phase zirconium hydride using the crystal plasticity model. *International Journal of Plasticity*, page 103675, 2023.

[184] Kaidi Li, Bin Tang, Mengqi Zhang, Liguo Zhao, Xudong Liu, Jiangkun Fan, and Jinshan Li. A hydrogen diffusion model considering grain boundary characters based on crystal plasticity framework. *International Journal of Plasticity*, 169:103740, 2023.

[185] PF Gao, MY Fei, M Zhan, and MW Fu. Microstructure-and damage-nucleation-based crystal plasticity finite element modeling for the nucleation of multi-type voids during plastic deformation of al alloys. *International Journal of Plasticity*, 165:103609, 2023.

[186] Hong Dai. *Geometrically-necessary dislocation density in continuum plasticity theory, FEM implementation and applications*. PhD thesis, Massachusetts Institute of Technology, 1997.

[187] R Hill and JR0254 Rice. Constitutive analysis of elastic-plastic crystals at arbitrary strain. *Journal of the Mechanics and Physics of Solids*, 20(6):401–413, 1972.

[188] R. J. Asaro. Crystal Plasticity. *Journal of Applied Mechanics*, 50(4b):921–934, 12 1983. ISSN 0021-8936. doi: 10.1115/1.3167205.

[189] TJ Ruggles, DT Fullwood, and JW Kysar. Resolving geometrically necessary dislocation density onto individual dislocation types using ebsd-based continuum dislocation microscopy. *International Journal of Plasticity*, 76:231–243, 2016.

[190] Paolo Cermelli and Morton E Gurtin. On the characterization of geometrically necessary dislocations in finite plasticity. *Journal of the Mechanics and Physics of Solids*, 49(7):1539–1568, 2001.

[191] Derek Hull and David J Bacon. *Introduction to dislocations*, volume 37. Elsevier, 2011.

[192] Rajat Arora, Xiaohan Zhang, and Amit Acharya. Finite element approximation of finite deformation dislocation mechanics. *Computer Methods in Applied Mechanics and Engineering*, 367:113076, 2020.

[193] H W Kuhn, A W Tucker, and Neyman J. Proceedings of the second berkeley symposium on mathematical statistics and probability. In *Nonlinear programming*, pages 481–492. Berkeley and Los Angeles, University of California Press, 1951.

[194] EP Busso, FT Meissonnier, and NP O'dowd. Gradient-dependent deformation of two-phase single crystals. *Journal of the Mechanics and Physics of Solids*, 48(11):2333–2361, 2000.

[195] A Ma, F Roters, and D Raabe. A dislocation density based constitutive model for crystal plasticity fem including geometrically necessary dislocations. *Acta Materialia*, 54(8):2169–2179, 2006.

[196] Mitsutoshi Kuroda. On large-strain finite element solutions of higher-order gradient crystal plasticity. *International Journal of Solids and Structures*, 48(24):3382–3394, 2011. ISSN 0020-7683. doi: https://doi.org/10.1016/j.ijsolstr.2011.08.008. URL https://www.sciencedirect.com/science/article/pii/S0020768311002873.

[197] Aldo Marano, Lionel Gélébart, and Samuel Forest. Intragranular localization induced by softening crystal plasticity: Analysis of slip and kink bands localization modes from high resolution fft-simulations results. *Acta Materialia*, 175:262–275, 2019.

[198] Fei-Fan Li and Gang Fang. Modeling of 3d plastic anisotropy and asymmetry of extruded magnesium alloy and its applications in three-point bending. *International Journal of Plasticity*, 130:102704, 2020. ISSN 0749-6419. doi: https://doi.org/10.1016/j.ijplas.2020.102704. URL https://www.sciencedirect.com/science/article/pii/S0749641919306953.

[199] TO Erinosho and FPE Dunne. Lattice strain distributions due to elastic distortions and gnd development in polycrystals. *Journal of the Mechanics and Physics of Solids*, 67:62–86, 2014.

[200] Yilun Xu. A non-local methodology for geometrically necessary dislocations and application to crack tips. *International Journal of Plasticity*, 140:102970, 2021. ISSN 0749-6419. doi: https://doi.org/10.

1016/j.ijplas.2021.102970. URL https://www.sciencedirect.com/science/article/pii/S0749641921000450.

[201] Zhonghao Jiang, Jianshe Lian, and B Baudelet. A dislocation density approximation for the flow stress—grain size relation of polycrystals. *Acta metallurgica et materialia*, 43(9):3349–3360, 1995.

[202] Haiming Zhang and Xianghuai Dong. Experimental and numerical studies of coupling size effects on material behaviors of polycrystalline metallic foils in microscale plastic deformation. *Materials Science and Engineering: A*, 658:450–462, 2016.

[203] Maoyuan Jiang, Zhengxuan Fan, Serge Kruch, and Benoit Devincre. Grain size effect of fcc polycrystal: A new cpfem approach based on surface geometrically necessary dislocations. *International Journal of Plasticity*, 150:103181, 2022.

[204] Dylan Agius, Anna Kareer, Abdullah Al Mamun, Christopher Truman, David M Collins, Mahmoud Mostafavi, and David Knowles. A crystal plasticity model that accounts for grain size effects and slip system interactions on the deformation of austenitic stainless steels. *International Journal of Plasticity*, 152:103249, 2022.

[205] Eralp Demir, Edward W Horton, Mehdi Mokhtarishirazabad, Mahmoud Mostafavi, and David Knowles. Grain size and shape dependent crystal plasticity finite element model and its application to electron beam welded ss316l. *Journal of the Mechanics and Physics of Solids*, page 105331, 2023.

[206] Romain Quey, PR Dawson, and Fabrice Barbe. Large-scale 3d random polycrystals for the finite element method: Generation, meshing and remeshing. *Computer Methods in Applied Mechanics and Engineering*, 200(17-20):1729–1745, 2011.

[207] Hojun Lim, Corbett C Battaile, Joseph E Bishop, and James W Foulk III. Investigating mesh sensitivity and polycrystalline rves in crystal plasticity finite element simulations. *International Journal of Plasticity*, 121:101–115, 2019.

[208] Vladislav Levkovitch and Bob Svendsen. On the large-deformation-and continuum-based formulation of models for extended crystal plasticity. *International Journal of Solids and Structures*, 43(24): 7246–7267, 2006.

[209] Ole Bøcker Pedersen, LM Brown, and WM Stobbs. The bauschinger effect in copper. *Acta Metallurgica*, 29(11):1843–1850, 1981.

[210] Marion Kreins, Simon Schilli, Thomas Seifert, AHS Iyer, Magnus Hörnqvist Colliander, Sebastian Wesselmecking, and Ulrich Krupp. Bauschinger effect and latent hardening under cyclic micro-bending of ni-base alloy 718 single crystals: Part i. experimental analysis of single and multi slip plasticity. *Materials Science and Engineering: A*, 827:142027, 2021.

[211] Peter J Armstrong, CO Frederick, et al. *A mathematical representation of the multiaxial Bauschinger effect*, volume 731. Berkeley Nuclear Laboratories Berkeley, CA, 1966.

[212] Wulf Dettmer and Stefanie Reese. On the theoretical and numerical modelling of armstrong–frederick kinematic hardening in the finite strain regime. *Computer Methods in Applied Mechanics and Engineering*, 193(1-2):87–116, 2004.

[213] Ling Li, Luming Shen, and Gwénaëlle Proust. A texture-based representative volume element crystal plasticity model for predicting bauschinger effect during cyclic loading. *Materials Science and Engineering: A*, 608:174–183, 2014.

[214] Megan Taylor, Dylan Agius, David Knowles, and Mahmoud Mostafavi. An investigation into the robustness of a crystal plasticity finite element model. In *Pressure Vessels and Piping Conference*, volume 83860, page V006T06A094. American Society of Mechanical Engineers, 2020.

[215] Simon Schilli, Thomas Seifert, Marion Kreins, and Ulrich Krupp. Bauschinger effect and latent hardening under cyclic micro-bending of ni-base alloy 718 single crystals: Part ii. single crystal plasticity modeling with latent kinematic hardening. *Materials Science and Engineering: A*, 830: 142030, 2022.

[216] Daniel Kiener, Christian Motz, W Grosinger, D Weygand, and Reinhard Pippan. Cyclic response of copper single crystal micro-beams. *Scripta Materialia*, 63(5):500–503, 2010.

[217] H-J Bunge. *Texture analysis in materials science: mathematical methods*. Elsevier, 2013.

[218] Erich Schmid and Walter Boas. *Kristallplastizität: mit besonderer Berücksichtigung der Metalle*, volume 17. Springer-Verlag, 2013.

[219] Benoît Beausir, László S Tóth, and Kenneth W Neale. Ideal orientations and persistence characteristics of hexagonal close packed crystals in simple shear. *Acta Materialia*, 55(8):2695–2705, 2007.

[220] Luca Gambirasio, Guido Chiantoni, and Egidio Rizzi. On the consequences of the adoption of the zaremba–jaumann objective stress rate in fem codes. *Archives of Computational Methods in Engineering*, 23:39–67, 2016.

[221] Alexandra J. Cackett, Chris D. Hardie, Joven J.H. Lim, and Edmund Tarleton. Spherical indentation of copper: Crystal plasticity vs experiment. *Materialia*, 7:100368, 2019. ISSN 2589-1529. doi: https://doi.org/10.1016/j.mtla.2019.100368. URL https://www.sciencedirect.com/science/article/pii/S2589152919301644.

[222] Stuart B. Brown, Kwon H. Kim, and Lallit Anand. An internal variable constitutive model for hot working of metals. *International Journal of Plasticity*, 5(2):95–130, 1989. ISSN 0749-6419. doi: https://doi.org/10.1016/0749-6419(89)90025-9. URL https://www.sciencedirect.com/science/article/pii/0749641989900259.

[223] T Vermeij, J Wijnen, RHJ Peerlings, MGD Geers, and JPM Hoefnagels. A quasi-2d integrated experimental–numerical approach to high-fidelity mechanical analysis of metallic microstructures. *Acta Materialia*, 264:119551, 2024.

[224] Andrew T Jennings, Michael J Burek, and Julia R Greer. Microstructure versus size: mechanical properties of electroplated single crystalline cu nanopillars. *Physical review letters*, 104(13):135503, 2010.

[225] U Essmann, U Gösele, and H Mughrabi. A model of extrusions and intrusions in fatigued metals i. point-defect production and the growth of extrusions. *Philosophical Magazine A*, 44(2):405–426, 1981.

[226] K Differt, U Esmann, and H Mughrabi. A model of extrusions and intrusions in fatigued metals ii. surface roughening by random irreversible slip. *Philosophical Magazine A*, 54(2):237–258, 1986.

[227] U Essmann and HJPMA Mughrabi. Annihilation of dislocations during tensile and cyclic deformation and limits of dislocation densities. *Philosophical Magazine A*, 40(6):731–756, 1979.

[228] Hael Mughrabi. Cyclic slip irreversibilities and the evolution of fatigue damage. *Metallurgical and Materials Transactions B*, 40:431–453, 2009.

[229] EA Repetto and M Ortiz. A micromechanical model of cyclic deformation and fatigue-crack nucleation in fcc single crystals. *Acta materialia*, 45(6):2577–2595, 1997.

[230] Michael D Sangid. The physics of fatigue crack initiation. *International journal of fatigue*, 57: 58–72, 2013.

[231] S Carpentier, RA Pitts, PC Stangeby, JD Elder, AS Kukushkin, S Lisgo, W Fundamenski, and

D Moulton. Modelling of beryllium erosion–redeposition on iter first wall panels. *Journal of Nuclear Materials*, 415(1):S165–S169, 2011.

[232] Kenneth A Walsh. *Beryllium chemistry and processing*. ASM international, 2009.

[233] T Ihli, TK Basu, LM Giancarli, S Konishi, S Malang, F Najmabadi, S Nishio, AR Raffray, CVS Rao, A Sagara, et al. Review of blanket designs for advanced fusion reactors. *Fusion Engineering and Design*, 83(7-9):912–919, 2008.

[234] Marek Rubel, A Widdowson, Justyna Grzonka, E Fortuna-Zalesna, Sunwoo Moon, Per Petersson, N Ashikawa, N Asakura, D Hamaguchi, Y Hatano, et al. Dust generation in tokamaks: Overview of beryllium and tungsten dust characterisation in jet with the iter-like wall. *Fusion engineering and design*, 136:579–586, 2018.

[235] Donald William Brown, JD Almer, Bjorn Clausen, PL Mosbrucker, Thomas A Sisneros, and Sven C Vogel. Twinning and de-twinning in beryllium during strain path changes. *Materials Science and Engineering: A*, 559:29–39, 2013.

[236] RK Govila. Metallographie observations on slow crack growth in beryllium monocrystals. *Journal of the Less Common Metals*, 21(2):215–222, 1970.

[237] M Ausloos and B Lalevic. On the cleavage plane of beryllium. *Solid State Communications*, 18(6): 709–711, 1976.

[238] Daniel J Long, Yang Liu, Weifeng Wan, and Fionn PE Dunne. A microstructure-sensitive analytical solution for short fatigue crack growth rate in metallic materials. *International Journal of Mechanical Sciences*, 253:108365, 2023.

[239] H Mecking and UF Kocks. Kinetics of flow and strain-hardening. *Acta metallurgica*, 29(11):1865–1875, 1981.

[240] V Mishin, I Shishov, E Ubyivovk, I Kasatkin, and A Shamshurin. Effect of texture on strain localization and crack initiation in polycrystalline beryllium under static tension: Experimental study and micromechanical simulations. *Metallurgical and Materials Transactions A*, 54(8):3211–3224, 2023.

[241] Ping Zhang, Lu Zhang, KP Baxevanakis, LG Zhao, and Chris Bullough. Modelling short crack propagation in a single crystal nickel-based superalloy using crystal plasticity and xfem. *International Journal of Fatigue*, 136:105594, 2020.

[242] MH Jones, RT Bubsey, and WF Brown Jr. Crack toughness evaluation of hot pressed and forged beryllium. *Journal of Testing and Evaluation*, 1(2):100–109, 1973.

[243] THOMAS COLE POLLOCK. *THE FRACTURE OF BERYLLIUM SINGLE CRYSTALS.* University of Virginia, 1977.

[244] II Papirov, PI Stoev, and GF Tikhinskii. Failure of single crystals of beryllium. *Strength of Materials*, 11(7):763–769, 1979.

[245] Heng-Tie Lee and RM Brick. Deformation of beryllium single crystals at 25 c to 500 c. 1953.

[246] Ali Abbaszadeh Bidokhti, Amir Reza Shahani, and Mohammad Reza Amini Fasakhodi. Displacement-controlled crack growth in double cantilever beam specimen: A comparative study of different models. *Proceedings of the Institution of Mechanical Engineers, Part C: Journal of Mechanical Engineering Science*, 231(15):2835–2847, 2017.

[247] Wendong Zhang, Xianmin Chen, and Jun Yang. A convenient method for simulating crack propagation in panel structures based on the secondary development of abaqus. *Engineering Proceedings*, 80(1):24, 2025.

[248] Albert Turon, Carlos G Davila, Pedro Ponces Camanho, and Josep Costa. An engineering solution for mesh size effects in the simulation of delamination using cohesive zone models. *Engineering fracture mechanics*, 74(10):1665–1682, 2007.

[249] E Harsono, S Swaddiwudhipong, and ZS Liu. The effect of friction on indentation test results. *Modelling and Simulation in Materials Science and Engineering*, 16(6):065001, 2008.